uOttawa

L'Université canadienne
Canada's university

FACULTÉ DES ÉTUDES SUPÉRIEURES ET POSTOCTORALES

uOttawa

L'Université canadienne
Canada's university

FACULTY OF GRADUATE AND POSDOCTORAL STUDIES

Meamer A. El Nakla

AUTEUR DE LA THÈSE / AUTHOR OF THESIS

Ph.D. (Mechanical Engineering)

GRADE / DEGREE

Department of Mechanical Engineering

FACULTÉ, ÉCOLE, DÉPARTEMENT / FACULTY, SCHOOL, DEPARTMENT

Experimental and Analytical Study of Inverted Annular Flow Film Boiling Heat Transfer in a Vertical Tube Using R-134A

TITRE DE LA THÈSE / TITLE OF THESIS

Shui-Chih Cheng

DIRECTEUR (DIRECTRICE) DE LA THÈSE / THESIS SUPERVISOR

Dionysius Groeneveld

CO-DIRECTEUR (CO-DIRECTRICE) DE LA THÈSE / THESIS CO-SUPERVISOR

EXAMINATEURS (EXAMINATRICES) DE LA THÈSE / THESIS EXAMINERS

Junjie Gu

Roger Milane

William Hallett

David Novog

Gary W. Slater

Le Doyen de la Faculté des études supérieures et postdoctorales / Dean of the Faculty of Graduate and Postdoctoral Studies

EXPERIMENTAL AND ANALYTICAL STUDY OF INVERTED ANNULAR FLOW FILM BOILING HEAT TRANSFER IN A VERTICAL TUBE USING R-134A

BY

MEAMER A. EL NAKLA

A dissertation submitted to the School of Graduate Studies and Research of the Ottawa-Carleton Institute for Mechanical and Aeronautical Engineering at the University of Ottawa in partial fulfillment of the requirements for the degree of Doctor of Philosophy in Mechanical Engineering.

UNIVERSITÉ D' OTTAWA
UNIVERSITY OF OTTAWA

Ottawa-Carleton Institute for Mechanical and Aeronautical Engineering
University of Ottawa, Ottawa, Ontario, Canada K1N 6N5

2007

Your file Votre référence
ISBN: 978-0-494-49342-7
Our file Notre référence
ISBN: 978-0-494-49342-7

EXPERIMENTAL AND ANALYTICAL STUDY OF INVERTED ANNULAR FLOW FILM BOILING HEAT TRANSFER IN A VERTICAL TUBE USING R-134A

Dr. S. C. Cheng, Co-Supervisor

Dr. D. C. Groeneveld, Co-Supervisor

Meamer A. El Nakla, Candidate

Dedication

To the two who love me without waiting to be rewarded

My parents

ABSTRACT

An experimental investigation of inverted annular film boiling heat transfer has been performed for vertical up-flow in a round tube. The working fluid was R-134a and the flow conditions covered a pressure range of 640 to 2390 kPa (water equivalent range: 4000 to 14000 kPa) and a mass flux range of 500 to 4000 $kgm^{-2}s^{-1}$ (water equivalent range: 700 to 5700 $kgm^{-2}s^{-1}$). The inlet qualities of the tests ranged from -0.75 to -0.03. The hot-patch technique is used to obtain the subcooled film boiling measurements.

The parametric trends of the heat transfer coefficient with respect to mass flux, inlet quality, heat flux and pressure are examined and compared to reported parametric trends from the literature. The comparison shows agreement between observed effects of flow parameters with those reported by other researchers. The heat transfer vs. quality curve is divided into four different regions. It is shown that these regions are dependent on pressure, mass flux and local quality.

A two-fluid one-dimensional model has been developed to predict the wall temperature of an internally-heated tube during IAFB. The model is derived using basic conservation equations of mass, momentum and energy. To simplify the derivation of the constitutive heat transfer relations, flow between two parallel plates is assumed. The model features shear stress and interfacial relations that make it accurately predicts the parametric effects and heat transfer characteristics of IAFB over a wide range of flow conditions. The model predicts wall temperatures of R-134a-cooled tubes with an average error of -1.21 % and an RMS error of 6.37 %. This corresponds to average and RMS errors in predicted heat transfer coefficients of 1.33% and 10.07%, respectively. Using water data, the model predicts wall temperatures with an average error of -1.76% and an RMS error of 7.78% which corresponds to average and RMS errors in predicted heat transfer coefficients of 4.16% and 15.06%, respectively.

ACKNOWLEDGEMENT

I must thank ALLAH almighty. Without the will and help of ALLAH I would not have finished this work.

I would like to offer my indebtedness and appreciation to my thesis supervisors Professor S.C. Cheng and Professor D.C. Groeneveld. They have been the main source of help and encouragement to complete this thesis. They were available when I needed not only as academic supervisors but also for caring for their students beyond professorial obligations.

I am very pleased to take this opportunity to thank my friend Mr. J. Yang, former research associate and student of Professor S.C. Cheng and Professor D.C. Groeneveld, for making my study at the University of Ottawa enjoyable.

The financial support provided by the Natural Science and Engineering Research Council of Canada (NSERC) and by Atomic Energy of Canada Ltd. (AECL) is gratefully acknowledged.

TABLE OF CONTENTS

LIST OF TABLES

LIST OF FIGURES

NOMENCLATURE

a	thermal diffusivity (m^{-2} s^{-1})
A	area (m^2)
C_D	drag coefficient (-)
Cp	heat capacity at constant pressure (J kg^{-1} K^{-1})
D	tube inside diameter (m)
D_h	equivalent hydraulic diameter (m)
d	droplet diameter (m)
f	Fanning friction factor (-)
F_{dc}	enhancement factor due to droplet cooling (-)
g	acceleration due to gravity (m s^{-2})
G	mass flux (kg m^{-2} s^{-1})
h	heat-transfer coefficient (W m^{-2} K^{-1} or $kWm^{-2}K^{-1}$)
H_{fg}	latent heat of vaporization = h_g - h_f (Jkg^{-1})
k	thermal conductivity ($Wm^{-1}K^{-1}$)
L	heated length (m)
n	droplet number density (m^{-3})
p	pressure (Pa = N m^{-2}, bar = 10^5 N m^{-2})
P	perimeter (m)
q'	heat transfer rate per unit axial distance (kWm^{-1})
q"	heat flux (kWm^{-2})
Q	volumetric flow rate (m^3s^{-1})
R, r	radius (m)
T	temperature (°C)
ΔT	temperature difference = T_w - T (K)
u	velocity (m s^{-1})
U	uncertainty (-)
U_r	relative velocity between liquid and vapour (ms^{-1})

S	slip ratio (-)
x	quality (-)
y	radial distance from the wall (m)
z	length (m)

Greek

α	void fraction (-)
δ	vapour film thickness (m)
ε	emissivity (-)
ε_H	turbulent diffusivity of heat transfer ($m^2\ s^{-1}$)
ε_M	turbulent diffusivity of momentum ($m^2\ s^{-1}$)
Γ	vapour generation source function ($kg\ m^{-3}\ s^{-1}$)
λ	enhancement parameter for interfacial disturbances (-)
λ_c	minimum wave length for Taylor instability (m)
μ	dynamic viscosity ($N\ s\ m^{-2} = kg\ m^{-1}\ s^{-1}$)
ν	kinematic viscosity ($m^2\ s^{-1}$)
Θ_W	wall superheat (K)
Θ_V	vapour superheat (K)
θ^*	influence coefficient (-)
ρ	fluid density ($kg\ m^{-3}$)
σ	Stephan-Boltzman constant ($W\ m^{-1}\ K^{-4}$)
σ	surface tension ($N\ m^{-1}$)
τ	shear stress ($N\ m^{-2}$)

Dimensionless Groups

Fo	Fourier number
Fr	Froude number
Gr	Grashof number

Nu	Nusselt number	(= hD/k)
Pr	Prandtl number	
Re	Reynolds number	(= GD/μ)
We	Weber number	

Subscripts

a	actual
bulk	at bulk-fluid conditions
c	convection
crit	critical conditions
d	droplet
dc	droplet cooling
do, DO	dryout
eff	effective
eq	equilibrium
f	saturated liquid
fg	difference between saturated vapour and saturated liquid properties
g	saturated vapour
hom	homogeneous
i	interface
l	liquid
lh	liquid heating
Q	at quench front
pred	predicted
rad	radiation
sat	saturation
sub	subcooled
table	PDO look-up table value
TP	two-phase
v	evaluated at vapour conditions

vf	vapour-film temperature
vh	vapour heating
w	wall conditions

Abbreviations

CHF	critical heat flux
DFFB	dispersed-flow film boiling
DNB	departure from nucleate boiling
FB	film boiling
IAFB	inverted annular-flow film boiling
LHS	left-hand side
LOCA	loss-of-coolant accident
LORA	loss-of-regulation accident
LUT	look-up table
MFB	minimum film boiling
NB	nucleate boiling
ONB	onset of nucleate boiling
RHS	right-hand side
RMS	root-mean squared
TB	Transition boiling

CHAPTER 1 INTRODUCTION

1.1. Background

Film boiling is a two-phase heat transfer mode during which the heated surface is separated from the liquid-phase by a vapor film. It is characterized by a low heat transfer coefficient due to the poor heat transfer in the vapor film layer. Flow film boiling is important in the safety analysis of water-cooled nuclear reactors. A part of the fuel bundle can experience film boiling during a loss of coolant accident (LOCA) occurrence. This mode of heat transfer can also be encountered during a loss-of-regulation accident (LORA) when the reactor power accidentally increases. Film boiling heat transfer may also be encountered in fossil-fuel-fired boilers, in direct-expansion evaporators, and in cooling of various high-heat-flux devices.

Flow film boiling heat transfer is generally divided into two main regimes, namely: (i) inverted annular flow film boiling (IAFB) at void fractions of less than 0.5, and (ii) dispersed flow film boiling (DFFB) at void fractions of greater than 0.8. The transition zone between these two regimes is called the agitated or inverted slug flow regime. In IAFB, a vapor film separates the heated wall from a continuous liquid core while in DFFB the liquid is entrained in a continuous vapor core in the form of small droplets. The IAFB regime is characterized by high heated surface temperatures, compared to the moderate heated surface temperatures in the DFFB regime. These high temperatures could lead to physical failure of the heated surface.

The choice of this thesis topic came from the need for a reliable prediction method for the IAFB regime to be applied in nuclear safety analysis. An investigation of the available experimental data revealed the lack of subcooled and low quality experimental data of water and the limited range of other fluids' experimental data. Also, the IAFB regime has received relatively little attention compared to the DFFB regime.

It is hoped that the results of the present study will contribute to an improved understanding of flow film boiling and can be used for enhancing thermalhydraulic codes for reactor design and safety analysis.

This thesis is subdivided as follows: in Chapter 2 a literature review of the boiling phenomena with the emphasis on film boiling heat transfer is presented. A description of post-CHF heat transfer models and prediction methods is also given. Chapter 3 describes the experimental techniques used to obtain inverted annular flow film boiling data. Chapter 4 discusses the experimentally observed parametric trends as documented in the literature. Chapter 5 provides a detailed description of the experimental equipment and procedure used during this study. Chapter 6 presents an analysis of the experimental results obtained during this study. Chapter 7 provides a theoretical analysis of the IAFB phenomena and describes the derivation of an improved IAFB model. Chapter 8 compares the IAFB model predictions with the experimentally derived inside wall temperature and heat transfer coefficient distributions. It also discusses the predicted and observed effect of various flow parameters on the heat transfer coefficient. This Chapter is concluded by examining the model's sensitivity to the choice of constitutive (closure) relations. Chapter 9 presents conclusions resulting from the study, and makes recommendations for future work.

1.2. Objectives

The main objective of this thesis is to develop a model for predicting subcooled film boiling heat transfer over a wide range of flow conditions (pressure, mass flux, heat flux, inlet subcooling, local quality and diameter) and various fluids. In order to achieve this objective, the following steps are undertaken:

- Review the available film boiling heat transfer data and prediction methods with emphasis on inverted annular flow film boiling heat transfer. This will include an examination of measured and predicted trends, and summary of experimental procedures applied to obtain subcooled data.

- Experimentally investigate the subcooled film boiling heat transfer for vertical up-flow in a directly heated tube using the refrigerant R-134a as test fluids and utilizing the indirect hot-patch techniques. This will cover a wide range of pressure (4000 to 14000 kPa water equivalent based on density ratio) and mass flux (500 to 4000 $kgm^{-2}s^{-1}$). The inlet quality and input heat flux to the test section will be controlled in a way to prevent Freon decomposition when maintaining a stable dry film.

- Assess the new model with the experimental data obtained and with the available film boiling data of water and compare its prediction capabilities with other available models.

CHAPTER 2 REVIEW OF BOILING HEAT TRANSFER MECHANISMS AND PREDICTION METHODS

2.1 Boiling Classifications

The most common classifications of the boiling phenomena are shown in Figure 2.1. Boiling can be classified as nucleate, transition, or film boiling depending on the surface temperature and /or heat flux. Based on the liquid velocity, the systems are classified as either pool boiling or flow boiling. In the absence of fluid motion, pool boiling occurs, while boiling systems where the flow is being circulated are said to be in flow boiling. Boiling can also be classified as saturated or subcooled boiling depending on the temperature of the bulk liquid. Boiling systems can also be classified into steady or transient boiling depending on how the system behaves as a function of time. Transient boiling refers to an unstable situation where the flow conditions change with time for a fixed location on the heated surface.

A combination of these categories will assist in defining a boiling problem. Taking the research topic under consideration as an example, it can be identified as steady state (time dependence) inverted annular (flow regime) flow (liquid velocity) film boiling (regime).

2.2. Pool Boiling Heat Transfer

A typical pool boiling curve, where the heat flux is plotted against the wall superheat, $(T_w - T_{sat})$ is shown in Figure 2.2. The pool boiling curve can be divided into four distinct heat transfer regimes; three transition points between these regimes can be identified. The heat transfer regimes are:

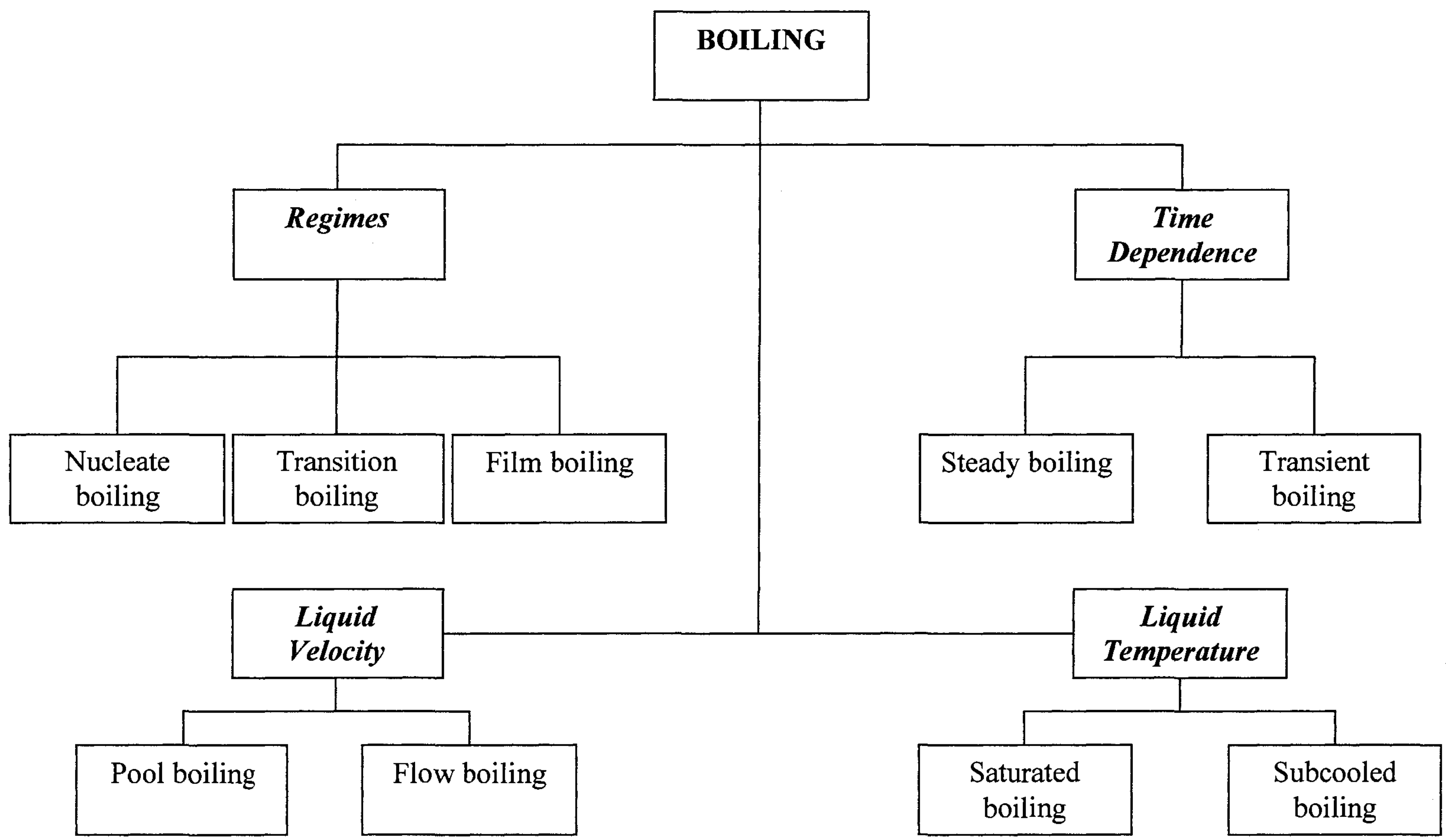

Figure 2. 1 Common boiling classifications.

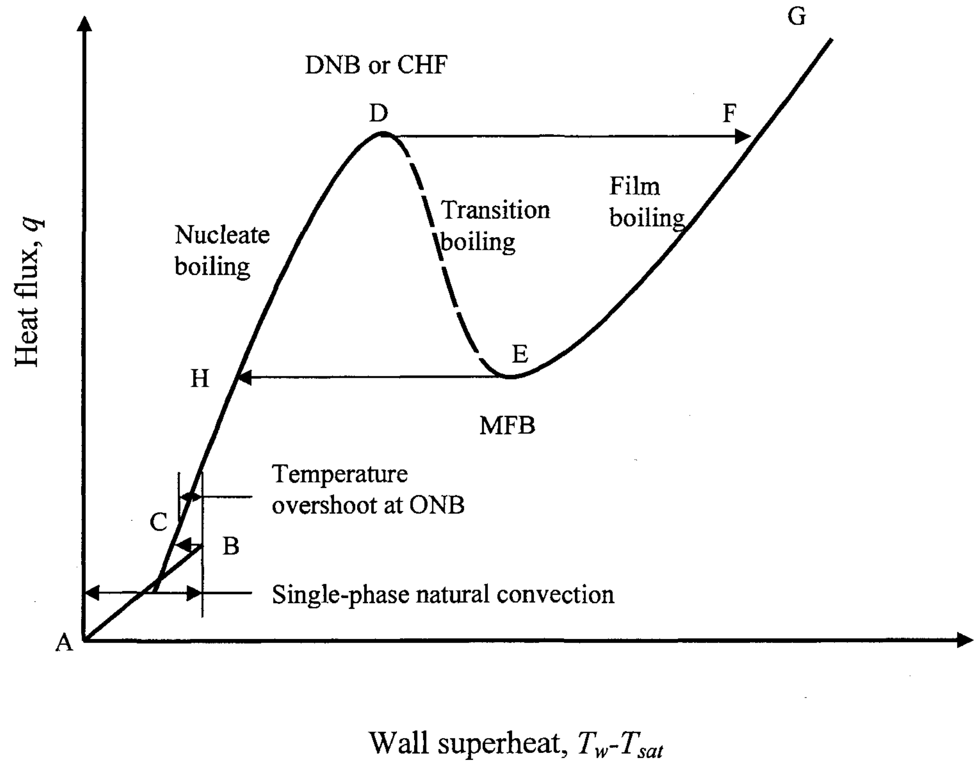

Figure 2. 2 A typical pool boiling curve.

1. Natural convection (path A-B). This is a single-phase natural convection from the heated surface to the liquid without formation of bubbles on the heated surface.
2. Nucleate boiling (path C-D). This is a two-phase natural convection process in which bubbles nucleate, grow, and depart from the heated surface.
3. Transition boiling (path D-E). This is an intermediate regime between the nucleate boiling and film boiling regimes.
4. Film boiling (path E-G). This regime is characterized by a stable vapor layer that separates between the heated surface and the liquid.

The first transition point is called onset of nucleate boiling (ONB), at which bubbles start to appear on the heated surface. The second is at point D in Figure 2.2 (the top of the nucleate boiling portion of the curve), referred to as departure from nucleate boiling (DNB), or the critical heat flux (CHF). The last transition point is located at the lower point (point E) and is called the minimum film boiling (MFB) point.

At low wall superheats, the wall temperature increases as the heat flux is increased until the first bubbles appear. These bubbles form at small cavities (imperfections) in the heated surface, which are called nucleation sites. Increasing the heat flux activates more nucleation sites until the surface is covered with bubbles that grow and depart rapidly. The heat flux increases dramatically for relatively modest increases in wall superheat. Increasing the heat flux further results in coalescing of departing bubbles into vapor jets. A further increase in heat flux eventually prevents the liquid from reaching the heated surface, which is referred to as the DNB or CHF. A complete blanketing of the heated surface by vapor occurs, accompanied by a rapid rise in the surface temperature.

After CHF is exceeded, the process follows a path that depends on the manner in which the heat flux is applied to the surface. For heat flux controlled systems, the process progresses on a horizontal line of constant heat flux so that the wall superheat jumps to point F, where film boiling prevails as shown in Figure 2.2. A further increase in heat flux will eventually bring the surface to the burnout point (point G), where the surface temperature reaches the melting point of the heater. By reducing the heat flux prior to burnout, the film boiling curve passes below point F until it reaches point E, the MFB point. After a further reduction in heat flux, the process path jumps horizontally from point E to point H at constant heat flux to the nucleate boiling curve, C-D.

For wall temperature controlled systems, the process path moves from the DNB (point D) to the MFB point (point E), and vice versa, following the transition boiling path. In transition boiling, the boiling process can be considered as a combination of nucleate boiling and film boiling, where each mode may coexist next to the other on the heated surface or may alternate at the same location on the surface. In film boiling, the wall is covered completely by a thin film of vapor, and therefore heat is transferred by heat conduction across the vapor film and by radiation from the wall to the liquid. The vapor film is stable in that liquid does not wet the heated surface. Large bubbles are formed during film boiling by evaporation at the vapor–liquid interface. These bubbles then depart and rise up through the liquid pool.

2.3. Forced Convective Boiling Heat Transfer

Taking as reference a heat-flux controlled vertical heated tube, two kinds of regimes are possible, depending on the heat flux, as sketched in Fig. 2.3. Referring to case A (low heat flux, which corresponds to a high quality at CHF) and, starting from single phase liquid at the inlet, nucleation is initiated at the wall when the bulk of the fluid is still subcooled (subcooled nucleate boiling) but the surface temperature exceeds the ONB point. At a location further downstream, the bulk of the fluid becomes saturated ($x = 0$), and saturated nucleate boiling takes place. The flow pattern in this region is gradually modified from bubbly to slug and annular due to coalescence of the bubbles. CHF occurs when the liquid film at the wall becomes depleted due to evaporation of the liquid film and entrainment of liquid droplets in the vapor core. Beyond the CHF point the dispersed flow film boiling (DFFB) region is entered. DFFB is maintained until all liquid droplets are vaporized, at which time the dominant heat transfer mode becomes single-phase heat transfer to the vapor.

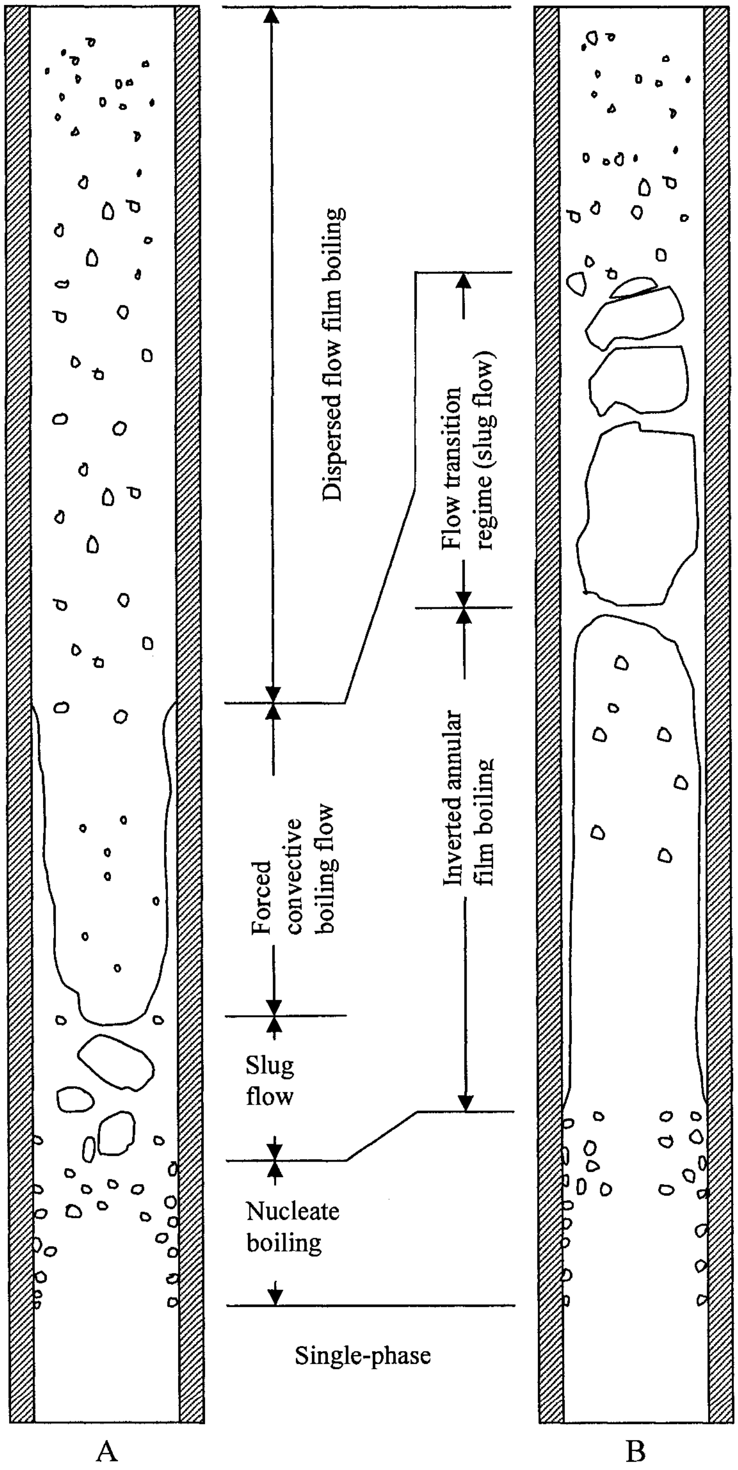

Figure 2. 3 Flow boiling regimes. A: low heat flux, B: high heat flux.

For case B at higher heat flux, the boiling crisis is reached directly from nucleate boiling conditions: at CHF the bubble density at the wall becomes so large that the inflow of fresh liquid to the wall is impeded, resulting in liquid superheating at the wall and the sudden creation of a continuous vapor layer at the wall. This phenomenon is called departure from nucleate boiling (DNB) and the type of flow regime after DNB point is called the inverted annular film boiling (IAFB) regime. As the quality increases, the liquid core starts to break-up to form slugs of liquid which eventually break-up more to enter the dispersed flow regime.

The heat transfer coefficients vary drastically along the heated length, but in the single phase flow regime the heat transfer coefficient is essentially constant. The transition to the nucleate boiling is accompanied by a large increase in heat transfer coefficient. This high heat transfer coefficient is maintained in the annular flow regime. Transition between nucleate/annular flow boiling to DFFB or IAFB is characterized by a sudden decrease of heat transfer coefficient and a consequent increase of wall temperature. The increase in vapor velocity in the post-CHF region (due to evaporation of liquid droplets in DFFB or increase in vapor layer in IAFB) results in increasing the heat transfer coefficient, up to the point of single-phase vapor where the heat transfer coefficient starts decreasing.

2.4. Post-CHF Heat Transfer Mechanisms

2.4.1. Transition boiling

This regime is encountered in experiments where the wall temperature is varied independently (i.e. wall-temperature-controlled system, such as a system where the heat is supplied by condensing steam) or when the slope of the boiling curve is positive in a heat-flux-controlled system [Groeneveld (2002)]. In this heat transfer mode, liquid and vapor co-exist momentarily on the heated surface. This phenomenon keeps the heated surface temperature between the CHF temperature (just above the saturation temperature) and the minimum film boiling temperature. The importance of this heat transfer mode arises in the case of loss-of-coolant accident (LOCA) in nuclear power plants when the heated surfaces (the fuel elements) act as a temperature-controlled surface during a fast transient. A comprehensive review of the published information on transition boiling under forced convection conditions has been made by Groeneveld and Fung (1976).

Johannsen (1988) performed a review on transition boiling and IAFB of water. He concluded that the MFB data are scarce and inaccurate. Moreover, the data are inconsistent even when they come from the same data base. This would create difficulties when studying the parametric trends of the MFB temperature.

2.4.2. Minimum film boiling (MFB) temperature

The minimum film boiling temperature can be identified differently based on the method of heating. For a temperature controlled system, the MFB temperature can be viewed as the minimum point on the boiling curve between transition boiling and film boiling. For a heat flux controlled pool boiling system, MFB is the point at which the flow regime changes from film boiling into nucleate boiling when the heat flux is reduced. Accurate prediction of the MFB temperature is important in many industrial applications as well as in providing the lower limit in the applicability of film boiling prediction methods. Different terminology is used in the literature for the MFB phenomenon. Some of the terms used are minimum film boiling, rewetting, film boiling collapse, Leidenfrost phenomenon, etc. A review of the MFB temperature has been reported by Chen et al. (1989).

2.4.3. Inverted annular film boiling (IAFB)

This heat transfer mode generally occurs at low qualities and subcooled conditions at void fractions less than 0.5. The main characteristics of IAFB are the low heat transfer coefficients. The phase distribution during IAFB consists of a continuous liquid core at the centre of the channel surrounded by a vapor blanket covering the heated surface. In this regime, convective heat is transferred from the wall to the vapor layer, and then from the vapor, through the liquid-vapor interface, to the liquid core. Heat transfer by radiation from the wall to the liquid may also be important. Heat is transferred by forced convective evaporation across the vapor-liquid interface. The vapor film is assumed to have a higher velocity than the liquid core, and the vapor velocity increases as the vapor layer thickness increases. This is due to the low viscosity and low density of the vapor, which enables the vapor flow to experience a higher acceleration than the dense core flow. Consequently, the high fluid velocity at the interfacial can cause liquid entrainment from the wavy interface with the possibility of having vapor bubbles in the liquid core (the vapor bubbles will condense almost immediately if the liquid is highly subcooled). Heat transfer rates during IAFB have been predicted using the modified Bromley equation [Bromley (1952) and Bromley et al. (1953)] for pool film boiling, turbulent-boundary-layer theories, and two-fluid models. A review of physical mechanisms in IAFB has been performed by Groeneveld (1984) and Groeneveld (1992).

2.4.4. Slug flow film boiling

The transition region between IAFB and DFFB regimes is called slug flow (or agitated/inverted slug) regime. The main feature of this regime is the presence of slugs of liquid flowing in the vapor core: this is generally considered to be an unstable regime. It is believed that this regime can exist at void fractions between 50% and 80%. The slug flow regime is usually observed downstream of the IAFB regime and prior to DFFB. Groeneveld (1984) assumes that the formation of slug flow is the result of low flow rates and low void fractions that will result in an intermediate flow regime in between the IAFB and DFFB regimes. The heat transfer characteristics in this region are often treated as a gradual transition between IAFB and DFFB regimes [Hammouda (1996)].

2.4.5. Dispersed flow film boiling (DFFB)

The DFFB is viewed as a continuous vapor core with entrained droplets and characterized by a moderate surface temperature increase. This type of flow regime can be encountered downstream of a liquid film dryout in annular flow or as the break-up of the liquid core downstream of the IAFB regime or slug flow film boiling regime (usually at void fractions > 80%). Generally, heat transfer in this regime is poor, but improves at higher mass flowrates and higher qualities. For the same pressure, p, the heat transfer coefficient is higher in DFFB than that in IAFB due to the higher vapor velocity.

Collier and Thome (1994) and Carey (1992) divided the heat transfer mechanisms in the dispersed flow film boiling into six components:

1. convective heat transfer from the wall to the vapor,
2. convection heat transfer from the vapor to the droplets,
3. direct contact wall-to-droplet heat transfer,
4. radiative heat transfer from the wall to the droplets,
5. radiative heat transfer from the wall to the vapor, and
6. evaporation of droplets.

Andreani and Yadigaroglu (1994) added a seventh contributor which is radiative heat transfer from vapor to droplets. It is difficult to include the effect of all the above mechanisms in one model or correlation. Several of the above mechanisms are often considered negligible to simplify modeling, resulting in reduced prediction accuracy.

2.5. Review of Post-CHF Heat Transfer Prediction Methods

In this section, a literature review of the available prediction methods for post-CHF heat transfer is presented. The review covers the transition boiling, IAFB, slug flow film boiling and DFFB regimes. The review also includes prediction methods of the minimum film boiling temperature. A more comprehensive review is given for the IAFB and DFFB due to their relevancy to the thesis.

2.5.1. Transition boiling

In a temperature-controlled system, the transition boiling starts when the CHF temperature is exceeded and ends when the minimum film boiling temperature is reached (points D and E in Figure 2.2). These limits can be determined as [Groeneveld (2002)]

$$(T_{CHF} - T_{sat}) = q_{CHF} / h_{NB} \tag{2.1}$$

and

$$(T_{MFB} - T_{sat}) = q_{MFB} / h_{FB} \tag{2.2}$$

where q_{CHF}, h_{NB}, T_{MFB} and h_{FB} can be obtained from CHF prediction methods, nucleate boiling correlations, and film boiling prediction methods.

Many attempts have been made to correlate heat transfer in the transition boiling region. One of the most useful available correlations is that by Tong and Young (1974) which is given in terms of the heat flux in the transition boiling region (q_{TB})

$$q_{TB} = q_{NB} \exp\left[-0.001 \frac{x^{2/3}}{(dx/dz)} \left(\frac{(T_w - T_{sat})}{55.6}\right)^{(1+0.00288(T_w - T_{sat}))}\right] \tag{2.3}$$

In Equation (2.3), q_{NB} is the nucleate boiling heat flux or the measured total heat flux based on the instantaneous local conditions in Wm^{-2} and $(T_w - T_{sat})$ is the temperature difference between the surface and the saturation condition in K. Equation (2.3) gave a satisfactory data fit for the range:

$$0 \leq x \leq 1.45, \quad and \quad 0 \leq (T_w - T_{sat}) \leq 149K$$

Mattson et al. (1974) performed regression analysis on available post-dryout flow boiling data. They correlated the heat transfer coefficient in the transition boiling region for flows in tubes and annuli and rod bundle geometries. The RMS error in both cases was relatively high due to the variation of relevant experimental data.

Collier and Thome (1994) suggest that a transition boiling correlation with a wide range of application may be developed if the heat flux and wall superheat at the points of maximum and minimum in the boiling surface can be predicted with confidence. At present, the prediction techniques allow an accurate prediction of q_{CHF} and also ΔT_{CHF} but the conditions at the minimum point are still subject to a large degree of uncertainty. Iloeje et al. (1974) demonstrated that the conditions at the minimum point are a complex function of the mass quality and flow-rate in the channel.

Based on shape of the boiling curve, Groeneveld (2002) recommended the use of a correlation which gives a correct asymptotic trend at all conditions:

$$\frac{\ln(q_{CHF}/q_{TB})}{\ln(q_{CHF}/q_{MFB})} = \frac{\ln(\Delta T_{TB}/\Delta T_{CHF})}{\ln(\Delta T_{MFB}/\Delta T_{CHF})} \tag{2.4}$$

2.5.2. The minimum film boiling temperature

A summary of the main theories describing the MFB phenomenon is given by Groeneveld (1984). Available MFB data related to the vapor film collapse of a stationary IAFB were obtained by Stewart and Groeneveld (1982), Cheng et al. (1985) and Chen et al. (1989). Stewart and Groeneveld (1982) derived for water a correlation for the MFB temperature as follows:

For $x \leq 0$ and $p \leq 9MPa$

$$T_{MFB}\left({}^{o}C\right) = 284.7 + 0.0441 - 3.72 \times 10^{-6} p^2 - \frac{x \times 10^4}{2.82 + 0.00122p} \tag{2.5a}$$

for $x > 0$ and $p \leq 9MPa$

$$T_{MFB}\left({}^{o}C\right) = 284.7 + 0.0441p - 3.72 \times 10^{-6} p^2 \tag{2.5b}$$

and for $p > 9MPa$

$$T_{MFB}\left({}^{o}C\right) = \left(\Delta T_{MFB}, 9MPa\right)\left(\frac{p_{crit} - p}{p_{crit} - 9}\right) + T_{sat} \tag{2.5c}$$

Cheng et al. (1985) measured the “true quench temperature”. They derived a correlation for the MFB temperature at low pressures (p = 101 – 1034 kPa) as

$$T_{MFB}\left({}^{o}C\right)=169.66+0.1050p+0.1444G+3.0347\Delta T_{sub} \tag{2.6}$$

where ΔT_{sub} represents the inlet subcooling, in K.

Chen et al. (1989) derived a correlation from the MFB temperature data for water of the vapor film collapse under steady state conditions. Their correlation is:

$$T_{MFB}\left({}^{o}C\right)=363.6+38.371p+0.02844p-3.86\times10^{-6}p^{2}+A\Delta T_{sub} \tag{2.7}$$

$A=\dfrac{17.1}{3.3+0.0013p}$ for $\Delta T_{sub}\geq 0$, and $A=0$ for $\Delta T_{sub}<0$

The correlation was derived for the following flow conditions:

- p = 115 to 6050 kPa
- G = 53 to 1209 $kgm^{-2}s^{-1}$
- x = -0.055 to +0.08

2.5.3. Inverted annular film boiling

There are basically four types of prediction methods for IAFB available in the literature. These methods are summarized as:

- Pool boiling correlations (applied to low mass velocity flows)
- Purely empirical correlations. This type of prediction does not account for any physical mechanism (thermal equilibrium between liquid and vapor and cooling the surface is maintained by convection from wall to vapor only, and correlations take the same form of the Dittus-Boelter equation)

- Correlations that consider the physical mechanisms and account for thermodynamic non-equilibrium (actual vapor temperature and actual quality)
- Theoretical or semi-theoretical methods to model various hydrodynamic and heat transfer processes; they are based on
  - Modified Bromley equation for pool boiling
  - Turbulent boundary layer theories
  - Two fluid models

2.5.3.1. Equations for low quality and subcooled IAFB

Groeneveld (1984) presented a review of the IAFB correlations. A summary of the correlations available up to present is given in Table 2.1. This table is an updated version of the Groeneveld (1984) table for low-quality and subcooled IAFB correlations.

IAFB equations are usually classified, based on the way they are derived and presented, into three categories:

A. Modified pool-boiling equations

These equations have the general form:

$$h_C = A\left[\frac{g k_v^3 \rho_v (\rho_l - \rho_v) H_{fg}}{\mu_v (T_w - T_{sat}) \lambda_C}\right]^{1/4} + h_{rad} \qquad (2.8)$$

where λ_C is the minimum wavelength for Taylor instability, and A is chosen to account for the velocity and subcooling effects. This type of equation considers conduction across a laminar vapor film and a smooth vapor-liquid interface. Equations in this category include those of Bromley (1952), Bromley et al. (1953), Berenson (1961) and Bailey (1972) (see Table 2.1 for more details).

Table 2. 1 Low quality and subcooled film boiling equations [updated from Groeneveld (1984)]

Authors	Equation	Range of application					Comments
		Test fluid	Geometry	Pressure MPa	Mass flux $kgm^{-2}s^{-1}$	Subcooling (°C) or quality	
Bromley (1952) and Bromley et al. (1953)	$h_c = h_{FB} + 3/4 h_{rad}$ $h_{FB} = 0.62\left[\frac{k_v^3 g\rho_v(\rho_f-\rho_v)H'_{fg}}{D\mu_v\Delta T_{sat}}\right]^{1/4}$ $h_{rad} = \frac{5.67\times10^{-8}(T_w^4 - T_{sat}^4)}{\left(\frac{1}{\varepsilon_w}+\frac{1}{\varepsilon_f}-1\right)\Delta T_{sat}}$ $H'_{fg} = H_{fg}\left(1+\frac{0.4C_p\Delta T_{sat}}{H_{fg}}\right)^2$	Nitrogen Water a-pentane benzene carbon tet-rachloride ethyl alcohol	Horizontal carbon cylinders OD-6.4mm – 9.5mm – 12.7mm	Not given	Pool boiling	Saturated	Pool film boiling from horizontal cylinders. Laminar theory
Ellion (1954)	$h = 4/3\left[\frac{k_v^3 g\rho_l\rho_v H'_{fg}}{12\mu_v\Delta T_{sat}L}\right]^{1/4} + q_{rad}$	Water	Vertical annulus OD-63.5 mm ID-6.4 mm length-76.2 mm	0.11-0.41	(0.336-1.53)x10^3	28°C-56°C	
Berenson (1961)	$h_{FB} = 0.425\left[\frac{k_v^3 g\rho_v(\rho_f-\rho_v)H'_{fg}}{\mu_v\Delta T_{sat}\sqrt{\frac{\sigma}{g(\rho_f-\rho_v)}}}\right]^{1/4}$		Horizontal surface		Pool boiling	Saturated	Theory only
Siviour and Ede (1970)	$q_v = 0.613\frac{k_v}{D}\Delta T_{sat}\left[\frac{g\rho_v(\rho_l-\rho_v)H'_{fg}}{\mu_v k\Delta T_s}\right]^{1/4} + q_{rad}$ $q_{tot} = q_l + q_v$ $q_l = 0.57\frac{k}{D}\Delta T_l(Gr\Pr^2)$ $Gr = g\frac{\beta_l\Delta T_l D^3}{v^2}$	Water Water plus detergent	Horizontal cylinders OD 3.2 – 6.4 mm	0.101	Pool boiling	0 – 90 deg c	Correlated their data well over the entire range of subcoolings
Bailey (1972)	$h = \left[\frac{2k_g^3 g\rho_g(\rho_f-\rho_v)^4 H_{fg}}{\mu_g\Delta T_{sat}D}\right]^{1/4}$	Theory	Vertical rods			Saturated	D=rod OD

Table 2.1 (continued)

Authors	Equation	Range of application					Comments
		Test fluid	Geometry	Pressure MPa	Mass flux $kgm^{-2}s^{-1}$	Subcooling (℃) or quality	
Andersen (1976)	$h_c = C_1\left[\frac{k_v^3 g^4 \rho_g^3(\rho_f-\rho_v)^4 H_{fg}^2}{\mu_v^4 \Delta T_{sat}^2 \sigma}\right]^{1/11}$ $0.3321 \le C_1 \le 0.5498$				Low flow rates	Saturated	Gives slightly higher heat transfer coefficient than Berenson's equation for $\Delta T_s > 200°C$ Theory only
Collier (1980)	$\left[\frac{h(z)z}{k_g}\right] = \left[\frac{z^3 g\rho_g(\rho_l-\rho_g)H_{fg}}{4k_g\mu_g\Delta T}\right]^{1/4}$	Theory	Vertical surface				Laminar vapor film
Collier (1980)	$\left[\frac{h(z)z}{k_g}\right] = 0.056\mathrm{Re}_g^{0.2}(\mathrm{Pr}\,Gr^*)^{1/3}$ $Gr^* = \left[\frac{z^3 g\rho_g(\rho_f-\rho_g)}{\mu_g^2}\right]$		Vertical surface				Turbulent vapor film
Lee and Kim (1987)	$q/q_w = (r_w - r_i q_{il}/q_w)(r^2-r_w^2)/r(r_w^2-r_i^2)+r_w/r$ $q_{il} = h_{il}(T_{sat}-T_l)$ $h_{il} = \rho_l C_{P,l}/(1.17B+1.83D)$ $B = r_i\int_0^{r_i}\frac{\cos\left(\frac{\pi r}{2r_i}\right)-1}{r(\varepsilon_M+\alpha)}dr$ $D = \int_0^{r_i}\frac{\sin\left(\frac{\pi r}{2r_i}\right)-1}{r(\varepsilon_M+\alpha)}dr$ q: heat flux distribution across the vapor layer ε_M : eddy diffusivity from the modified Reichardt's equations.	theory	Vertical tube			Saturated or subcooled	Turbulent boundary layer analysis. Applicable to the flow region immediately downstream of the rewetting front

Table 2.1 (concluded)

Authors	Equation	Range of application					Comments
		Test fluid	Geometry	Pressure MPa	Mass flux $kgm^{-2}s^{-1}$	Subcooling (°C) or quality	
Mosaad and Johannsen (1988)	$h = h_{FB} + 3/4 h_{rad}$ $h_{FB} = \lambda\left(1 + 0.4\theta_s + 0.075\theta_s^2\right)h_{sat}$ $\theta_{sat} = \Delta T_l h_{il} / \left(\Delta T_{sat} h_{sat}\right)$ $h_{sat} = \left[g\rho_v\left(\rho_l - \rho_v\right)H'_{fg} / \left(16\mu_v \Delta T_{sat} H_v z\right)\right]^{1/4}$ $H'_{fg} = H_{fg}\left[1 + 0.5C_{P,v}\left(T_w - T_{sat}\right)\right]$ $h_{il} = h_{il,\infty}\left[1 + 2.5\left(D/z\right)\right]$ $h_{il,\infty} = 3.66\frac{k_l}{D - 2\delta}, \mathrm{Re} < 2000$ $h_{il,\infty} = 0.023\frac{k_l \mathrm{Re}^{0.8} \mathrm{Pr}_l^{0.4}}{D - 2\delta}, \mathrm{Re} \geq 2000$ $\lambda = 1 + 7.5\frac{\delta_{sat}}{D}$; $\delta_{sat} = k_v / h_{sat}$ $h_{rad} = 5.67\times10^{-8}\left(T_w^4 - T_{sat}^4\right)/\left(1/\varepsilon_w + 1/\varepsilon_l - 1\right)\left(T_w - T_{sat}\right)$ $\varepsilon_l = 0.8, \varepsilon_w = 0.95$	Water	Vertical tube OD-12 mm ID-9 mm length-280 mm	0.101	50-500	0-30	Laminar boundary layer analysis
Takenaka et al. (1989)	$q_v = \frac{r_w q}{r_i - y_v}\left[1 - \frac{r_w q - r_i q_{il}\int_0^{y_v}\left(r_i - y_v\right)u_v dy_v}{r_w q\int_0^{r_i}\left(r_i - y_v\right)u_v dy_v}\right]$ $q_l = \frac{r_i q_{il}}{r_i - y_l}\left[1 - \frac{\int_0^{y_l}\left(r_i - y_l\right)u_l dy_l}{\int_0^{r_i}\left(r_i - y_l\right)u_l dy_l}\right]$ $q_{il} = \frac{\rho_l C_{P,l}\left(T_{sat} - T_l\right)}{1 - \frac{\int_0^{y_l}\left(r_i - y_l\right)u_l dy_l}{\int_0^{r_i}\frac{\int_0^{r_i}\left(r_i - y_l\right)u_l dy_l}{\left(r_i - y_l\right)\left(a_l + \varepsilon_l\right)}dy_l}}$	R-113	Vertical tube OD-11 mm ID-10 mm length 900-1485 mm	0.10	136-1280	10-40	Turbulent boundary layer analysis using modified Reichadt equations. This analysis is limited to the region where the actual quality >>0. q_v and q_l are the heat fluxes retained by the vapor and the liquid phases, respectively.

To simplify the modeling of the heat transfer mechanisms in the IAFB regime, Collier and Thome (1994) and Carey (1992) suggested the use of a method similar to annular film condensation but with inverting the role of the liquid and vapor and the direction of heat flow. By assuming that the interfacial shear and the acceleration pressure gradient are small, Carey (1992) obtained a Nusselt-type equation for the heat transfer coefficient as

$$h = \left[\frac{\rho_v (\rho_f - \rho_v) g H'_{fg} k_v^3}{4(z - z_{do}) \mu_v (T_w - T_{sat})} \right]^{1/4} \tag{2.9a}$$

where

$$H'_{fg} = H_{fg} \left[1 + \frac{3}{8} \frac{C_{P,v} (T_w - T_{sat})}{H_{fg}} \right] \tag{2.9b}$$

This equation is similar to that of Bromley (1950).

B. Convection-type equations

The convective equations are generally used to calculate different paths of heat transfer (wall-to-vapor, vapor-to-interface, etc.). The heat transfer coefficient is considered to be a function of Reynolds and Prandtl numbers,

$$Nu = a \mathrm{Re}^b \mathrm{Pr}^c F \tag{2.10}$$

where a, b, and c are constants and F is to approximately account for the entrance length effect. Equations such as Collier (1980) and Mosaad and Johannsen (1988) in Table 2.1 belong to this category.

C. Phenomenological equations

These equations take into account the different physical mechanisms of film boiling heat transfer. They are semi-theoretical models with parameters correlated empirically. These equations are more complex than the other types of equations, and may be based on modified pool-boiling equations [e.g., Ellion (1954), Table 2.1] and the convection-type equations. However, phenomenological equations are easier to apply than models.

2.5.3.2. Phenomenological models

Heat transfer predictions of IAFB are generally based on (i) modified Bromley (1950) equations for pool film boiling, (ii) turbulent boundary layer theories, or (iii) two fluid models. For the latter two theories, most of the uncertainties are related to assumptions with respect to interfacial heat and mass transfer. These assumptions are often oversimplifications of the physical mechanisms governing film boiling, in order to facilitate a mathematical solution.

Dougall and Rohsenow (1963) used a turbulent flow model by implementing a three layer velocity model to predict the heat transfer in saturated inverted annular flow of low qualities inside vertical tubes. Their results show agreement between predictions and experimental data of R-113 flow.

A one-dimensional model with the use of the continuity and energy equations was developed by Kalinin et al. (1977). The momentum equation was not used in the derivation due to the assumption that the interface slip is zero. Kalinin et al. argued that this assumption is valid for large flow velocities and small pressure drop along the channel.

Other models including Hammouda et al. (1997), Cachard (1994) and Analytis and Yadigaroglu (1987) are based on solving the one-dimensional conservative equations for the liquid and vapor phases. The major components in these models are the relations for the shear stress and the heat transfer rates. Table 2.2 summarizes the IAFB models available in the literature. The table is an updated version of Groeneveld's (1984) table for IAFB models.

2.5.4. Slug flow film boiling

Not much attention has been given to the slug flow film boiling compared to other film boiling regimes. In most cases it is treated as a transition between IAFB and DFFB and the heat transfer coefficient is calculated by interpolating the transition region [e.g. Hammouda (1996)]. Chi (1966, 1967), and Chi and Pierse (1970) studied slug flow film boiling to boiling hydrogen. From their data it is shown explicitly that the liquid core will break up into slugs equal in lengths to the most unstable wavelength of interfacial waves. The effect of subcooling is to make the liquid-vapor interface stable, resulting in reducing the possibility of the formation of slug flow.

2.5.5. Dispersed flow film boiling

Basically, there are three prediction methods of DFFB heat transfer coefficient available in the literature. These are:

1. empirical correlation,
2. phenomenological models, and
3. mechanistic models.

Table 2. 2 IAFB Models [updated from Groeneveld (1984)]

Reference	Assumptions	Heat flux components	Comments
Kalinin et al. (1970)	$u_v = u_l$ $T_v = T_{sat}$	$Nu_{wv} = f(\mathrm{Re}_v, \mathrm{Pr}_v, T_w / T_{sat})$ $Nu_{il} = f(\mathrm{Re}_l, \mathrm{Pr}_l, z / D_e)$	Model was compared to nitrogen data
Groeneveld (1972)	At dryout $u_v = u_l$ $\tau_i = k\delta_v (u_v - u_l)^2$ $T_l = T_v = T_{sat}$	$Nu_{wv} = a\mathrm{Re}_v^b \mathrm{Pr}_v^c (\mu_v / \mu_w)^d C_r$ $C_r \equiv$ enhancement in h_{wv} due to liquid-wall interactions and turbulence in vapor film	Model permits entrained vapor in liquid core. Compared to Freon data
Kaufman (1976)	$T_v = (T_w + T_{sat})/2$ $f_i = 0.005(1 + 300\delta / D)$	$\mathrm{Re}_v < 100: Nu_{wv} = 1, else\ Nu_{wv} = f(\mathrm{Re}, \mathrm{Pr})$ $\mathrm{Re}_v < 2000: Nu_{il} = 3.66, else\ Nu_{il} = f(\mathrm{Re}, \mathrm{Pr})$	Interfacial heat transfer and frictional enhancement by factor $1 + 300\delta / D$
Chan and Yadigaroglu (1980)	$\tau_i = 0$ $H'_{fg} = H_{fg} + 0.34 C_{P,v} (T_v - T_{sat})$	$q_{w,tot} = q_{rad,wi} + q_{wi}$ $q_{wi} \equiv$ conduction across laminar vapor film $Nu_{il} = 0.023 \mathrm{Re}_l^{0.8} \mathrm{Pr}_l^{0.4} C, C = 1.5 - 2.0$	Vapor entrained in liquid core
Fung (1981)	$T_v = (T_w + T_{sat})/2$ $U_i = U_l$	$q_{il} = k_{eff} dT_l / dr, k_{eff}$ includes eddy diffusivity $q_{wi} = k_v (T_w - T_{sat}) / \delta_{sat}$	Compared well with Fung's low pressure data. $\delta_{sat} \equiv$ laminar vapor film or thermal sublayer thickness
Elias and Chambre' (1981)	Vapor entirely generated at the quench front. Constant vapor film thickness. $T_l \le T_{sat}, T_w = const.$	$q_{w,tot} = q_{rad,w-i} + q_{w-i}$ $q_{wi} = f(Pe_v, u_v, \delta, k_v)$ $Pe_v \equiv$ vapor Peclet number. $q_{il} \equiv$ heat flux from boundary layer in the liquid at the interface.	Model is restricted to the entrance subcooled region. Compared to Fung's data
Han and Bankoff (1982)	τ_i according to Barathan (1979)	$q_{wi} \equiv$ conduction across laminar sublayer q_{il} use one-seventh power law in liquid core	Entrained droplets in vapor phase
Kawaji and Banerji (1987)	Laminar flow in core $u_i = u_l$	q_{il} from thermal entry problem in laminar flow q_{wv} and q_{vi} from formulation of convection between parallel plates.	Stability analysis predicts transition to slug or dispersed flow film boiling.
Laperriere (1983)	$T_v = (T_w + T_{sat})/2$ $u_i = (u_v + u_l)/2$	Nu_{wv}, Nu_{vi} and Nu_{il} all have the form of $Nu = a\mathrm{Re}^b \mathrm{Pr}^c f$	f : the heat transfer enhancement factor. Results compared to Stewart's (1981) and Laperriere's (1983) data.
Hsu et al. (1986)	Turbulent flow in both vapor and liquid core $u_i = u_l = u_v$ at interface flow field is divided into two regions: - region I: $\delta =$ constant and interface is slightly subcooled - region II: $\delta = f(z)$ and interface is at saturation	$q_{w,tot} = q_{wi} + q_{rad,wi}$ $q_{wi} = k_v dT / dr$; $q_{il} = k_l dT / dr$ $k_v = f(k_{vL}, u_v, \rho_v, C_{P,v})$ in region I $k_v = k_{v,regionII} + f(T_{sat}, T_l, k_{vL})$ in region II $k_l = f(k_{lL}, \delta, u_l, C_{P,l})$ $k_{vL} \equiv$ vapor thermal conductivity in laminar flow $k_{lL} \equiv$ liquid thermal conductivity in laminar flow	Model is two-dimensional, two-region and two-fluid model. Compared to Stewart's (1981) data
Wang and Shi (1984)	Similarity to single-phase turbulent boundary layer flow is assumed. $u_l = const.$ $u_v \sim (1/\delta)^{1/7}$	$q_{w,tot} = q_v + q_{il}$ $q_{w,tot}$ is by using Karman's theory. $q_v \equiv$ heat flux to evaporate the liquid $q_{w,tot} = A(T_w - T_{sat}), A = f(\tau_w, \mathrm{Pr}_v, u_i)$ $q_v = f(u_l, \delta, H_{fg})$ $q_{il} = k_{eff} dT_l / dr, k_{eff}$ includes eddy diffusivity	Model valid for turbulent flow on horizontal plate. Compared to water data.

Table 2.2 (concluded)

Reference	Assumptions	Heat flux components	Comments
Denham (1984)	$T_v = (T_w + T_{sat})/2$	$q_{wi} = k_v(T_w - T_{sat})/\delta$ $q_{il} = k_l(T_{sat} - T_l)f(u_l, u_Q, F_o)$ $k_l = k_{l,lam}\dfrac{Nu_{turb}}{Nu_{lam}}$	δ from Bromley's laminar flow theory. $F_o \equiv$ Fourier factor
Yan (1987)	Laminar flow in vapor film $T_w = const.$ two boundary conditions for interface are considered: $\tau_i = 0$ or $u_i = u_l$ turbulent flow in vapor film $\tau_i = 0, \tau_w = \delta(\rho_l - \rho_v)g$	$q_{w,tot} = q_{rad,w-i} + q_{w-i}$ $q_{wi} = k_v(T_w - T_{sat})/\delta$ $q_{il} = h(T_l - T_{sat})$ $\mathrm{Re}_l < 2200; h = f(\mathrm{Re}_l, \mathrm{Pr}_l, Gr_l)$ $\mathrm{Re}_l > 2200; h = f(\mathrm{Re}_l, \mathrm{Pr}_l)$ $q_{wi} = \rho_v C_{P,v}(k_v + \varepsilon_v)dT/dy$	Model is applicable to laminar and turbulent flow. Compared to water data
Analytis and Yadigaroglu (1987)	In core both laminar and turbulent flow are considered $u_i = u_l$	$q_{il} = h_l(T_{sat} - T_l)$ $\mathrm{Re}_l < 2000; h_l = 3.66 k_l F/(R-\delta)$ $\mathrm{Re}_l > 2000; h_l = f(\mathrm{Re}, \mathrm{Pr})F$ $F = 1 + 1.4R/z$ q_{wv} and q_{vi} from formulation of convection between parallel plates.	Interfacial heat transfer and friction enhancement factor $1 + 300\delta/D$ (for more details see Table 7.1)
Wang et al. (1988)	$u_{inlet} = u_l = const.$ $\delta_x = bx^n$ no vapor superheat	$q_{w,tot} = q_v + q_{i-l}$ $q_v \equiv$ heat flux to evaporate the liquid $q_{w,tot} = 0.023\rho_v C_{P,v}(T_w - T_{sat})f(u_i, \delta)$ $q_v = (d\delta/dx)f(H_{fg}, u_i, \delta)$ $q_{il} = \rho_l C_{P,l}\varepsilon_{M,l} dT_l/dr$ $\varepsilon_M \equiv$ turbulent diffusivity of momentum exchange.	Model is restricted to liquid flowing with high velocity. Compared to R11 data and Dougall and Rhosenow (1963) data
Chen et al. (1988)	$T_v = (T_w + T_b)/2$ $T_b \equiv$ bulk liquid temperature Uniform liquid velocity	$q_{vi} + q_{rad,wi} = q_{il} + q_v$ $q_v \equiv$ heat flux to evaporate the liquid $q_v = H_{fg}/(2\pi r_i)d\Gamma/dz$ $\Gamma \equiv$ vapor flow rate $q_{vi} = \rho_v C_{P,v}(\varepsilon_v + \alpha_v)dT/dr$ $q_{il} = \rho_l C_{P,l}(\varepsilon_l + \alpha_l)dT/dr$ $\varepsilon_v = f(u_v, \delta, \Delta T_{sat}, H_{fg})$ $\varepsilon_l = 0.05 U_l \delta$	Model was compared to water data
Cachard (1994)	$\tau_{vi} = f_{vi}\rho_v \lvert u_v - u_i\rvert \dfrac{(u_v - u_i)}{2}$ $\tau_{il} = \tau_{vi}$	$q_{il} = h_l(T_{sat} - T_l)$ $\mathrm{Re}_l < 2000; h_l = 3.66 k_l F/(R-\delta)$ Otherwise, $h_{il} = \dfrac{\lvert\tau_i\rvert c_{p,l}}{\lvert u_l - u_i\rvert \mathrm{Pr}_l^{2/3}}$	Model was compared to low pressure and low flow water data (for more details see Table 7.1)
Hammouda (1996)	$\tau_i = \tau_w$ $u_i = u_l$	$q_{il} = q_{vi}\dfrac{T_v - T_{sat}}{T_{sat} - T_l}$ $q_{vi} = q_{wv}\dfrac{T_v - T_{sat}}{T_w - T_v}$	Model was compared to Freon and water data (for more details see Table 7.1)

A brief description of each method and the work done is given below. Most attention will be given to the better-known correlations and models.

2.5.5.1. Empirical correlations

Generally, empirical correlations for convective heat transfer coefficient for DFFB are modifications of the well-known Dittus-Boelter equation for single-phase flow heat transfer,

$$Nu = \frac{hD}{k_g} = 0.023\,\mathrm{Re}_g^{0.8}\,\mathrm{Pr}_g^{0.4} \qquad (2.11)$$

Empirical correlations can be classified as thermal equilibrium correlations and thermal non-equilibrium correlations.

A. Thermal equilibrium correlations

Thermal-equilibrium correlations usually are based on the two major assumptions: (i) thermodynamic equilibrium between the phases and (ii) turbulent convective heat transfer from the heated wall to the vapor phase. Generally, the film boiling mechanisms are not considered when using thermal equilibrium correlations.

Comprehensive reviews of published heat transfer correlations can be found in papers by Groeneveld and Gardiner (1977), Mayinger and Langner (1978), Chen (1986) and Groeneveld and Snoek (1986). Table 2.3 is reproduced from Groeneveld and Snoek (1986) and represents a summary of most of the empirical equilibrium equations found in the published literature.

Thermal equilibrium empirical correlations give reasonably accurate predictions of heat transfer coefficient in their range of data. It is not recommended to extrapolate thermodynamic equilibrium correlations outside their stated range of application. One of the best-known and most representative equilibrium correlations is that of Dougall and Rohsenow (1963). It was derived by assuming a complete thermodynamic equilibrium between the vapor phase and the liquid phase. Dougall and Rohsenow modified the Dittus-Boelter equation to justify their work by postulating that if the amount of fluid present is small, a modified form of Dittus-Boelter equation would give a fairly accurate prediction of the heat transfer coefficient in the DFFB. To represent the flow field due to the presence of liquid droplets, Dougall and Rohsenow defined a two-phase velocity that is to be used in the Reynolds number as

$$u = \frac{Q_l + Q_v}{A} \tag{2.12}$$

where Q_l is the average volumetric flow rate of liquid, Q_v is the average volumetric flow rate of vapor, and A is the fluid flow cross sectional area. Equation (2.12) represents the velocity as the total volumetric flow rate of the fluid across the cross sectional area. Substituting Equation (2.11) into the Dittus-Boelter equation and rearranging the terms results in terms of two-phase Reynolds number. The Nusselt number is given as

$$Nu = \frac{hD}{k_g} = 0.023\left[\left(\frac{GD}{\mu_g}\right)\left(x + \frac{\rho_g}{\rho_f}(x-1)\right)\right]^{0.8} \Pr_g^{0.4} \tag{2.13}$$

The fluid properties in Equation (2.13) are evaluated at the saturated temperature. Dougall and Rohsenow recommended the use of their correlation at moderate qualities, without specifying the recommended quality range.

Table 2. 3 DFFB empirical equations [reproduced from Groeneveld and Snoek (1986)]

Equation and reference	Range of applicability of equation				Equation agrees with data from reference	Comments
	P, MPa	G, $Mgm^{-2}s^{-1}$	X	Geometry		
$Nu_{vf} = 0.00136 \mathrm{Re}_{vf}^{0.853} \mathrm{Pr}_{vf}^{1/3} \left(\frac{x}{1-x}\right)^{0.147} \left(\frac{\rho_f}{\rho_g}\right)^{2/3}$ Polomik et al. (1961)	5.60-10.2	1.00-2.45	0.40-0.70	Annulus	Polomik et al. (1961)	Exponents and coefficients for these equations are obtained from least-square error analysis using data from Polomik (1961)
$Nu_{vf} = 0.416 \mathrm{Re}_{vf}^{0.509} \mathrm{Pr}_{vf}^{1/3} \left(\frac{1-x}{x}\right)^{0.616} \left(\frac{\rho_g}{\rho_f}\right)^{0.208}$ Polomik et al. (1961)	5.60-10.2	1.00-2.45	0.40-0.70	Annulus	Polomik et al. (1961)	
$Nu_{vf} = 0.023 \mathrm{Re}_{vf}^{0.292} \mathrm{Pr}_{vf}^{1/3} \left(\frac{1-x}{x}\right)^{0.01} \left(\frac{\rho_f}{\rho_g}\right)^{0.091} q^{0.417}$ Polomik et al. (1961)	5.60-10.2	1.00-2.45	0.40-0.70	Annulus	Polomik et al. (1961)	
$q\left[D_e^{0.2}/(Gx)^{0.8}\right] = C(T_w - T_s)^m, m = 1.284 - 0.00312G, C = \frac{1}{389}e^{0.01665G}$ Collier (1962)	7.03	>1.00	0.15-1.00	Round tubes and annuli	Polomik et al. (1961) Bertoletti (1961)	$T_w - T_{sat}$ must be below 200°C
$q\left[D_e^{0.2}/(Gx)^{0.8}\right] = 0.018(T_w - T_{sat})^{0.921}$ Collier (1962)	7.03	See comments	0.15-1.00	Round tubes and annuli	Polomik et al. (1961) Bertoletti (1961)	Correlation may be used if either $G < 1 Mg/m^2.s$ or $T_w - T_{sat} > 200°C$
$h = 0.023\frac{k_g}{D}\mathrm{Re}_g^{0.8}\mathrm{Pr}_g^{0.4}, \mathrm{Re}_g = \frac{GD}{\mu_g}\left[x_{eq} + \frac{\rho_g}{\rho_f}(1-x_{eq})\right]$ Dougall and Rohsenow (1963)	<3.5	1.66-3.65	<0.5	Tubes	Dougall and Rohsenow (1963)	
$Nu_g = 0.023\left\{\mathrm{Re}_g\left[x + \frac{\rho_g}{\rho_f}(1-x)\right]\right\}^{0.8} \mathrm{Pr}_w^{0.8} Y$ $Y = 1 - 0.1\left(\frac{\rho_f}{\rho_g} - 1\right)^{0.4}(1-x)^{0.4}$ Miropolskiy (1963)	4.05-22.3	0.7-2.0	0.06-1.00	Tubes	Swenson et al. (1961) Schmidt (1960) Miropolski (1963)	Factor Y was determined empirically

Table 2.3 (continued)

Equation and reference	Range of applicability of equation				Equation agrees with data from reference	Comments
	P, MPa	G, $Mgm^{-2}s^{-1}$	X	Geometry		
$Nu_w = 0.005\left(\frac{D_e u_m \rho_w}{\mu_w}\right)^{0.8} Pr_g^{0.5}$ Tong (1965)	>14.0	>0.7	<0.10	Tubes	Bishop et al. (1962) Bishop et al. (1964)	Design equation. To be used only at low-quality or subcooled conditions.
$Nu_{vf} = 0.098\left[Re_w \frac{\rho_w}{\rho_g}\left(x + \frac{\rho_g}{\rho_f}(1-x)\right)\right]^{0.8} Pr_w^{0.83}\left(\frac{\rho_g}{\rho_f}\right)^{0.50}$ Bishop et al. (1964)	16.8-21.9	1.35-3.40	0.1-1.00	Round tubes	Bishop et al. (1964) Swenson et al. (1961) Miropolski (1963)	Based on high-pressure data
$Nu_{vf} = 0.055\left[Re_w \frac{\rho_w}{\rho_g}\left(x + \frac{\rho_g}{\rho_f}(1-x)\right)\right]^{0.82} Pr_w^{0.96}\left(\frac{\rho_g}{\rho_f}\right)^{0.34}\left(1 + \frac{26.9}{L/D}\right)$ Bishop et al. (1964)	16.8-21.9	1.35-3.40	0.1-1.00	Round tubes	Bishop et al. (1964)	
$Nu_{vf} = 0.0193 Re_{vf}^{0.8} Pr_{vf}^{1.23}\left(\frac{\rho_g}{\rho_f}\right)^{0.068}\left[x + \frac{\rho_g}{\rho_f}(1-x)\right]^{0.68}$ Bishop et al. (1965)	4.80-21.9	0.70-3.40	0.07-1.00	Round tubes	Polomik et al. (1961) Bishop et al. (1962) Bishop et al. (1964) Bishop et al. (1965) Swenson et al. (1961)	
$Nu_w = 0.033 Re_w^{0.8} Pr_w^{1.25}\left(\frac{\rho_g}{\rho_f}\right)^{0.197}\left[x + \frac{\rho_g}{\rho_f}(1-x)\right]^{0.738}$ Bishop et al. (1965)	4.80-21.9	0.70-3.40	0.07-1.00	Round tubes	Polomik et al. (1961) Bishop et al. (1962) Bishop et al. (1964) Bishop et al. (1965) Swenson et al. (1961)	
$Nu_{vf} = 0.00115 Re_g^{0.9} Pr_g^{0.3}\left(\frac{T_w}{T_{sat}} - 1\right)^{-0.15}$, T in F Polomik (1967)	4.08-10.2	0.70-2.70	0.20-1.00	2-rod	Hench (1964)	Has additional temperature parameter to allow for property variations at the heater wall ± 20% variation with data from Hench (1964)
$Nu_g = 0.0039\left[Re_g\left(x + \frac{\rho_g}{\rho_f}(1-x)\right)\right]^{0.9}$ Polomik (1967)	4.08-10.2	0.70-2.70	0.20-1.00	2-rod	Hench (1964)	±10% variation with data from Hench (1964). Better than above equation

Table 2.3 (continued)

Equation and reference	Range of applicability of equation				Equation agrees with data from reference	Comments
	P, MPa	G, $Mgm^{-2}s^{-1}$	X	Geometry		
$Nu_w = 0.06\left\{\left[\mathrm{Re}_w\left(x+\frac{\rho_g}{\rho_l}(1-x)\right)\right]\left(\frac{\rho_w}{\rho_g}\right)\mathrm{Pr}_w\right\}^{0.8}\left(\frac{G}{G_0}\right)^{0.4}\left(\frac{p}{p_c}\right)^{2.7}$ $G_0 = 10^3 kg/(m^2 s)$ Herkenrath et al. (1967)	14.2-22.3	0.75-4.10	0.10-1.00	Tubes	Herkenrath et al. (1967) Bishop et al. (1964) Swenson et al. (1961)	
$Nu_{vf} = 0.0089\left(\mathrm{Re}_{vf}\frac{x}{a}\right)^{0.84}\mathrm{Pr}_{vf}^{1/3}\left(\frac{1-x_{DO}}{x-x_{DO}}\right)^{0.124}$ Bervi et al. (1969)	5.06	0.5-3.0	0.4-1.0	Tubes	Bervi et al. (1969)	
$T_w - T_{sat} = 1.915\left[\frac{q}{G\left(x+\frac{1-x}{4.15}\right)}\right]^2$ Lee (1970)	14.2-18.2	1.00-4.00	0.3-0.75	Tubes	Lee (1970)	Based on data obtained with 1.3 cm ID indirectly heated tube
$Nu_g = 1.604\times10^{-4}\left\{\mathrm{Re}_g\left[x+\frac{\rho_g}{\rho_f}(1-x)\right]\right\}^{0.838}\mathrm{Pr}_w^{1.81}q^{0.278}\left(\frac{k_g}{k_{crit}}\right)^{0.508}$ Slaughterbeck et al. (1973)	6.88-20.2	1.05-5.30	0.12-0.90	Tubes	Bennett et al. (1967) Bishop et al. (1965) Bertoletti et al. (1964)	

Table 2.3 (concluded)

Equation and reference	Range of applicability of equation				Equation agrees with data from reference	Comments
	P, MPa	G, $Mgm^{-2}s^{-1}$	X	Geometry		
$Nu_g = a\left\{Re_g\left[x+\frac{\rho_g}{\rho_f}(1-x)\right]\right\}^b Pr_w^c Y^d q^e$ $Y = 1-0.1\left(\frac{\rho_f}{\rho_g}-1\right)^{0.4}(1-x)^{0.4}$ i) $a = 0.000185, b = 1.00, c = 1.57, d = -1.12, e = 0.131$ $a = 0.00109, b = 0.989, c = 1.41, d = -1.15, e = 0$	6.88-21.8	0.70-5.30	0.10-0.90	Tubes	Bennett et al. (1967) Era et al. (1967) Bishop et al. (1964), (1965) Bertoletti (1961) Bertoletti et al. (1964) Swenson et al. (1961) Schmidt (1960) Era et al. (1967) Bennett et al. (1964) Groeneveld (1969) Polomik et al. (1961)	
ii) $a = 0.013, b = 0.664, c = 1.68, d = -1.12, e = 0.133$ $a = 0.052, b = 0.688, c = 1.26, d = -1.06, e = 0$	3.44-10.1	0.80-4.10	0.10-0.90	Annuli	Bennett et al. (1967), (1964) Era et al. (1967) Groeneveld (1969) Bishop et al. (1964), (1965) Bertoletti (1961) Bertoletti et al. (1964)	
iii) $a = 0.000775, b = 0.902, c = 1.47, d = -1.54, e = 0.112$ $a = 0.00327, b = 0.901, c = 1.32, d = -1.5, e = 0$ Groeneveld (1973)	3.44-21.8	0.70-5.30	0.10-0.90	Tubes and annuli		
$q = q_{TB} + 0.023(T_w - T_v)\frac{k_v}{D_e}\left(\frac{\rho_v V_m D_e}{\mu_v}\right)^{0.8} Pr_v^{0.333}$ $q_{TB} \equiv$ transition boiling heat flux $V_m \equiv$ near wall mixture velocity Tong and Young (1974)	4.05-10.1	0.4-5.15	0.2-1.45	Tubes	Bennett et al. (1967) Era et al. (1967) Keeys et al. (1971).	Correlation also valid for transition boiling region if q_{TB} reported by Tong (1974) is used
$h = 0.114\,Re_g^{0.244} Pr_{g,w}^{2.54} D_e^{-0.304} k_g^{0.334}$ Mattson et al. (1974)	4.18-9.88	1.00-4.10	0.10-0.90	Annuli	Groeneveld (1969) Polomik (1967)	RMS error: 17.5%
$Nu_{vf} = 0.0089\left(\frac{GxD}{\alpha\mu_{vf}}\right)^{0.84}\left(\frac{C_{P,vf}\mu_{vf}}{k_{vf}}\right)^{1/3}\left(\frac{1-x_{DO}}{x-x_{DO}}\right)^{1/8}$ Cumo and Urbani (1974)	7	1.03-2.00	0.45-1.20	Annuli	Cumo and Urbani (1974)	Error:10-25%

At low flow, non-equilibrium becomes very significant which, generally, results in a large error when using thermal equilibrium correlations. The vapor superheat increases with increased thermal non-equilibrium, resulting in lower heat transfer coefficient. As a result, thermal equilibrium correlations over predict heat transfer coefficient for low flows. The accuracy of the thermal equilibrium correlations diminishes considerably at low flows and low qualities, where the flow regime might be that of the inverted annular and since thermal equilibrium correlations are only applicable to the high positive quality region.

B. Thermal non-equilibrium correlations

The main assumptions when formulating thermal non-equilibrium equations are the thermodynamic non-equilibrium between the phases, and turbulent convective heat transfer from the heated wall to the vapor phase. Thermal non-equilibrium equations are expected to give better results than thermal equilibrium equations [Andreani and Yadigaroglu (1994)].

Thermal non-equilibrium can be expressed as the ratio or the difference between the actual quality to the equilibrium quality, which is related to the actual average vapor enthalpy as

$$\frac{x_a}{x_{eq}} = \frac{H_{fg}}{H_v - H_f} \tag{2.14}$$

Thermal non-equilibrium can also be expressed by the bulk vapor superheat or T_v-T_{sat}.

If the vapor temperature is known, the wall heat flux is calculated from

$$q_w = h(T_w - T_v) \tag{2.15}$$

Probably the best-known correlation of this kind is that of Groeneveld and Delorme (1976). Predictions from the Groeneveld-Delorme correlation are in good agreement with data from a variety of sources. Groeneveld and Delorme have shown that the correlation exhibits correct asymptotic trends. The use of the correlation outside its database range can lead to large prediction errors. Good performance of this correlation under high mass flux conditions has been reported by Kumamaru et al. (1987).

In order to estimate the actual vapor qualities, Groeneveld and Delorme (1976) calculated values of actual quality x_a from data of wall temperature measurements. They also used the Hadaller and Banerjee (1969) correlations with the vapor properties calculated at the film temperature and replaced the Reynolds number with a two-phase Reynolds number used by Dougall and Rohsenow (1963). The heat transfer coefficient calculated using the Groeneveld and Delorme (1976) correlation is given as

$$\frac{hD}{k_g} = \frac{qD}{(T_w - T_{g,a})} = a\left[\left(\frac{GD}{\mu_{fg}}\right)\left(x_a + \frac{\rho_g}{\rho_f}(x_a - 1)\right)\right]^b \Pr_{fg}^c \left(e + f\frac{D}{L}\right)^g \tag{2.16a}$$

where

$$x_a = \frac{H_{fg} x_e}{H_v(p, T_v) - H_f}, \tag{2.16b}$$

$$\frac{H_v(p, T_v) - H_v(p, T_{sat})}{H_{fg}} = \exp(-\tan\psi), \tag{2.16c}$$

$$\psi = a_1 \Pr_g^{a_2} \mathrm{Re}_{\mathrm{hom}}^{a_3} \left(\frac{q_{D,c_{p,g,e}}}{k_g H_{fg}} \right)^{a_4} \sum_{i=0}^{2} b_i x_e^i , \tag{2.16d}$$

if $\psi < 0$ then $\psi = 0$, if $\psi > \pi/2$ then $\psi = \pi/2$,

and,

$$\mathrm{Re}_{\mathrm{hom}} = \left(\frac{GD}{\mu_{v,eq}} \right) \left(x_l + \frac{\rho_v}{\rho_f} (1 - x_l) \right) \tag{2.16e}$$

$(0 < x_l = x_{eq} < 1)$

For flows in tubes, the constants in Equation (2.16) are given as

$a_1 = 0.13864, a_2 = 0.2031, a_3 = 0.20006, \text{and } a_4 = -0.09232$

and,

$b_0 = 1.3072, b_1 = -1.0833, \text{and } b_2 = 0.8455$

Hein and Kohler (1984) provided a non-equilibrium equation which gives very good agreement with the database of water, Freon-12 and hydrogen, as reported by Andreani and Yadigaroglu (1994). Its range of application covers high pressures, moderate to high mass fluxes and high qualities. Table 2.4 is updated from Hammouda (1996) and lists the better-known non-equilibrium post-dryout equations.

2.5.5.2. Models

There are two types of models used to predict post-dryout heat transfer in the liquid deficient region. These are the phenomenological models and the mechanistic models. The primary objective of phenomenological models is to calculate the vapor superheat based on the physical processes involved. The wall-liquid contact heat transfer and radiative heat transfer are usually neglected with these models. The phenomenological models can be divided into local-conditions models and history-dependent models.

- The local-condition models calculate the vapor superheat and the wall transfer at any location downstream from the dryout point based on local thermodynamic parameters, such as x_{eq}, p, G, and T_w or q_w. The correlations used are not only based on regression analysis of measured or inferred data but they are based also on simplified phenomenological description of the physical processes. Models in this category are those of Chen et al. (1979) (also known as the CSO model), Yoder and Rohsenow (1983) and Varone and Rohsenow (1984).

- The history-dependent models estimate the vapor superheat at any location downstream from the dryout point, recognizing that thermal non-equilibrium is dependent on upstream conditions starting from the CHF point. Thermal non-equilibrium is calculated from a stepwise integration of the conservation of mass equation for the vapor phase, which includes an actual volumetric vapor generation function Γ,

$$\frac{dx_a}{dx_{eq}} = \frac{\Gamma}{\Gamma_{eq}} \tag{2.17}$$

where $\Gamma_{eq} = 4q/(DH_{fg})$ is the volumetric vapor generation function at equilibrium.

Table 2. 4 Non-equilibrium post-dryout equations [updated from Hammouda (1996)]

Reference	Non-equilibrium equation	To be used in conjunction with	Comments
Tong and Young(1974)	$\frac{x_a}{x_{eq}} = 1 + aB - 0.12\left[x_{eq} - \exp\left(bB^{0.8}\right)\right]$ $B = 0.05 + G/1350$ $G < 945\, kg/(m^2 s), a = -0.49, b = -0.26$ $1080 < G < 3375; a = -0.29, b = -0.57$ $945 < G < 1080;$ *interpolate*	$q = q_{TB} + q_{FB};$ $q_{TB} = q_{NB} + \exp\left[f(\Delta T, x_{eq}, q)\right]$ q_{FB} *get it from,* $Nu_v = 0.023\left\{\frac{GD}{\mu_v}\left[\frac{x_a \frac{\rho_v}{\rho_g} + S(1-x_a)\frac{\rho_v}{\rho_f}}{x_a + S(1-x_a)}\right]\right\}^{0.8} \Pr_v^{0.4}$	Non-equilibrium is assumed to disappear for $\Delta T < 111$ °C or $G >$ 3375 kg/(m^2.s)
Groeneveld and Delorme (1976)	$\frac{H_v - H_{v,eq}}{H_{fg}} = \exp(-\tan\Psi)$ $\Psi = a_1 \Pr_{v,eq}^{a_2} \mathrm{Re}_{hom}^{a_3}\left(\frac{qDC_{P,v,eq}}{k_{v,eq}H_{fg}}\right)^{a_4} \sum_{i=0}^{i=2} b_i x_{eq}^i$ $a_1 = 0.13864, a_2 = 0.2031, a_3 = 0.20006, a_4 = -0.09232$ $b_0 = 1.3072, b_1 = -1.0833, b_2 = 0.8455$ $if\ \Psi < 0 \rightarrow \Psi = 0, if\ \Psi > \frac{\pi}{2} \rightarrow \Psi = \frac{\pi}{2}$ $\mathrm{Re}_{hom} = GDx_l / \mu_{v,eq}\alpha_{hom}, x_l = \min(x_{eq}, 1)$	$Nu_{vf} = 0.008348\left\{\frac{GD}{\mu_{vf}}\left[x_a + \frac{\rho_v}{\rho_f}(1-x_a)\right]\right\}^{0.8774} \Pr_{vf}^{0.6112}$	Overpredicts T_v measured by Najhawan (1980): x_a=*max* (predicted value x_{do}), i.e., just downstream of dryout x_a=x_{do} until T_v is reached
Plummer et al. (1976)	$\frac{x_a - x_{do}}{x_{eq} - x_{do}} = K = 0.07\ln\left[G(1-x_{DO})^5\sqrt{\frac{D}{\rho_v}}\right] + 0.4$	$q = h_{wv}(T_w - T_v) + h_{wd}(T_w - T_{sat})$ $Nu_v = 0.23\left(\frac{Gx_a D}{\mu_v \alpha}\right)^{0.8} \Pr_v^{1/3}\left(\frac{\mu_v}{\mu_w}\right)^{0.14}\left[1 + 0.3\left(\frac{D}{0.01D + L_{FB}}\right)^{0.7}\right]$ $h_{wd} = \frac{k_{vf}}{d}(1-\alpha)\exp\left(-2\frac{D}{L_{FB}}\right); d = 1.22\times10^{-4} m$	To evaluate the slip ratio, S, use an iterative procedure: $S = f(D_{do}, K, x_{eq}, x_{do})$ S needed to calculate the void. L_{FB} is the film boiling length
Chen et al. (1979)	$\frac{x - x_a}{x} = \frac{0.26(T_v - T_{sat})}{\left[1.15 - \left(\frac{p}{p_c}\right)^{0.65}\right](T_w - T_v)}$	$h_{wv} = \frac{f}{2} G x_a C_{P,vf} \Pr_{vf}^{2/3}$ $f = 0.037\left\{\frac{DG}{\mu_v}\left[x_a + \frac{\rho_v}{\rho_f}(1-x_a)\right]\right\}^{-0.17}$	Underpredicts T_v measured by Nijhawan (1980)

Table 2.4 (concluded)

Reference	Non-equilibrium equation	To be used in conjunction with	Comments
Shah (1980)	for $\frac{q}{H_{fg}G} > 4.5\times10^{-4}; x_a = f(x_{DO}, x_{eq}, Fr_f)$ $Fr_f = G^2/(\rho_f^2 g D)$ $f \equiv$ graphical relationship may also be obtained from table	$Nu_{vf} = 0.008348\left[\frac{GD}{\mu_{vf}}\left(x_a + \frac{\rho_v}{\rho_f}(1-x_a)\right)\right]^{0.8774} \mathrm{Pr}_{vf}^{0.6112}$	F_{DC} : droplet cooling factor
Hein and Kohker (1984)	$\frac{x_a}{x_{eq}} = \frac{2}{\sqrt{1+\frac{4C_{P,v}q}{H_{fg}(h_iF)}}-1}$ $T_v = T_{sat} + \frac{H_{fg}}{2C_{P,v}}\left[\sqrt{1+\frac{4C_{P,v}q}{H_{fg}(h_iF)}}-1\right]$	$(h_iF) = \begin{cases} 1.473\times10^{-7}(G/L_{La})^{1.33} & \text{for } G/L_{La} < 1767\times10^3 \\ 3.078\times10^{-24}(G/L_{La})^4 & \text{for } G/L_{La} > 1767\times10^3 \end{cases}$ $Nu_{wv} = \frac{(f_w/8)(\mathrm{Re}_v - 1000)\mathrm{Pr}_v}{1+12.7\sqrt{f_w/8}(\mathrm{Pr}_v^{2/3}-1)}$ $f_w = (1.82\log_{10}\mathrm{Re}_v - 1.64)^{-2}$ $\mathrm{Re}_v = \frac{GD}{\mu_v}\left[x_a + (1-x_a)\frac{\rho_v}{\rho_L}\right]$ $L_{La} = \sqrt{\frac{\sigma}{g(\rho_L-\rho_v)}}$	(h_iF) expressed in kW/m^2 q expressed in kW/m^2 G expressed in kg/(m^2.s)
Sergeve (2005)	$\frac{dx_a}{dx} = Cm\frac{k_v}{\sigma\rho_l}\frac{P_g(\rho W)^2}{\sum_j (qP_h)_j}x_a(1-x_a)\left(\frac{x-x_a}{x_a}\right)^n$	$Nu_v = 0.028\mathrm{Re}_v^{0.8}\mathrm{Pr}_v^{0.4}(\rho_w/\rho_v)^{1.15}$, $Nu_v = 0.023\mathrm{Re}_v^{0.8}\mathrm{Pr}_v^{0.4}(T_v/T_w)^{0.5}$	

The main feature for identifying these models is the method used in attempting to estimate Γ. Examples of such models are those of Jones and Zuber (1977), Webb et al. (1982) and Webb and Chen (1984). Andreani and Yadigaroglu (1994) do not recommend the use of history-dependent models. Their argument is that more experimental work is needed to improve these phenomenological models.

The mechanistic models are all based on the same calculation method: at any elevation z the heat transfer processes are calculated by taking into account the local values of the flow variables, as obtained by a stepwise integration of the conservation of mass, momentum and energy equations downstream starting from the point of onset of dispersed flow. All of them aim at the mechanistic prediction of the wall-to-vapor and vapor-to-droplet heat transfer (two-step models): some consider also the direct contact heat exchange between the wall and the droplets (three-step models) and/or radiation.

2.6. Film Boiling Look-up Table

The success of the critical heat flux look-up table [Groeneveld et al. (1986)] led Leung and Groeneveld (1988) to propose a film boiling look-up table (FB-LUT). The new FB-LUT of Groeneveld et al. (2003) is a four dimensional normalized data bank and provides fully developed film boiling heat transfer coefficients as a function of pressure, mass flux, equilibrium quality, and wall superheat or wall heat flux. The advantage of this table is that it is applicable to a very wide range of conditions and provides good prediction accuracy for the film-boiling heat transfer coefficient.

The main steps followed in building the FB-LUT of Groeneveld et al. (2003) are:

- constructing a skeleton table
- updating the skeleton table with the University of Ottawa database for experimental post-dryout heat transfer coefficient

- smoothening of the table to minimize fluctuations due to the scattering of experimental data

Five different skeleton tables were constructed using the most accurate prediction methods available to date. The methods used are of Groeneveld and Delorme (1976), Köhler and Hein (1986), Hammouda (1996), Chen and Chen (1998) and Shah and Siddiqui (2000). Each skeleton table was divided into 64 sub-regions and these sub-regions were assessed against the database. The final skeleton table then was constructed by taking the best prediction of the five methods in each sub-region. Moreover, the skeleton table values are filtered to be at least equal to the heat-transfer coefficient of laminar flow of the vapor:

$$h_{table} = Max\left(h_{model},\ 4.3636\frac{k_{vf}}{D} \right) \quad (2.18)$$

The vapor-film properties were evaluated at the vapor-film temperature defined as

$$T_{vf} = \frac{T_W + T_{bulk}}{2} \quad (2.19)$$

where

$T_{bulk} = T_{sat}$ for $x \le 1$, and

$T_{bulk} = T_v$ for $x > 1$.

The skeleton table values are then smoothened manually to remove discontinuities between sub-regions and then modified with the University of Ottawa film boiling database. A final LUT was obtained after smoothing the modified skeleton table using the method of Huang and Cheng (1994) for multi-dimensional smoothening.

The principal advantage of the FB-LUT is in its ability to predict the heat transfer coefficient for a very wide range of application (p = 100 to 20000 kPa; G = 0 to 7000 kg.m^{-2}.s^{-1}; x = -0.2 to 2.0; ΔT_w = 5 to 1200 °C). It is able to predict the heat transfer coefficient as well as the correlations and models used in the regions where there are no experimental data available. In regions which are enhanced (modified) with experimental data, the look-up table predicts the heat transfer coefficient with an RMS error of 10.57 % and an average error of 1.7% which is better prediction accuracy than most of the available prediction methods.

The FB-LUT is divided into three main regions indicated by color code. These regions are: the experimental data dependent region, the correlations and models region, and the "impossible to occur" region which is used for the purpose of interpolation. Unfortunately, the experimental data dependent region represents a small part of the table due to the scarcity of data. Improvements of the table can be achieved by either finding new data from the unpublished sources (most film boiling data can only been found in unpublished reports) or by performing experiments at conditions where data are unavailable , possibly in fluids other than water with the proper fluid-to-fluid modeling techniques.

CHAPTER 3 REVIEW OF EXPERIMENTAL METHODS FOR IAFB HEAT TRANSFER

3.1. General

The occurrence of CHF in a heat flux controlled system will result in a large increase in wall temperature of the heated surface. This increase might cause physical burn-out of the heated surface. This is especially true for subcooled water where the heat flux at CHF is very high. Although the resulting IAFB conditions are impossible to obtain during normal operation of nuclear reactors, they could occur during a LOCA. Experiments to measure IAFB are nearly impossible to obtain using a conventional heat flux controlled system. To overcome the difficulties associated with obtaining IAFB data, the "hot-patch" techniques are implemented. Currently there are two successfully implemented hot-patch methods, (i) the indirectly heated hot-patch and (ii) the directly heated hot-patch. They are described in the following two subsections. Subsequent to the introduction of this technique, large amounts of data have been generated for water flowing upwards in vertical tubes. These data include data of Fung (1981), Stewart and Groeneveld (1982), Laperriere (1983), Swinnerton et al. (1988), Mosaad and Johannsen (1988), and Chen et al. (1988).

3.2. The Indirectly Heated Hot-Patch Technique

This experimental technique uses a cylindrical copper block brazed onto the test section, as shown schematically in Figure 3.1. The hot patch is heated by cartridge heaters

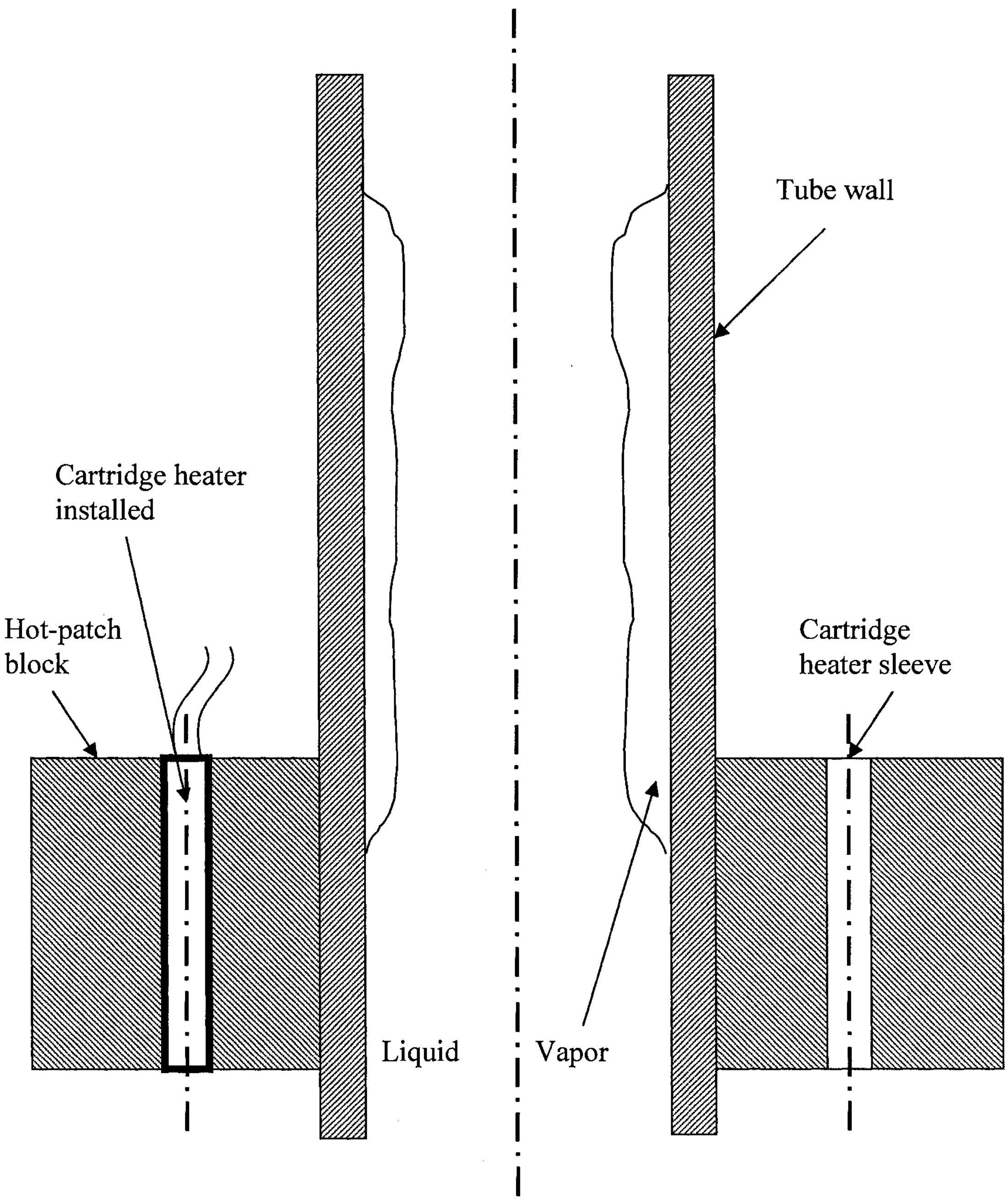

Figure 3. 1 Schematic diagram of the indirectly heated hot-patch technique.

embedded in the copper block. The power supply to the hot patch heaters is independent from the power supply used for heating the remainder of the test section. This will allow the hot patch heat flux to exceed the critical heat flux, while the test section heat flux is still low enough to prevent failure. IAFB data using the indirectly heated hot-patch technique have been obtained by several authors and are summarized in Table 3.1.

3.3. The Directly Heated Hot-Patch Technique

In this method the wall thickness of the tube test section is reduced over a short length at both ends (a notch or groove), to increase the electrical resistance of the tube at the reduced thickness location (see Figure 3.2). This produces more heat flux at the notch location for the same power applied to the test section. The power to the hot patch and the test section may be controlled separately. This method was first applied by Chen and Li (1984) to obtain IAFB data. Table 3.1 summarizes the test conditions of IAFB experiments that have used the directly heated hot-patch technique.

3.4. Use of non-Aqueous Fluids

Some of the issues related to using water as a working fluid are safety (high-pressure and high-temperature conditions), and operational (high power and high operating cost). The use of lower pressure and lower boiling temperature fluids is more attractive in such cases using suitable fluid-to-fluid modeling relationships for film boiling. A similar approach has been used by many investigators for critical heat flux experiments where Freon is usually the modeling fluid of choice because of its low latent heat and low boiling points. Freon was also used as a coolant in IAFB experiments, including those of Hammouda (1996) and Takenaka et al. (1989) as shown in Table 3.1. Appendix C describes the fluid-to-fluid modeling methodology applied to film boiling.

Table 3. 1 Summary of subcooled and low-quality data obtained by hot-patch techniques for tube geometry

Reference	Test Fluid	Pressure (kPa)	Mass Flux (kg m^{-2} s^{-1})	Inlet quality	Hot-patch Technique*
Fung (1981)	Water	100	50-500	-0.131 to -0.009	Indirect
Stewart (1981)	Water	2000-9000	110-2750	-0.160 to -0.026	Indirect
Laperriere (1983)	Water	9600	1000-4500	-0.190 to 0.150	Indirect
Chen and Li (1984)	Water	100	134 – 646	-0.101 to 0.000	Direct
Chen (1987)	Water	1000 - 5500	130 – 920	-0.144 to 0.000	Direct
Chen et al. (1988)	Water	105 - 1024	25 - 512	-0.029 to 0.12	Direct
Swinnerton et al. (1988)	Water	200 - 2000	47-1010	-0.075 to -0.005	Indirect
Takenaka et al. (1989)	R-113	100	136-1280	-0.075 to -0.019	Indirect
Chen et al. (1989)	Water	410 - 6000	47.5 – 1462	-0.05 to 0.24	Direct
Mosaad and Johannsen (1989)	Water	100	50 – 500	-0.056 to 0.000	Direct
Chen and Chen (1996)	Water	110 - 5830	23.9 – 1460	-0.056 to 0.872	Direct
Hammouda et al. (1996)	R-12, R-22 and R-134a	830 - 1600	530 – 3000	Inlet subcooling 5 – 28 °C	Indirect

* Direct hot patch: using a groove in the test section.
Indirect hot patch: using a heater block.

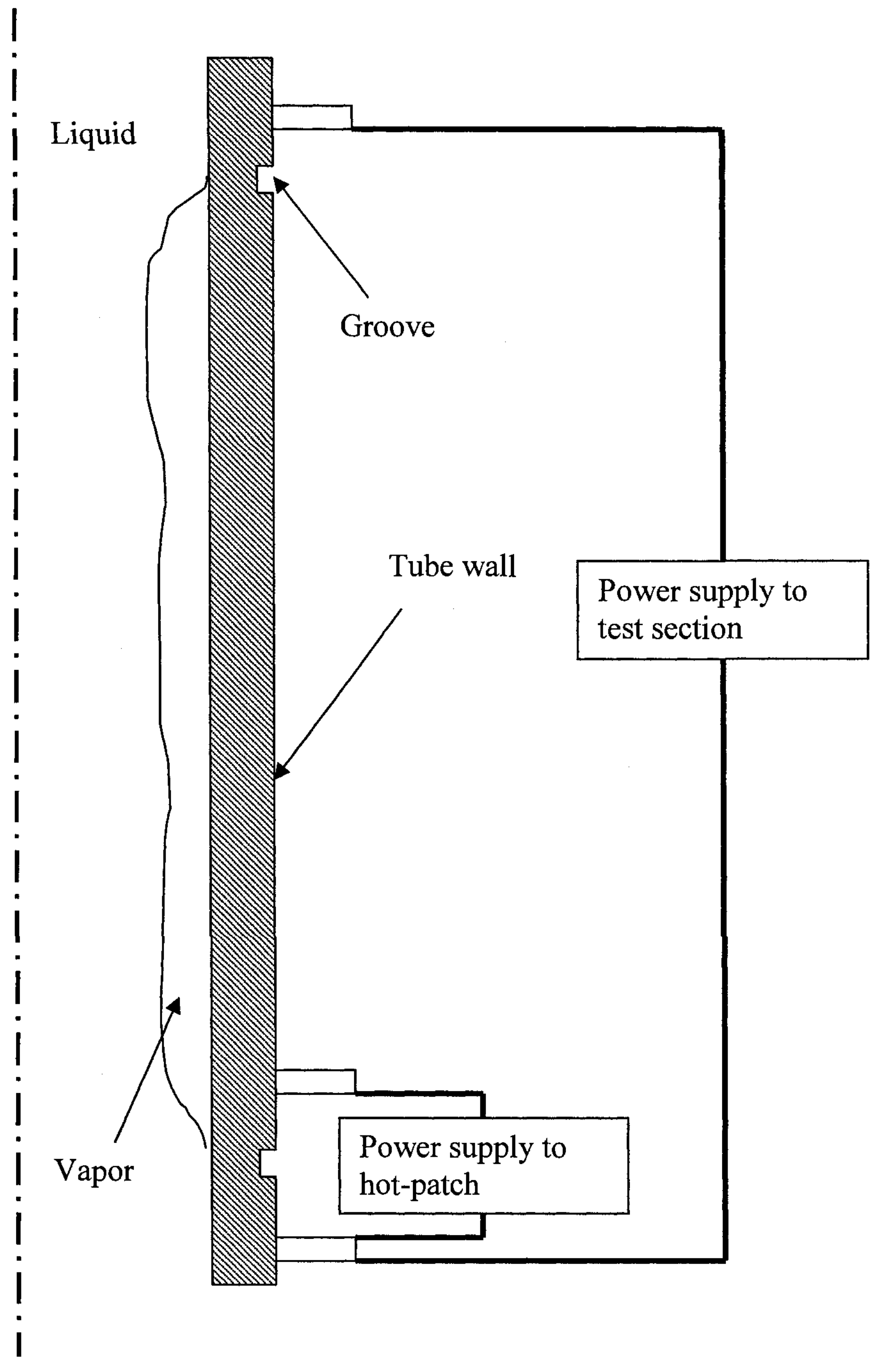

Figure 3. 2 Schematic diagram of the directly heated hot-patch technique.

CHAPTER 4 REVIEW OF OBSERVED PARAMETRIC TRENDS OF IAFB HEAT TRANSFER

4.1. General

The overall film boiling heat transfer coefficient is affected by flow parameters such as pressure, mass flux, heat flux and liquid subcooling, and some other secondary factors. The parametric trends observed in experimental studies are discussed below.

4.2. Pressure Effect

The general observed trend of the pressure effect is that the IAFB heat transfer coefficient increases with increasing pressure. No systematic experimental studies have been carried out on the pressure effect on IAFB. Pressure affects the values of the thermophysical properties of the vapor, especially the thermal conductivity k that increases with increased pressure (see Section 6.4). Single phase equations show that the heat transfer coefficient scales with $k^{0.67}$.

Stewart and Groeneveld (1982) found that in general the heat transfer coefficient decreases with a decrease in pressure. They also found that, at higher pressures, the axial temperature distribution is more uniform than at lower pressure. These observed trends by Stewart and Groeneveld (1982) of the pressure effect on heat transfer coefficient are demonstrated in Figure 4.1. Chen (1987) observed that at low subcooling and low flow rates the heat transfer coefficient increases with pressure. At higher subcooling and lower flow rates the trend is reversed. Further Chen et al. (1988, 1989) reported that the general trend of heat transfer coefficient is that it increases with increasing pressure.

4.3. Mass Flux Effect

In general, as mass flux increases, the heat transfer coefficient increases. This is explained by the increase in vapor Reynolds number with increased mass flux which results in better mixing in the vapor film (more turbulence which might result in increased entrainment). This will reduce the vapor film superheat and enhance the heat transfer coefficient. At high subcooling, the mass flux has less effect on heat transfer coefficient. In this region, the vapor film is thin and heat transfer is mostly controlled by conduction.

Bromley et al. (1953) studied film boiling of liquid in upward flow over horizontal tubes. They observed that the heat transfer coefficient increases with mass flux. Kalinin (1969), Fung (1981), Denham (1984), Chen (1987), Chen et al. (1988, 1990) and Mosaad (1988) observed a similar trend. Stewart and Groeneveld (1981) found that the heat transfer coefficient increases with an increase in mass flux. At high inlet subcoolings, the mass flux effect is strong. At lower inlet subcooling mass flux effect is much smaller. The findings of Stewart and Groeneveld (1981) appear to differ from these findings. Laperriere (1983) observed that at low subcooling and positive inlet quality, the heat transfer coefficient is strongly affected by mass flux. Takenaka et al. (1989) found that, using R-113, mass flux effect on heat transfer coefficient is stronger when $G > 320$ $kgm^{-2}s^{-1}$. For $G < 210$ $kgm^{-2}s^{-1}$, the heat transfer coefficient is less affected by mass flux. A representative result on the effect of mass flux on heat transfer coefficient is shown in Figure 4.2. The figure shows that the effect of mass flux on heat transfer coefficient is weak at low qualities and the effect increases as quality increases.

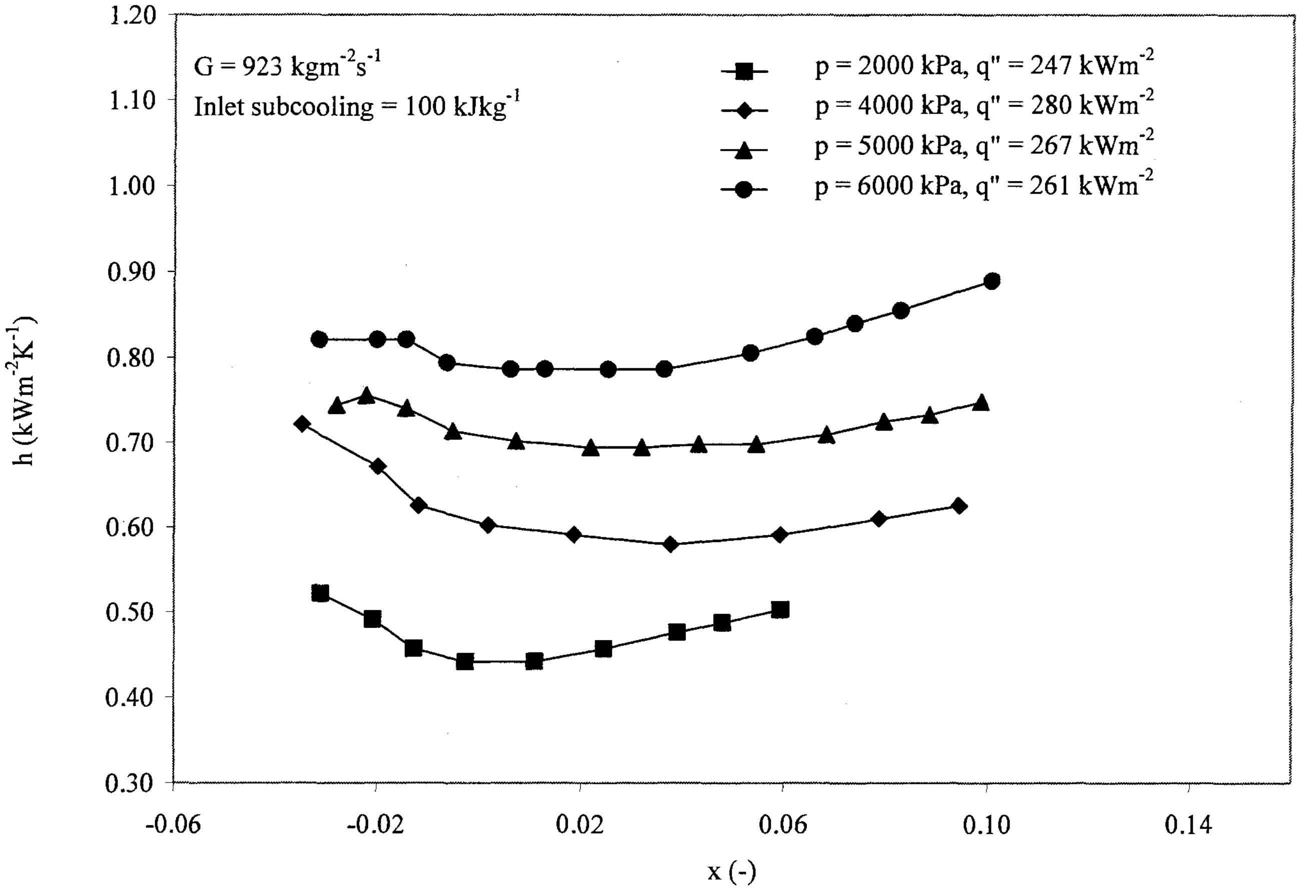

Figure 4. 1 General trend of effect of pressure on heat transfer coefficient [water data, reproduced from Stewart and Groeneveld (1982)].

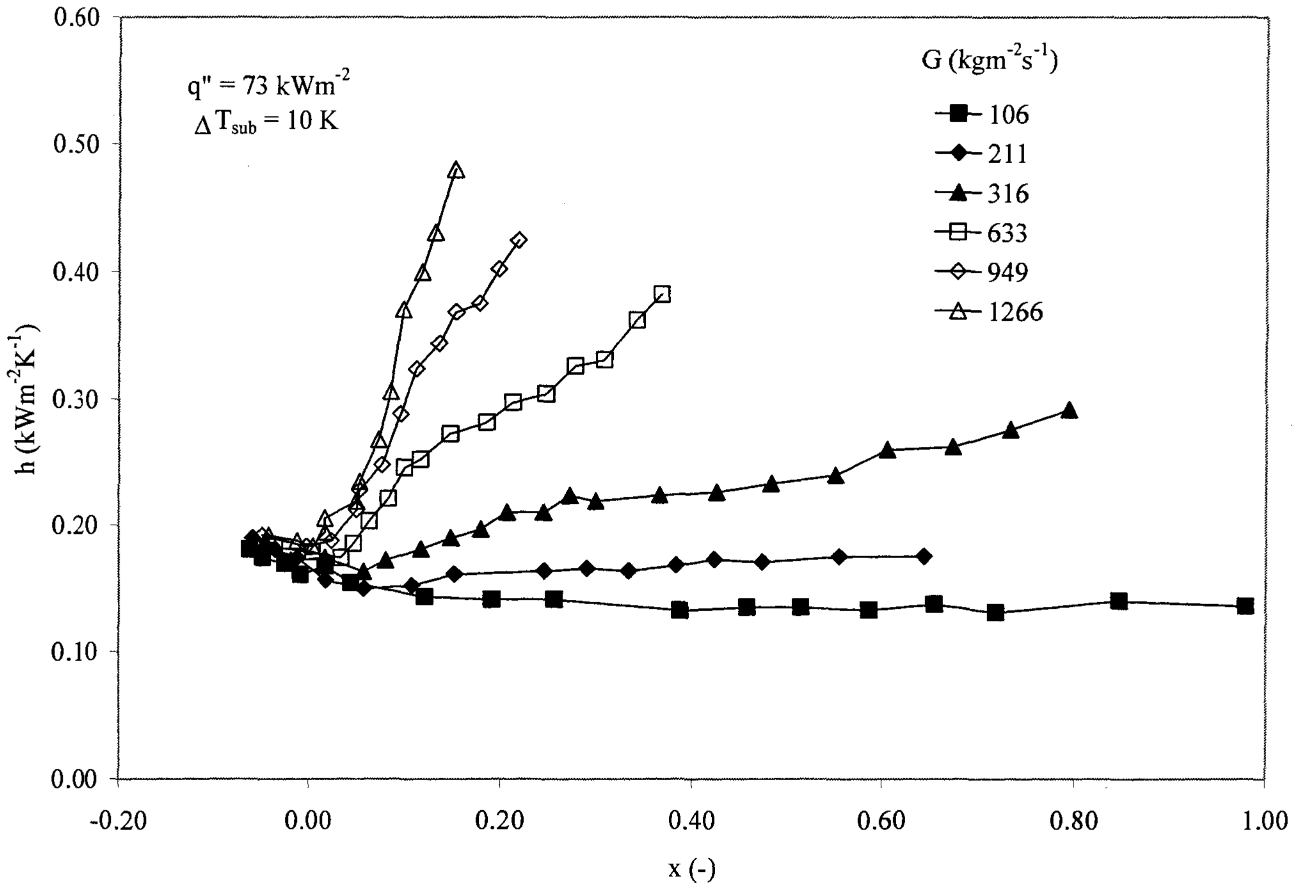

Figure 4. 2 General trend of effect of mass flux on heat transfer coefficient [reproduced from Takenaka et al. (1989)].

4.4. Heat Flux Effect

There is no definitive conclusion on the effect of heat flux on heat transfer coefficient. Mosaad and Johannsen (1989) showed that higher heat transfer coefficient values resulted at higher heat fluxes (Figure 4.3). For higher pressures and mass fluxes, Hammouda (1996) observed the same effect of heat flux on heat transfer coefficient as Mosaad and Johannsen (1989). On the other hand, Stewart (1981) observed that the heat transfer coefficient decreases as the heat flux increases (see Figure 4.4). This effect becomes more pronounced as the mass flux increases in the negative quality region. Also Laperriere (1983) reported that the heat transfer coefficient increases with decreasing heat flux. For higher mass fluxes, the heat flux effects are more noticeable at the upstream region of IAFB, especially at lower heat flux. In the downstream region, this effect decreases. The general observation of Chen and Li (1984) is that heat transfer coefficient decreases with increasing heat flux. Chen et al. (1989) found that in general in the subcooled region an increase in the heat flux produces a decrease in the heat transfer coefficient; however, the trend is reversed at positive qualities

There are two opposing components that can contribute to the effect of heat flux on heat transfer coefficient during subcooled IAFB:

- as the heat flux increases, the vapor layer thickness increases, and since conduction is the dominant heat transfer mode, the heat transfer coefficient drops.
- as the vapor layer thickness increases, the velocity increases and the flow becomes turbulent, resulting in an increase in heat transfer coefficient.

The balance between these two effects determines the overall effect of heat flux on heat transfer coefficient.

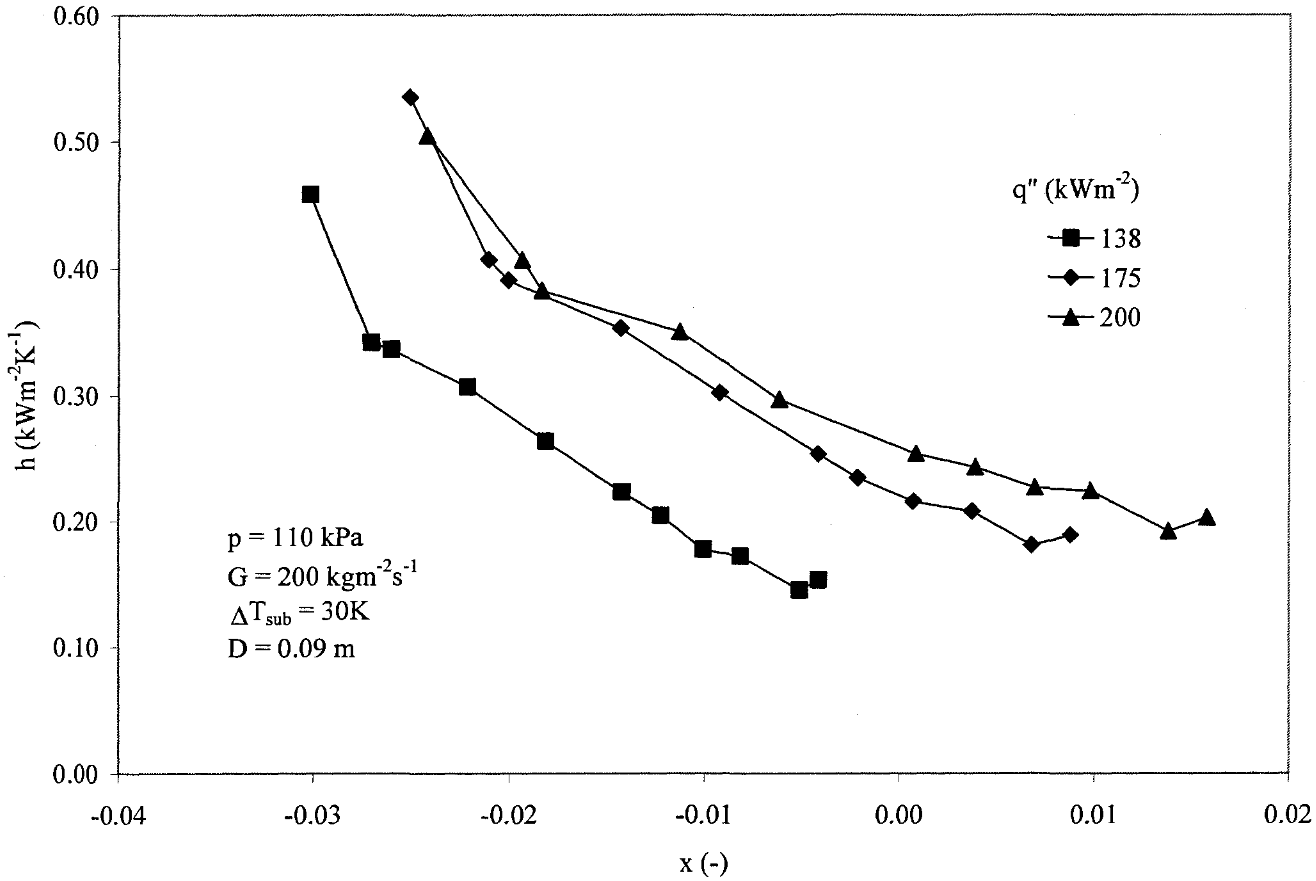

Figure 4. 3 Heat flux effect on heat transfer coefficient as observed by Mosaad and Johannsen (1989) [reproduced from Mosaad and Johannsen (1989)].

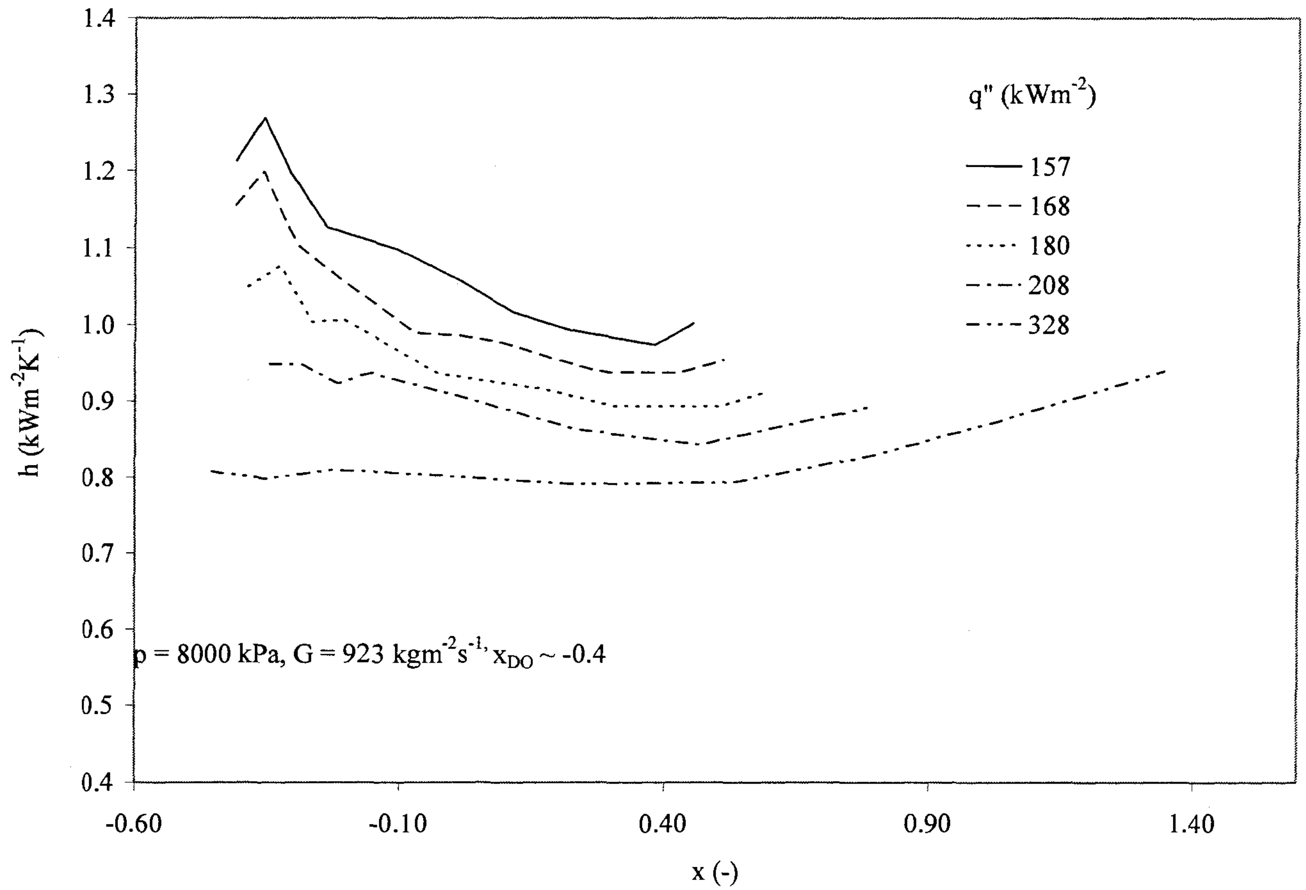

Figure 4. 4 Heat flux effect on heat transfer coefficient as observed by Stewart (1981) [reproduced from Stewart (1981) with modification].

4.5. Inlet Subcooling Effect

Stewart (1981) found that inlet subcooling has no effect on heat transfer coefficient at low mass fluxes and low pressures. He also found that the heat transfer coefficient is higher at higher inlet subcooling, when mass flux and pressure are increased. The effect of inlet subcooling becomes less pronounced as local quality increases. Chen (1987) reported that the heat transfer coefficient increased significantly with increased inlet subcooling. This increase seems less steep at lower inlet subcooling. In a more recent study, Chen et al. (1989) observed that the inlet quality effect is most significant over a short region near the dryout point (subcooled region). Similar findings were observed by Hammouda et al. (1996).

In general it can be concluded that the heat transfer coefficient is affected by inlet subcooling downstream of the CHF location. The effect of inlet subcooling on heat transfer coefficient decreases and even vanishes as local quality increases for the different inlet subcooling data. Figure 4.5 shows how inlet subcooling affects the heat transfer coefficient as observed by Chen et al. (1989) and Hammouda et al. (1996).

4.6. Effect of Length and Local Quality

Both length and local quality have the same general effect on heat transfer coefficient due to the linear proportionality between them. Fung (1981) and Fung et al. (1979) observed that, when moving downstream along the test section, the heat transfer coefficient initially decreases, then levels off towards the end of the test section (Figure 4.6). Chen and Li (1984) found that at low inlet subcooling, the heat transfer coefficient decreases continuously along the test section. At high inlet subcooling the heat transfer coefficient increases to a maximum, then decreases further downstream. Denham (1984) and Mosaad and Johannsen (1989) reported that from negative to positive quality, the heat

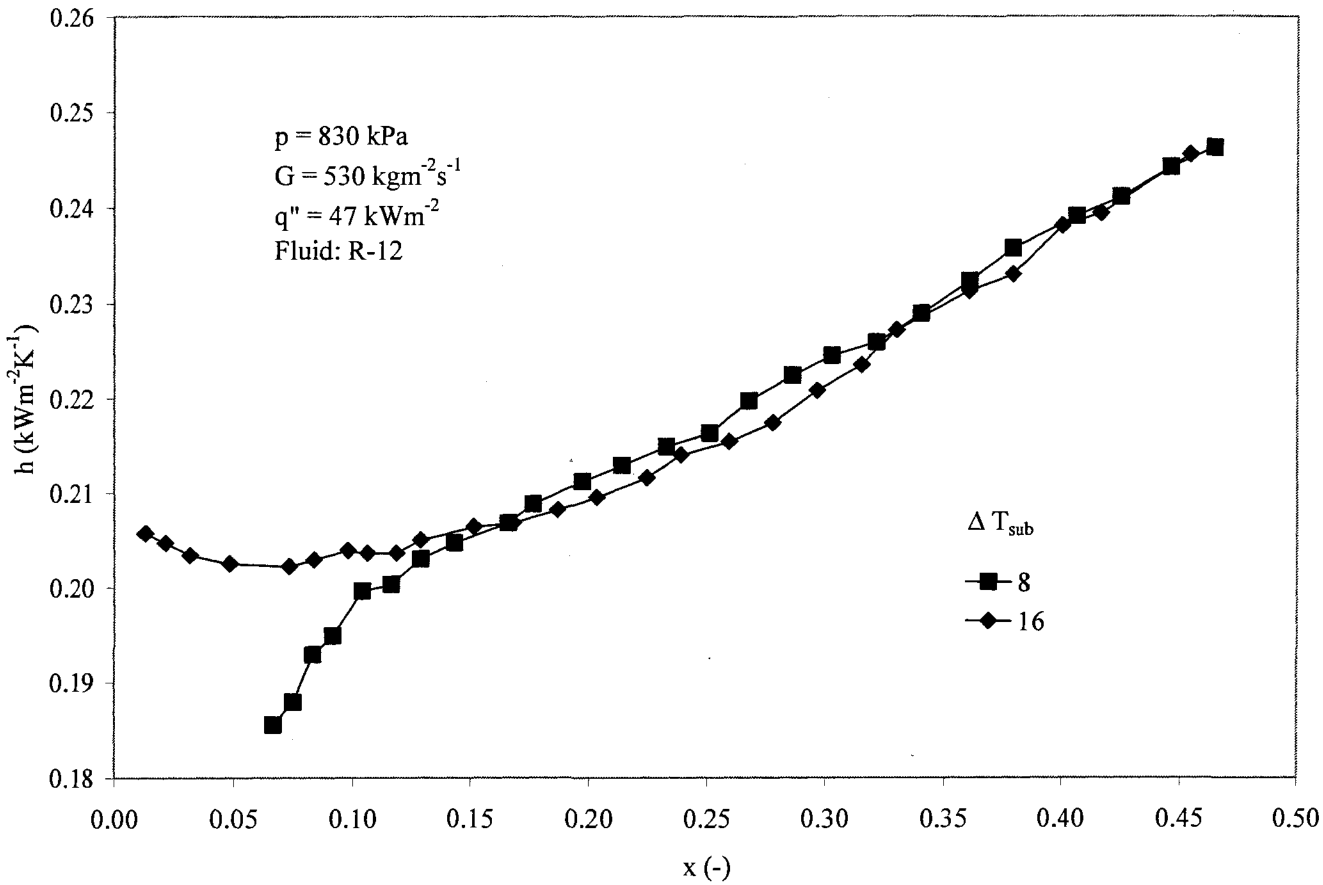

Figure 4. 5 Effect of inlet subcooling on heat transfer coefficient [reproduced from Hammouda et al. (1996)].

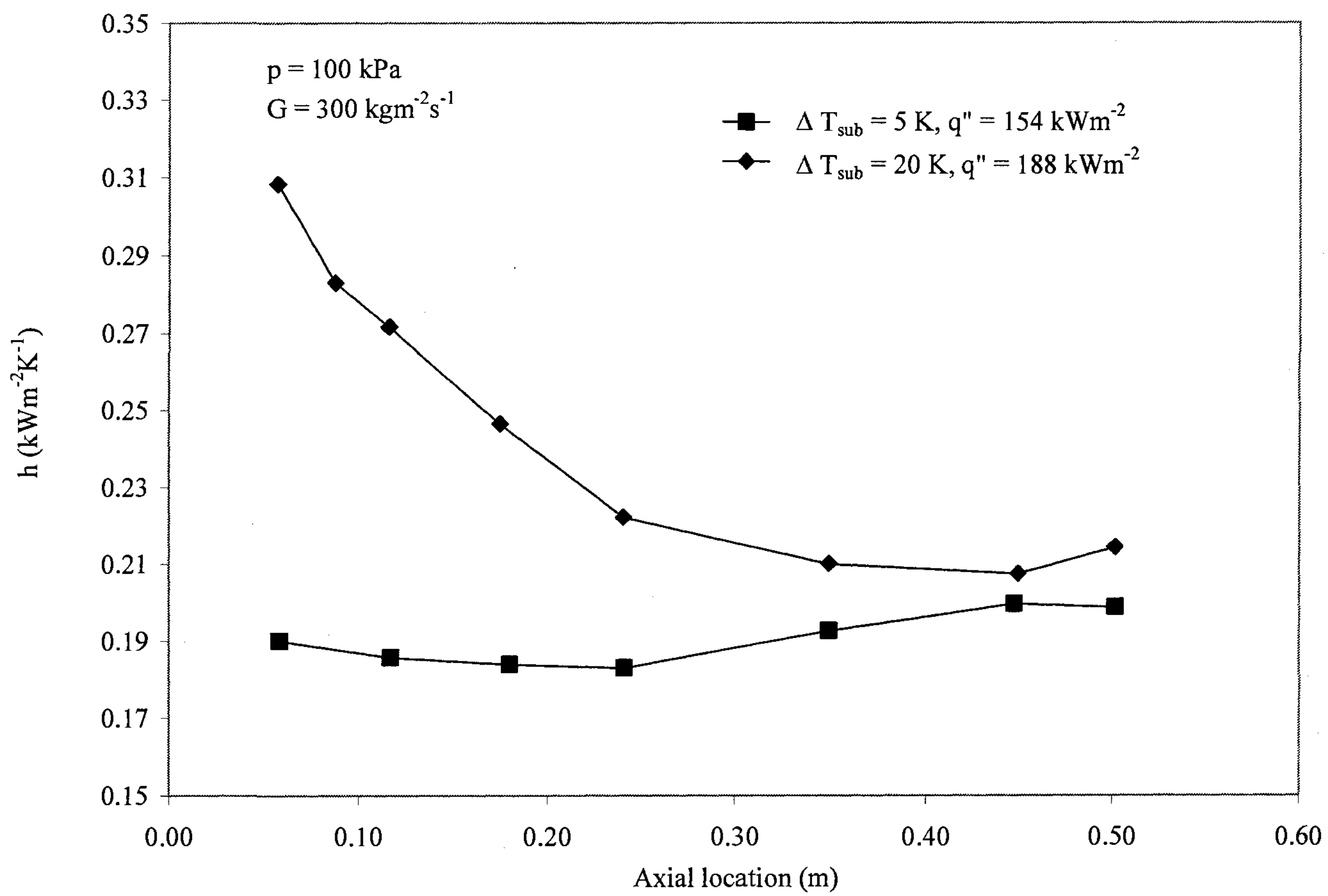

Figure 4. 6 Length effect on heat transfer coefficient [reproduced from Fung et al. (1979)].

transfer coefficient shows a continuous decrease along the axial direction downstream of the quench front. Chen (1987) observed that at very low inlet subcooling, the heat transfer coefficient distribution is rather uniform. At higher subcooling and mass flux, the heat transfer coefficient increases to a maximum, then decreases. At lower mass flux, it decreases along the heated length. Chen et al. (1989) also observed that at lower mass flux, the heat transfer coefficient decreases continuously along the heated length. As mass flux increases, the heat transfer coefficient levels off, then it increases at higher mass flux. The same observed length effect is applicable to the local quality effect on heat transfer coefficient.

Although the various observations show different trends of heat transfer coefficient vs. quality or length, these trends are usually mass flux dependent and are a result of opposing effects:

- the initial decrease in heat transfer coefficient with decreasing subcooling is due to heat transfer in the IAFB region being dominated by conduction at high subcoolings: with a decrease in subcooling the vapor thickness increases, hence the resistance increases as well
- at locations further downstream, the positive quality region is reached where convective heat transfer becomes important. For high mass velocities the vapor superheat is minimal, and an increase in quality will result in an increase in vapor velocity and hence an increase in heat transfer coefficient
- for low mass velocities, the convection also becomes more important with an increase in quality for $x > 0$. However, because the vapor superheat also increases, the net effect of a quality increase on heat transfer coefficient h [h is generally defined as $q''/(T_w - T_{sat})$] can be very small or even negative.

4.7. Heat Transfer Regions

Takenaka et al. (1989) performed steady-state IAFB experiments in a vertical tube using R-113. Three heat transfer regions were identified and attributed to the different flow patterns. They concluded that these regions can be determined by the mass flux and thermodynamic equilibrium quality, and that these regions are slightly affected by the heat flux and inlet subcooling. Ishii and Denton (1988) observed similar flow patterns in their experimental study but divided the film boiling length into four regions related to the smooth, rough wavy, agitated and dispersed flow regimes. Hammouda et al. (1996) classified their observations based on Ishii and Denton (1988) conclusions. Figure 4.7 shows the four heat transfer regions as interpreted by Hammouda et al. (1996). The heat transfer mechanisms involved in the heat transfer regions will be explained in Section 6.2.

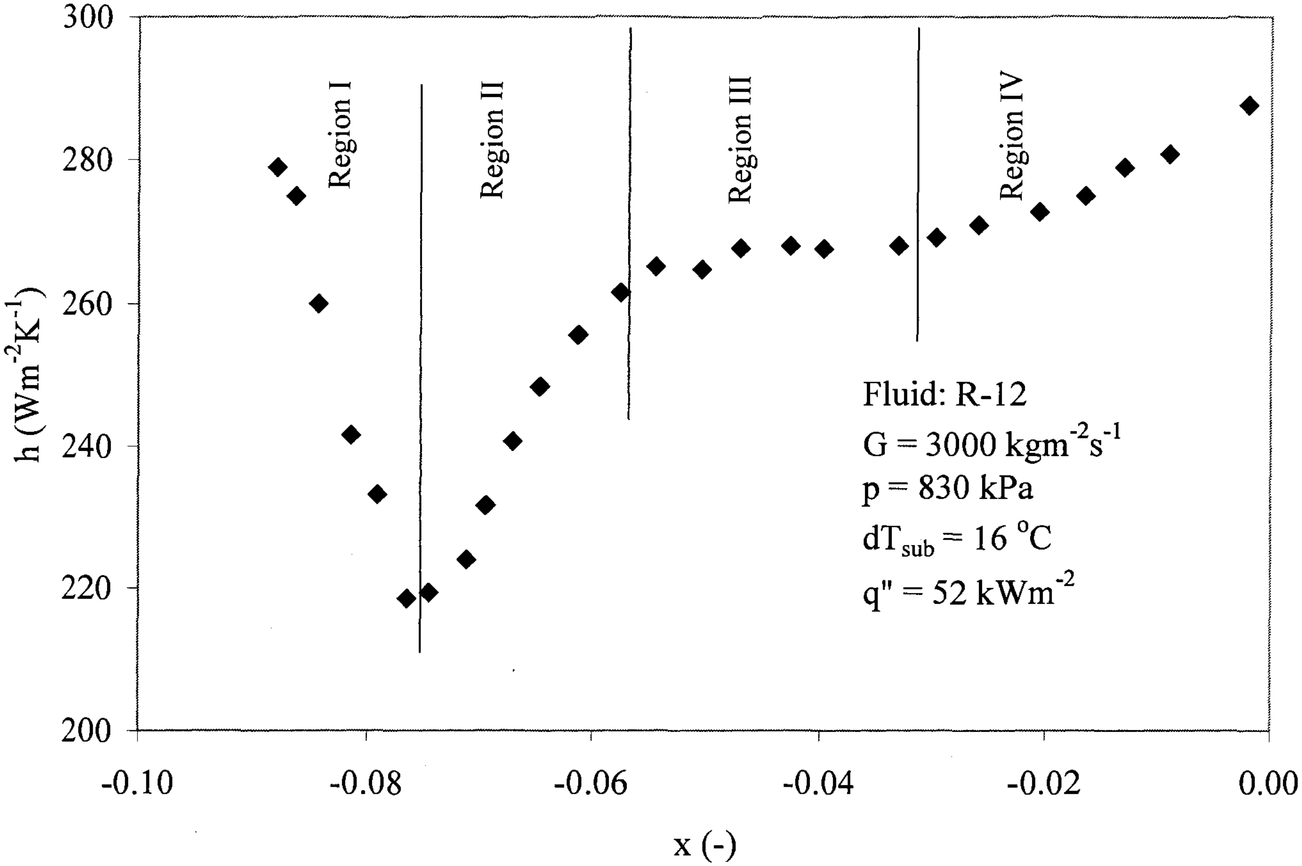

Figure 4. 7 Heat transfer regions in the IAFB as interpreted by Hammouda et al. (1996). [Reproduced from Hammouda et al. (1996)]

CHAPTER 5 DESCRIPTION OF FILM BOILING EXPERIMENTS

5.1. Experimental Loop Description

The experimental test facility is located in the Thermalhydraulics Laboratory of the University of Ottawa. It consists of a multi-fluid loop, shown in Figure 5.1, which is connected to a data acquisition system. Currently, all experiments are performed using HFC-134a as a working fluid.

The Freon is pumped around the loop by two gear pumps connected in series with bypass valve to control the flow rate. The Freon flow is measured by a Coriolis type flow meter with accuracy better than 0.5% (flow range 0-0.34 kgs^{-1}). An electric pre-heater (maximum power of 5 kW) and a coaxial heat exchanger (with hot water on the secondary side) are located between the pumps and the test section. They are used to adjust the test section inlet fluid temperature or inlet mass quality to the desired values. The coolant flows vertically upwards through the test section, that is directly heated by a 12 kW DC power supply (40V, 300 A). The fluid temperatures at the inlet and outlet of the test section are measured by RTDs. The pressure in the loop is controlled by a pressurizer. The pressurizer contains a heating coil, located at the bottom, and a cooling coil near the top. The power to the pressurizer heater (maximum 500 W) is regulated by an adjustable AC transformer. The vapor generated in the test section is condensed by a coaxial heat exchanger prior to the fluid being recirculated to the pump inlet.

A description of quality assurance and calibration procedures, and error estimates for temperature, pressure, mass flow rates, and power measurements are given in Appendix-B.

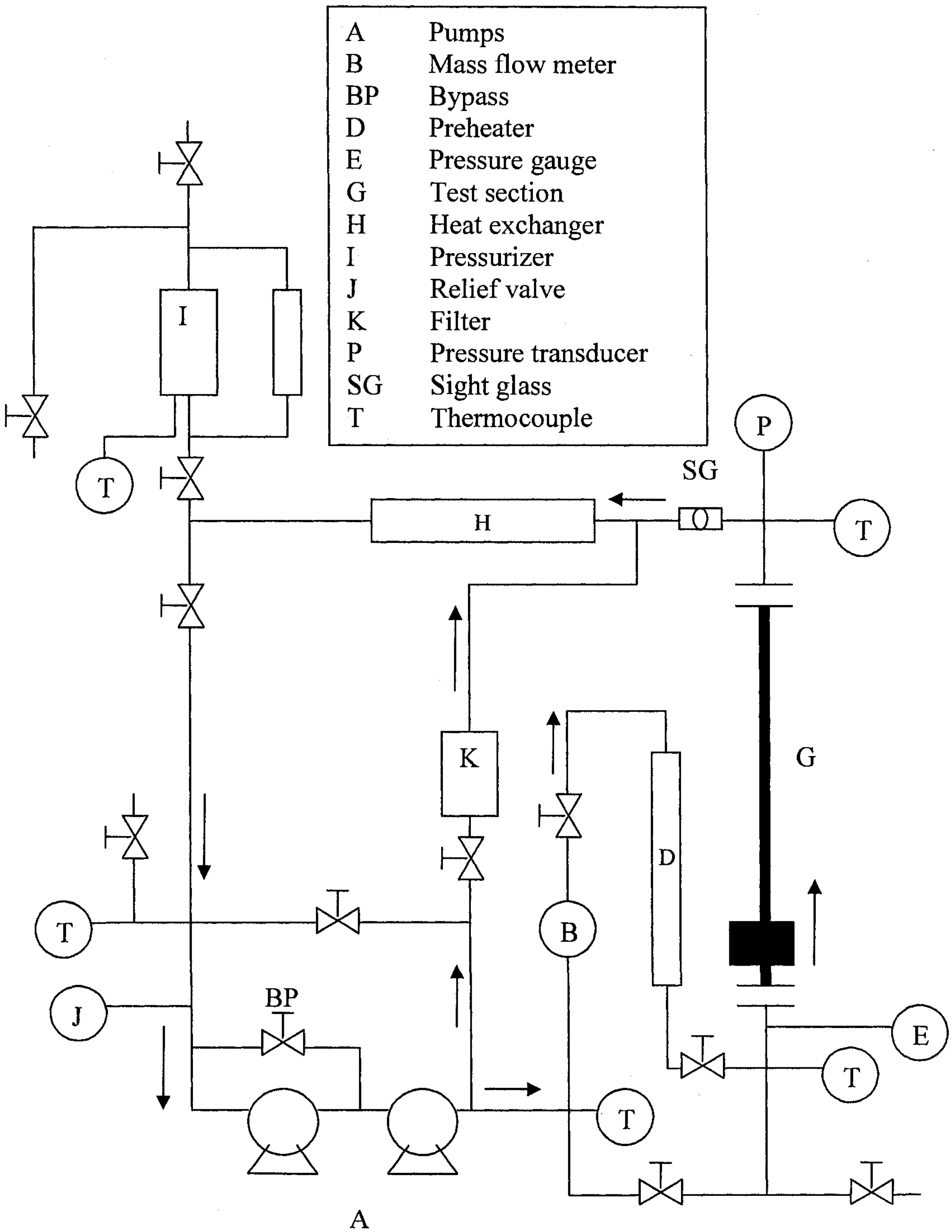

Figure 5. 1 Schematic diagram of the experimental facility.

5.2. Test Section Description

The test section is made of Inconel 600, and has an inside diameter of 5.46 mm and an outside diameter of 7.54 mm. The test section is installed in a vertical orientation and heated by a direct DC current supplied through copper power terminals clamped tightly to the tube. The heated length of the test section is 1.20 m. The outer wall temperatures of the test section are measured by attaching 24 K-type self-adhesive thermocouples (a pair of thermocouples at each plane in 12 locations). Figure 5.2 shows the test section schematic with the dimensions and the thermocouple locations. Inside wall temperature calculations are explained in Appendix-A.

The indirectly heated hot-patch technique, described in Section 3.2 is used to facilitate IAFB measurements at low powers. The hot-patch is silver-brazed to the Inconel tube and equipped with six 200W cartridge heaters heated by a separate DC power supply. The purpose of the hot-patch is to prevent the quench front from propagating downstream and to avoid refrigerant decomposition (due to excessive temperatures needed to maintain IAFB flow without the use of the hot-patch technique). Figure 5.3 shows a schematic of the hot-patch block.

5.3. Controls and Instrumentation

Controls are located at the front panel of the loop. They perform the following functions:

- Control temperatures (inlet and outlet of pump, inlet and outlet of test section, etc.).
- Control loop pressure.
- Control flow rate in the test loop.
- Control the flow rate in the heat exchangers.

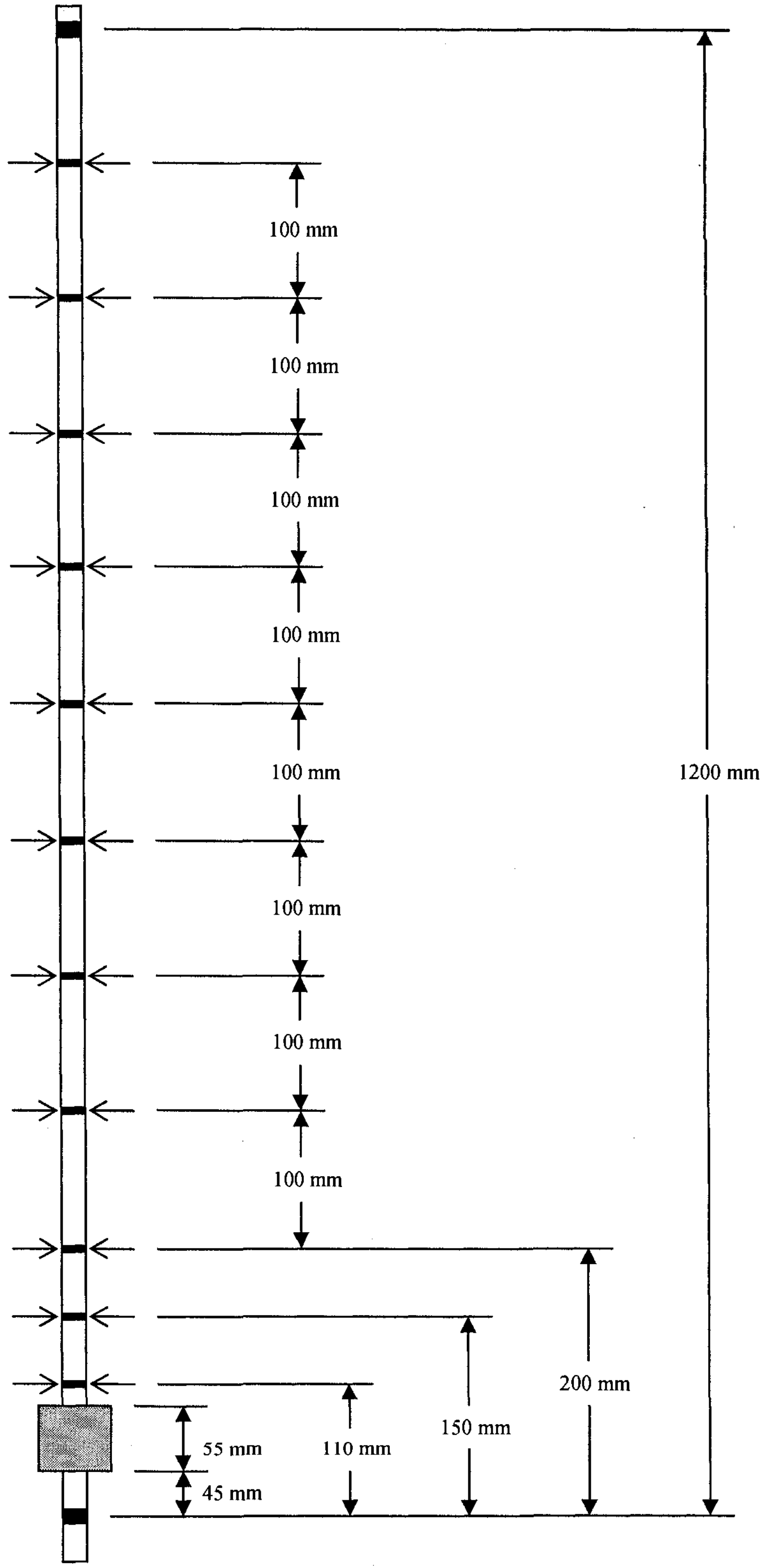

Figure 5. 2 Test section and thermocouple locations.

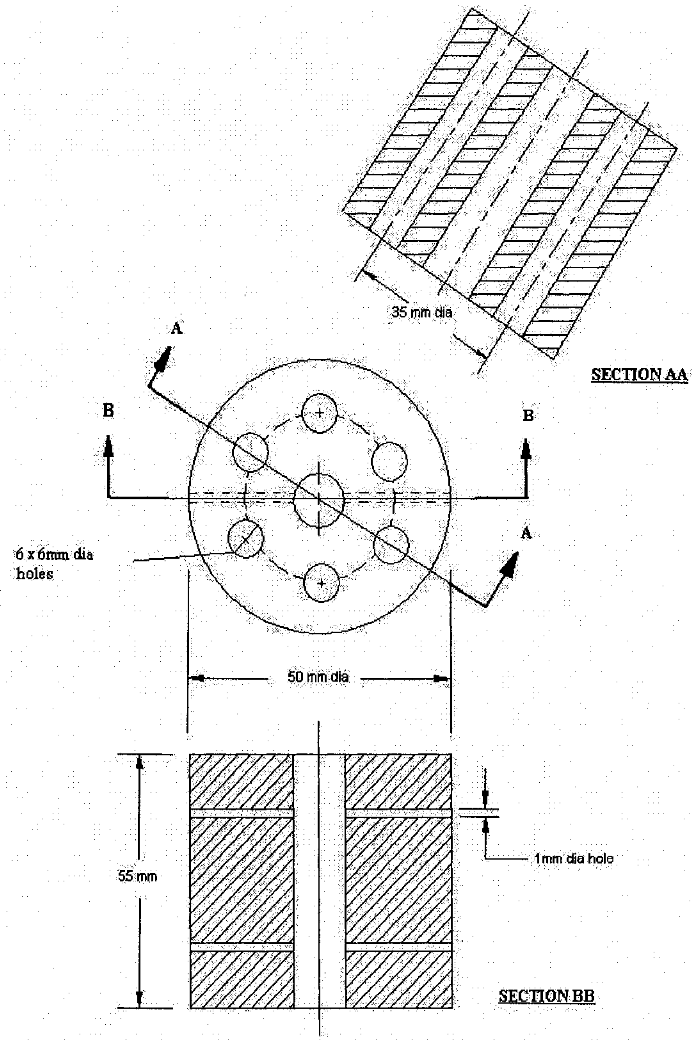

Figure 5. 3 Hot-patch dimensions.

The instrumentation used to perform the film boiling experiments provides the following measurements:

- Mass flowrate in the test section: Flow around the loop was provided by two 350 W gear pumps manufactured by the Micropump Corporation. Each pump is equipped with a flow bypass, to prevent flow instabilities. Flow control valves are manually operated from the front control panel of the loop and are used to vary the flow through the test section and the bypass. The mass flow rate is measured directly with a high- precision Coriolis-type mass flow meter, covering a range from 0 to 300 kgh^{-1}. The mass flow meter signal is converted to D.C. voltage and processed by the data acquisition system.

- Coolant temperature at the inlet and outlet of the test section: Inlet and outlet temperatures to the test section are measured with calibrated RTDs inserted in the flow stream. Fluid inlet and outlet temperatures of the heat exchanger are measured with chromel-alumel thermocouples to monitor loop operation.

- Pressure at the inlet and outlet of the test section: The absolute pressure at the exit of the tube is measured by a pressure transducer. The pressure drop across the test section is measured using differential pressure transducer located at inlet. The pressure at the inlet of the tube is obtained by adding the pressure drop to the outlet pressure. The pressure at the inlet is also monitored with a pressure gage.

- Power to the test section and the hot-patch: The D.C. power applied to the test section is measured by monitoring the voltage across the test section and the hot patch, and the current across a calibrated shunt in series with the tube. Both readings are connected to the data acquisition system for recording and on-line display on the monitor. The hot-patch power reading is directly read from the power supply dial and inserted manually into the data file prior to processing.

- Test section outside wall temperatures: Measurements of wall temperatures of the test section are made with self-adhesive chromel-alumel thermocouples. All thermocouples are connected directly to the data acquisition system for monitoring and recording.

All sensor outputs are displayed on a computer (CRT) monitor. The data acquisition system is composed of an IBM PC compatible as the host computer for data processing, a PCI interface card (PCI-MIO-16E-1), 30 channels (SCXI-1303), 8 channels (SCXI-1327), and 4 channels (SCXI-1320) terminal blocks, and a table-top chassis (SCXI-1000) to encase the terminal blocks. The interface card, terminal blocks and chassis are manufactured by National Instruments Inc. LabVIEW (version 6.0) is the software used for controlling the data acquisition process.

5.4. Experimental Procedure

To establish steady film boiling conditions in the test section, the following procedure is followed:

- Establish the flow conditions at the test section inlet.
- Increase the hot-patch power to achieve the desired film boiling temperature. This can be detected when the dry-patch reaches the first thermocouple location located 10 mm downstream from the hot-patch.
- The test section power is then increased gradually until the dry-patch starts to propagate in the test section downstream from the hot patch. The test section power is then kept steady.
- When film boiling conditions are established along the complete length of the test section, the test section power is adjusted to a safe level in order to prevent Freon decomposition.
- Sufficient time is allowed for test conditions to stabilize. Then a scan of the readings is taken and stored for off-line processing.

- The test section power is then reduced in steps. At each power level, the flow conditions will be allowed to stabilize, and a data scan is taken and stored until the test section rewets. .

5.5. Test Matrix

A survey of subcooled experimental data (for water and Freon) was performed to determine the range of flow conditions for which experimental data are not available. This was used to establish the range of flow conditions for the experimental work. The test matrix of the experimental program is based on the experimental loop limitations, flow condition limitations, the gaps in the available experimental data and the need of a continuous range of data. Table 5.1 shows the test matrix. The water-equivalent pressure is also shown and is calculated based on equal density ratio for both Freon R-134a and water (see Appendix C for details).

5.6. Test Section Heat Loss and Heat Balance

5.6.1. Heat loss test

Heat loss tests were performed by applying the power to the test section without insulation after removing the Freon from the test section. After all readings of the thermocouples installed on the test section showed that the surface temperatures had stabilized, the power supplied to the test section was recorded. In this case, the power supplied to the test section was assumed to equal the heat loss from the outside tube surface to the surroundings. The heat loss was measured at various wall temperature levels up to a maximum of 200°C which approximately correspond to the maximum average outer surface temperature during the IAFB tests. The results of the heat loss test are shown in Figure 5.4. The maximum heat loss corresponding to the temperature level of 200°C is 0.044 kW, which is less than 4% of the total power supplied to the test section during the experiment. No correction for heat loss was applied to the results.

Table 5. 1 Test matrix of the experimental work

Pressure, p (kPa)	Water equivalent pressure*, p_{equiv} (kPa)	Mass flux, G (kg m^{-2} s^{-1})	Range of inlet quality, x_{in} (-)
635	4000	500 to 4000	-0.13 to -0.03
793	5000	500 to 4000	-0.20 to -0.03
961	6000	500 to 4000	-0.29 to -0.03
1307	8000	500 to 4000	-0.38 to -0.03
1667	10000	500 to 4000	-0.38 to -0.03
2032	12000	500 to 4000	-0.47 to -0.03
2390	14000	500 to 4000	-0.75 to -0.03

*Equivalent pressure is based on equal density ratio of both water and R-134a.

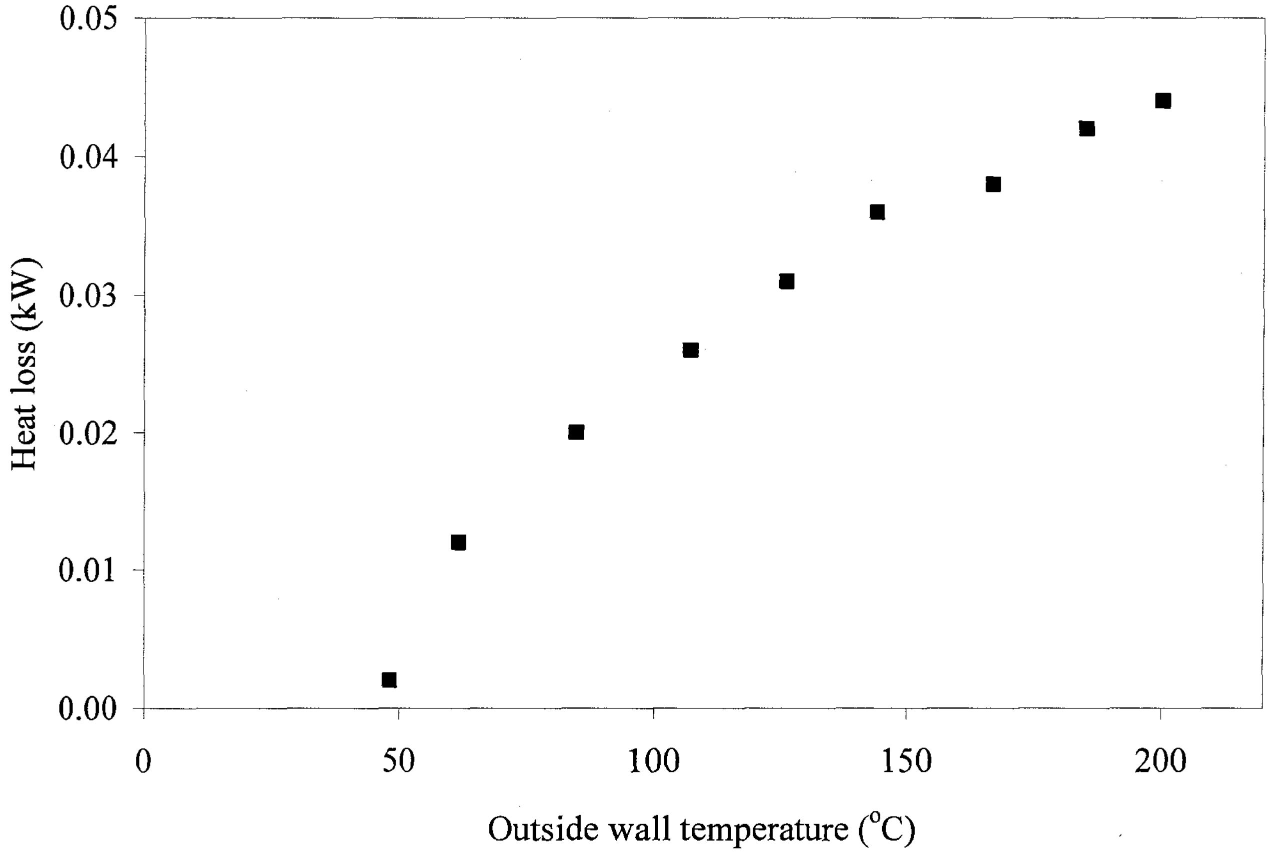

Figure 5. 4 Heat loss test results.

5.6.2. Heat balance test

Heat balance tests were performed before the start of experiment to check whether all instrumentation systems were working correctly. Heat balance tests were conducted by supplying the power to the test section while a single-phase liquid flowed through the test section at a pressure of 2300 kPa, and mass flux of 4500 $kgm^{-2}s^{-1}$. The power supplied to the test section was compared with the enthalpy rise of the fluid. The heat balance results are shown in Figure 5.5. The difference between the power supplied to the test section and the enthalpy rise of the working fluid is less than 1%.

5.7. Data Reduction

The outer wall temperatures are measured during the experiment. No thermal insulation was applied to the test section due to the low heat losses (see Section 5.6.1 for further details). The inner wall temperatures were calculated after correcting for the temperature drop across the heated wall. Appendix-A gives a detailed derivation of the equation used to account for the temperature drop across the wall. Heat transfer coefficients are evaluated based on the difference between the inside wall temperature and the saturation temperature corresponding to pressure at the outlet of the test section. The effect of pressure drop on saturation temperature was relatively small and was therefore ignored.

$$h = \frac{q''}{T_w - T_{sat}} \tag{5.1}$$

A study of the parametric trends of the heat transfer coefficient with respect to the flow parameters (pressure, mass flux, inlet quality and heat flux) is made based on the calculated values of inside wall temperature and the heat transfer coefficient. The thermodynamic properties of R-134a are obtained by using the International Standard Formulation for HFC-134a [Tillner-Roth and Baehr (1994)]; and transport properties are according to Krauss et al. (1993).

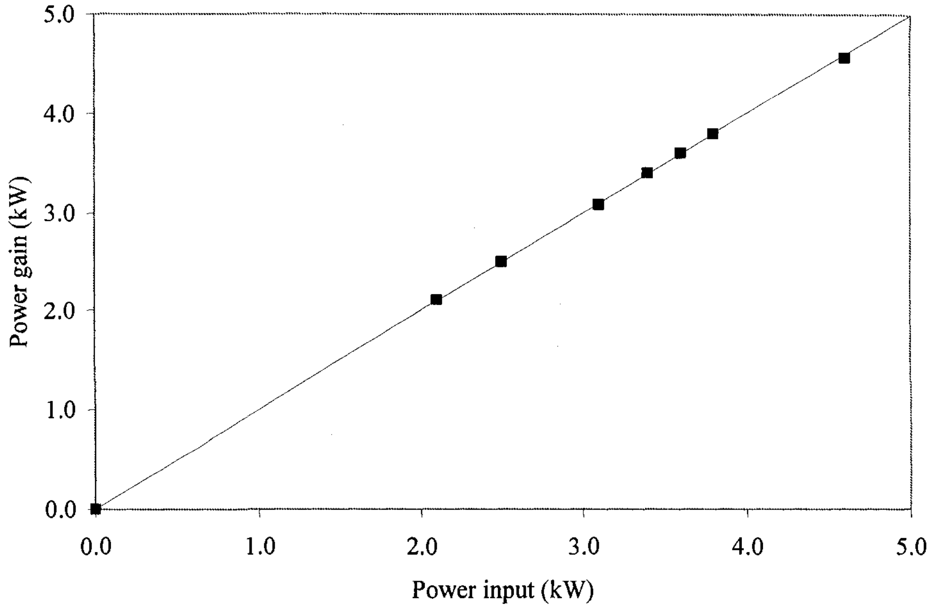

(a)

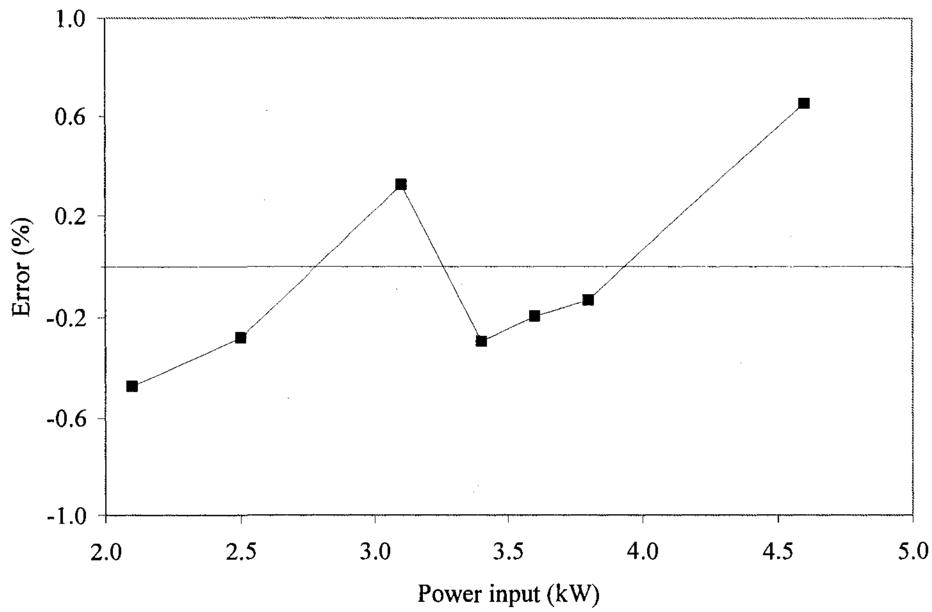

(b)

Figure 5. 5 Heat balance test results. (a) Heat balance, (b) error in data. (Power input denotes the electric power, Power gain denotes the power calculated from the enthalpy rise)

5.8. Data Reproducibility

Hammouda (1996) discussed the problems due to Freon decomposition at elevated wall temperatures. This decomposition could result in changing the thermophysical properties of Freon and make the experimental data non-producible. It would also affect the inside surface of the heated tube and would require extensive cleaning. During the current experimental work, the wall and hot-patch temperatures were kept below 220 ^{o}C to avoid this phenomenon. Also at each pressure level, the test section was removed and the inside wall surface of the tube was cleaned using a smooth brush and flushed with alcohol.

To assure the reproducibility of the data, several runs were repeated at different periods of time. The flow conditions for these runs were kept the same. Figure 5.6 shows the measured outside wall temperature vs. axial location. It is clear in the figure that the outside wall temperature is reproducible and hence the heat transfer coefficient.

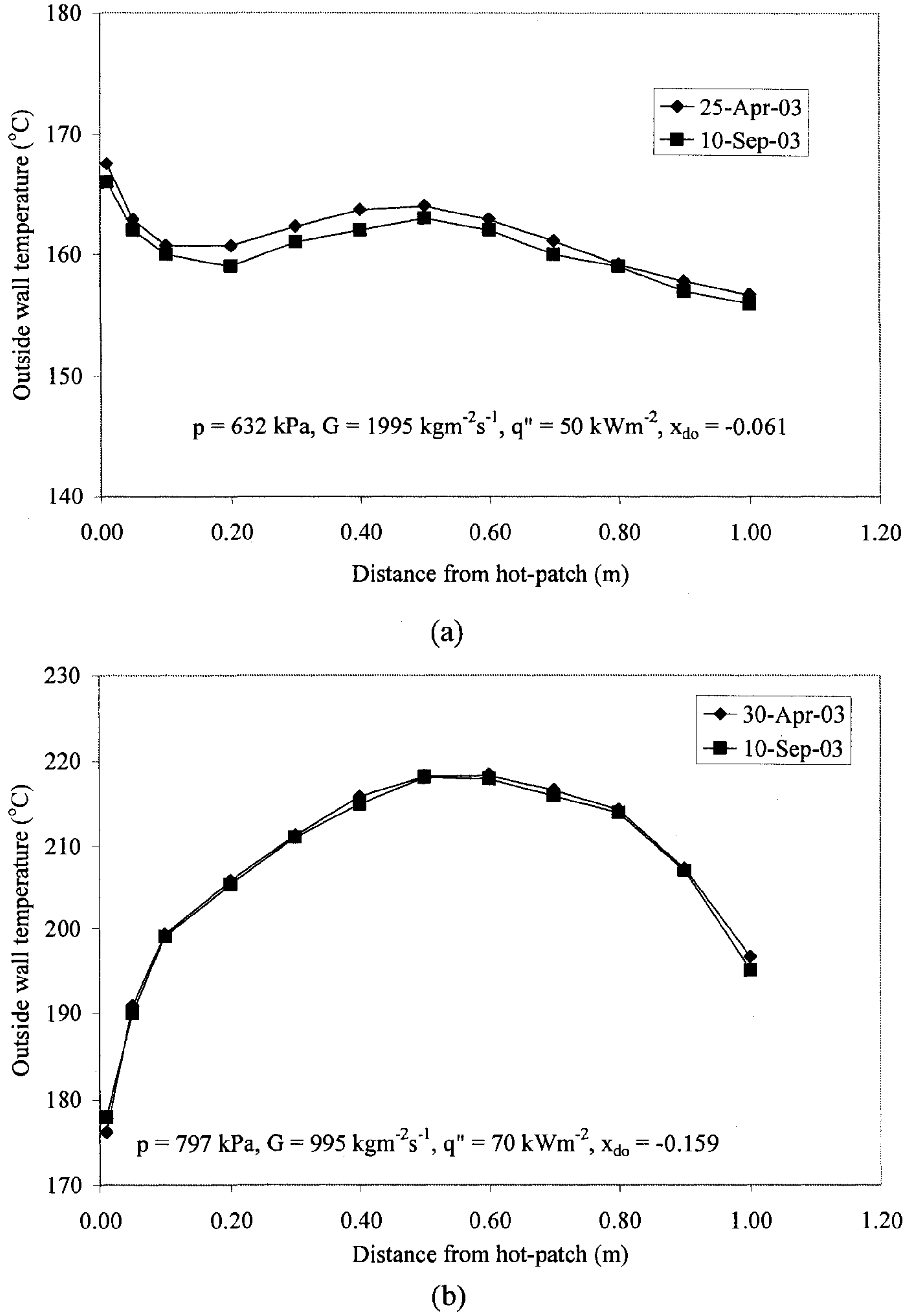

Figure 5. 6 Reproducibility tests of outside wall temperature vs. axial location.

CHAPTER 6 EXPERIMENTAL RESULTS AND DISCUSSION

6.1. CHF Location

The exact location of the starting point (CHF) of film boiling along the hot-patch was not measured during the experiment. However, the correct determination of CHF location is important in determining initial conditions for numerical solution of history-dependent analytical models. Fung (1981) and Hammouda (1996) assumed that CHF occurred at the inlet to the hot-patch, and the corresponding quality was calculated based on that assumption. However a different approach is followed in the current analysis and is explained below.

The hot-patch block has two 1-mm holes at each side drilled to reach the tube wall (see Figure 5.3 for details). Sheathed thermocouples were inserted in the holes all the way to reach the wall of the test section. This method was described by Hammouda (1996) to determine the occurrence of CHF at the inlet of the hot-patch. Using this method does not demonstrate that CHF occurs at the inlet to the hot-patch block, due to the following observations:

1. First, the thermocouple readings are strongly affected by conduction from the hot-patch block. This was observed when gradually increasing the power supplied to the hot-patch block. The increase in power was accompanied by a simultaneous increase in thermocouple temperature readings regardless of their location along the hot-patch block.
2. Also when switching off the power supplied to the hot-patch, the inserted thermocouple readings stayed above saturation (> 20 ^{o}C) with the test section experiencing re-wetting.

3. The final observation is that when having complete dryout in the test section and the power to the hot-patch is gradually reduced, the temperature distribution along the test section stays the same. This happens even when experiencing partial re-wetting just downstream of the hot-patch block.

In this analysis it is assumed that the CHF occurs at the downstream end of the hot-patch (as in CHF experiments where CHF is measured at the exit of the test section). To check this assumption, the average hot-patch heat flux has been compared to the corresponding CHF value using CHF look-up table of Groeneveld et al. (1995). The comparison is performed by applying fluid-to-fluid modeling techniques. The following example is used to demonstrate the correctness of assuming that CHF occurs at the exit of the hot patch.

Example:

R-134a flow conditions: pressure = 1667 kPa, mass flux = 1000 $kgm^{-2}s^{-1}$, hot-patch power = 0.36 kW (correspond to an average heat flux of 381 kWm^{-2}), quality at exit of hot-patch = -0.095.

Using fluid-to-fluid modeling, the approximate water equivalent values are: pressure = 10000 kPa, mass flux = 1400 $kgm^{-2}s^{-1}$.

For CHF quality of -0.095, the CHF look-up table gives the CHF value of around 4580 kWm^{-2} (for a diameter of 0.008 m). After correcting for the diameter effect and using fluid-to-fluid modeling backward, the corresponding CHF value for R-134a is around 403 kWm^{-2}. This value is close to the average hot-patch heat flux which validates the assumption of having the CHF location closer to the exit of the hot-patch.

6.2. Heat Transfer Regions

Four separate heat transfer coefficient regions are previously described in Section 4.7 at moderate to high mass flux (see also Figure 6.1). As Figure 6.1 shows, region I represents a sharp drop in heat transfer coefficient. In this region conduction is the dominant heat transfer mode: as the liquid core temperature increases, the condensation rate decreases resulting in an increase in vapor film thickness which in turn results in a drop in heat transfer coefficient. As the liquid core temperature increases, the heat transfer rate to the liquid core decreases and the excess heat increases the evaporation rate. This results in an increase in vapor velocity and convection starts to dominate in region II. In region III, the heat transfer coefficient levels, with small increase or decrease with respect to increasing quality. Region IV is again characterized by an increasing heat transfer coefficient as quality increases, presumably due to the start of DFFB regime. In this regime, evaporation rates increase with quality resulting in increased heat transfer coefficient. It is observed that the regions I and II usually appear in the subcooled IAFB region ($x < 0$) and regions III and IV extend from the negative to the positive quality regions. The effect of the flow parameters on these four regions will be discussed in more detail in the following section.

6.3. Effect of Axial Location

The axial location has a strong effect on heat transfer coefficient (see Figure 6.2). Generally, the heat transfer coefficient decreases, then it either levels off or increases, depending on flow conditions. Fung et al. (1979) attributed the axial location effect to: (i) entrance effect, (ii) change in vapor film thickness, and (iii) increase in vapor superheat. The effect of various flow parameters (pressure, mass flux, heat flux and CHF quality) on heat transfer coefficient with respect to axial location is also shown in Figure 6.2. It seems that the only effect of flow parameters is to change the magnitude of heat transfer coefficient while keeping the general shape of the curve.

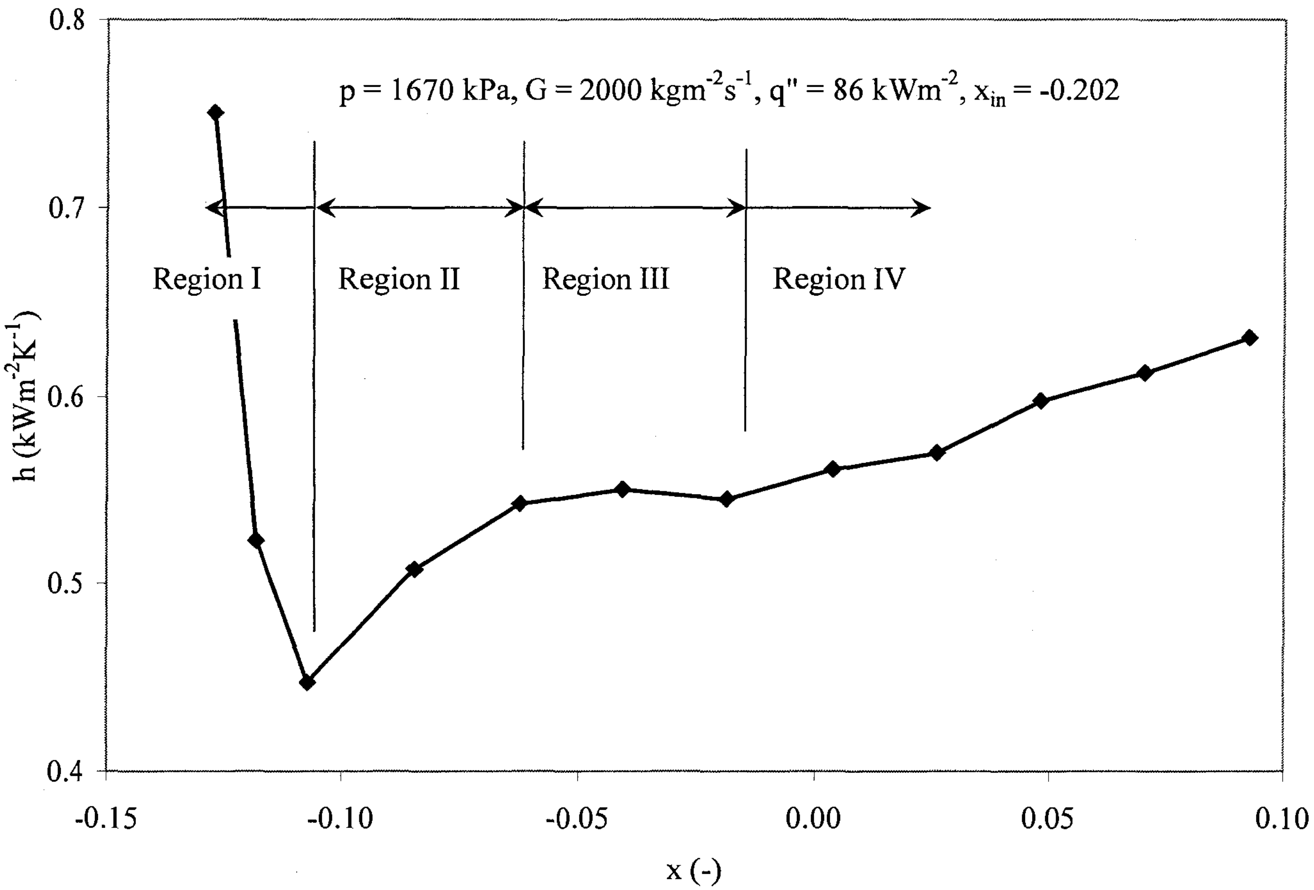

Figure 6. 1 Heat transfer regions during IAFB.

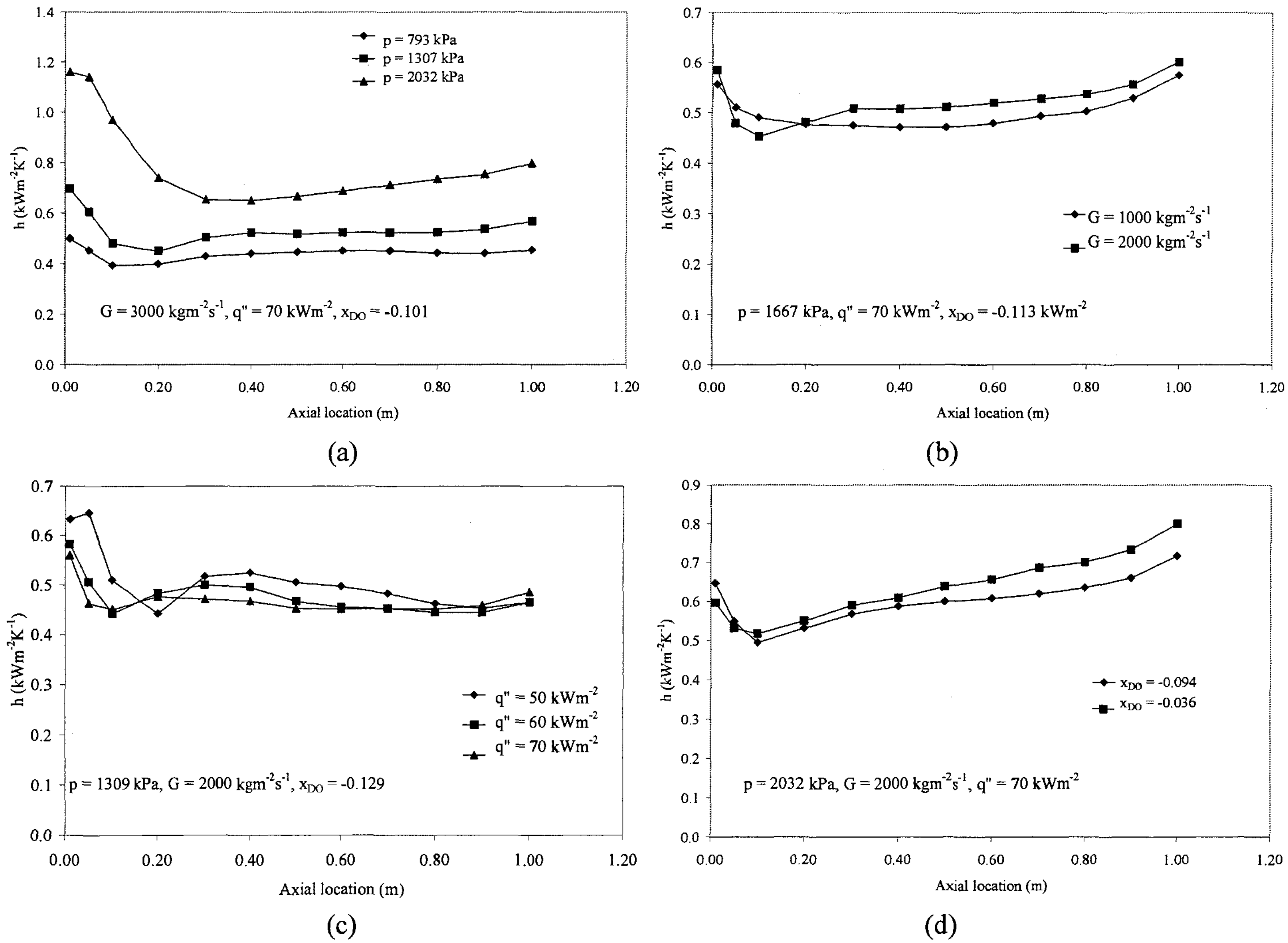

Figure 6. 2 Effect of axial location on heat transfer coefficient.

6.4. Effect of Pressure

Figure 6.3 shows that the heat transfer coefficient increases with increasing pressure for low, moderate and high mass fluxes. Hammouda (1996) reported that at low mass flux the effect was less pronounced. The figure shows a clear effect of pressure on the heat transfer coefficient even at a low mass flux (G = 1000 $kgm^{-2}s^{-1}$). The increase in heat transfer coefficient with pressure is primarily due to the increase in thermal conductivity of the vapor (Figure 6.4).

The relation between pressure and heat transfer regions (Section 6.2) can also be identified in Figure 6.3. It is observed that at lower pressures and low to moderate mass fluxes (Figure 6.3 a, b) heat transfer region II does not appear. At high pressures, region II appears regardless of the value of mass flux. Another observation from the figure is that at low pressures, the heat transfer coefficient following region I is almost constant (probably due to the presence of the saturated inverted annular flow regime). The observed effect of pressure on heat transfer coefficient is consistent with observations by previous investigators [e.g. Hammouda et al. (1996) and Stewart (1981)].

6.5. Effect of Mass flux

A strong effect of mass flux on the heat transfer coefficient was reported in the literature by most investigators (see Section 4.3). Figure 6.5 shows that the observed mass flux effect agrees with the reported mass flux effect on heat transfer coefficient: an increasing mass flux always increases the heat transfer coefficient. At low mass velocities only regions III and IV appear present, but the number of regions increases as the mass flux increases. At moderate pressure, the four regions become distinctive at moderate mass flux (Figure 6.4b).

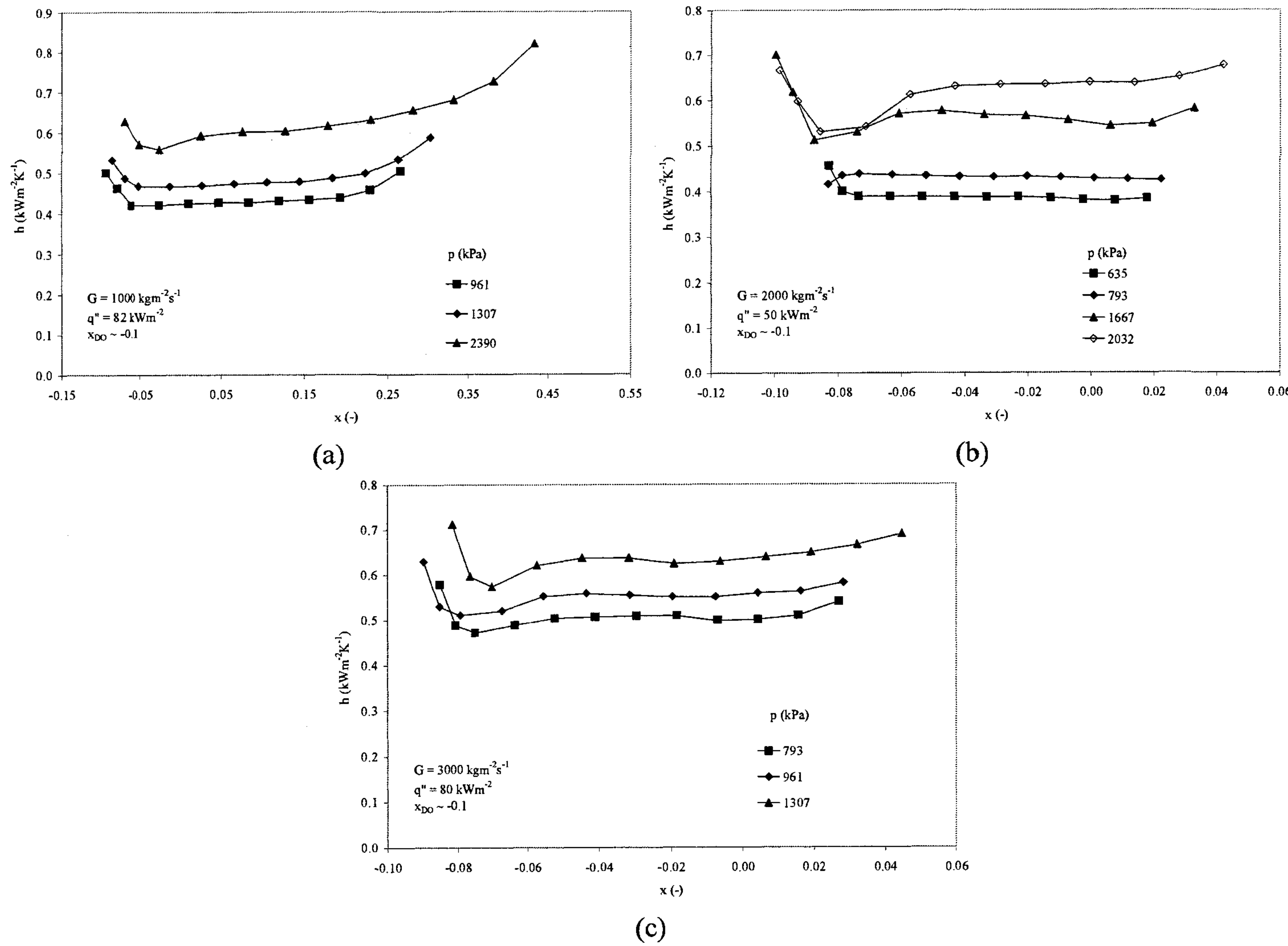

Figure 6. 3 Effect of pressure on heat transfer coefficient at (a) low, (b) moderate, and (c) high mass fluxes.

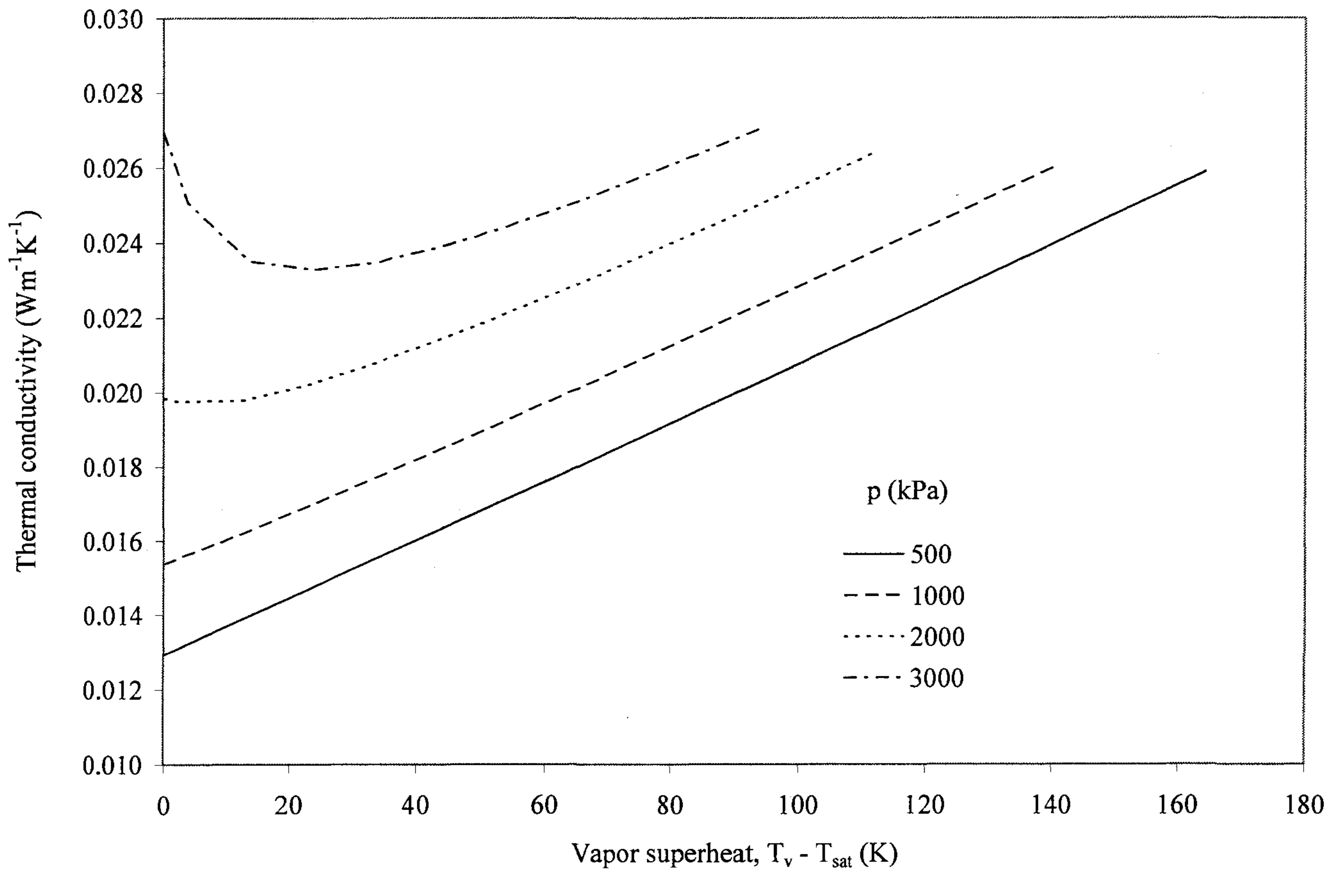

Figure 6. 4 Variation of vapor thermal conductivity of R-134a with pressure.

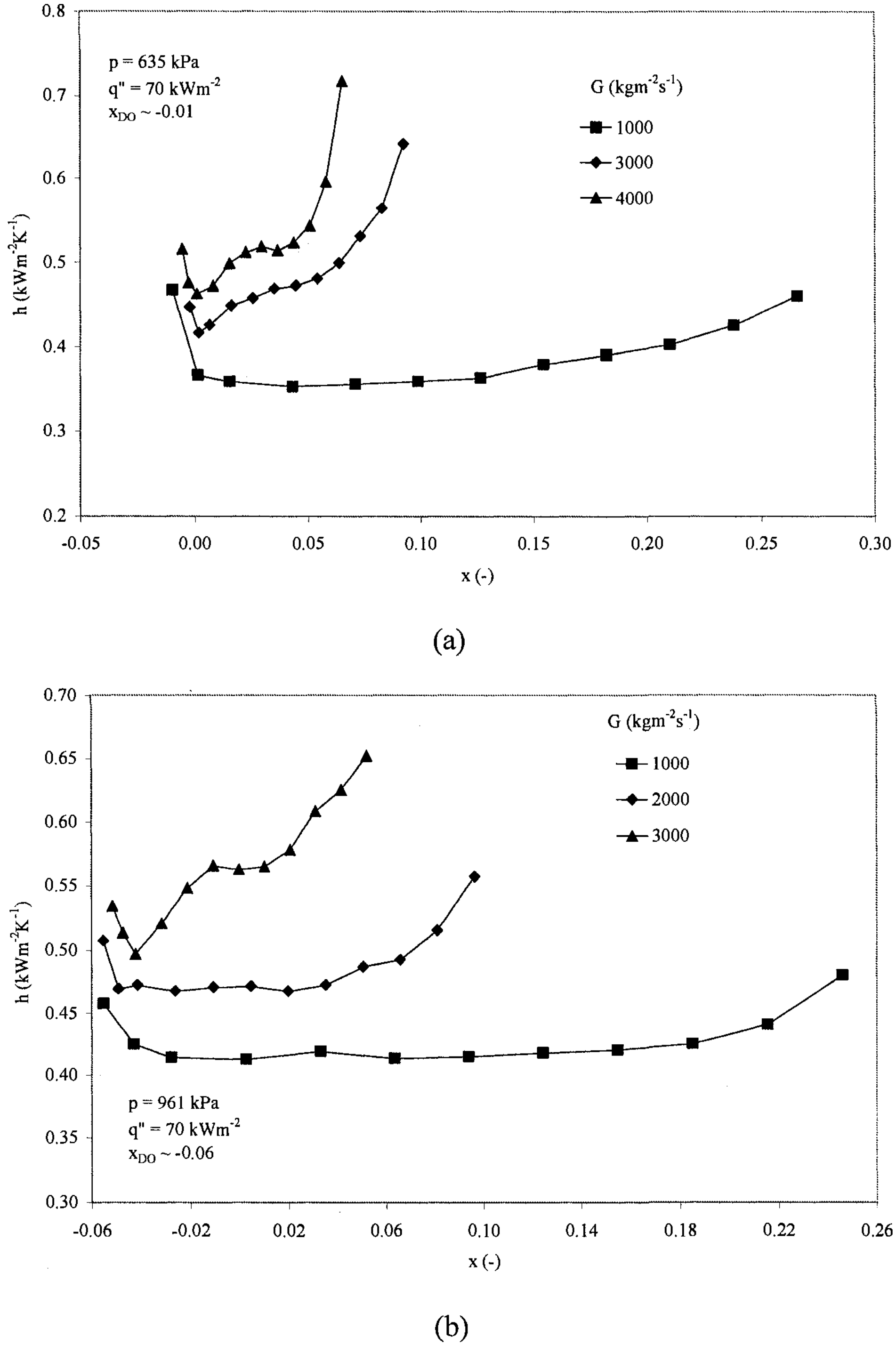

Figure 6. 5 Effect of mass flux on heat transfer coefficient at (a) low, and (b) moderate pressures.

As the mass flux is reduced from 3000 $kgm^{-2}s^{-1}$ to 2000 $kgm^{-2}s^{-1}$, region II starts to become less pronounced and, with further decrease to 1000 $kgm^{-2}s^{-1}$, this region disappears. This might be attributed to the quality range of the subcooled IAFB region. At high mass fluxes, the transition from subcooled (regions I and II which are characterized with thin vapor film) to saturated inverted annular film (region III which is characterized with higher qualities and higher vapor generation) occurs further downstream in the test section than for low mass fluxes.

6.6. Effect of Heat flux

In general, varying the heat flux has a weak effect on heat transfer coefficient. This effect is demonstrated in Figure 6.6 for different flow conditions. In most cases, heat transfer coefficient marginally increases with increasing heat flux. An explanation of this effect is given in Section 4.4.

At all pressures, the shape of the heat transfer coefficient vs. quality curves stays the same for all regions (regions I-IV). Also it is noticed that the transition quality between regions I and II always occurred at the same quality regardless of the variation in heat flux. This is the same observation made by Hammouda (1995).

A final remark on the effect of heat flux on the heat transfer coefficient is that region II is not always evident at low pressures (e.g. Figure 6.5a). This might be attributed to the higher qualities at this pressure.

6.7. Effect of Inlet Subcooling

Figure 6.7 shows the effect of inlet quality/subcooling on the heat transfer coefficient at different flow conditions. It is clear that as the quality increases, the heat transfer coefficient curves for different inlet qualities (keeping other flow conditions the same) converge to a single curve.

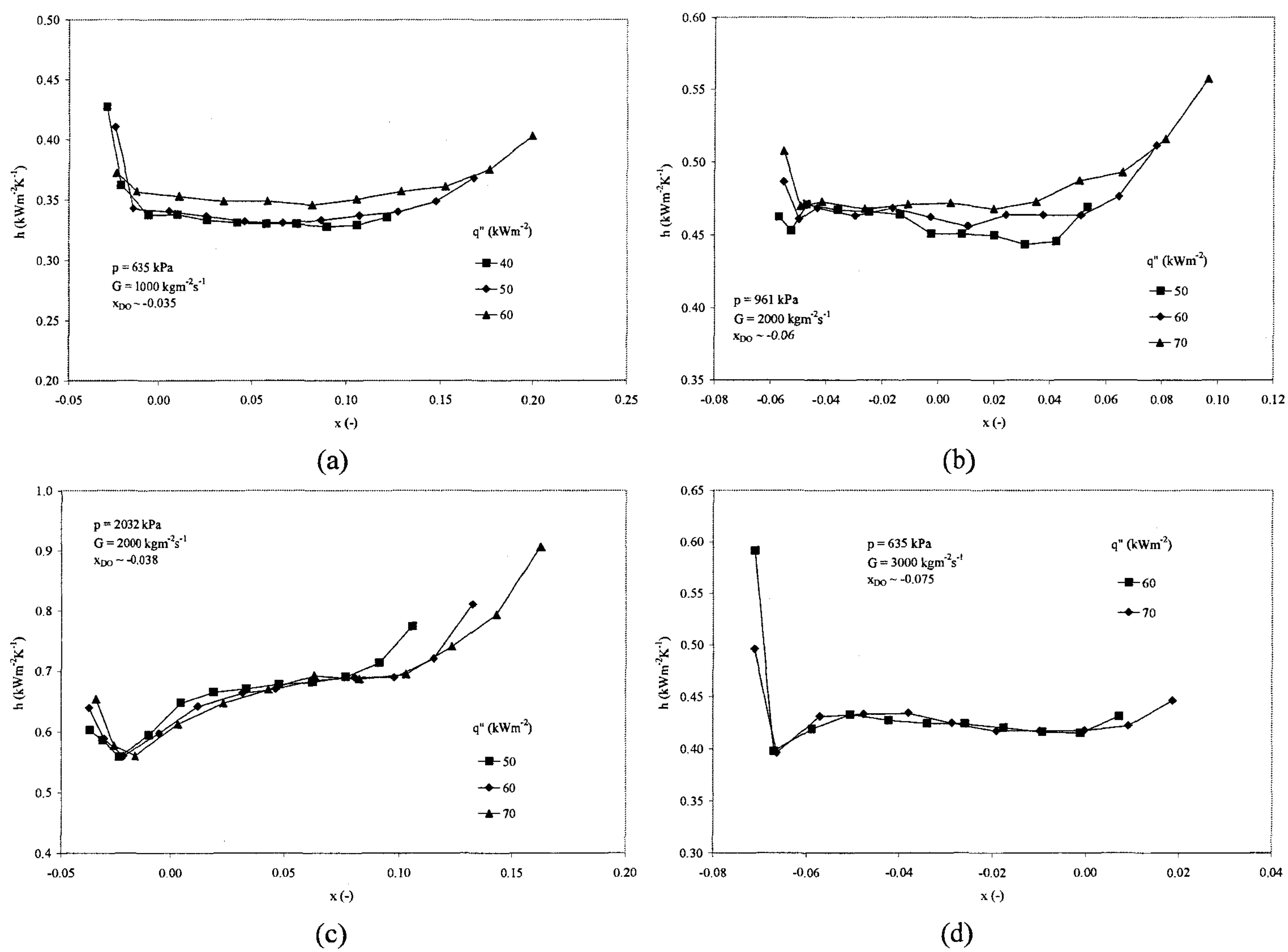

Figure 6. 6 Effect of heat flux on heat transfer coefficient.

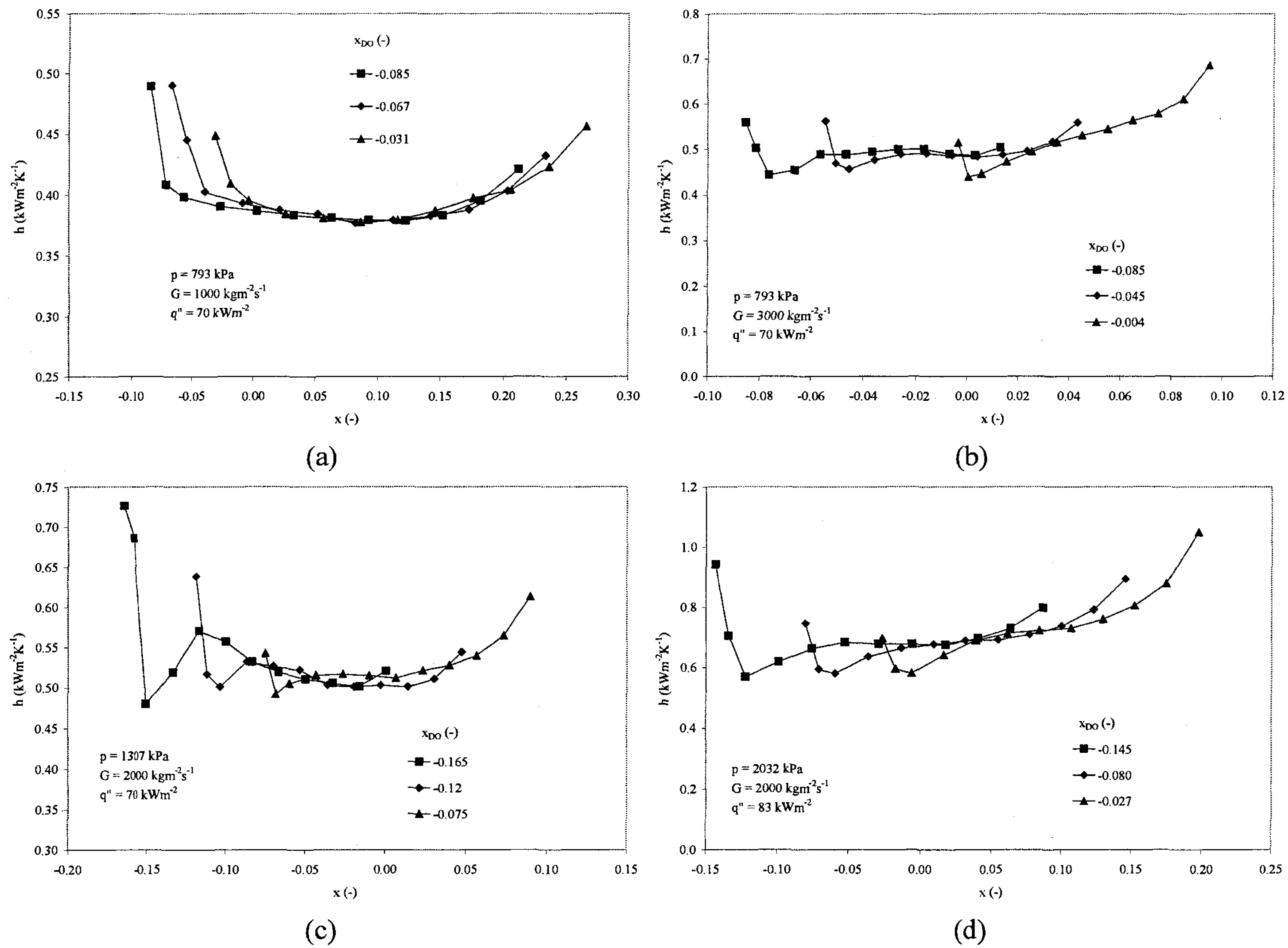

Figure 6. 7 Effect of inlet subcooling on heat transfer coefficient.

An increase in inlet subcooling shifts the transition between region I and II to lower qualities as shown in Figure 6.7 b-d. At moderate and high pressures and high inlet subcoolings, region IV is hardly present since the whole heat transfer coefficient curve is in the subcooled region ($x < 0$, see Section 6.2 for explanation). As the inlet subcooling decreases this region starts to develop at the expense of regions II and III and becomes the dominant region as the inlet temperature approaches saturation. As explained earlier this is due to the increase in vapor generation and the change in the flow regime from subcooled inverted annular flow to saturated inverted annular flow or even to dispersed flow regime. Also at higher inlet subcoolings the drop in heat transfer coefficient in region I is slightly larger and the minimum heat transfer coefficient becomes smaller. This explains the large wall temperature gradient directly after critical heat flux point in highly subcooled flow.

Figure 6.8 represents the same data of Figure 6.7 plotted versus axial location. The figure shows that the minima in heat transfer coefficient curves coincide along the test section regardless of inlet subcooling and flow conditions. This suggests that the main contributor to this reduction in heat transfer coefficient is the entrance effect since after L/D = 20-30 the minimum appears to have been reached.

6.8. Effect of Hot-Patch

Several runs were performed to check the hot-patch effect on the wall temperature. These runs were carried out by switching off the power supplied to the hot-patch and waiting for the hot-patch temperature to drop. The temperature drop resulted in gradual re-wetting of the test section. Figures 6.9 - 6.12 show the variation of wall temperature (and heat transfer coefficient) as the quench front moves downstream from the hot patch towards the outlet of the test section for different flow conditions. The figures show that after quenching of the hot-patch, the wall temperature changes slightly. The effect of quench front propagation on heat transfer coefficient is shown in parts (b) and (d) in the figures. The region next to the quench front (developing heat transfer region) is the

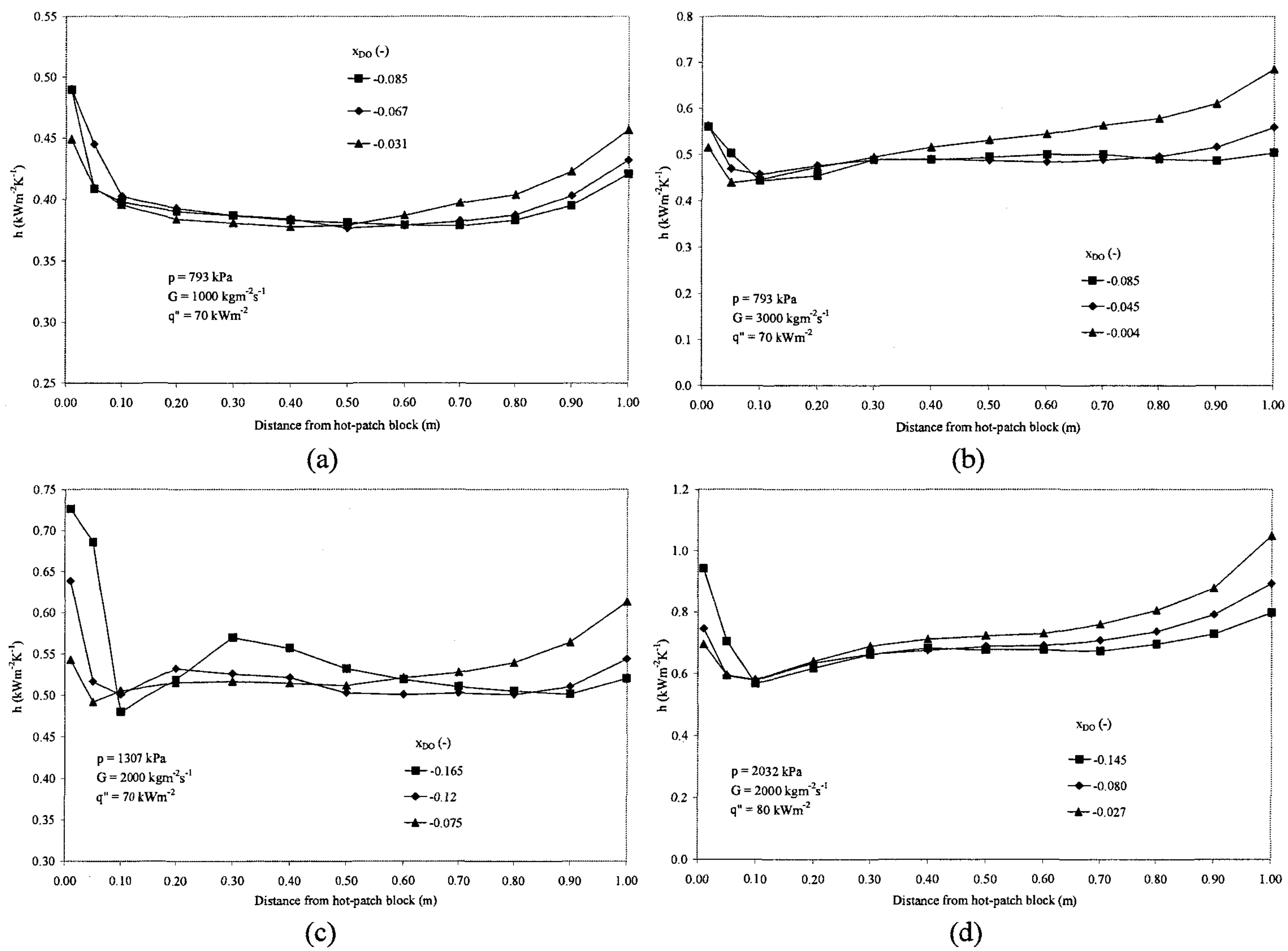

Figure 6. 8 Effect of inlet subcooling on heat transfer coefficient considering distance from hot-patch block.

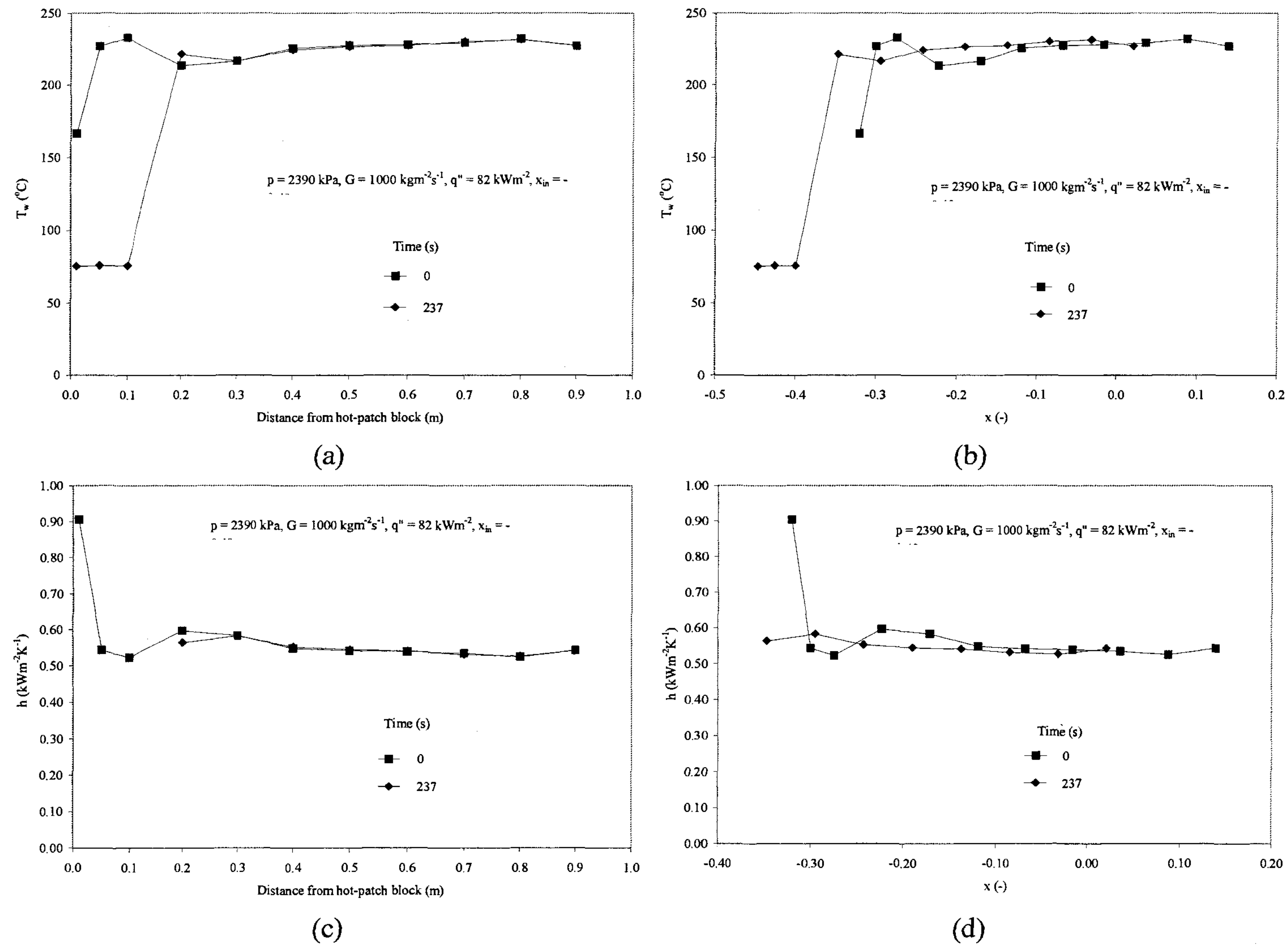

Figure 6. 9 Effect of quench front propagation on wall temperature and heat transfer coefficient.

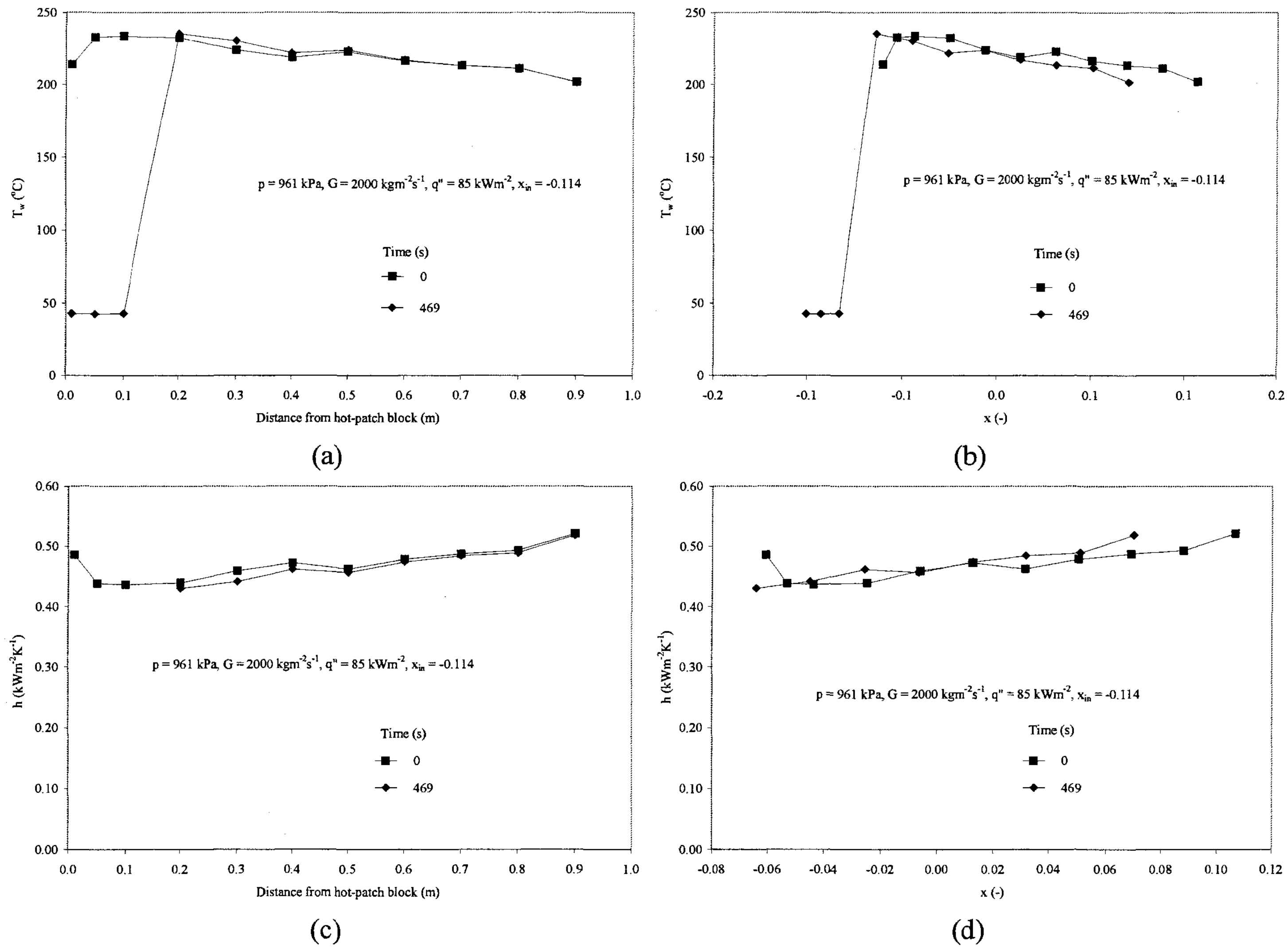

Figure 6. 10 Effect of quench front propagation on wall temperature and heat transfer coefficient.

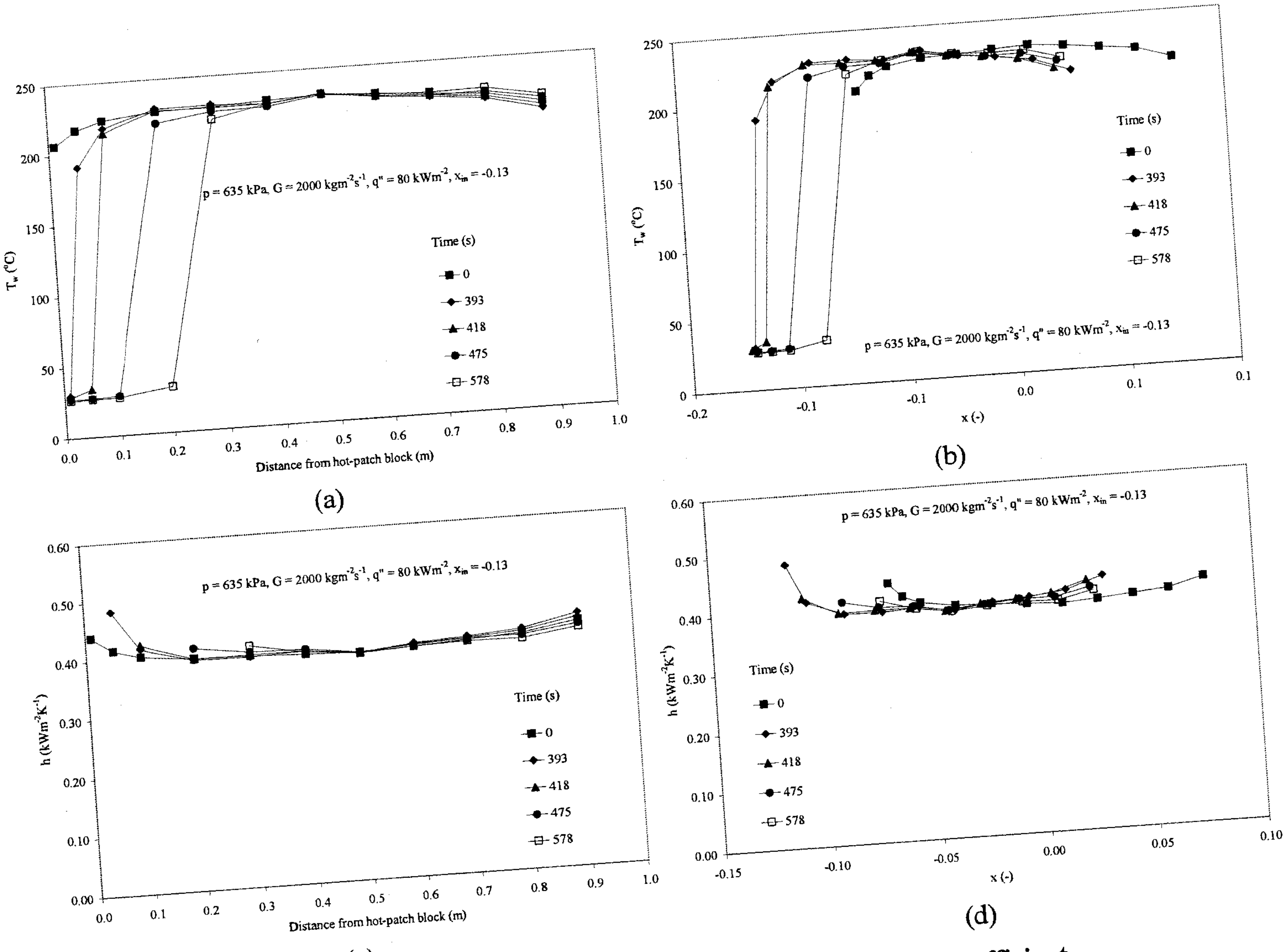

Figure 6. 11 Effect of quench front propagation on wall temperature and heat transfer coefficient.

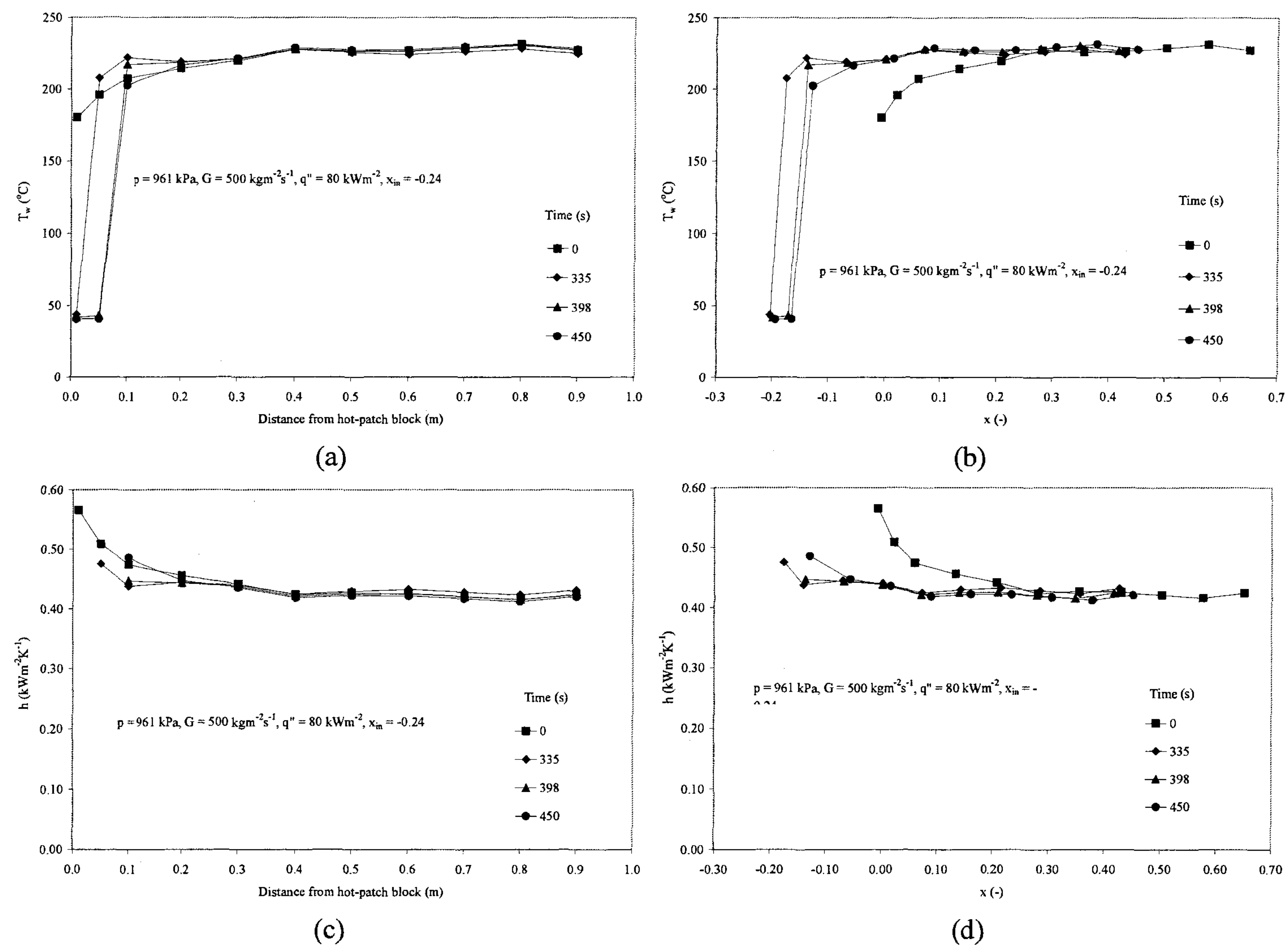

Figure 6. 12 Effect of quench front propagation on wall temperature and heat transfer coefficient.

mostly affected part of the heat transfer coefficient curve. Further downstream from the quench front, the deviation between heat transfer coefficient curves starts to disappear (fully developed heat transfer region). This effect is similar to the effect of inlet subcooling on heat transfer coefficient. Figure 6.13 is reproduced from Groeneveld and Gardiner (1978) for the boiling curve of R-12 with and without using hot-patch. The figure shows that the CHF at the hot-patch does not affect the film boiling temperature. Hot-patch effect data used in the analysis are listed in Appendix D.

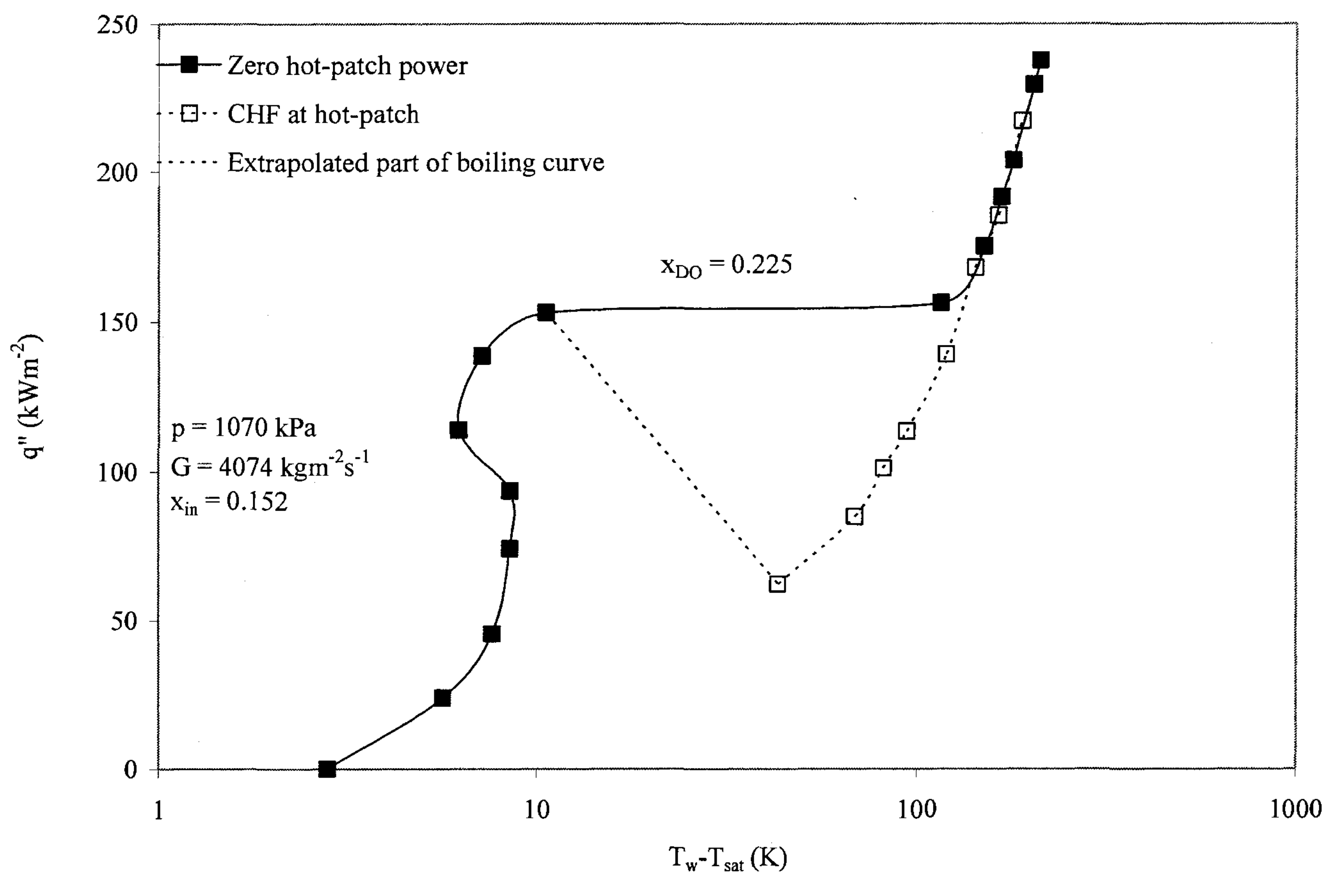

Figure 6. 13 Boiling curve of R-12 for hot-patch equipped test section (reproduced from Groeneveld and Gardiner (1978)].

CHAPTER 7 THEORETICAL MODEL

7.1. General

There are many models available to predict film boiling heat transfer. The majority of these models are for DFFB, and are not applicable for IAFB due to the different heat transfer mechanism. Also, most of the available IAFB models are fine-tuned to a specific range of flow conditions. Because of these reasons, there is a need for a more general IAFB model that is applicable over a wider range of conditions.

In this chapter, the derivation of a new two-fluid (vapor and liquid) model to predict heat transfer in the subcooled and low quality region (or IAFB) is presented. The new model derivation starts with the general form of conservation equations (mass, momentum and energy). This will be based on the one-dimensional separated flow model as conservation equations are considered for liquid and vapor phases separately. The conservation equations are then simplified to have them in the form of ordinary differential equations that are solved numerically as an initial value problem.

The conservation equations can not be solved without having constitutive (closure) relations. These relations control the different modes of heat transfer and the wall and interfacial characteristics (shear stress relations) of the flow. The heat transfer modes that are considered in the course of derivation are:

- convection heat transfer from the heated wall to the bulk vapor,
- radiation from the heated wall to the vapor-liquid interface,
- convection from the bulk vapor to the vapor-liquid interface, and
- convection/conduction (depending on flow condition) from the vapor-liquid interface to the liquid core.

The shear stress relations are major components in the model derivation. These include shear stress relations for the wall, vapor-to-interface, and interface-to-liquid.

The model is optimized with more general constitutive relations and more physical phenomena involved than with previous models. It is believed that this will improve the prediction accuracy for a wider range of application (at least for the flow conditions covered in the experimental program of the thesis) with capabilities to predict for different fluids (e.g. Freon, water, etc.).

In principle, the general derivation technique followed is similar to that of Analytis and Yadigaroglu (1987), Cachard (1994) and Hammouda (1996). The previous three models have many common considerations such as assuming the vapor flow between two parallel plates and considering convective heat transfer between the wall and vapor, and between vapor and vapor-liquid interface. Most of other older models [e.g., Denham (1984), Fung (1981), and Chan and Yadigaroglu (1980)] followed a different strategy by considering conduction through the vapor film (heat is transferred directly to the vapor-liquid interface by conduction through the vapor layer), which limited the applicability of the models to low mass fluxes. A detailed comparison between the new model and the Analytis and Yadigaroglu (1987), Cachard (1994) and Hammouda (1996) models will be given at the end of this chapter.

7.2. Assumptions

For the IAFB regime, the mass, momentum and energy equations are derived based on the following assumptions:

- The flow is one-dimensional incompressible for both vapor and liquid phases.
- The mean flow is steady.
- The interface is always assumed to be at the saturation temperature

- The vapor film flow is assumed to be the same as a vapor flow between parallel plates. This is a reasonable assumption for a thin vapor film.
- At any cross-section along the heated length, vapor, interface and liquid exist at the same pressure.
- The flow in the vapor film is turbulent. This assumption is based on the observation of Hsu and Westwater (1959) that the transition to turbulent flow in the vapor phase occurs at very low Reynolds number (around 100).
- No vapor is present in the core and no entrainment of the liquid is present in the vapor film. Lee and Kim (1987) showed a smooth liquid core in examining IAF visually without significant entrainments in the vapor film. Also in there flow visualization experiment, Ishii and de Jarlais (1987) found that at subcooled conditions, the liquid core is smooth up to high void fractions (void fractions of 0.3 to 0.4). This was also discussed by Nelson and Unal (1992) in their model development.
- There is no direct contact between liquid and heated surface.
- The heat transfer coefficient between wall and vapor is equal to that between vapor and interface.
- Thermodynamic non-equilibrium is present in the IAFB regime.
- There is no effect of liquid core oscillation perpendicular to the flow on heat transfer [Baum et al. (1978)].
- The vapor film is transparent and the wall is gray. Radiation is transferred directly to the vapor-liquid interface.

7.3. Conservation Equations

7.3.1. Conservation of mass

For the control volume shown in Figure 7.1, the conservation of mass for the liquid phase only can be written as

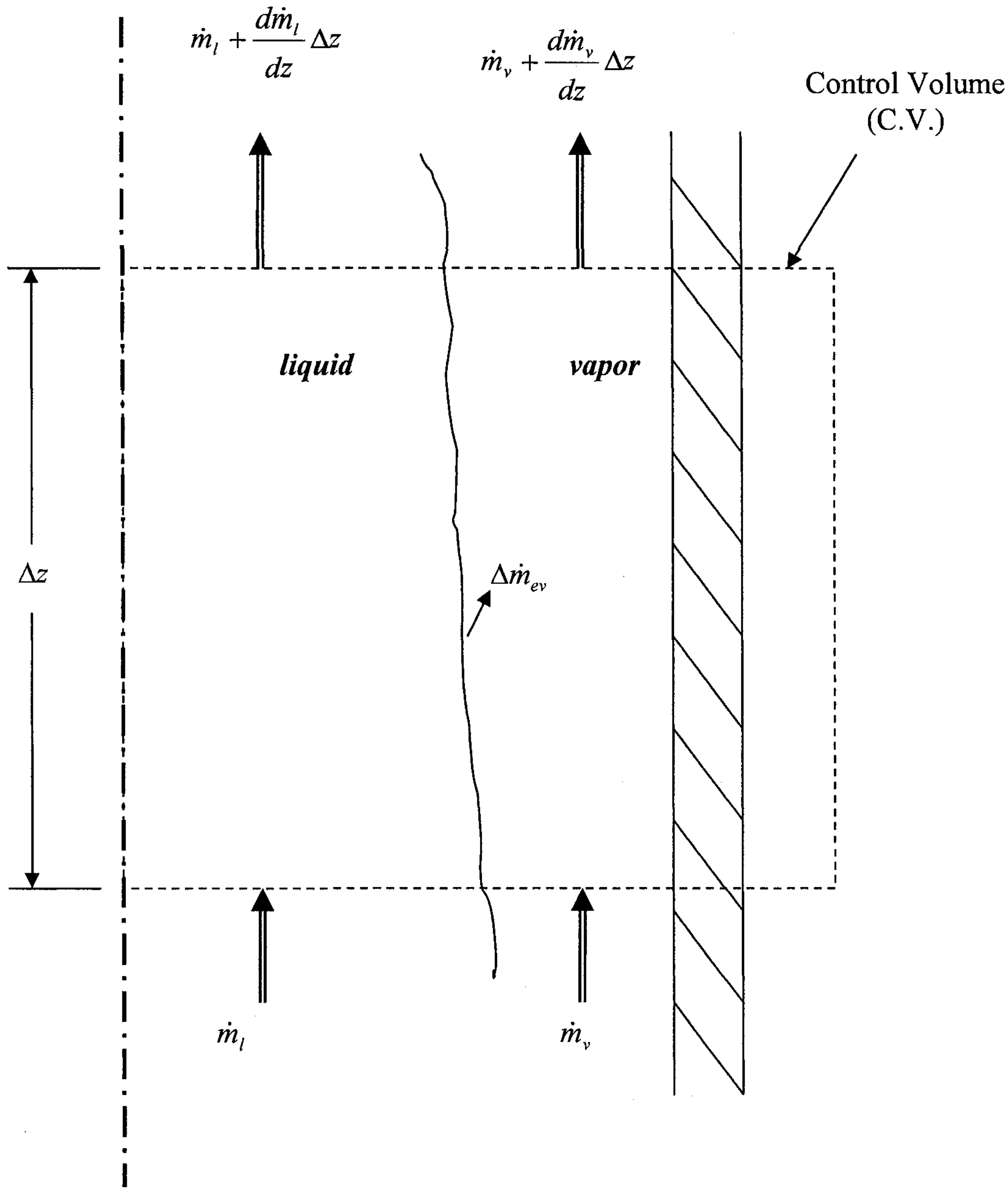

Figure 7. 1 Control volume for deriving conservation of mass equations for the new IAFB model.

$$\left(\dot{m}_l + \frac{d\dot{m}_l}{dz} \Delta z \right) - \dot{m}_l = -\Delta \dot{m}_{ev} \tag{7.1}$$

But

$$\dot{m}_l = \rho_l u_l A_l \tag{7.2}$$

Then

$$\frac{d}{dz}[\rho_l u_l A_l] \Delta z = -\Delta \dot{m}_{ev} \tag{7.3}$$

For one-dimensional flow, the void fraction α is defined as the fraction of flow area occupied by the vapor phase, or

$$\alpha = \frac{A_v}{A} = 1 - \frac{A_l}{A} \tag{7.4}$$

Then for a constant tube cross-sectional area the mass conservation equation for the liquid phase becomes

$$\frac{d}{dz}[(1-\alpha)\rho_l u_l] = -\frac{\Gamma}{A} \tag{7.5}$$

where $\Gamma = \Delta \dot{m}_{ev} / \Delta z$ is the amount of liquid evaporated per unit axial length in the differential control volume.

In a similar manner as explained above, the mass conservation equation for the vapor phase can be written as

$$\left(\dot{m}_v + \frac{d\dot{m}_v}{dz} \Delta z \right) - \dot{m}_v = \Delta \dot{m}_{ev} \tag{7.6}$$

which is simplified to:

$$\frac{d}{dz}\left[\alpha \rho_v u_v\right] = \frac{\Gamma}{A} \tag{7.7}$$

It should be noted that the rate of liquid evaporated from the liquid core is equal to the rate of vapor added to the vapor film. This would lead to the continuity equation for the two phase mixture,

$$\frac{d}{dz}\left[\alpha_l \rho_l u_l\right] + \frac{d}{dz}\left[\alpha_v \rho_v u_v\right] = 0 \tag{7.8}$$

7.3.2. Conservation of momentum

For the control volume shown in Figure 7.2, a force balance can be written over the liquid phase cross-sectional area to give

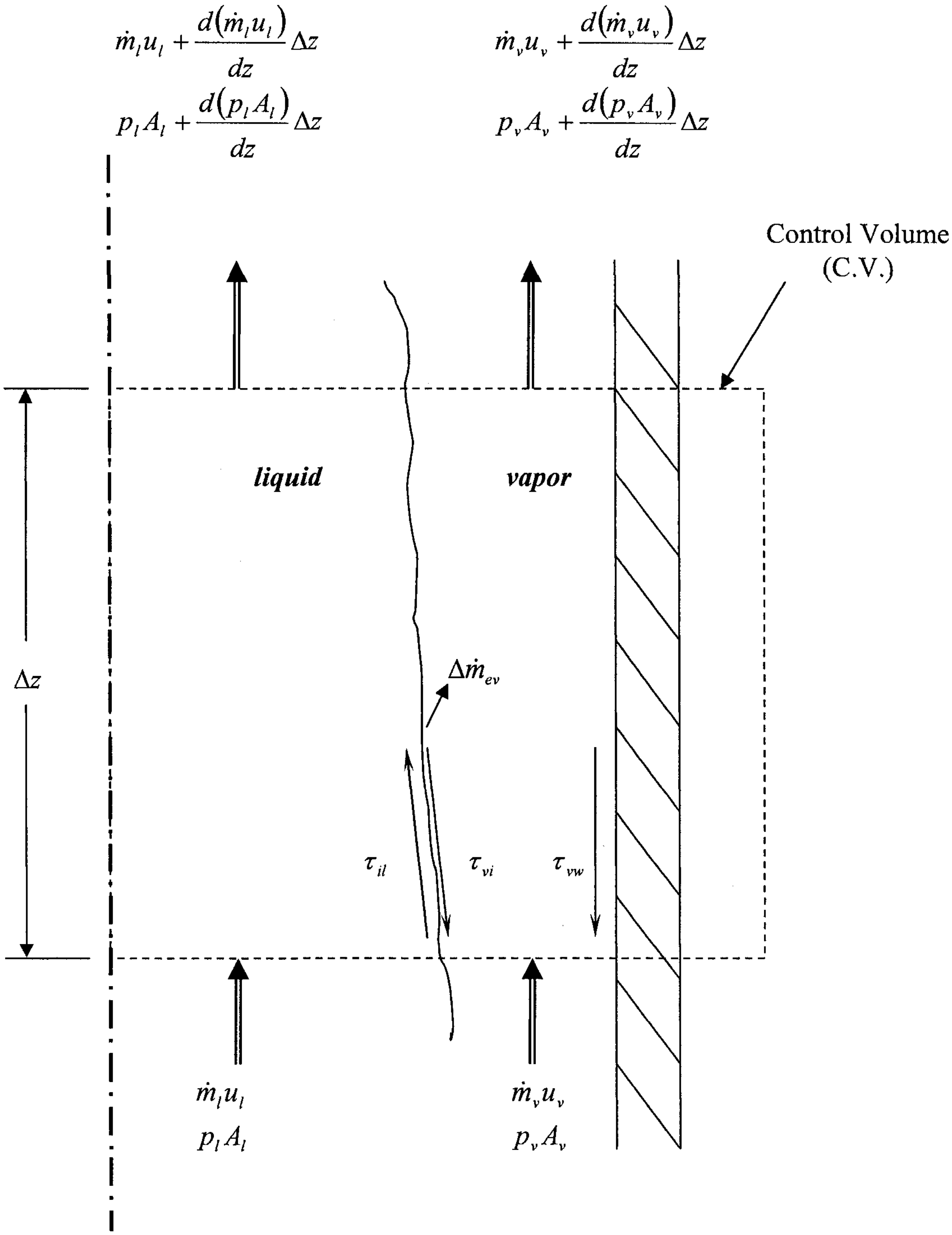

Figure 7. 2 Control volume for deriving conservation of momentum equations for the new IAFB model.

$$-\left[p_l A_l + \frac{dp_l A_l}{dz}\Delta z\right] + p_l A_l + p_i \frac{dA_l}{dz}\Delta z - \rho_l g A_l \Delta z + \tau_i P_i \Delta z - \Gamma u_i \Delta z = \left(\dot{m}_l u_l + \frac{d\dot{m}_l u_l}{dz}\Delta z\right) - \dot{m}_l u_l \tag{7.9}$$

or

$$-\frac{dp_l A_l}{dz} + p_i \frac{dA_l}{dz} - \frac{d\dot{m}_l u_l}{dz} = \rho_l g A_l - \tau_i P_i + \Gamma u_i \tag{7.10}$$

The first two terms in the LHS of Equation (7.10) represent the pressure forces on the element and the third term the rate of inflow of liquid phase momentum. The terms on the RHS represent the gravitational forces, the interfacial shear force, and the rate of generation of momentum due to mass transfer, respectively.

Applying the same procedure on the vapor phase, results in the following force balance

$$-\left[p_v A_v + \frac{dp_v A_v}{dz}\Delta z\right] + p_v A_v + p_i \frac{dA_v}{dz}\Delta z - \rho_v g A_v \Delta z - \tau_i P_i \Delta z - \tau_w P_w \Delta z + \Gamma u_i \Delta z = \left(\dot{m}_v u_v + \frac{d\dot{m}_v u_v}{dz}\Delta z\right) - \dot{m}_v u_v \tag{7.11}$$

or

$$-\frac{dp_v A_v}{dz} + p_i \frac{dA_v}{dz} - \frac{d\dot{m}_v u_v}{dz} = \rho_v g A_v + \tau_i P_i + \tau_w P_w - \Gamma u_i \tag{7.12}$$

7.3.3. Conservation of energy

An energy balance on the liquid core would produce (Figure 7.3)

$$\left[\dot{m}_l e_l + \frac{d(\dot{m}_l e_l)}{dz}\Delta z\right] - \dot{m}_l e_l = q'_{lh}\Delta z - \Delta\dot{m}_{ev} e_i \tag{7.13}$$

or

$$\frac{d(\dot{m}_l e_l)}{dz} = q'_{lh} - \Gamma e_i \tag{7.14}$$

where the specific energy, e, and interfacial specific energy, e_i, are respectively defined as

$$e_k = H_k + \frac{u_k^2}{2} + gz, \qquad k = l \text{ or } v \tag{7.15}$$

and

$$e_i = H_{ki} + \frac{u_i^2}{2} + gz, \qquad k = l \text{ or } v \tag{7.16}$$

The first term in Equation (7.14) represents the rate of change of energy per unit axial distance for a control volume around the liquid core. The second term, q'_{lh}, is the rate at which heat enters the liquid phase within the control volume per unit axial distance (the amount of heat transfer used for liquid core heating). The last term is the rate at which

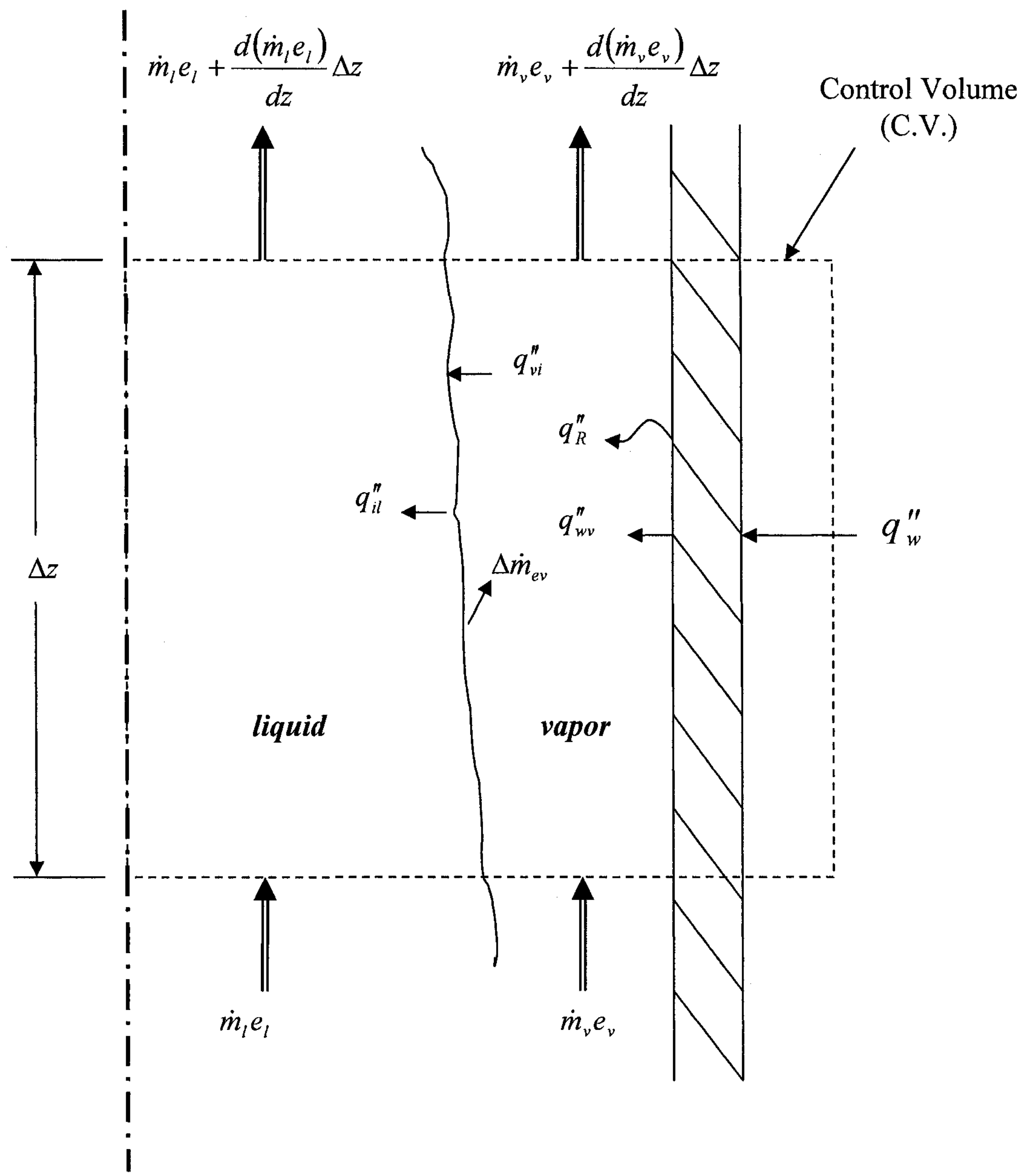

Figure 7. 3 Control volume for deriving conservation of energy equations for the new IAFB model.

energy is removed (evaporation) from the liquid phase by the mass transfer across the interface per unit axial distance.

A similar formulation for the vapor phase can be obtained by applying a differential energy balance on the control volume over the vapor film. This would produce

$$\frac{d(\dot{m}_v e_v)}{dz} = q'_{vh} + \Gamma e_i \tag{7.17}$$

where q'_{vh} is the amount of heat transfer used to heat the vapor film.

7.3.4. Simplification of conservation equations

7.3.4.1. Simplification of mass conservation equations

Equations (7.5) and (7.7) can be expanded and re-written, respectively, as

$$-\rho_l u_l \frac{d\alpha}{dz} + (1-\alpha)u_l \frac{d\rho_l}{dz} + (1-\alpha)\rho_l \frac{du_l}{dz} = -\frac{\Gamma}{A} \tag{7.18}$$

and

$$\rho_v u_v \frac{d\alpha}{dz} + \alpha u_v \frac{d\rho_v}{dz} + \alpha \rho_v \frac{du_v}{dz} = \frac{\Gamma}{A} \tag{7.19}$$

The variation of liquid density along the heated length is negligibly small. Also by neglecting the variation of vapor density along the heated length (which is valid if the vapor temperature variation is small like the case of IAFB), Equations (7.18) and (7.19) can be simplified to

$$-\rho_l u_l \frac{d\alpha}{dz} + (1-\alpha)\rho_l \frac{du_l}{dz} = -\frac{\Gamma}{A} \tag{7.20}$$

and

$$\rho_v u_v \frac{d\alpha}{dz} + \alpha\rho_v \frac{du_v}{dz} = \frac{\Gamma}{A} \tag{7.21}$$

This form of equation is more practical for numerical analysis.

7.3.4.2. Simplification of momentum conservation equations

By assuming that the interfacial pressure, p_i, the liquid pressure, p_l, and the vapor pressure, p_v, are all equal to flow pressure, p, the first term on the LHS of Equation (7.10) can be expanded and combined with the second term

$$-\frac{dA(1-\alpha)p}{dz} + p\frac{dA(1-\alpha)}{dz} = -A(1-\alpha)\frac{dp}{dz} \tag{7.22}$$

Also, the third term in the same equation can be expanded, and with the use of the mass conservation equation for the liquid phase [Equation (7.5)], it can be written as

$$-\frac{d\dot{m}_l u_l}{dz} = \Gamma u_l - A(1-\alpha)\rho_l u_l \frac{du_l}{dz} \tag{7.23}$$

Substituting Equations (7.22) and (7.23) into Equation (7.10) and rearranging yields

$$-(1-\alpha)\frac{dp}{dz} - (1-\alpha)\rho_l u_l \frac{du_l}{dz} = (1-\alpha)\rho_l g - \frac{\tau_i P_i}{A} - \frac{\Gamma(u_l - u_i)}{A} \tag{7.24}$$

By following the same practice of combining the first two terms and expanding the third term for the vapor phase [Equation (7.12)] and upon substitution, the momentum equation will be

$$-\alpha\frac{dp}{dz} - \alpha\rho_v u_v \frac{du_v}{dz} = \alpha\rho_v g + \frac{\tau_i P_i}{A} + \frac{\tau_w P_w}{A} + \frac{\Gamma(u_v - u_i)}{A} \tag{7.25}$$

7.3.4.3. Simplification of energy conservation equations

By neglecting the kinetic and potential parts of Equations (7.15) and (7.16) and after substitution, Equations (7.14) and (7.17) become, respectively,

$$(1-\alpha)A\rho_l u_l \frac{dH_l}{dz} = q'_{lh} - \Gamma(H_f - H_l) \tag{7.26}$$

and

$$\alpha A \rho_v u_v \frac{dH_v}{dz} = q'_{vh} + \Gamma\left(H_g - H_v\right) \tag{7.27}$$

By calculating enthalpy as

$$dH = c_p dT\,, \tag{7.28}$$

the final form of the energy conservation equations for the liquid and vapor phase can be expressed as,

$$(1-\alpha)u_l \frac{dT_l}{dz} = \frac{q'_{lh}}{c_{pl}\rho_l A} - \frac{\Gamma\left(H_f - H_l\right)}{c_{pl}\rho_l A} \tag{7.29}$$

and

$$\alpha u_v \frac{dT_v}{dz} = \frac{q'_{vh}}{c_{pv}\rho_v A} + \frac{\Gamma\left(H_g - H_v\right)}{c_{pv}\rho_v A} \tag{7.30}$$

7.4. Other Relations

The vapor layer thickness can be expressed as a function of the tube radius and the void fraction,

$$\delta = R\left(1 - \sqrt{1-\alpha}\right) \tag{7.31}$$

and the cross-sectional area, inside tube wall peripheral length, and the peripheral length of the vapor-liquid interface, respectively, are

$$A = \pi R^2, \qquad R = \text{tube radius} \tag{7.32}$$

$$P_w = 2\pi R, \tag{7.33}$$

and

$$P_i = 2\pi(R - \delta) \qquad (= P_w\sqrt{1-\alpha}\,) \tag{7.34}$$

7.5. Constitutive Equations

7.5.1. Heat transfer relations

The heat balance on the control volume (Figure 7.3) can be used to obtain the relation between the different modes of heat transfer. The total power per unit axial distance transferred by the test section to the coolant is given by

$$q'_w = q''_w P_w = q''_{wv} P_w + q''_{rad} P_w \tag{7.35}$$

It is assumed that the vapor film is transparent and all radiation heat transfer goes to the interface. The power per unit axial distance used for heating the vapor flow is

$$q'_{vh} = q''_{wv} P_w - q''_{vi} P_i \tag{7.36}$$

The evaporation heat transfer is

$$q'_{ev} = q''_{ev}P_i = q''_{vi}P_i + q''_{rad}P_w - q''_{il}P_i \tag{7.37}$$

Finally, the amount of heat transfer used for liquid heating is

$$q'_{lh} = q''_{il}P_i \tag{7.38}$$

The heat transfer components in Equations (7.35) - (7.38), based on the conservation of energy principle, should satisfy the following conditions:

$q'_{vh} \geq 0$,*

$q'_{lh} \leq q''_{vi}P_i + q''_{rad}P_w$,

and

$q'_{lh} \leq q'_w$

Next, proper relations are needed for wall-to-vapor, vapor-to-interface, interface-to-liquid, and radiation heat fluxes.

* This is not true if the heat flux is non uniform and part of the wall, is unheated

7.5.1.1. Heat transfer from wall-to-vapor and from vapor-to-interface

By assuming the vapor gap to be much smaller than the tube radius ($\delta << D$), the problem can be simplified as flow between two parallel plates. Then from Kays and Crawford (1986), the wall-to-vapor and vapor-to-interface heat transfer coefficients can be expressed, respectively, as

$$h_{wv} = \frac{k_v Nu_v}{2\delta\left(1 - \frac{q''_{vi}}{q''_{wv}}\theta^*\right)} \tag{7.39}$$

and

$$h_{vi} = \frac{k_v Nu_v}{2\delta\left(1 - \frac{q''_{wv}}{q''_{vi}}\theta^*\right)} \tag{7.40}$$

where

$$q''_{wv} = h_{wv}\left(T_w - T_v\right), \tag{7.41}$$

and

$$q''_{vi} = h_{vi}\left(T_v - T_{sat}\right), \tag{7.42}$$

Nu_v is the vapor Nusselt number, and θ^* the influence coefficient (or non-dimensional temperature) defined as the ratio between dimensionless temperatures of the heated wall and the interface. A detailed explanation of the derivation of Equations (7.40) and (7.41) is given in Kays and Leung (1963).

To calculate the heat transferred from wall-to-vapor and from vapor-to-interface, it is assumed that the vapor-to-interface heat transfer coefficient is equal to that of the wall-to-vapor one, or

$$h_{vi} = h_{wv} \tag{7.43}$$

The vapor velocity relative to the wall (stationary wall) is higher than the vapor velocity relative to the moving interface. For a vapor film temperature equal to the arithmetic average of wall temperature and saturation and a perfectly smooth interface, which is a common assumption in modeling IAFB heat transfer, Equation (7.43) is not exactly true. Considering the heat transfer coefficient to be defined as

$$h = c\frac{k}{D_{hy}}\mathrm{Re}^a\,\mathrm{Pr}^b, \tag{7.44}$$

where a, b, and c are constants, the ratio of heat transfer coefficients will be

$$\frac{h_{vi}}{h_{wv}} = \left(1 - \frac{u_i}{u_v}\right)^a \tag{7.45}$$

This implies, in general, that the vapor-to-interface heat transfer coefficient is less than that of the wall-to-vapor. However, the interface is not perfectly smooth due to turbulence in the vapor layer, and the bulk vapor temperature is generally less than the vapor film temperature due to oscillation of the interface and turbulence [Analytis and Yadigaroglu (1987) and Mosaad and Johannsen (1989)]. This will enhance the heat transfer coefficient at the interface and will move it closer to the equality relationship (7.43). It will also decrease the vapor superheat for the same heat flux [see Equation (7.42)]. Using this assumption [Equation (7.43)] with Equations (7.41) and (7.42), the heat flux that crosses the vapor-liquid interface is related to the wall-vapor heat flux as

$$q''_{vi} = q''_{wv} \frac{T_v - T_{sat}}{T_w - T_v} \tag{7.46}$$

This equation is used without using an enhancement factor as the enhancement is implicitly included. This derivation is different than that of Analytis and Yadigaroglu (1987) and Cachard (1994). In their analysis, Analytis and Yadigaroglu solved Equations (7.39) and (7.40) simultaneously and used an empirical factor (λ) to account for the enhancement in heat flux from the vapor to the interface, where λ is defined as

$$\lambda = 1 + \frac{300\delta}{D}$$

The value of this factor increases with void fraction and reaches around 45 at a void fraction of 0.5. On the other hand, Cachard (1994) used the same equations of Analytis and Yadigaroglu (1987) but with a complex correction factor derived empirically from available low pressure data from Fung (1981). These correction factors may limit the application of the model to the range for which they were derived for.

Now upon substitution of Equation (7.46) into Equation (7.39), the wall-to-vapor heat transfer coefficient can be written as

$$h_{wv} = \frac{k_v Nu_v (T_w - T_v)}{2\delta\left[(T_w - T_v) - (T_v - T_{sat})\theta^*\right]} \tag{7.47}$$

Finally, the heat flux from the wall to the vapor will be:

$$q''_{wv} = \frac{k_v Nu_v (T_w - T_v)^2}{2\delta\left[(T_w - T_v) - (T_v - T_{sat})\theta^*\right]} \tag{7.48}$$

For laminar flow between two parallel planes, Nu_v and θ are given by $Nu_v = 5.385$ and $\theta^* = 0.346$. For turbulent flow between two stationary parallel plates, Kays and Leung (1963) give Nu_v and θ^* in tabular form up to a Reynolds number of 10^6, and Prandtl numbers from 0 to 1000. Approximate linear correlations for Nu_v and θ^* are derived by neglecting Prandtl number effect as:

$$Nu_v = 5.086 + 0.00299\,\mathrm{Re}_v \tag{7.49}$$

and

$$\theta^* = 0.34762 - \frac{0.16\,\mathrm{Re}_v}{9900} \tag{7.50}$$

7.5.1.2. Heat transfer from vapor-liquid interface to the liquid core

For the turbulent liquid core, the heat transfer coefficient is calculated using the Dittus-Boelter equation for flow in a circular tube of diameter $(D - 2\delta)$. For laminar flow, the Nusselt number is considered to be equal to 3.66.

$$h_{il} = \begin{cases} 3.66 \dfrac{k_l}{D - 2\delta} F, & \mathrm{Re}_l < 2000 \\ 0.023 \dfrac{k_l}{D - 2\delta} \mathrm{Re}_l^{0.8} \mathrm{Pr}_l^{0.4} F, & \mathrm{Re}_l > 2000 \end{cases} \tag{7.51}$$

where the liquid core Reynolds number, Re_l, relative to the interface and the coefficient F are defined, respectively, as

$$\mathrm{Re}_l = \frac{\rho_l |u_l - u_i| (D - 2\delta)}{\mu_l} \tag{7.52}$$

and

$$F = 1 + 0.7 \frac{D}{z} \tag{7.53}$$

The heat transfer from the interface to the liquid core is calculated using

$$q''_{il} = h_{il} \left(T_{sat} - T_l \right) \tag{7.54}$$

The coefficient F [Equation (7.53)] is used to account for the entrance effect. Its influence decreases downstream of the dryout location. Equation (7.51) is similar to the one used by Analytis and Yadigaroglu (1987) to account for the interface-to-liquid core heat transfer. It should be noted here that Hammouda (1996) assumed a relation between vapor-to-interface and interface-to-liquid heat fluxes which has a similar form as Equation (7.46):

$$q''_{il} = q''_{vi} \frac{T_v - T_{sat}}{T_{sat} - T_l} \tag{7.55}$$

In applying Equation (7.55) it was found that the liquid heated up and approached saturation very rapidly since almost all the heat transferred from the wall-to-interface was used to heat the liquid core without evaporation.

7.5.1.3. Radiation heat transfer

By assuming the vapor film is transparent and that the wall is gray, radiation to the vapor-liquid interface, q_{rad}, can be expressed as

$$q''_{rad} = \frac{\sigma\left(T_w^4 - T_{sat}^4\right)}{\dfrac{1}{\varepsilon_w} + \dfrac{1}{\varepsilon_l\sqrt{1-\alpha}} - 1} \tag{7.56}$$

where σ is the Stefan-Boltzman constant, and ε_w and ε_l are the emissivities of the wall and vapor-liquid interface, respectively. Equation (7.56) is the Siegel and Howell (1972) equation to calculate radiation heat transfer.

7.5.2. Shear stress relations

7.5.2.1. Wall shear stress

The wall shear stress is expressed by

$$\tau_w = f_w \rho_v \frac{u_v^2}{2} \tag{7.57}$$

where f_w is the wall friction factor. The most common friction factor form used by the majority of researchers is used here [Analytis and Yadigaroglu (1987)]:

$$f_w = \frac{0.085}{\mathrm{Re}_v^{0.25}} \tag{7.58}$$

where the vapor Reynolds' number is defined as

$$\mathrm{Re}_v = \frac{\rho_v u_v (2\delta)}{\mu_v} = \frac{\rho_v u_v D\left(1-\sqrt{1-\alpha}\right)}{\mu_v} \tag{7.59}$$

7.5.2.2. Interfacial shear stress

The vapor-to-interface and interface-to-liquid shear stresses are, respectively, calculated from

$$\tau_{vi} = f_{vi} \rho_v |u_v - u_i| \frac{u_v - u_i}{2} \tag{7.60}$$

and

$$\tau_{il} = -f_{il} \rho_l |u_l - u_i| \frac{u_l - u_i}{2} \tag{7.61}$$

where f_{vi} is the interface friction factor at the vapor side and f_{il} is the interface friction factor at the liquid side.

The reason behind having Equations (7.60) and (7.61) is to calculate the velocity at the interface. In this model, the velocity of the interface is needed to calculate heat transfer from the vapor-liquid interface to the liquid core. To tackle this issue, the most common practice is to assume the velocity at interface to be [Donevski et al. (1992)]:

$$u_i = \frac{u_v + u_l}{2} \tag{7.62}$$

Due to the higher viscosity of liquid compared to vapor, it is expected that the interfacial velocity will be less than the average of vapor and liquid velocity (close to liquid velocity, Figure 7.4). This means that Equation (7.62) over-predicts the interfacial velocity and subsequently results in under-predicted vapor-to-interface and over-predicted interface-to-liquid heat transfer values. Other researchers [e.g., Analytis and Yadigaroglu (1987)] assumed the interfacial velocity to be equal to liquid velocity. In addition to contradicting the physical phenomenon, this assumption creates even more complications and assumptions to predict the amount of heat transfer needed to heat the liquid core.

In the current derivation, the interfacial velocity is calculated by equating the shear stress at both sides of the interface [Equations (7.60) and (7.61)] and using iteration techniques. This method would provide a more realistic estimate of the velocity of the interface with more physical phenomena involved in the derivation. The friction factor for the vapor side is taken to be

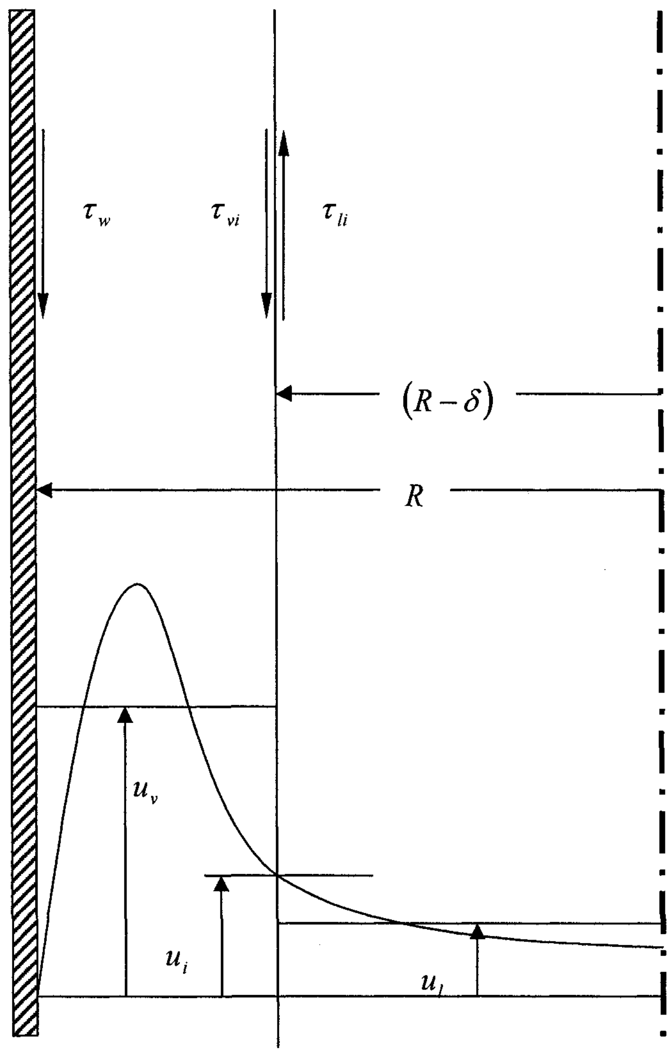

Figure 7. 4 Schematic of shear stresses and flow velocities used in modeling IAFB heat transfer.

$$f_{vi} = \frac{0.085}{\mathrm{Re}_{vi}^{0.25}} \tag{7.63}$$

where

$$\mathrm{Re}_{vi} = \frac{\rho_v |u_v - u_i| D\left(1 - \sqrt{1-\alpha}\right)}{\mu_v} \tag{7.64}$$

and for the liquid side,

$$f_{il} = \begin{cases} \dfrac{16}{\mathrm{Re}_l}, & \mathrm{Re}_l < 2000 \\ \dfrac{0.085}{\mathrm{Re}_l^{0.25}}, & \mathrm{Re}_l > 2000 \end{cases} \tag{7.65}$$

7.5.3. Vapor generation

The evaporation heat flux can be calculated from Equation (7.37). Then the vapor generation rate per unit axial length can be determined from a simple heat balance given by:

$$\Gamma = \frac{q''_{ev} P_i}{H_{fg}} \tag{7.66}$$

where H_{fg} is the latent heat of vaporization.

7.5.4. Termination of IAFB regime

There are several limiting criteria for the IAFB regime. Analytis and Yadigaroglu (1987) suggested the use of a critical Weber number. However, in this study a void fraction of 0.5 will be considered as the termination limit for IAFB. This void fraction value was suggested by Groeneveld (1992) and used by many other researchers.

$$\alpha \leq 0.5 \tag{7.67}$$

In addition the IAFB regime can only be maintained if $Tw > T_{MFB}$ else the vapor film will collapse and heated surface will rewet.

7.6. Summary and Implementation of the New Model

7.6.1. Summary of the new model

Conservation equations

$$-\rho_l u_l \frac{d\alpha}{dz} + (1-\alpha)\rho_l \frac{du_l}{dz} = -\frac{\Gamma}{A} \tag{7.20}$$

$$\rho_v u_v \frac{d\alpha}{dz} + \alpha\rho_v \frac{du_v}{dz} = \frac{\Gamma}{A} \tag{7.21}$$

$$-(1-\alpha)\frac{dp}{dz} - (1-\alpha)\rho_l u_l \frac{du_l}{dz} = (1-\alpha)\rho_l g - \frac{\tau_i P_i}{A} - \frac{\Gamma(u_l - u_i)}{A} \tag{7.24}$$

$$-\alpha \frac{dp}{dz} - \alpha \rho_v u_v \frac{du_v}{dz} = \alpha \rho_v g + \frac{\tau_i P_i}{A} + \frac{\tau_w P_w}{A} + \frac{\Gamma(u_v - u_i)}{A} \tag{7.25}$$

$$(1-\alpha) u_l \frac{dT_l}{dz} = \frac{q'_{lh}}{c_{pl} \rho_l A} - \frac{\Gamma(h_f - h_l)}{c_{pl} \rho_l A} \tag{7.29}$$

$$\alpha u_v \frac{dT_v}{dz} = \frac{q'_{vh}}{c_{pv} \rho_v A} + \frac{\Gamma(h_g - h_v)}{c_{pv} \rho_v A} \tag{7.30}$$

Hear flux components:

$$q'_w = q''_w P_w = q''_{wv} P_w + q''_{rad} P_w \tag{7.35}$$

$$q'_{vh} = q''_{wv} P_w - q''_{vi} P_i \tag{7.36}$$

$$q'_{ev} = q''_{ev} P_i = q''_{vi} P_i + q''_{rad} P_w - q''_{il} P_i \tag{7.37}$$

$$q'_{lh} = q''_{il} P_i \tag{7.38}$$

$$q''_{wv} = \frac{k_v Nu_v (T_w - T_v)^2}{2\delta\left[(T_w - T_v) - (T_v - T_{sat})\theta^*\right]} \tag{7.48}$$

$$Nu_v = 5.086 + 0.00299\,\mathrm{Re}_v \tag{7.49}$$

$$\theta^* = 0.34762 - \frac{0.16\,\mathrm{Re}_v}{9900} \tag{7.50}$$

$$q''_{vi} = q''_{wv}\,\frac{T_v - T_{sat}}{T_w - T_v} \tag{7.46}$$

$$q''_{il} = h_{il}\left(T_{sat} - T_l\right) \tag{7.54}$$

$$h_{il} = \begin{cases} 3.66\dfrac{k_l}{D-2\delta}F, & \mathrm{Re}_l < 2000 \\ 0.023\dfrac{k_l}{D-2\delta}\mathrm{Re}_l^{0.8}\,\mathrm{Pr}_l^{0.4}\,F, & \mathrm{Re}_l > 2000 \end{cases} \tag{7.51}$$

$$\mathrm{Re}_l = \frac{\rho_l\left|u_l - u_i\right|\left(D - 2\delta\right)}{\mu_l} \tag{7.52}$$

$$F = 1 + 0.7\frac{D}{z} \tag{7.53}$$

$$q''_{rad} = \frac{\sigma\left(T_w^4 - T_{sat}^4\right)}{\dfrac{1}{\varepsilon_w} + \dfrac{1}{\varepsilon_l\sqrt{1-\alpha}} - 1} \tag{7.56}$$

$$\Gamma = \frac{q''_{ev} P_i}{H_{fg}} \tag{7.67}$$

Shear stress relations:

$$\tau_w = f_w \rho_v \frac{u_v^2}{2} \tag{7.57}$$

$$f_w = \frac{0.085}{\mathrm{Re}_v^{0.25}} \tag{7.58}$$

$$\mathrm{Re}_v = \frac{\rho_v u_v (2\delta)}{\mu_v} = \frac{\rho_v u_v D\left(1-\sqrt{1-\alpha}\right)}{\mu_v} \tag{7.59}$$

$$\tau_{vi} = f_{vi} \rho_v \left|u_v - u_i\right| \frac{u_v - u_i}{2} \tag{7.60}$$

$$f_{vi} = \frac{0.085}{\mathrm{Re}_{vi}^{0.25}} \tag{7.63}$$

$$\mathrm{Re}_{vi} = \frac{\rho_v \left|u_v - u_i\right| D\left(1-\sqrt{1-\alpha}\right)}{\mu_v} \tag{7.64}$$

$$\tau_{il} = -f_{il}\rho_l |u_l - u_i| \frac{u_l - u_i}{2} \tag{7.61}$$

$$f_{il} = \begin{cases} \dfrac{16}{\mathrm{Re}_l}, & \mathrm{Re}_l < 2000 \\ \dfrac{0.085}{\mathrm{Re}_l^{0.25}}, & \mathrm{Re}_l > 2000 \end{cases} \tag{7.65}$$

Model applicability:

$$\alpha \le 0.5 \tag{7.67}$$

$$T_w > T_{MFB} \tag{7.68}$$

7.6.2. Implementation of the new model

The model summarized in Section 7.6.1. is solved numerically as an initial value problem. After reading the input of flow parameters (*p, G, q", and* x_{in}), and determining initial conditions (x_{DO}, u_v, u_l, *and* α) at (z = 0.0), the program calculates the heat transfer components and shear stress relations to determine the gradients of the conservation equations. These gradients are used to calculate values at step (z = z + Δz) which are considered as initial conditions of the next step. The program predicts the wall temperature using iteration techniques with heat flux input to the test section and predicted total heat flux.

7.7. Comparison of the New Model with Previous Similar Models

The derivation of conservation equations is very similar in most one-dimensional, two-fluid models. These models differ from each others by the way constitutive relations are derived. Table 7.1 summarizes the constitutive relations of the new model and the models of Analytis and Yadigaroglu (1987), Cachard (1994) and Hammouda (1996). The reason for choosing these models is due to the similarity of derivation. All these models treat the vapor film flow as flow between two parallel plates. Another common feature of these models is that heat transfer at the wall-vapor-interface is based on solution/modification of the Kays and Crawford (1986) equation. The table shows that the new model does not include correction factors or "tuning" factors and it uses the least empirical correlations to account for the different heat transfer and shear stress effects.

Table 7. 1 Comparison of constitutive (closure) relations of the current model with other similar models

Closure relation	Reference	Equation	Remarks
Wall-to-vapor heat transfer	Analytis and Yadigaroglu (1987)	$q''_{wv} = \frac{k_v Nu_v}{2\delta(1-\theta^{*2})}\left[(T_w - T_v) - \theta^*(T_v - T_{sat})\right]$ For laminar flow: $Nu_v = 5.385$ and $\theta^* = 0.346$ For turbulent flow, a linear interpolation is used for $\mathrm{Re}_v = 10000$ $(Nu_v = 35, \theta^* = 0.186)$	
	Cachard (1994)	$q'_{wv} = \lambda_{hv}\frac{k_v Nu_v}{2\delta(1-\theta^{*2})}\frac{P_w + P_i}{2}\left[(T_w - T'_v) - \theta^*(T'_v - T_{sat})\right]$ $\lambda_{hv} = 0.679\left\{\delta\left[\frac{\rho_v(\rho_l - \rho_v)g}{\mu_v^2}\right]^{\frac{1}{3}}\right\}^{0.509}$ $T'_v = T_v + (\lambda_{hv} - 1)(T_v - T_{sat})$; $Nu_v = 5.385$; $\theta^* = 0.346$	Similar to Analytis and Yadigaroglu (1987) with enhancement factor to correct for vapor temperature. Enhancement factor is derived based on Fung (1981) water data
	Hammouda (1996)	$q''_{wv} = \frac{Nu_v}{\left[1 - \frac{T_v - T_{sat}}{T_w - T_v}\theta^*\right]}\frac{k_v}{D\left(1-\sqrt{1-\alpha}\right)}(T_w - T_v)$ $Nu_v = \frac{5.071}{\mathrm{Pr}_v^{0.0439}} + 0.0028\,\mathrm{Pr}_v^{0.645}\,\mathrm{Re}_v$; $\theta^* = 0.3476\,\mathrm{Pr}_v^{0.0026} - \frac{0.146\,\mathrm{Pr}_v^{0.5418}\,\mathrm{Re}_v}{9900}$	
	The new model	$q''_{wv} = \frac{k_v Nu_v (T_w - T_v)^2}{2\delta\left[(T_w - T_v) - (T_v - T_{sat})\theta^*\right]}$ $Nu_v = 5.086 + 0.00299\,\mathrm{Re}_v$ $\theta^* = 0.34762 - \frac{0.16\,\mathrm{Re}_v}{9900}$	Modified Kays and Crawford (1986) with the assumption $h_{wv} = h_{vi}$

Table 7.1 (Continued)

Closure relation	Reference	Equation	Remarks
Interface-to-liquid heat transfer	Analytis and Yadigaroglu (1987)	$q_{il} = h_{il}(T_{sat} - T_l)$ $h_{il} = 3.66\dfrac{k_l}{D-\delta}F$, for $\mathrm{Re}_l < 2000$ $h_{il} = 0.023\dfrac{k_l}{D-2\delta}\mathrm{Re}_l^{0.8}\,\mathrm{Pr}_l^{0.4}\,F$, for $\mathrm{Re}_l > 2000$ $\mathrm{Re}_l = \dfrac{\rho_l \lvert u_l \rvert (D-2\delta)}{\mu_l}$ and $F = 1 + 1.4\dfrac{R}{z}$	Interfacial velocity is equal to liquid velocity. However when calculating Re_l the liquid velocity is considered since the relative velocity between liquid and interface is zero.
	Cachard (1994)	$q'_{il} = h_{il}P_i(T_{sat} - T_l)$ $h_{il} = 3.66\dfrac{k_l}{D-\delta}$ for $\mathrm{Re}_l < 2000$ $h_{il} = \dfrac{\lvert \tau_i \rvert c_{p,l}}{\lvert u_l - u_i \rvert \mathrm{Pr}_l^{2/3}}$ for $\mathrm{Re}_l > 2000$	The largest value is used
	Hammouda (1996)	$q''_{il} = q''_{vi}\dfrac{T_v - T_{sat}}{T_{sat} - T_l}$	Based on the assumption that ($h_{vi} = h_{il}$). No enough justification is given in the analysis.
	The new model	$q_{il} = h_{il}(T_{sat} - T_l)$ $h_{il} = \begin{cases} 3.66\dfrac{k_l}{D-2\delta}F, & \mathrm{Re}_l < 2000 \\ 0.023\dfrac{k_l}{D-2\delta}\mathrm{Re}_l^{0.8}\,\mathrm{Pr}_l^{0.4}\,F, & \mathrm{Re}_l > 2000 \end{cases}$ $\mathrm{Re}_l = \dfrac{\rho_l \lvert u_l - u_i \rvert (D-2\delta)}{\mu_l}$ $F = 1 + 0.7\dfrac{D}{z}$	Same formulation as in Analytis and Yadigaroglu (1987) model but with Reynolds number calculated based on relative velocity between liquid and interface.

Table 7.1 (Continued)

Closure relation	Reference	Equation	Remarks
Vapor-to-interface heat transfer	Analytis and Yadigaroglu (1987)	$q''_{vi} = \frac{\lambda k_v Nu_v}{2\delta\left(1-\theta^{*2}\right)}\left[\left(T_v - T_{sat}\right) - \theta^*\left(T_w - T_v\right)\right]$ $\lambda = 1 + \frac{150\delta}{R}$	
	Cachard (1994)	$q'_{vi} = \lambda_{hv} \frac{k_v Nu_v}{2\delta\left(1-\theta^{*2}\right)} \frac{P_w + P_i}{2}\left[\left(T'_v - T_{sat}\right) - \theta^*\left(T_w - T'_v\right)\right]$	
	Hammouda (1996)	$q''_{vi} = q''_{wv} \frac{T_v - T_{sat}}{T_w - T_v}$	
	The new model	$q''_{vi} = q''_{wv} \frac{T_v - T_{sat}}{T_w - T_v}$	
Radiation heat transfer	Analytis and Yadigaroglu (1987)	$q''_{rad} = \frac{\sigma\left(T_w^4 - T_{sat}^4\right)}{\frac{1}{\varepsilon_l} + \frac{1}{\varepsilon_w} - 1}$	
	Cachard (1994)	$q'_{rad} = \frac{\sigma P_i\left(T_w^4 - T_{sat}^4\right)}{\frac{1}{\varepsilon_l} + \frac{P_i}{P_w}\left(\frac{1}{\varepsilon_w} - 1\right)}$ $\varepsilon_l = 0.96$; $\varepsilon_w = 1.979 \times 10^{-4} T_w + 0.5735$	
	Hammouda (1996)	$q''_{rad} = \frac{\sigma\left(T_w^4 - T_{sat}^4\right)}{\frac{1}{\varepsilon_l\sqrt{1-\alpha}} + \frac{1}{\varepsilon_w} - 1}$	
	The new model	$q''_{rad} = \frac{\sigma\left(T_w^4 - T_{sat}^4\right)}{\frac{1}{\varepsilon_l\sqrt{1-\alpha}} + \frac{1}{\varepsilon_w} - 1}$	

Table 7.1 (Continued)

Closure relation	Reference	Equation	Remarks
Wall shear stress	Analytis and Yadigaroglu (1987)	$\tau_w = \frac{f_w \rho_v u_v^2}{2}$ where $f_w = \frac{0.085}{\mathrm{Re}_v^{0.25}}$; $\mathrm{Re}_v = \frac{\rho_v u_v 2\delta}{\mu_v}$	
	Cachard (1994)	$\tau_w = \frac{f_w \rho_v u_v \lvert u_v \rvert}{2}$ where $f_w = \frac{24}{\mathrm{Re}_w}$, for $\mathrm{Re}_w < 2000$ and $f_w = \frac{0.085}{\mathrm{Re}_w^{0.25}}$, for $\mathrm{Re}_w > 2000$; $\mathrm{Re}_w = \frac{\rho_v \lvert u_v \rvert 2\delta}{\mu_v}$	
	Hammouda (1996)	$\tau_w = \frac{f_w}{2} \rho_v u_v^2$; Laminar flow: $f_w = \frac{24}{\mathrm{Re}_{wv}}$; $\mathrm{Re}_{wv} = \frac{\rho_v u_v 2\delta}{\mu_v}$; Turbulent flow: $f_w = \left(1 + 0.0925 r^*\right) f_c$; $\frac{1}{\sqrt{f_c}} = 1.7372 \ln\left[\frac{\mathrm{Re}_v}{1.964 \ln(\mathrm{Re}_v) - 3.8215}\right]$ $\mathrm{Re}_v = \frac{\rho_v u_v D_l}{\mu_v}$; $r^* = (1-\alpha)^{1/2}$; $D_l = \frac{1 + r^{*2} + \frac{1 - r^{*2}}{\ln(r^*)}}{(1 - r^*)^2} 2\delta$ For $\mathrm{Re}_v < 5\times 10^3$ or $\mathrm{Re}_v > 10^7$: $f_w = \frac{0.085}{\mathrm{Re}_{wv}^{0.25}}$	
	The new model	$\tau_w = f_w \rho_v \frac{u_v^2}{2}$ $f_w = \frac{0.085}{\mathrm{Re}_v^{0.25}}$ $\mathrm{Re}_v = \frac{\rho_v u_v (2\delta)}{\mu_v} = \frac{\rho_v u_v D\left(1 - \sqrt{1-\alpha}\right)}{\mu_v}$	

Table 7.1 (Concluded)

Closure relation	Reference	Equation	Remarks
Interfacial shear stress	Analytis and Yadigaroglu (1987)	$\tau_i = \frac{f_i \rho_v u_v^2}{2}\lambda$; $f_i = \frac{0.085}{\mathrm{Re}_i^{0.25}}$; $\mathrm{Re}_i = \frac{\rho_v u_v 2\delta}{\mu_v}$	$u_i = u_l$
	Cachard (1994)	$\tau_{vi} = f_{vi}\rho_v \lvert u_v - u_i \rvert \frac{(u_v - u_i)}{2}$; $\tau_{il} = \tau_{vi}$ $f_{vi} = \lambda_{fv}\frac{24}{\mathrm{Re}_{vi}}$; $\mathrm{Re}_{vi} = \rho_v \lvert u_v - u_i \rvert \frac{2\delta}{\mu_v}$; $\lambda_{fv} = 0.036\left\{\delta\left[\frac{\rho_v(\rho_l - \rho_v)g}{\mu_v^2}\right]^{\frac{1}{3}}\right\}^{1.96}$	
	Hammouda (1996)	$\tau_i = \tau_w$	Simplification of momentum equation
	The new model	$\tau_{vi} = f_{vi}\rho_v \lvert u_v - u_i \rvert \frac{u_v - u_i}{2}$ $f_{vi} = \frac{0.085}{\mathrm{Re}_{vi}^{0.25}}$; $\mathrm{Re}_{vi} = \frac{\rho_v \lvert u_v - u_i \rvert D\left(1 - \sqrt{1-\alpha}\right)}{\mu_v}$ $\tau_{il} = -f_{il}\rho_l \lvert u_l - u_i \rvert \frac{u_l - u_i}{2}$ $f_{il} = \begin{cases} \frac{16}{\mathrm{Re}_{li}}, & \mathrm{Re}_{li} < 2000 \\ \frac{0.085}{\mathrm{Re}_{li}^{0.25}}, & \mathrm{Re}_{li} > 2000 \end{cases}$ $\mathrm{Re}_{li} = \frac{\rho_l \lvert u_l - u_i \rvert D\sqrt{1-\alpha}}{\mu_l}$	

CHAPTER 8 MODEL ASSESSMENT

8.1. General

The new model described in Chapter 7 is expected to predict the parametric trends correctly. It is also intended to predict the heat transfer in the IAFB regime accurately covering a wide range of flow conditions. The observed parametric effects on film boiling heat transfer are explained in Chapter 4. Further discussion of these effects is given in Chapter 6 as a part of the experimental program for this thesis.

During the analysis, the limit for terminating the model prediction is set to be for a void fraction of 0.5. The model's prediction is not extended beyond this point to maintain accurate results. So the model excludes predicting heat transfer region IV (Figure 6.1).

The model is assessed by:

- examining the effect of flow parameters (pressure, mass flux, heat flux and inlet quality) on predicted heat transfer coefficient,
- comparing the predicted wall temperatures and heat transfer coefficient distribution in Freon 134a as described in Section 6 to corresponding experimental values,
- comparing actual quality as predicted by the model with equilibrium quality and the effect of flow parameters on the relation between these two values,
- performing a sensitivity analysis on the model,
- comparing the new model's predictions with the predictions of other models, and
- comparing the predicted wall temperatures and heat transfer coefficient distribution to the corresponding experimental values obtained in water.

8.2. Examination of the Predicted Parametric Trends of the New Model

8.2.1. Effect of inlet subcooling and quality

Figure 8.1 shows the effect of inlet subcooling on heat transfer coefficient as predicted by the new model at different flow conditions. The figure shows that increasing inlet subcooling results in shifting the heat transfer coefficient curve to lower qualities while keeping the shape of curve intact. Another observation from the figure is that at high pressure and mass flux, the predicted minimum heat transfer coefficient (between region I and II, see Figure 6.1) decreases with increasing inlet subcooling which is previously observed from experiment (Section 6.7). It is clear that inlet subcooling strongly affects the region just downstream of the CHF location. At locations further downstream, the inlet subcooling effect gradually disappears and the heat transfer curves for different inlet subcoolings collapse on a single curve

The effect of local quality on predicted heat transfer coefficient can also be observed from Figure 8.1. Two trends can be identified.

- At low pressure and low mass flux, and as quality increases, the predicted heat transfer coefficient decreases (region I) then becomes more or less constant (region III).
- At high pressure and high mass flux, the predicted heat transfer coefficient drops sharply (region I) then increases steeply (region II) and finally levels off with little increase or decrease (region III).

The heat transfer region predicted by the model are in agreement with the University of Ottawa observed trends described in Chapter 6 and other reported studies.

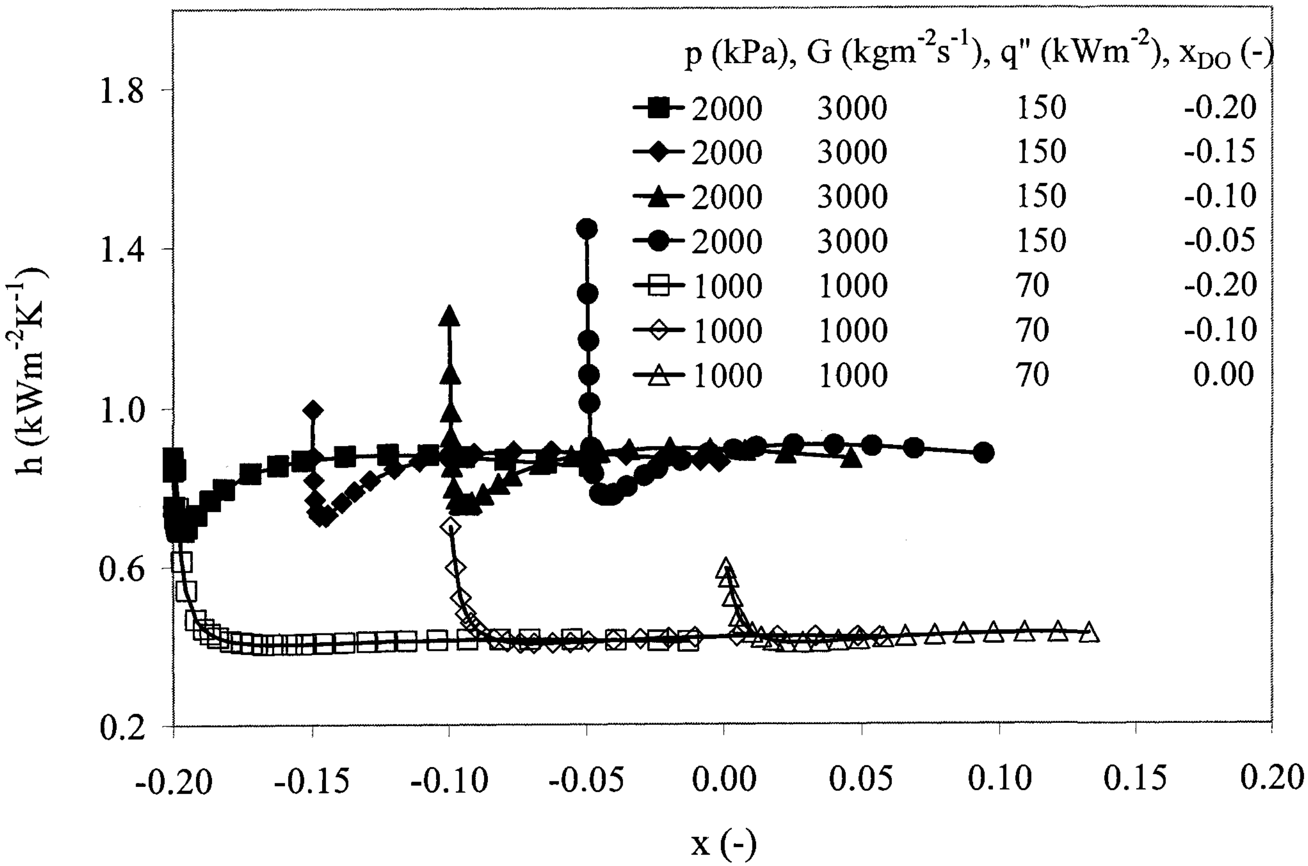

Figure 8. 1 Inlet subcooling effect on predicted heat transfer coefficient at different flow conditions.

Figures 8.2 and 8.3 show comparisons between measurement and model predictions of wall temperatures and heat transfer coefficients. The model correctly predicts these values with some discrepancy in predicting the near CHF region.

8.2.2. Effect of pressure

Figure 8.4 shows the effect of pressure on predicted heat transfer coefficient vs. quality at two different mass fluxes. The figure clearly shows that the model correctly predicts this effect: as explained in Section 6.3, the heat transfer coefficient increases with increasing pressure. The figure also shows that region II starts to appear as pressure increases. The presence of region II becomes more pronounced at high mass flux. This is in agreement with the observed effect of pressure on heat transfer coefficient.

Figures 8.5 and 8.6 compare measurements to predicted values of wall temperatures and heat transfer coefficient. The model prediction is in good agreement with experimental results. Some discrepancies are observed in the figures between measurements and predictions at high pressures for locations just downstream of the CHF location.

8.2.3. Effect of mass flux

Figure 8.7 shows the effect of mass flux on the predicted heat transfer coefficient vs. quality curves. The new model correctly predicts an increase in heat transfer coefficient increases with increasing mass flux. Figure 8.7 shows that the existence of heat transfer region II becomes evident at high mass flux. The same observation is supported by experimental data as explained in Section 4.6 and Chapter 6.

Comparisons between predicted and measured values of wall temperatures and heat transfer coefficients with varying mass flux as a parameter are shown in Figures 8.8 and

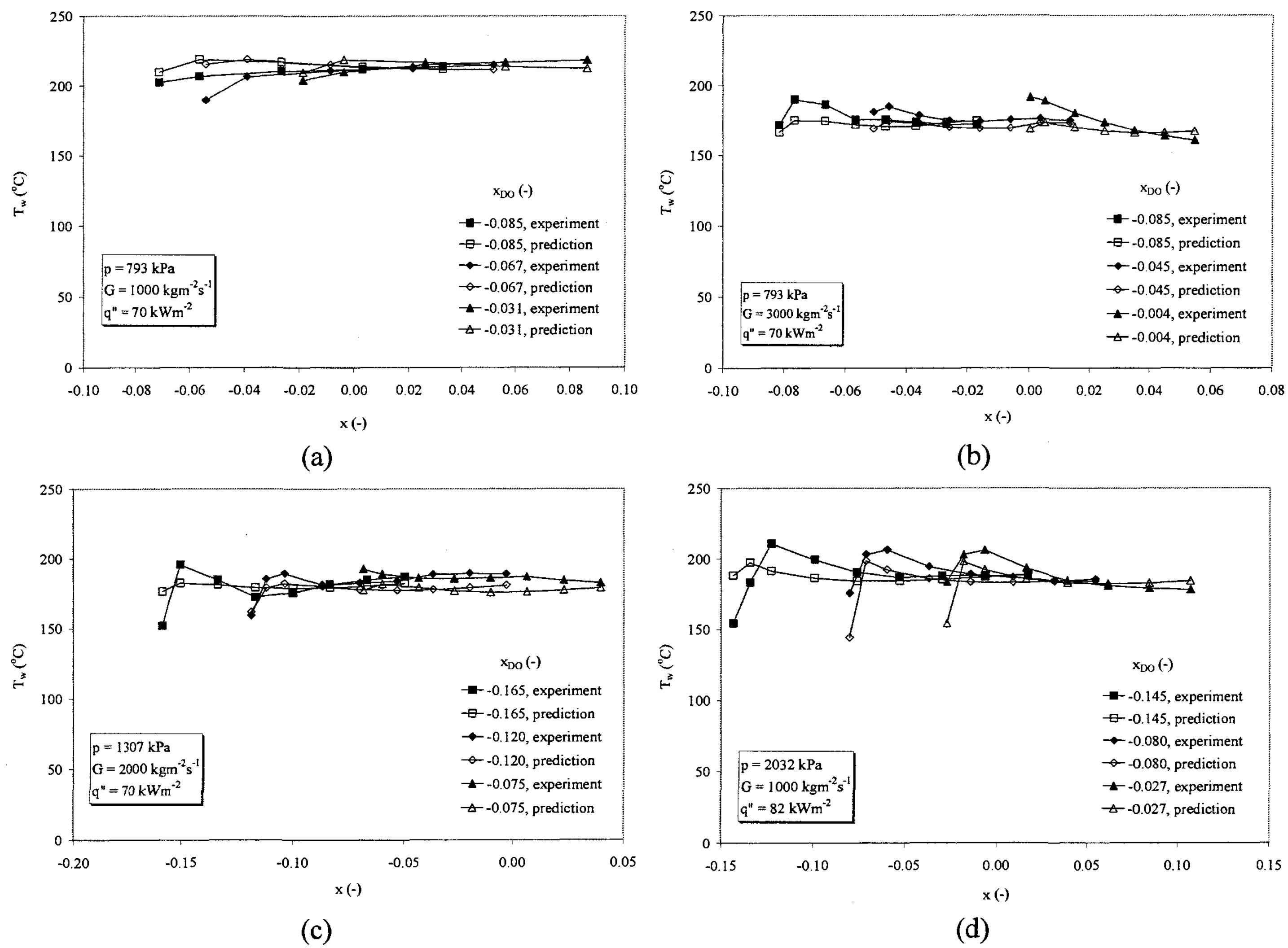

Figure 8. 2 Comparison between model predictions of wall temperature and data from Figure 6.7.

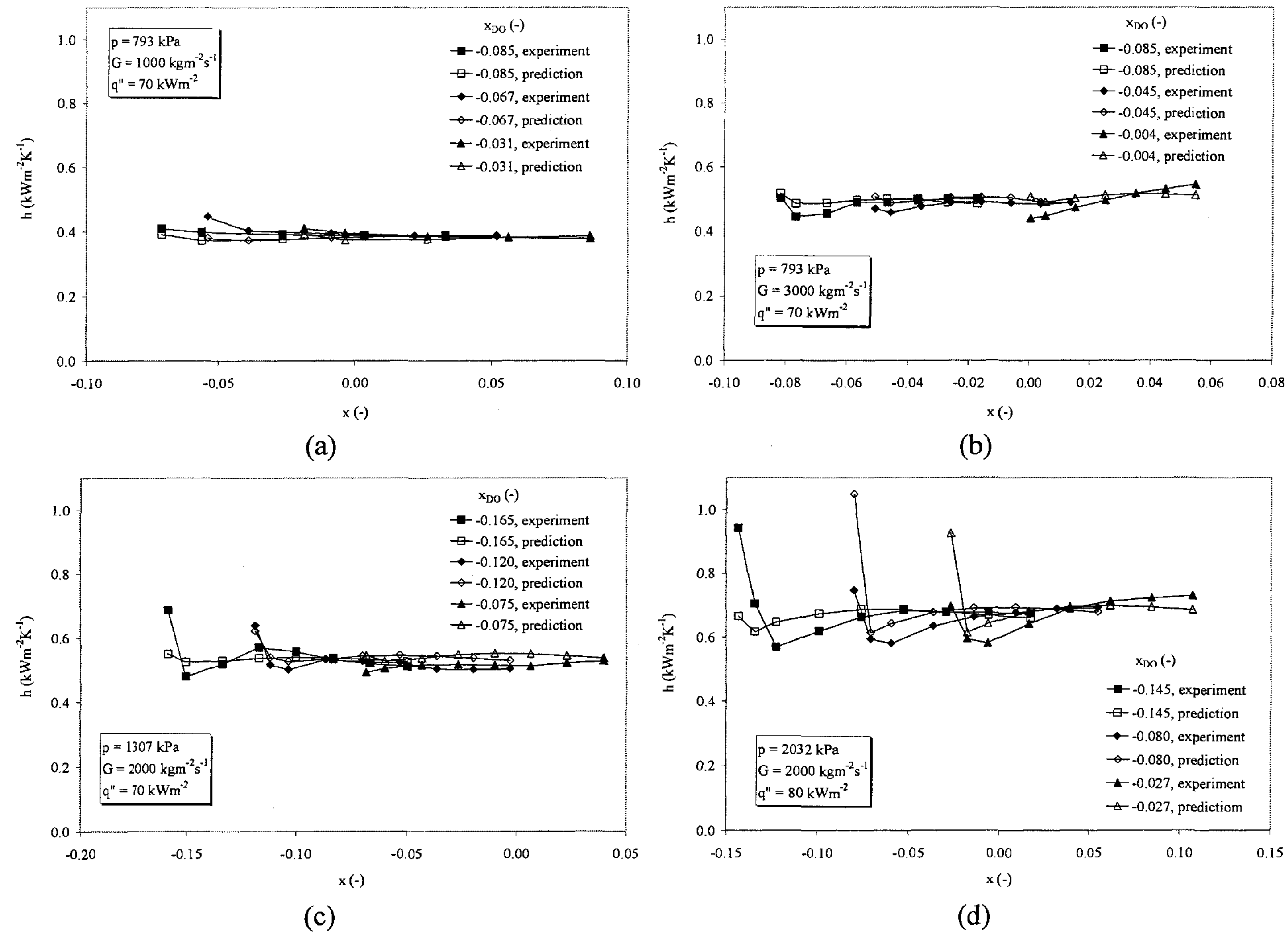

Figure 8. 3 Comparison between model predictions of heat transfer coefficient and data from Figure 6.7.

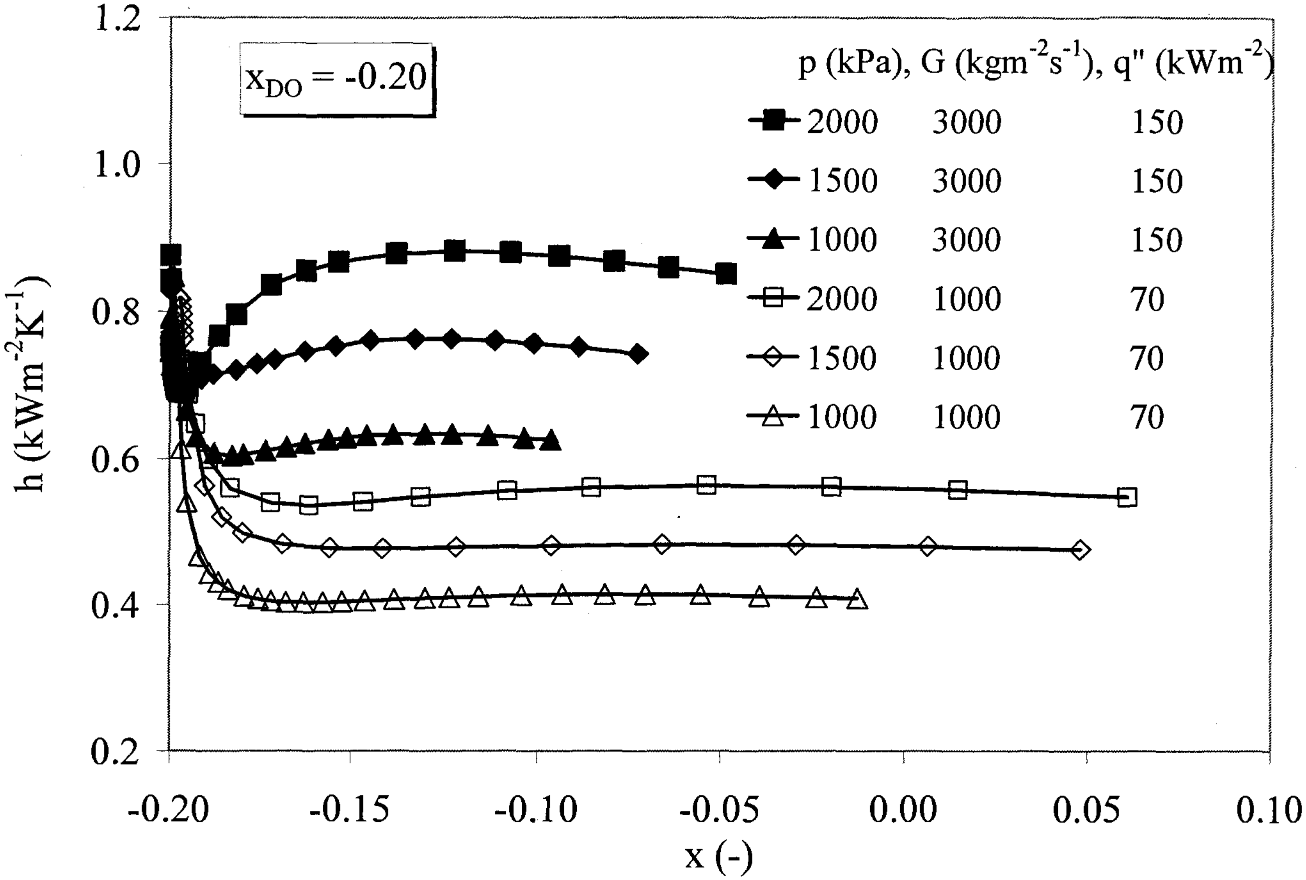

Figure 8. 4 Pressure effect on predicted heat transfer coefficient at different flow conditions.

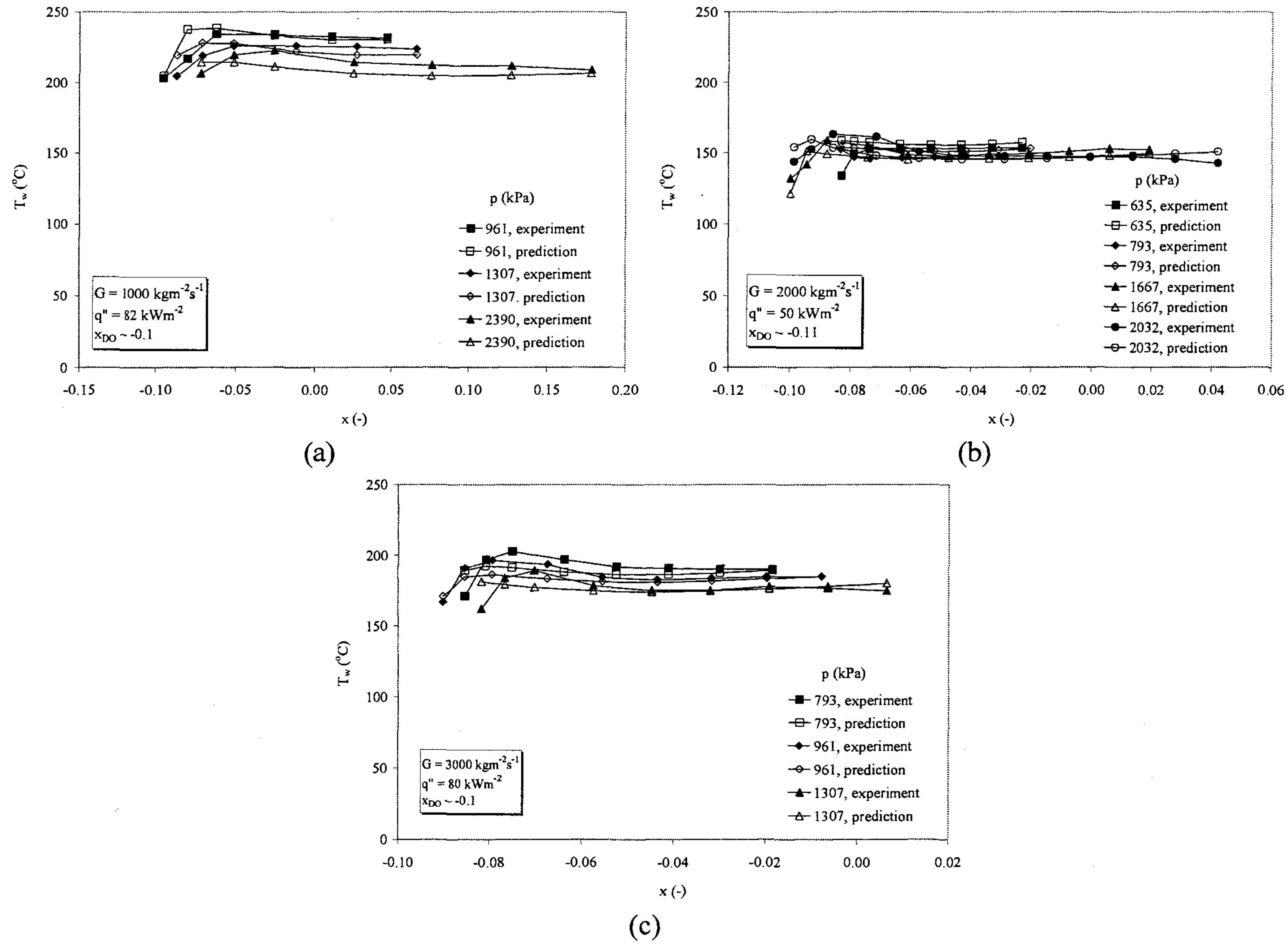

Figure 8. 5 Comparison between model predictions of wall temperature and data from Figure 6.3.

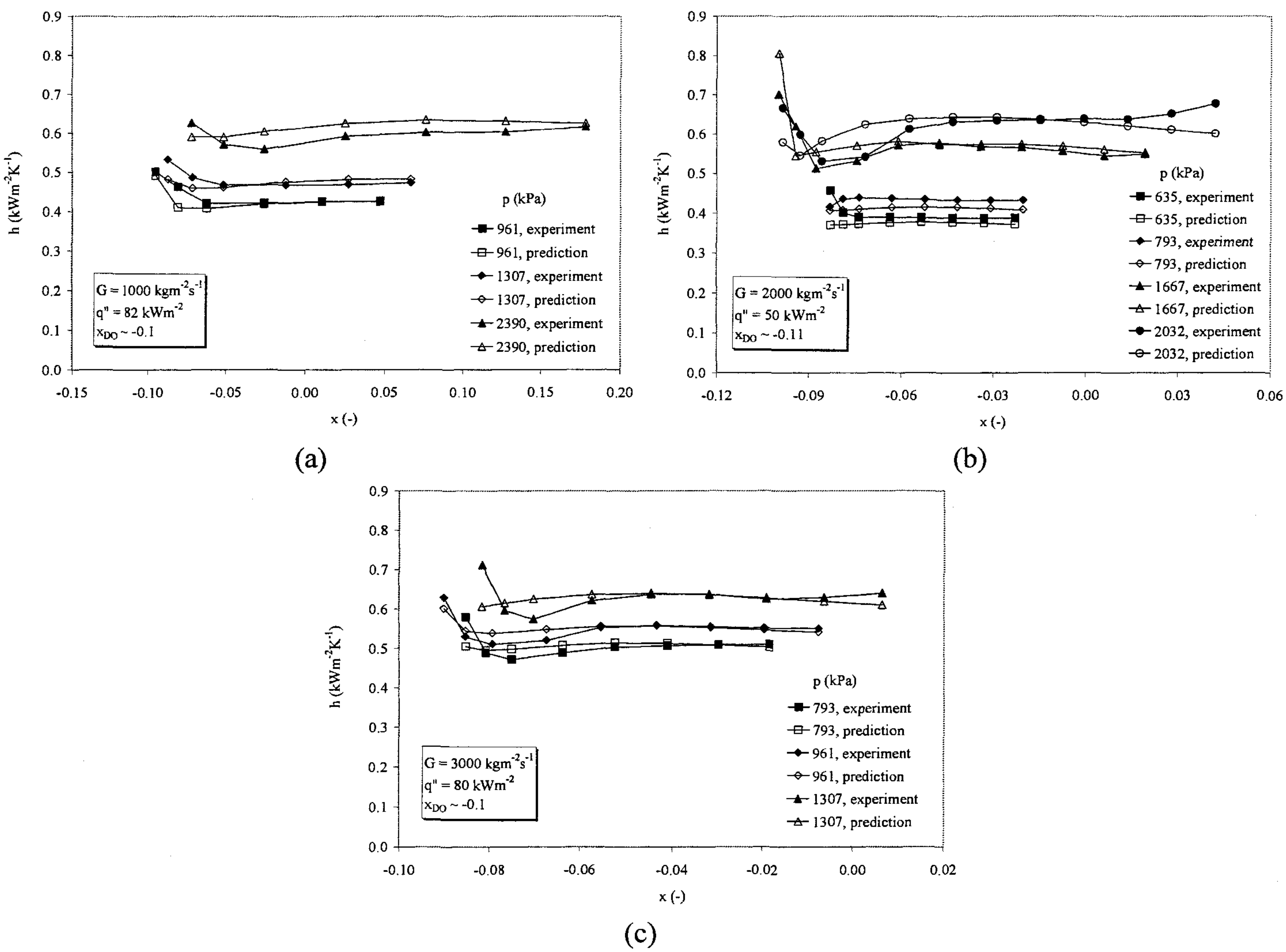

Figure 8. 6 Comparison between model predictions of heat transfer coefficient and data from Figure 6.3.

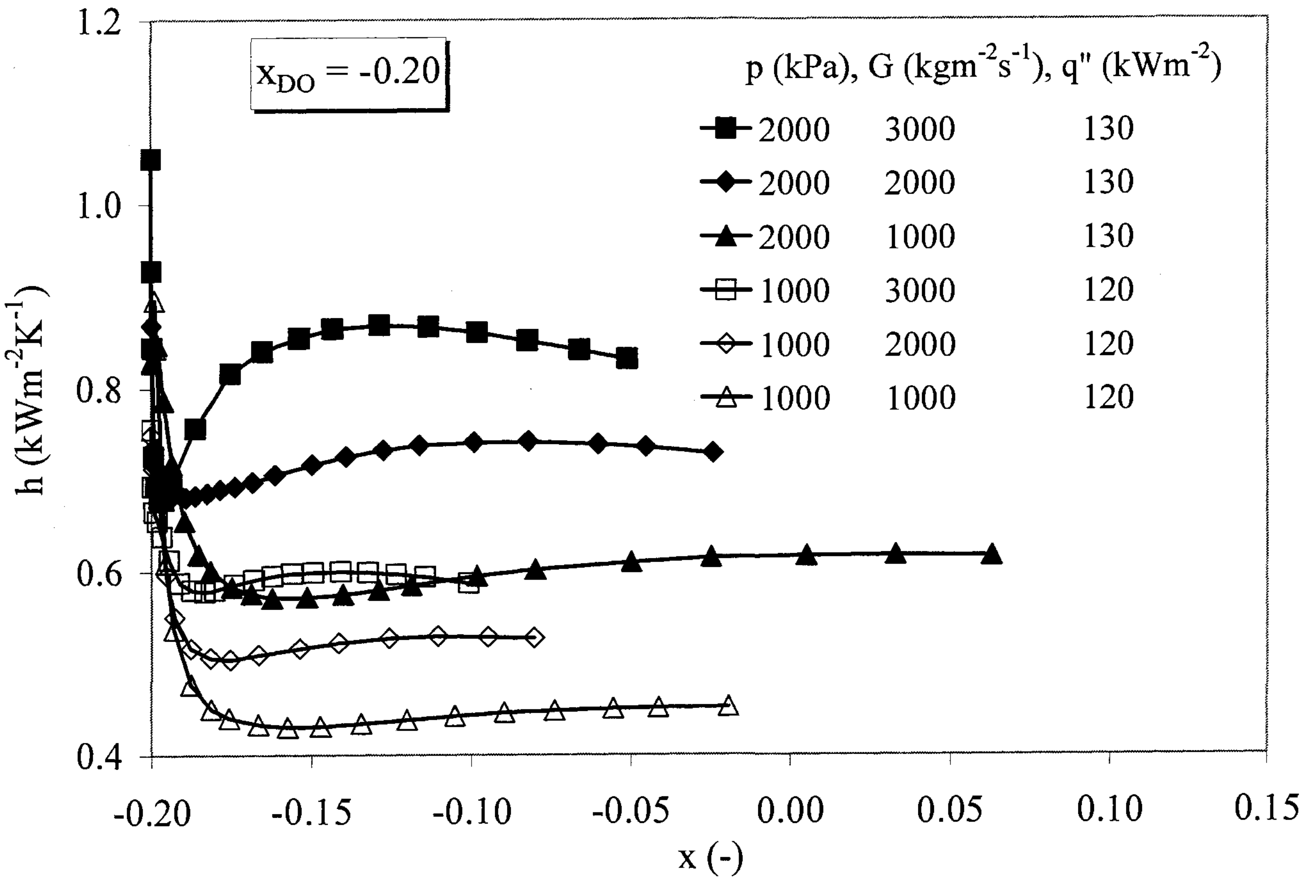

Figure 8. 7 Effect of mass flux on predicted heat transfer coefficient at different flow conditions.

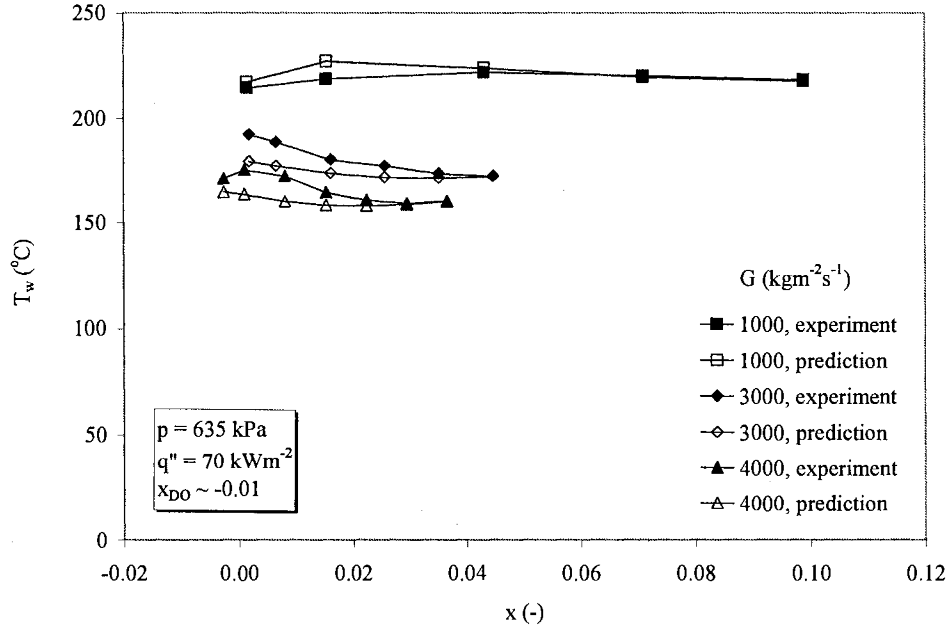

(a)

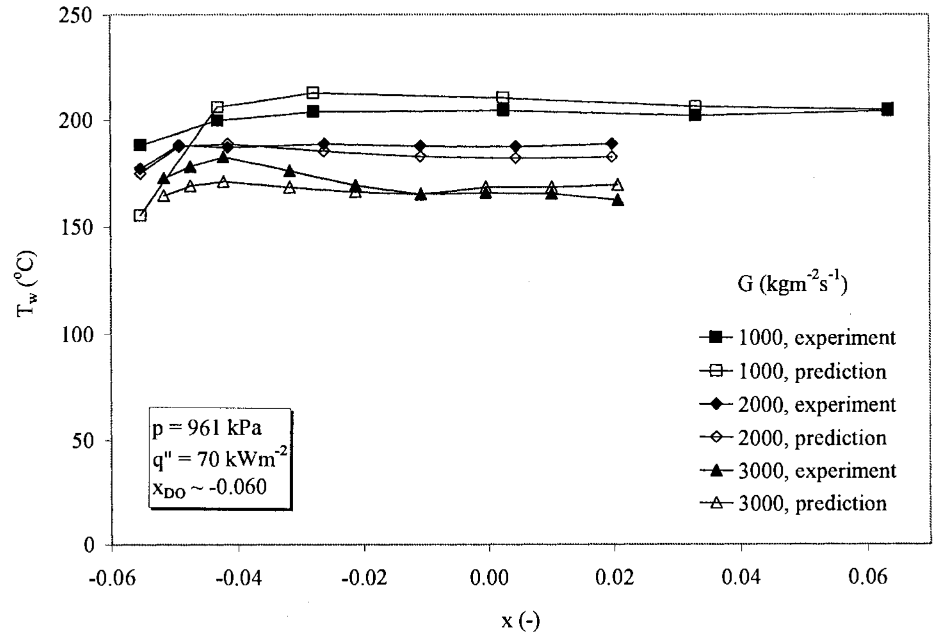

(b)

Figure 8. 8 Comparison between model predictions of wall temperature and data from Figure 6.5.

8.9. It is clear from these figures that the model predicts wall temperatures and heat transfer coefficients for all values of mass flux.

8.2.4. Effect of heat flux

The effect of heat flux on predicted heat transfer coefficient is shown in Figure 8.10. Varying heat flux level has a weak effect on the predicted heat transfer coefficient. This effect is demonstrated by the slight increase in predicted heat transfer coefficient with increasing heat flux. Compared to the measurements, the model shows a stronger heat flux effect on heat transfer coefficient at high pressures and high mass fluxes. An explanation of the effect of heat flux on heat transfer coefficient is given in Sections 4.4 and 6.6. This observation is consistent with the findings in Chapter 6, and reported observations of Hammouda (1996) and Mosaad and Johannsen (1989).

Figures 8.11 and 8.12 compare the effect of heat flux on predicted and measured wall temperature and heat transfer coefficient at different pressures and mass fluxes. The model predictions are in good agreement with the data. As expected the data and predictions show that the wall temperatures are higher for higher heat fluxes.

8.2.5. Effect of diameter

The effect of diameter on film boiling heat transfer has not received much attention in the open literature. An examination of the diameter effect on heat transfer coefficient in IAFB heat transfer is needed in order to assess the capability of the model in predicting IAFB heat transfer for different tube diameters. The relation between diameter and heat transfer coefficient can be derived based on

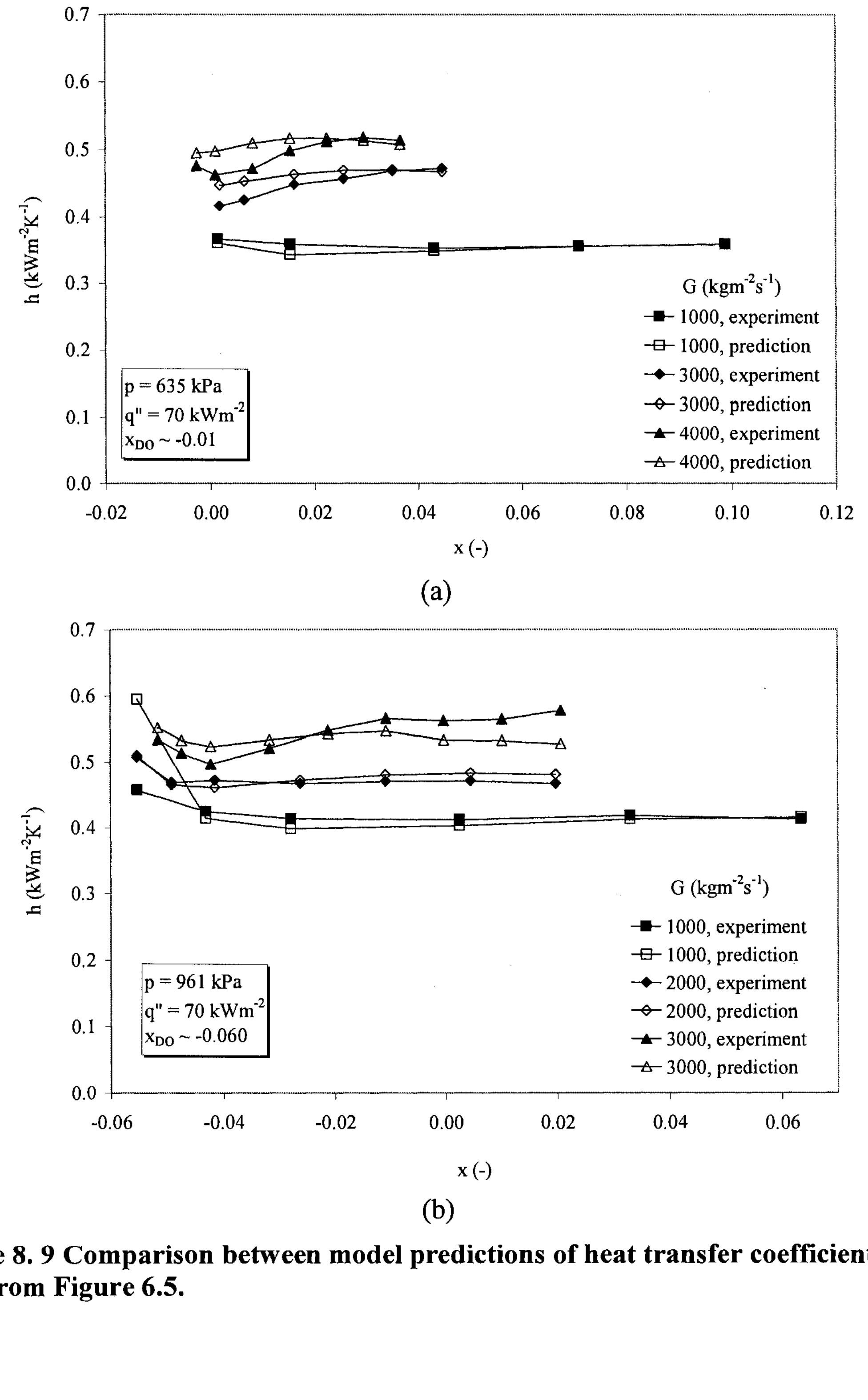

Figure 8. 9 Comparison between model predictions of heat transfer coefficient and data from Figure 6.5.

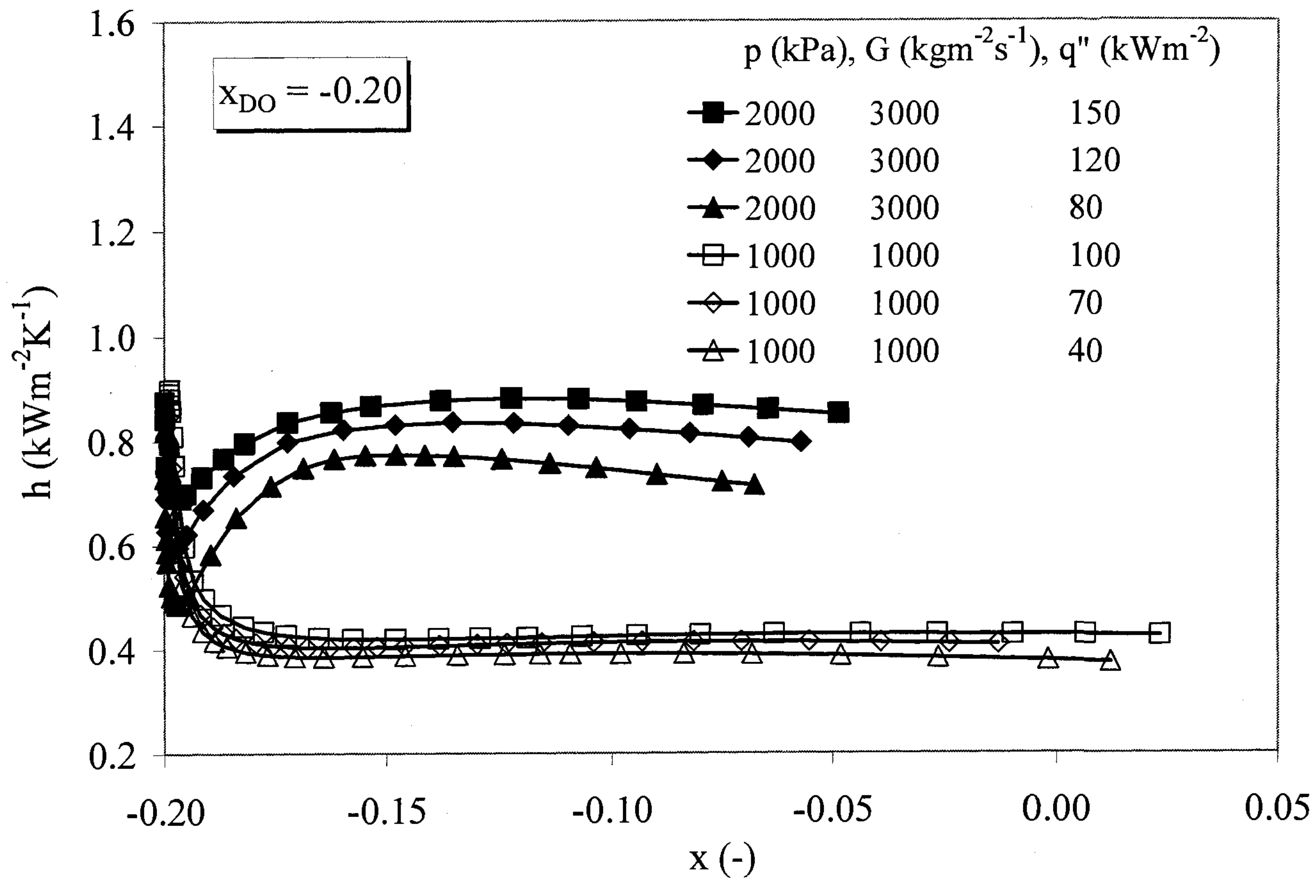

Figure 8. 10 Effect of heat flux on predicted heat transfer coefficient at different flow conditions

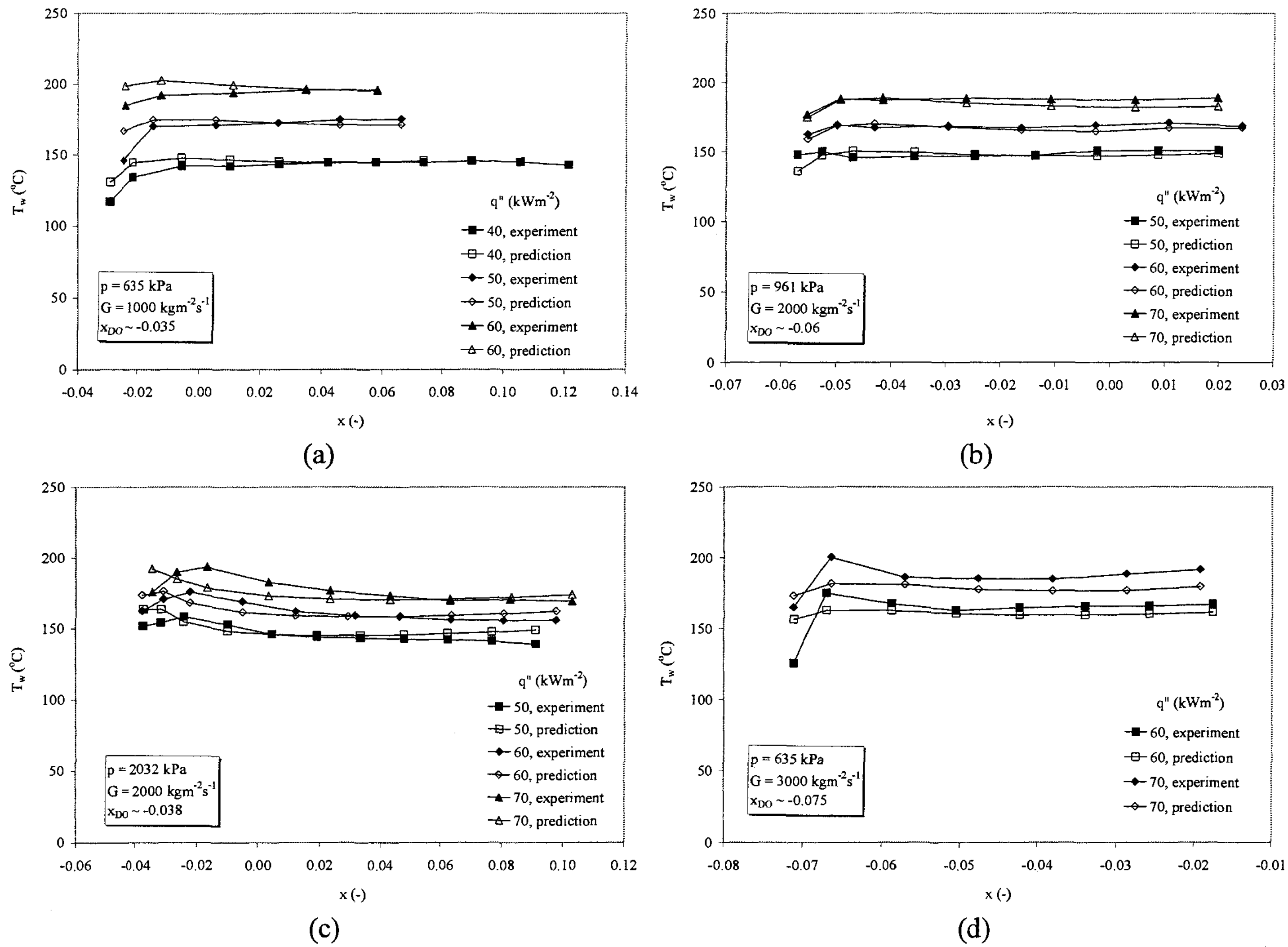

Figure 8. 11 Comparison between model predictions of wall temperature and data from Figure 6.6.

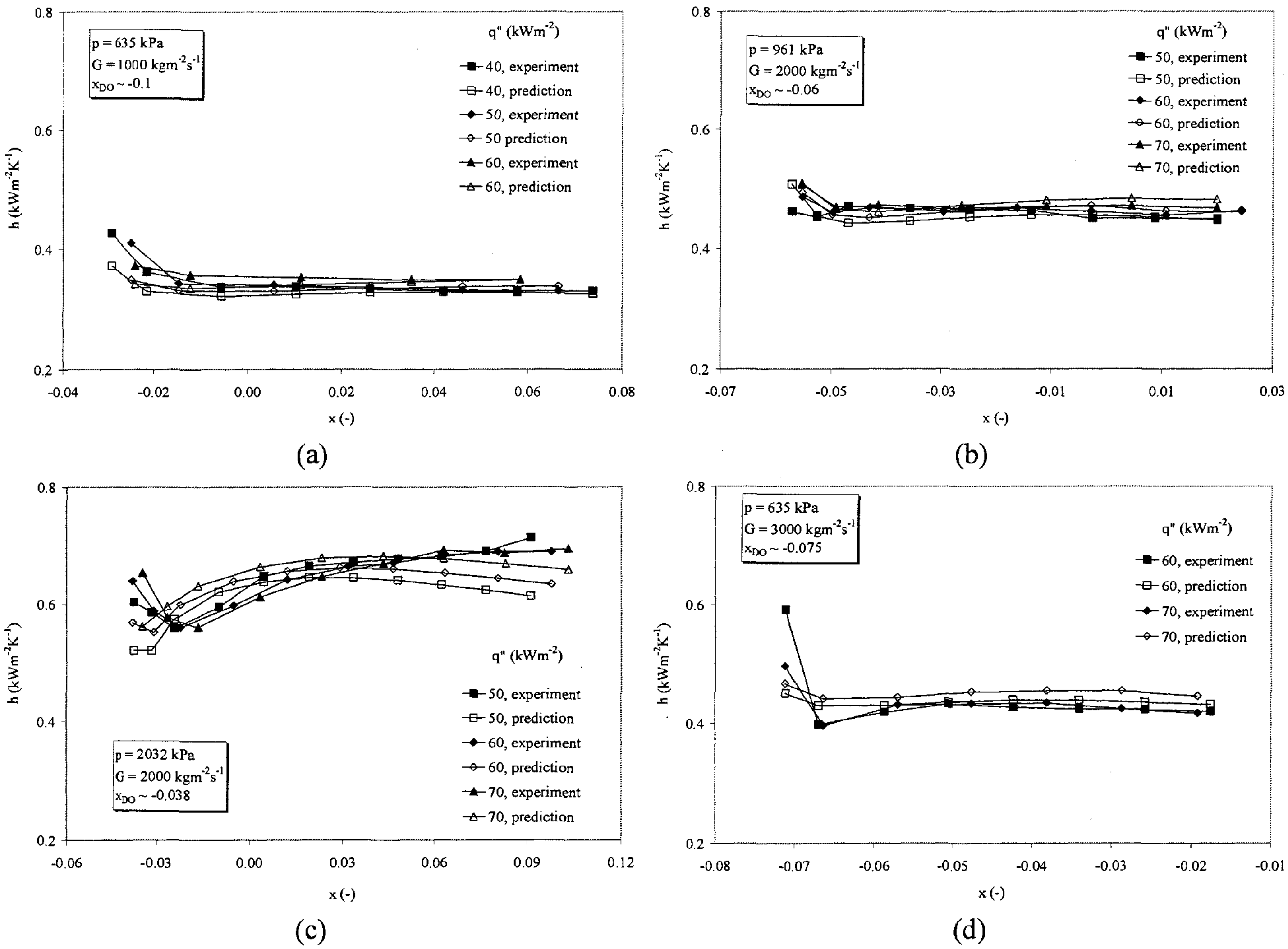

Figure 8. 12 Comparison between model predictions of heat transfer coefficient and data from Figure 6.6.

$$Nu = \frac{hD}{k} = C\,\mathrm{Re}^a\,\mathrm{Pr}^b \tag{8.1}$$

This would yield

$$\frac{h_{D_2}}{h_{D_1}} = \left(\frac{\mathrm{Re}_2}{\mathrm{Re}_1}\right)^a \left(\frac{\mathrm{Pr}_2}{\mathrm{Pr}_1}\right)^b \frac{D_1}{D_2} \tag{8.2}$$

Considering $\mathrm{Re} = \frac{GD}{\mu}$ and for same mass flux and pressure, the Equation (8.2) can be simplified to

$$h_{D_2} = \left(\frac{D_1}{D_2}\right)^{1-a} h_{D_1} \tag{8.3}$$

The coefficient a is usually considered to be around 0.8 (from the Dittus-Boelter equation). This gives a qualitative indication of the diameter effect on heat transfer coefficient. From Equation (8.3) it can be seen that the heat transfer coefficient increases as the tube diameter is reduced.

Figure 8.13 shows the effect of varying tube diameter on predicted heat transfer coefficient. The new model prediction is in agreement with the expected diameter effect. This trend spreads over a relatively wide range of diameters. However, the model prediction of diameter effect becomes weaker at larger diameters. No experimental data are available to verify this effect.

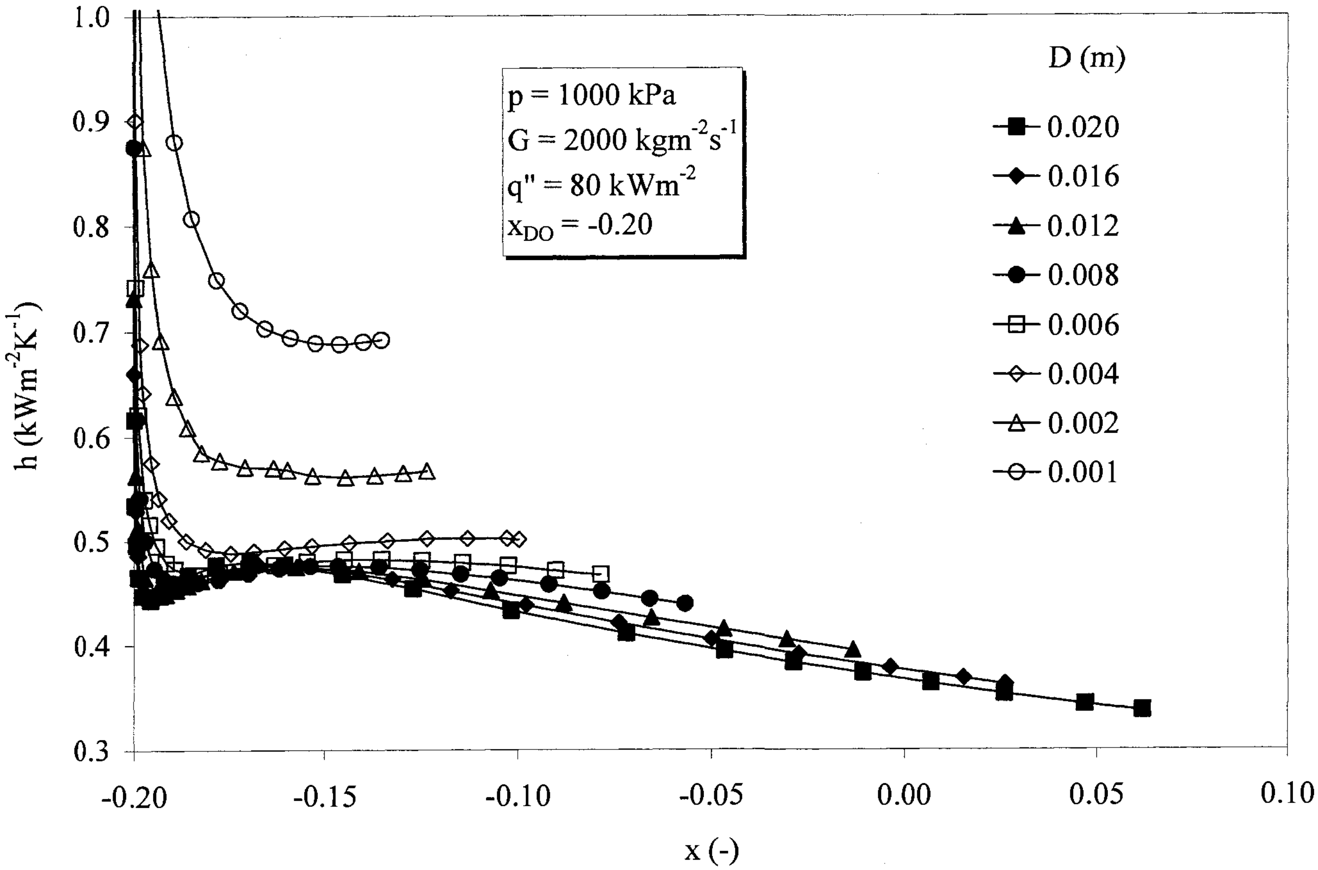

Figure 8. 13 Diameter effect on model prediction of heat transfer coefficient.

8.3. Assessment of Other Model Parameters

8.3.1. Prediction of actual quality and thermodynamic non-equilibrium

The new model is derived based on the assumption of thermal non-equilibrium in the inverted annular flow regime. As a quantitative measure of thermal non-equilibrium, the predicted actual quality is compared to equilibrium quality. Actual quality (or thermodynamic non-equilibrium quality) is related to void fraction through the relation:

$$\alpha = \frac{x_a}{x_a + S\frac{\rho_v}{\rho_l}(1 - x_a)} \tag{8.4}$$

where S is the slip ratio defined as the ratio of vapor to liquid velocities. The results of x_a vs. x comparisons are shown in Figures 8.14 – 8.17 for the different values of pressure, mass flux, heat flux and inlet subcooling. The figures also show the effect of these flow parameters on predicted vapor temperature vs. non-equilibrium quality, vapor film thickness and void fraction which are connected to the actual quality via Equation (8.4). Pressure, heat flux and mass flux have little effect on the thermodynamic non-equilibrium. The thermodynamic non-equilibrium is lower for higher pressure, and lower for higher heat flux. The effect of inlet subcooling (or quality at CHF, since the CHF location is close to the inlet) on the thermodynamic non- equilibrium is similar to that of pressure. At higher inlet subcooling, the vapor superheat decreases, resulting in lower thermal non-equilibrium. The model does not show any specific trend for the effect of mass flux on thermodynamic non-equilibrium.

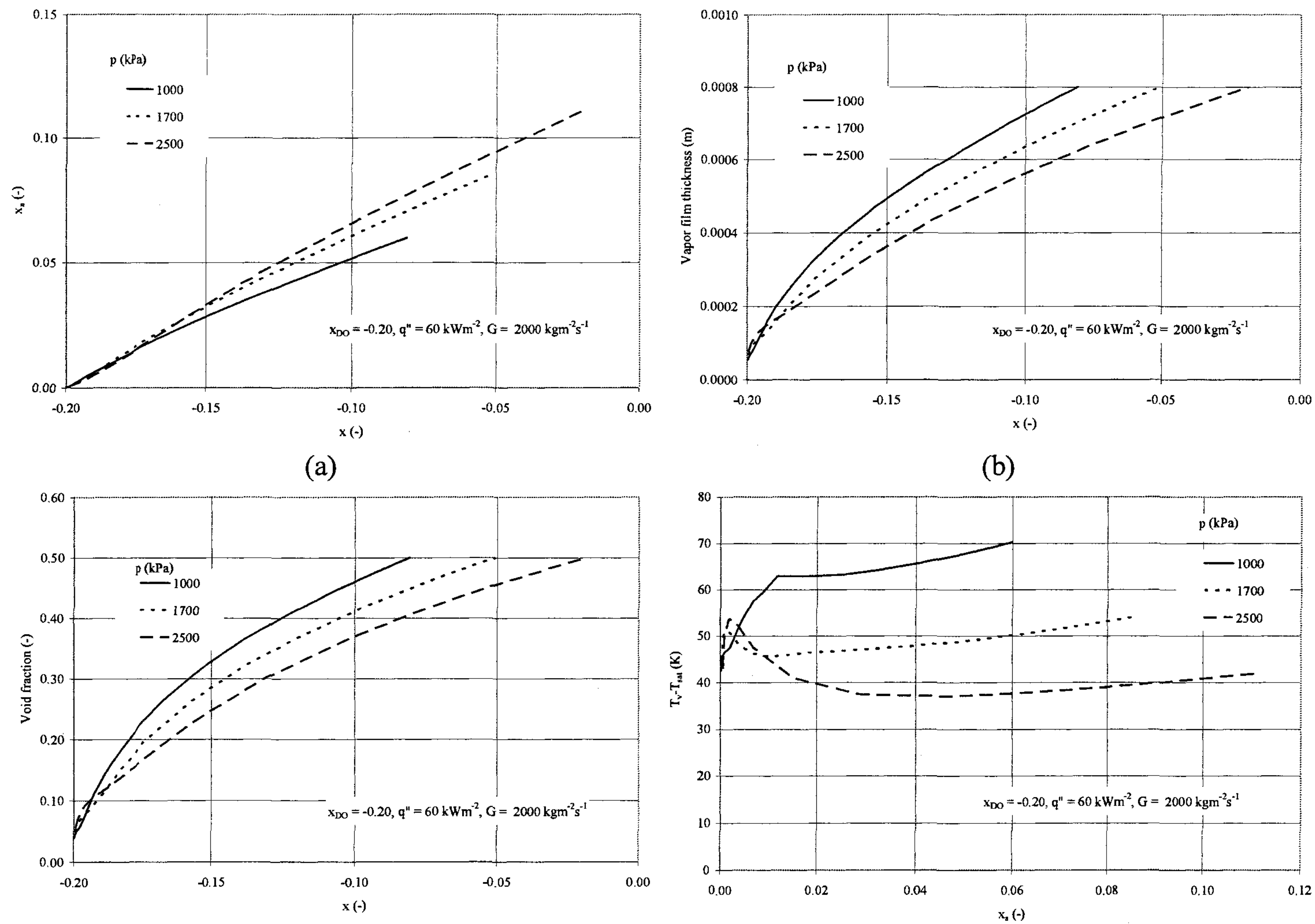

(a) (b) (c) (d)

Figure 8. 14 Effect of pressure on predicted (a) x_a, (b) vapor film thickness, (c) α, and (d)T_v-T_{sat} vs. x_a.

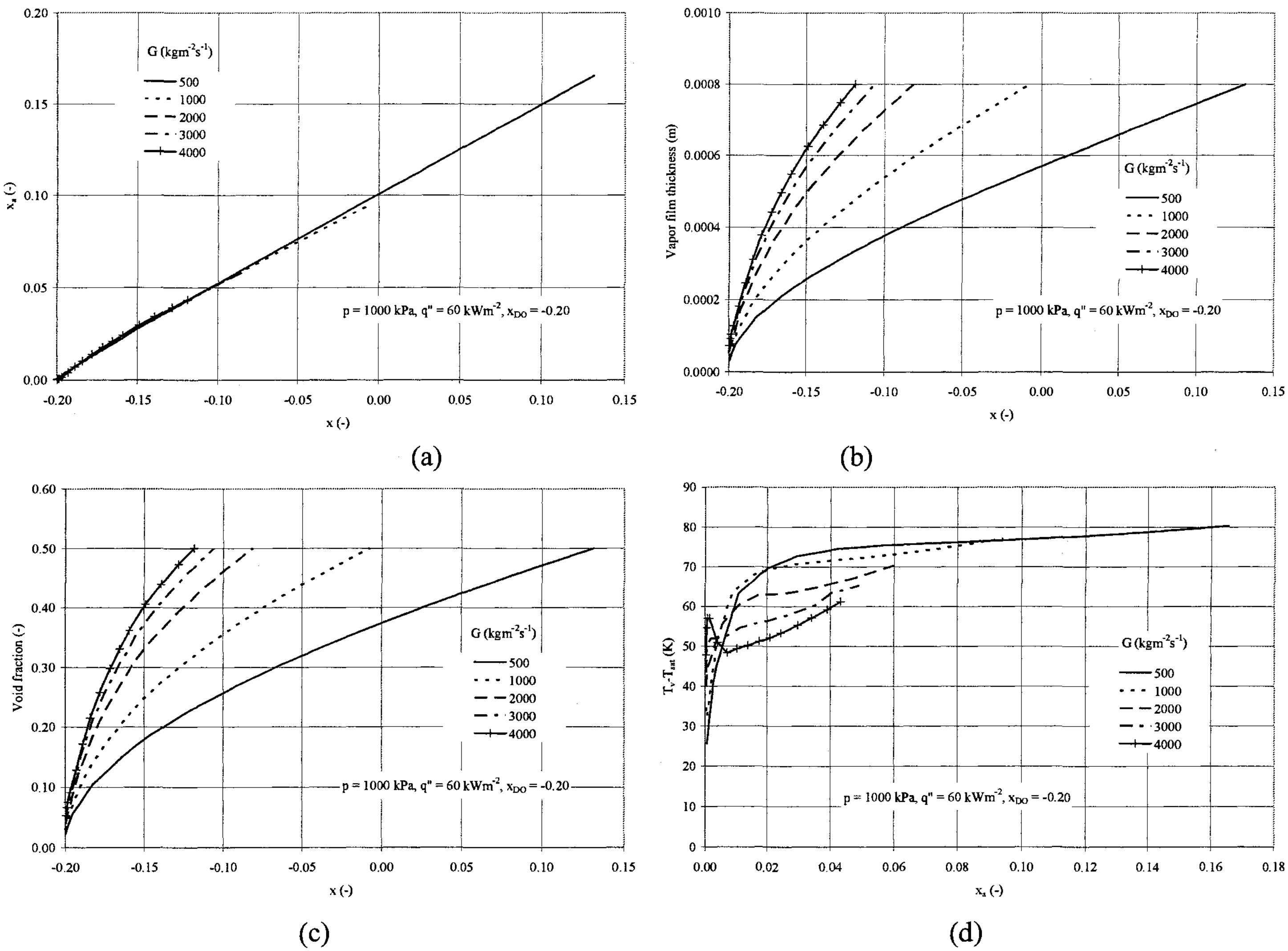

Figure 8. 15 Effect of mass flux on predicted (a) x_a, (b) vapor film thickness, (c) α, and (d)T_v-T_{sat} vs. x_a.

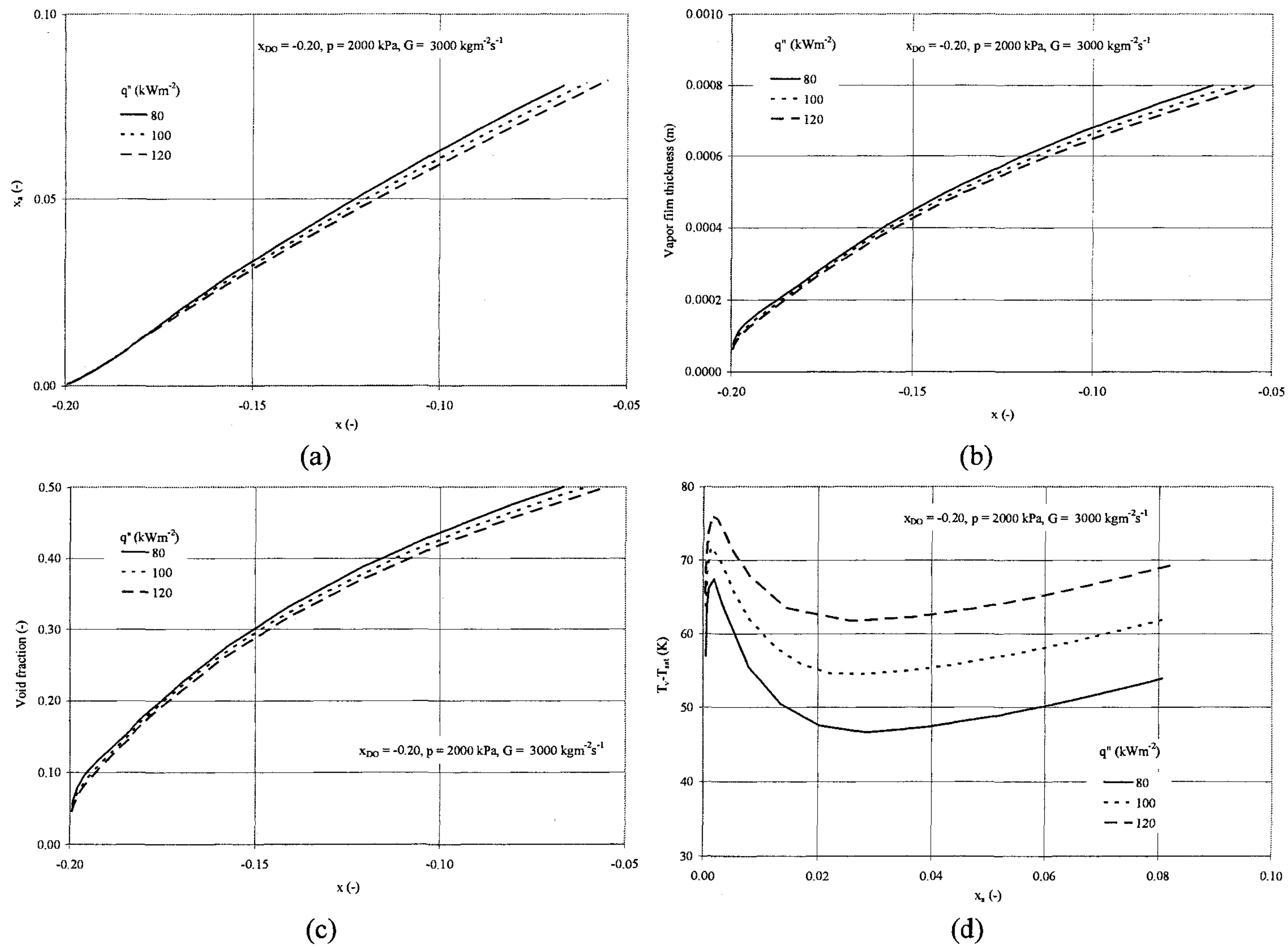

Figure 8. 16 Effect of heat flux on predicted (a) x_a, (b) vapor film thickness, (c) α, and (d)T_v-T_{sat} vs. x_a.

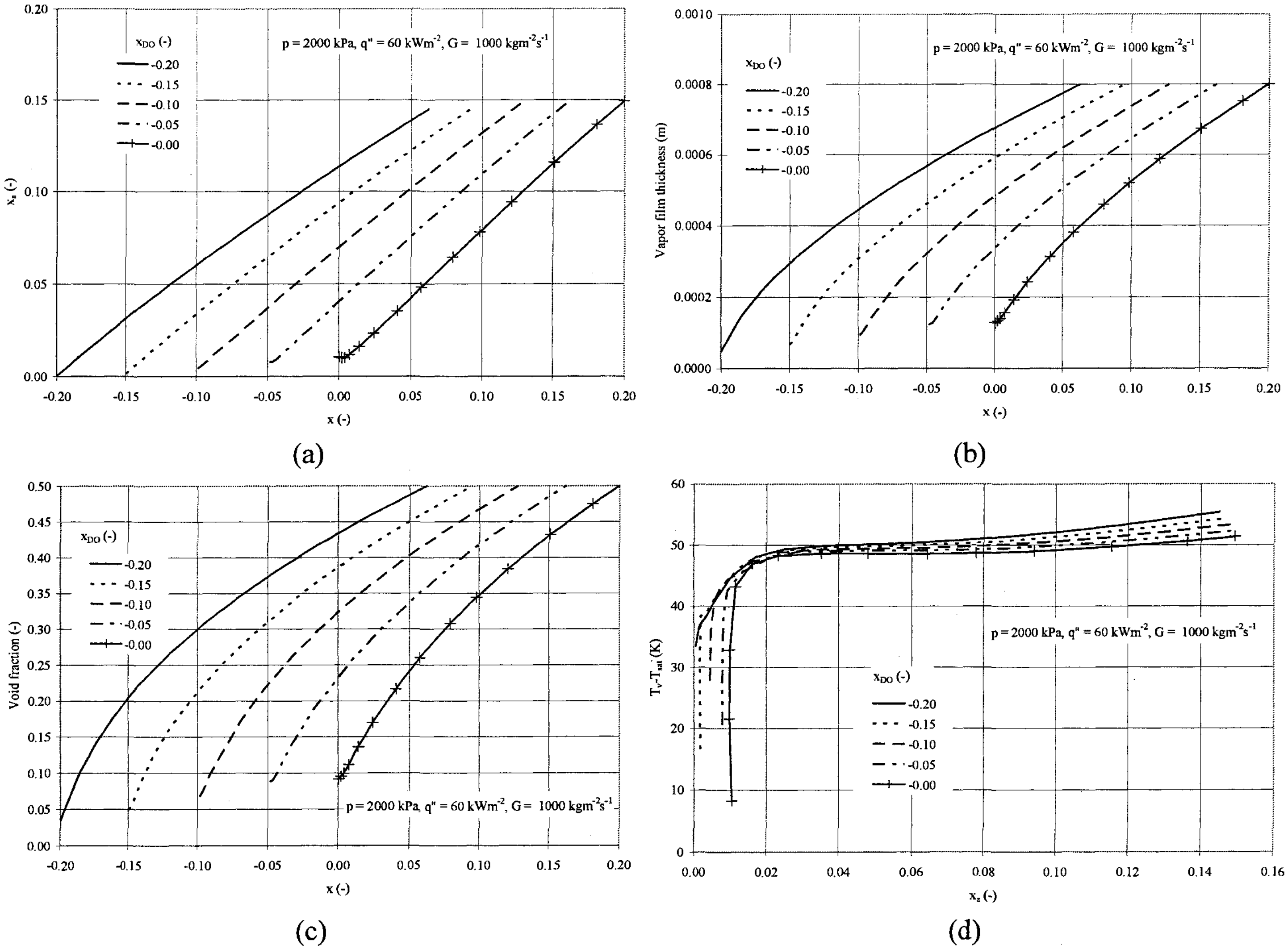

Figure 8. 17 Effect of inlet subcooling on predicted (a) x_a, (b) vapor film thickness, (c) α, and (d) T_v-T_{sat} vs. x_a.

The model predicts the effect of flow parameters on vapor film thickness and void fraction in the same manner due to the relation between these two values:

$$\delta = R\left(1-\sqrt{1-\alpha}\right) \tag{7.31}$$

Figure 8.14b shows that as pressure increases, the predicted vapor film thickness (and void fraction in Figure 8.14c) decreases. The reduction in vapor film thickness results in increased heat transfer coefficient due to the inverse proportionality between these values:

$$h_v \propto \frac{k_v}{\delta^{0.2}} \tag{8.5}$$

The model also shows a decrease in predicted vapor superheat (Figure 8.14d) as pressure is increased. This provides additional explanation for the observed higher heat transfer coefficient at higher pressures ($h = q''/\Delta T$).

Increasing the mass flux (Figure 8.15b, c) increases the predicted vapor film thickness. This might be attributed to the increase in heat transfer rate between the heated wall and vapor-liquid interface which results in consuming the liquid core. The effect of increasing mass flux on the predicted vapor temperature vs. non-equilibrium quality (Figure 8.15d) is similar to pressure effect.

The model shows a weak relation between heat flux and vapor film thickness as demonstrated in Figure 8.16b. However, the predicted vapor film thickness decreases with increasing heat flux. This could be explained by Figure 8.16d. As heat flux is increased, the predicted vapor temperature increases. This implies that a larger fraction of the wall heat flux is used to heat-up the vapor film and a smaller fraction will be available to heat up and evaporate the liquid core.

The effect of inlet subcooling on predicted vapor film thickness is shown in Figure 8.17b. As the figure shows, increasing inlet subcooling results in shifting the curves to lower qualities. It also affects the initial vapor film thickness which becomes thinner at higher inlet subcooling. However the effect of inlet subcooling on predicted vapor temperature stays small (Figure 8.17d).

8.3.2. Prediction of vapor temperature

The vapor temperature is expected to be lower than the vapor film temperature which is calculated as

$$T_{vf} = \frac{T_w + T_{sat}}{2} \tag{8.6}$$

Figure 8.18 shows a comparison between vapor film temperature calculated by Equation (8.6) and predicted vapor temperature, for low and high mass fluxes. The figure shows clearly that vapor temperature is lower than vapor film temperature. It also shows that at high mass flux, the two temperature values are closer than at lower mass flux. This might be explained as a result of lower wall temperature at higher mass fluxes.

8.3.3. Prediction of vapor, liquid and interfacial velocity

Figure 8.19 shows the predicted velocities of vapor, liquid and interface for different mass fluxes. The figure clearly shows that the velocity at the interface is closer to liquid velocity. Also as the mass flux increases, all the three velocities increase in response. However, the rate of increase in liquid velocity is less than that of vapor velocity due to the higher inertia of the liquid core. A final observation is made for high mass flux where the vapor velocity is less than liquid velocity near the CHF location. For a very small

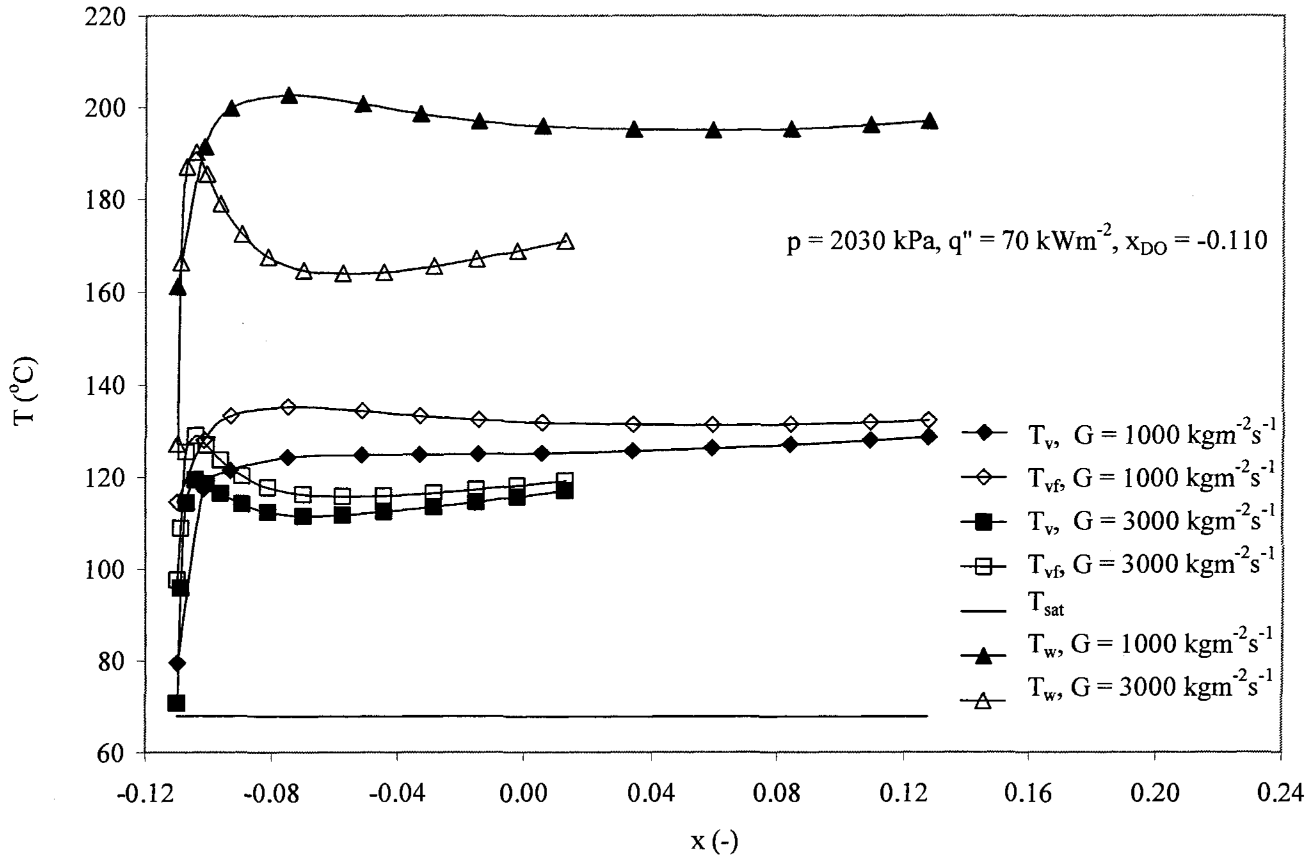

Figure 8. 18 Comparison between predicted vapor temperature and vapor film temperature.

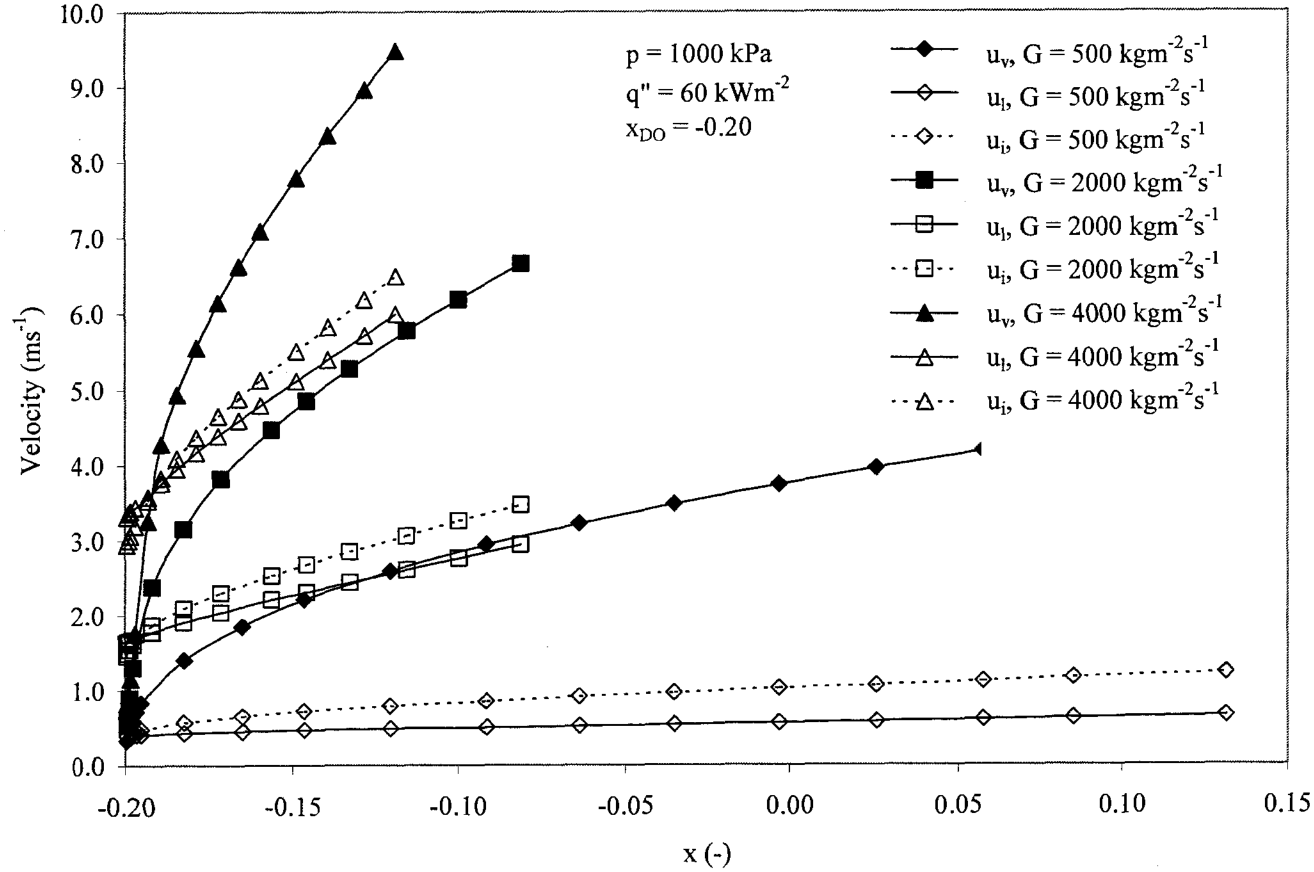

Figure 8. 19 Model prediction of velocity of vapor, liquid and interface.

increase in quality the vapor accelerates rapidly and its velocity exceeds the liquid velocity.

8.3.4. Comparing predicted void fraction to measurements

Many previous studies considered conduction heat transfer in the vapor film (see Table 2.2). However, this model in addition to some older models [e.g. Analytis and Yadigaroglu (1987)] assumed convection heat transfer in the vapor film. The argument that led to considering convective heat transfer in the vapor film is the low Reynolds number at which transition to turbulent flow occurs ($\mathrm{Re} = 100$) due to the work of Hsu and Westwater (1959). Figures 8.14 – 8.17 show that considering convection in the vapor film leads to earlier than expected termination of IAFB regime even, in some cases, at negative qualities. This suggests a rapid increase in void fraction (or vapor film thickness) along short length of the test section downstream from the CHF location.

Fung and Groeneveld (1980) performed void fraction measurements in IAFB heat transfer of water at atmospheric pressure and for low mass flux. Since these data are the only data available to the author, they are used to compare the new model prediction of void fraction to measurements. Figure 8.20 shows the comparison between predicted and measured void fraction vs. equilibrium quality. The experimental data of Fung and Groeneveld (1980) show that the void fraction increases from 0.08 to 0.6 for a relatively small increase in quality ($\Delta x \approx 0.02$). A similar trend and magnitude are predicted by the new model as shown in the figure. This implies that assuming convective heat transfer in the vapor film is a valid assumption.

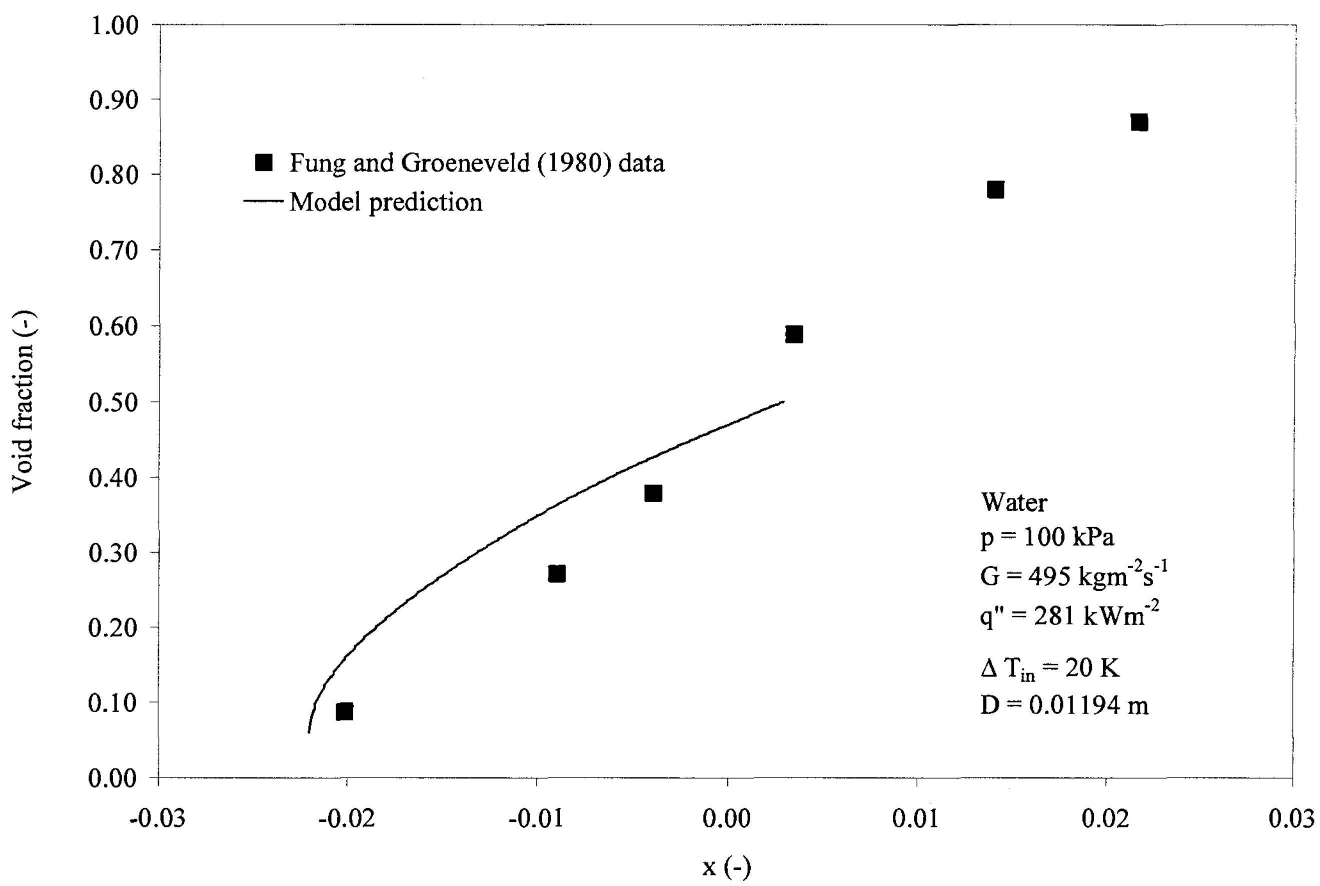

Figure 8. 20 Comparison between void fraction measurement of Fung and Groeneveld (1980) and the new model prediction.

8.4. Sensitivity Analysis

8.4.1. Sensitivity of the model to interfacial velocity

The model sensitivity to interfacial velocity is examined for two cases. The first case is by computing u_i based on equal shear stress across the interface (as in the model). The second case is with taking the interfacial velocity as the average of vapor and liquid velocity [Equation (7.62)]. Another possible case is assuming the velocity of the interface equals liquid velocity [e.g., Analytis and Yadigaroglu (1987) and Hammouda (1996)]. This case is not considered due to the changes in the physics of the model on how to calculate liquid Reynolds number.

The effect of changing the velocity of the interface on wall temperature distribution is shown in Figure 8.21. The figure shows that the new model better predicts the magnitude of wall temperature with velocity of the interface based on equal shear stress across the interface.

8.4.2. Sensitivity of the model to the assumption ($h_{vi} = h_{wv}$)

In deriving the model it is assumed that the heat transfer coefficients from wall-to-vapor and vapor-to-interface are equal. Figure 8.22 shows a comparison of the measured and predicted wall temperature for various values of the ratio h_{vi}/h_{wv} (from 0.6 to 1.4) . The figure shows that the best predictions by the new model correspond to a h_{vi}/h_{wv} ratio of unity.

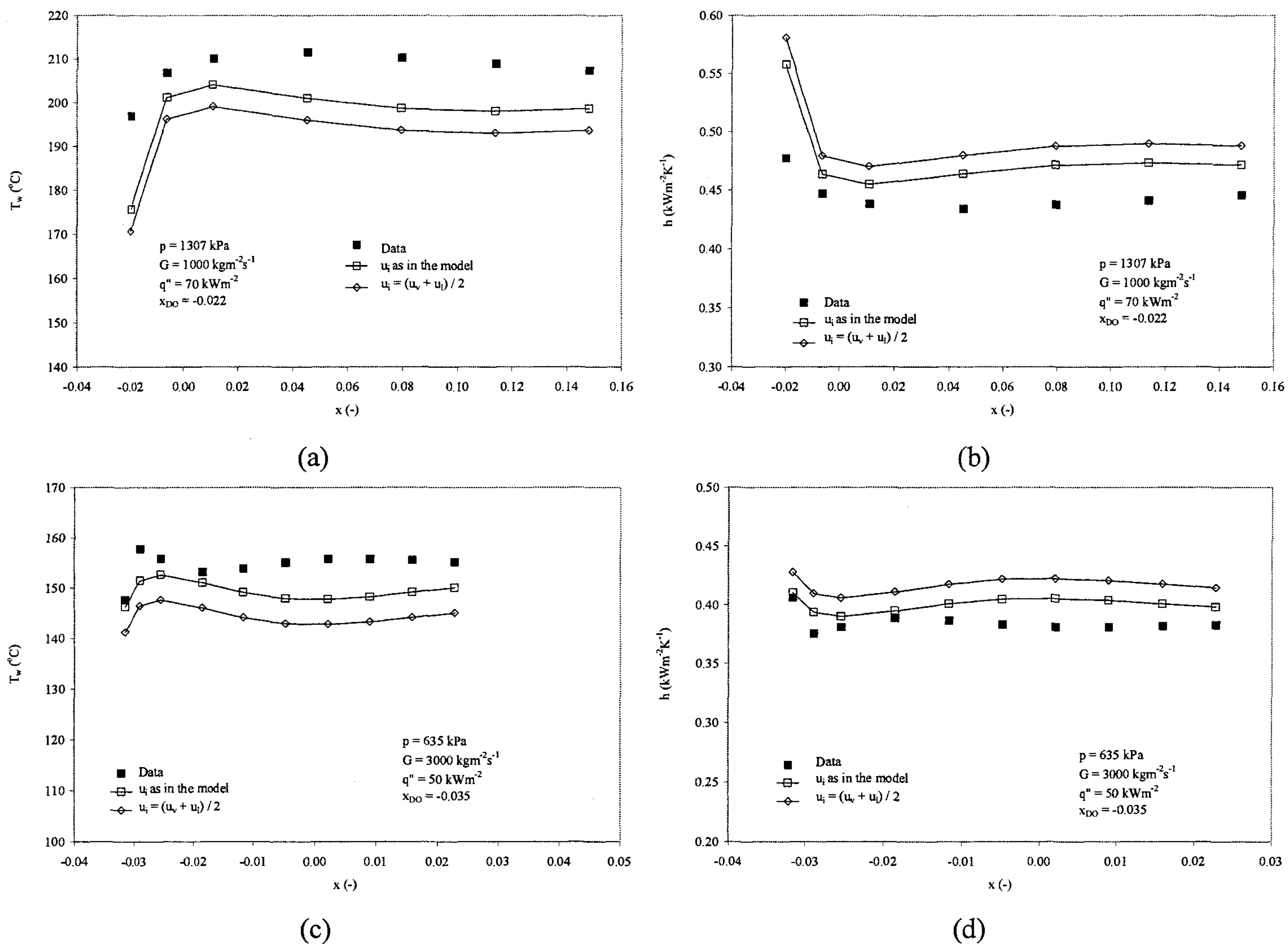

Figure 8. 21 Sensitivity of the new model to interfacial velocity.

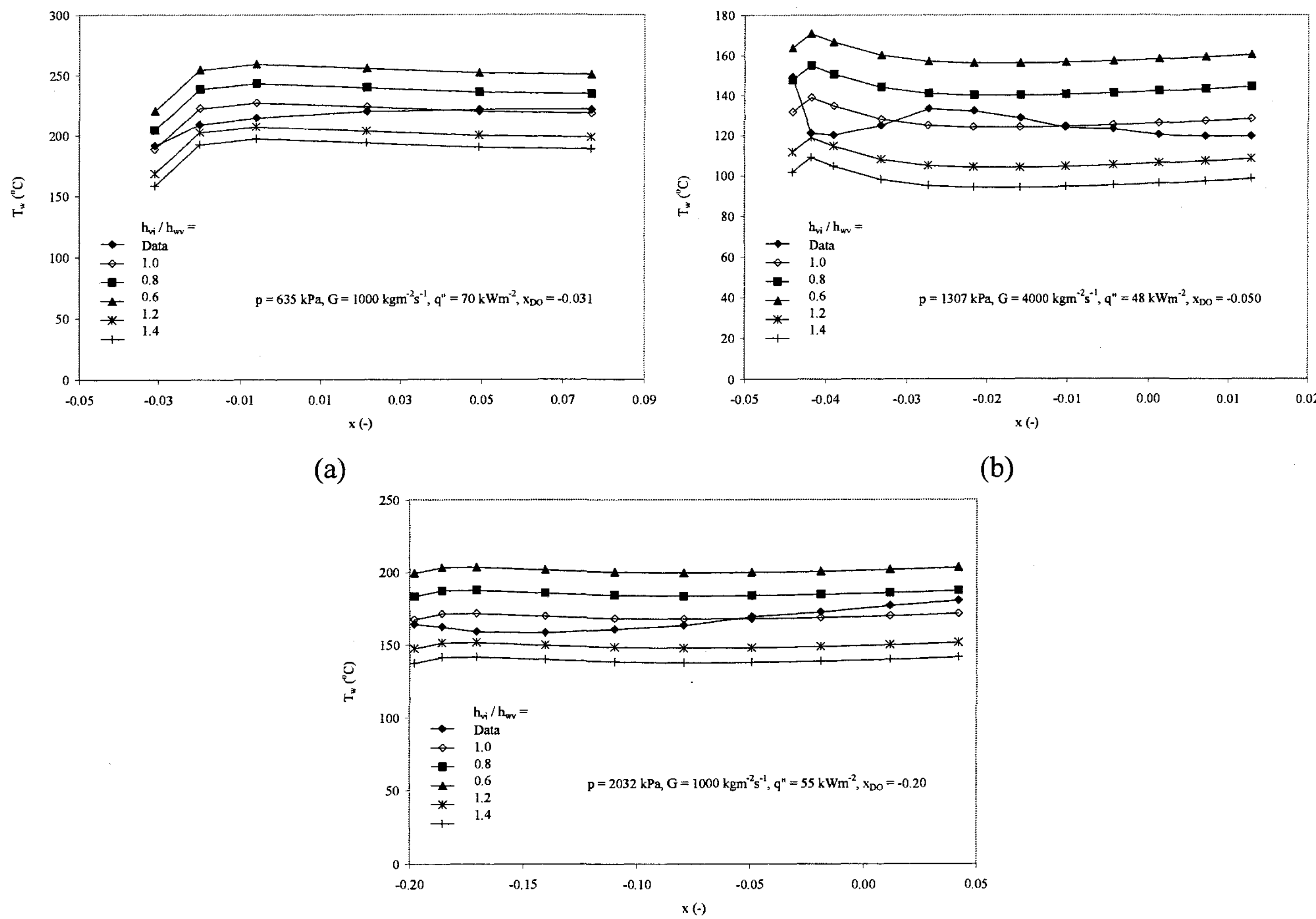

(c)

Figure 8. 22 Sensitivity of the new model to the ratio (h_{vi} / h_{wv}).

8.5. Comparison with other prediction methods

Wall temperature predictions using Analytis and Yadigaroglu (1987), Cachard (1994) and Hammouda (1996) models and the new model are shown in Figures 8.23 – 8.25. The figures are for low, moderate and high pressures and low and high mass fluxes, which basically cover most of the range of pressures and mass fluxes in the experimental program of the thesis. For the range of flow conditions considered, the new model provides a better prediction of the wall temperature and heat transfer coefficient than the other models. In the figures, Cachard (1994) and Hammouda (1995) models failed to predict in the positive quality region, which limit the applicability of their models.

The average (avg) and root mean square (RMS) errors in the new model prediction are calculated, respectively, as

$$Error_{avg} = \frac{1}{n}\sum_{i=1}^{i=n} Error_i \tag{8.6}$$

and

$$Error_{RMS} = \sqrt{\frac{1}{n}\sum_{i=1}^{i=n}\left(Error_i\right)^2} \tag{8.7}$$

where

$$Error_i = \frac{prediction - measurement}{measurement} \tag{8.8}$$

The model predicts wall temperature of R-134a with an average error of -1.21 % and an RMS error of 6.37 % using 4219 data points. The corresponding average and RMS errors

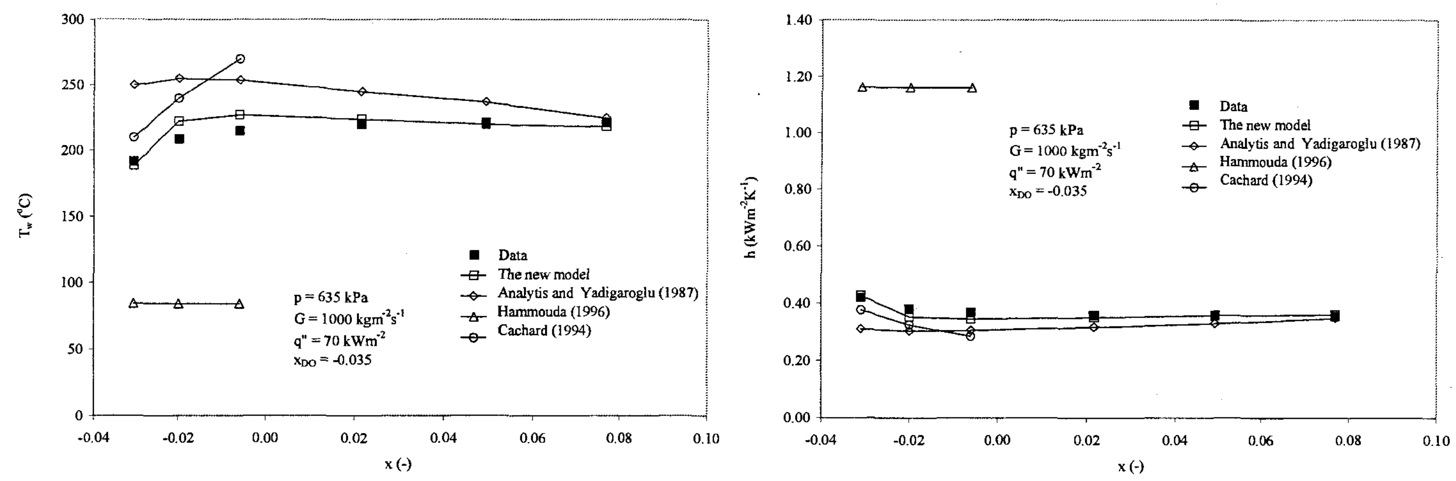

(a)

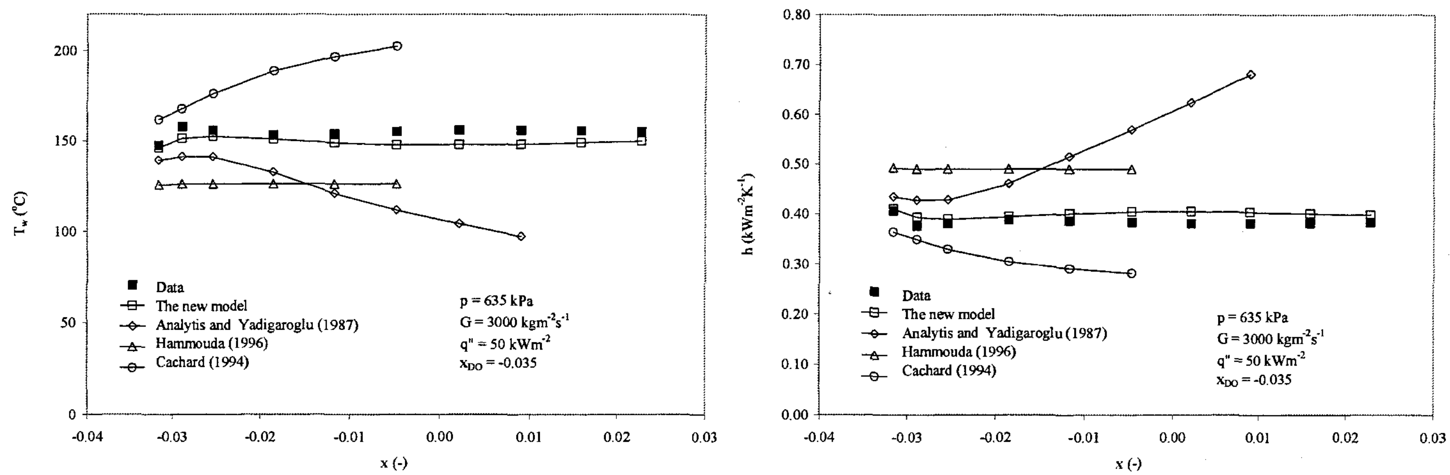

(b)

Figure 8. 23 Comparison of the new model predictions at low pressure and (a) low, and (b) high mass flux.

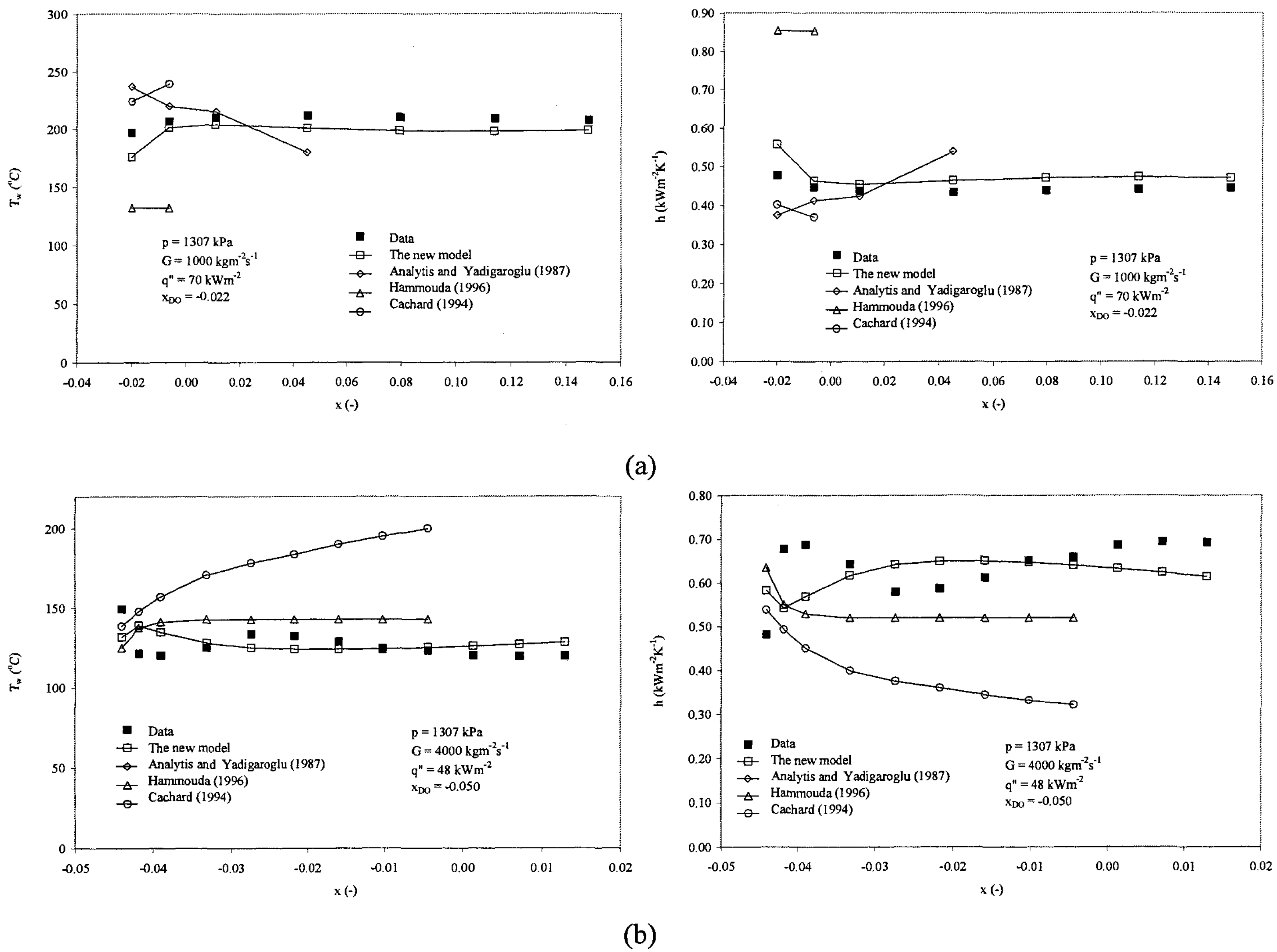

Figure 8. 24 Comparison of the new model predictions at moderate pressure and (a) low, and (b) high mass flux.

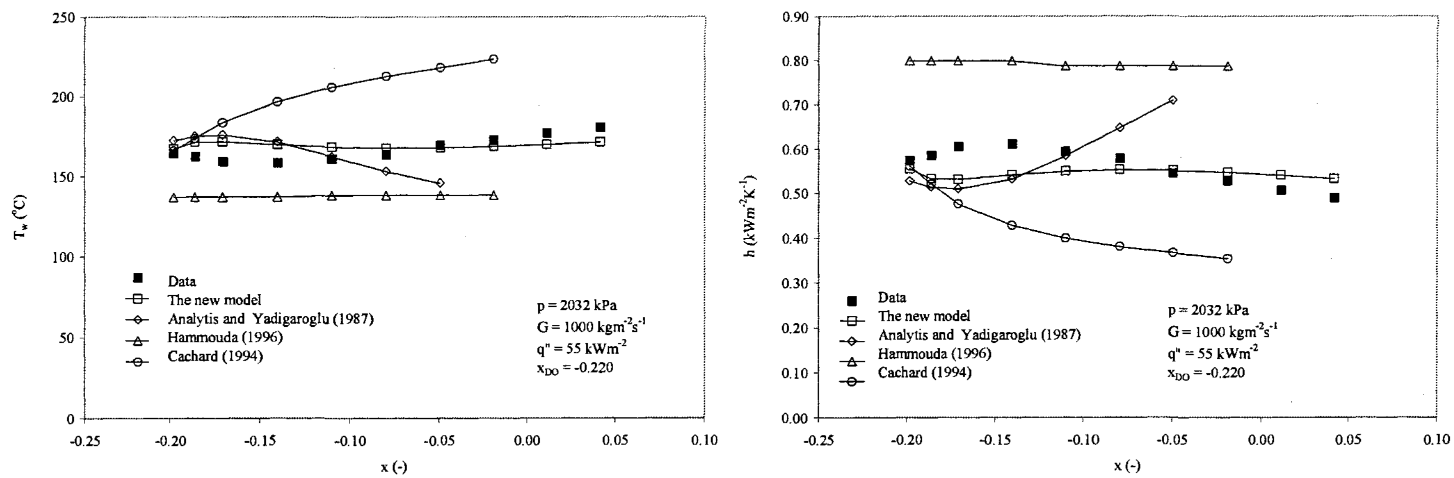

(a)

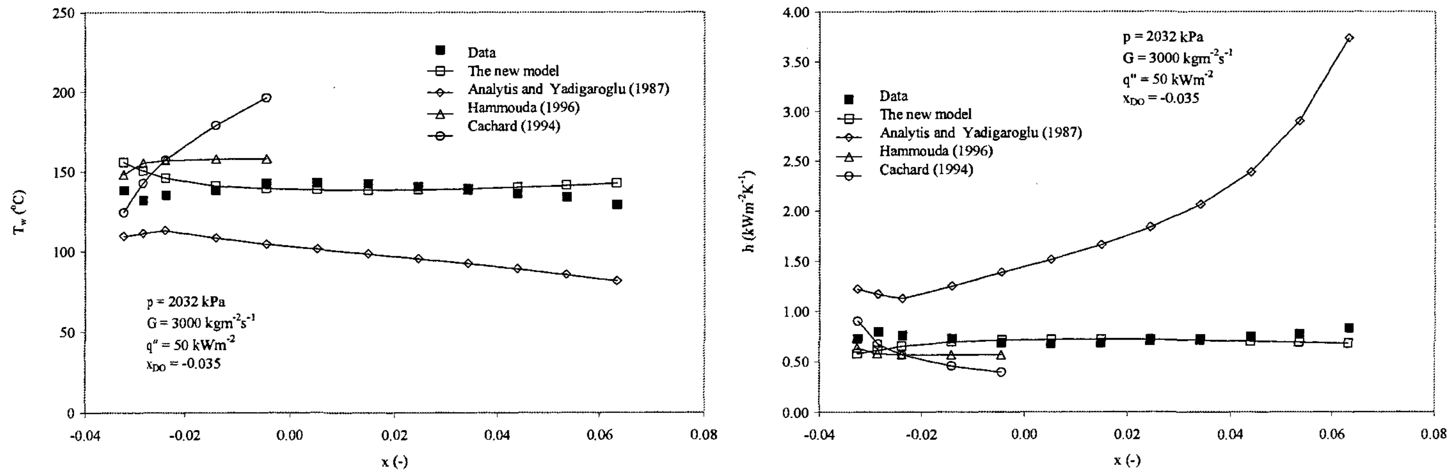

(b)

Figure 8. 25 Comparison of the new model predictions at high pressure and (a) low, and (b) high mass flux.

for the predicted heat transfer coefficient are 1.33% and 10.07%, respectively. These data points include the data directly after the hot-patch which usually results in higher errors.

8.6. Application of the Model to Water

One of the major applications of IAFB models is the prediction of IAFB heat transfer during a LOCA in a water-cooled nuclear reactor. Another application of the model is to improve the prediction accuracy of the film boiling look-up table [FB-LUT (2004), El Nakla et al. (2004)]. The look-up table approach is currently recognized by nuclear industry as one of the most accurate prediction methods for a very wide range of flow conditions.

The previous assessment of the model was against R-134a data. However, the new model is intended to be applied to predict IAFB heat transfer for variety of fluids. To assess the new model's applicability to water, comparisons against measured wall temperatures in water based on experiments by Fung (1981), Laperriere (1983) and Stewart (1981) have been made. Figures 8.26 – 8.30 show comparison of the current model against (i) measured wall temperatures, (ii) predictions of Analytis and Yadigaroglu (1987), Cachard (1994) and Hammouda (1996), and (iii) the film boiling look-up table. The figures cover the whole range of flow conditions of the data sets used in the comparison. Note that the new model clearly outperforms the other models. In some cases the model also outperforms the LUT for fully developed film boiling conditions, even though the LUT has been optimized with experimental data[1]. The model predicts wall temperature of water with an average error of -1.76% and an RMS error of 7.78% using 1938 data points. Using the same data points, the average and RMS errors in predicting heat transfer coefficient are 4.16% and 15.06%, respectively.

[1] The LUT was developed for fully developed film boiling conditions and therefore ignores entrance effects or developing film boiling effects; therefore its agreement with the data at locations just downstream is generally not satisfactory.

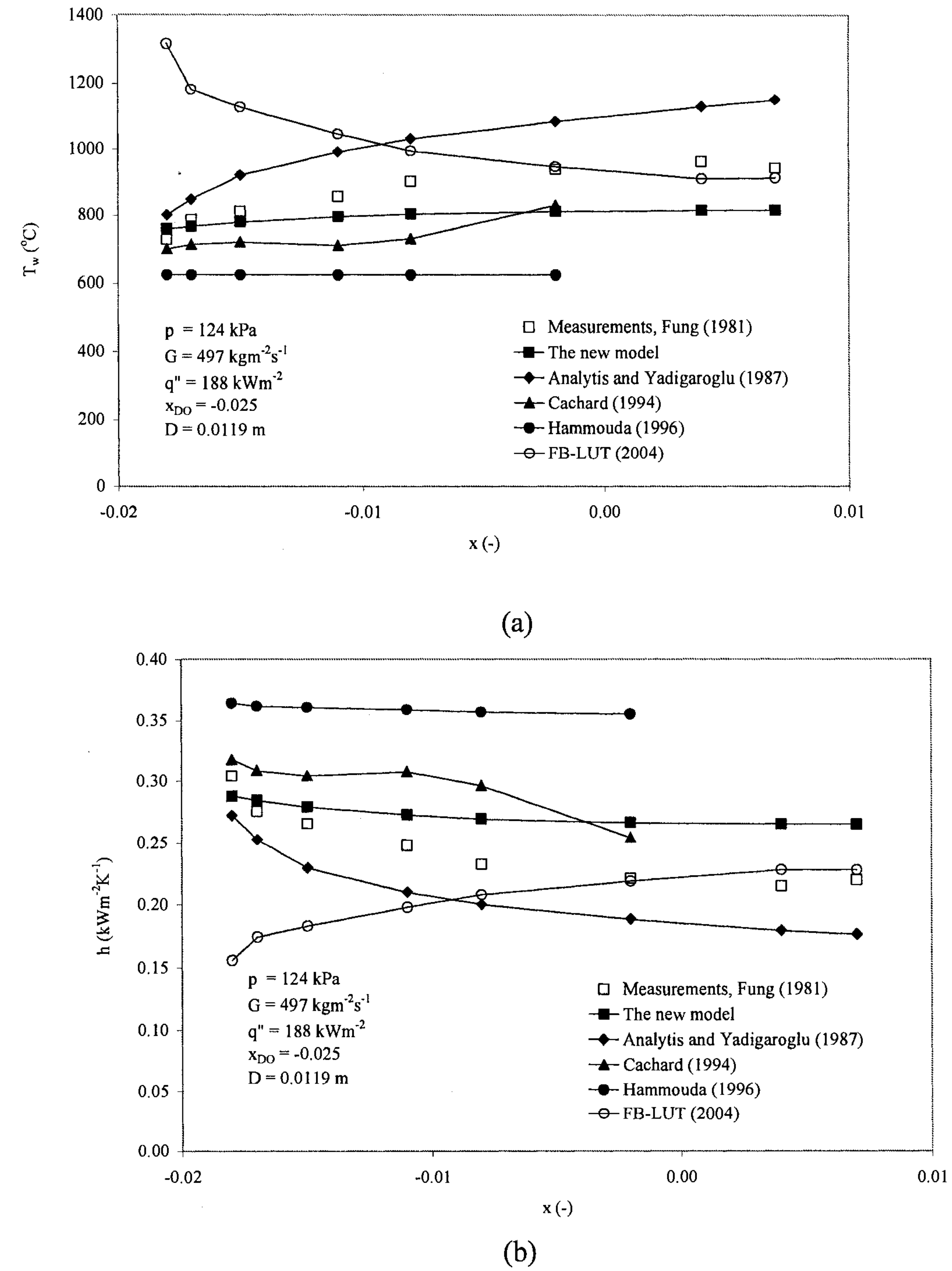

Figure 8. 26 Comparison of the new model prediction with atmospheric pressure data from Fung (1981).

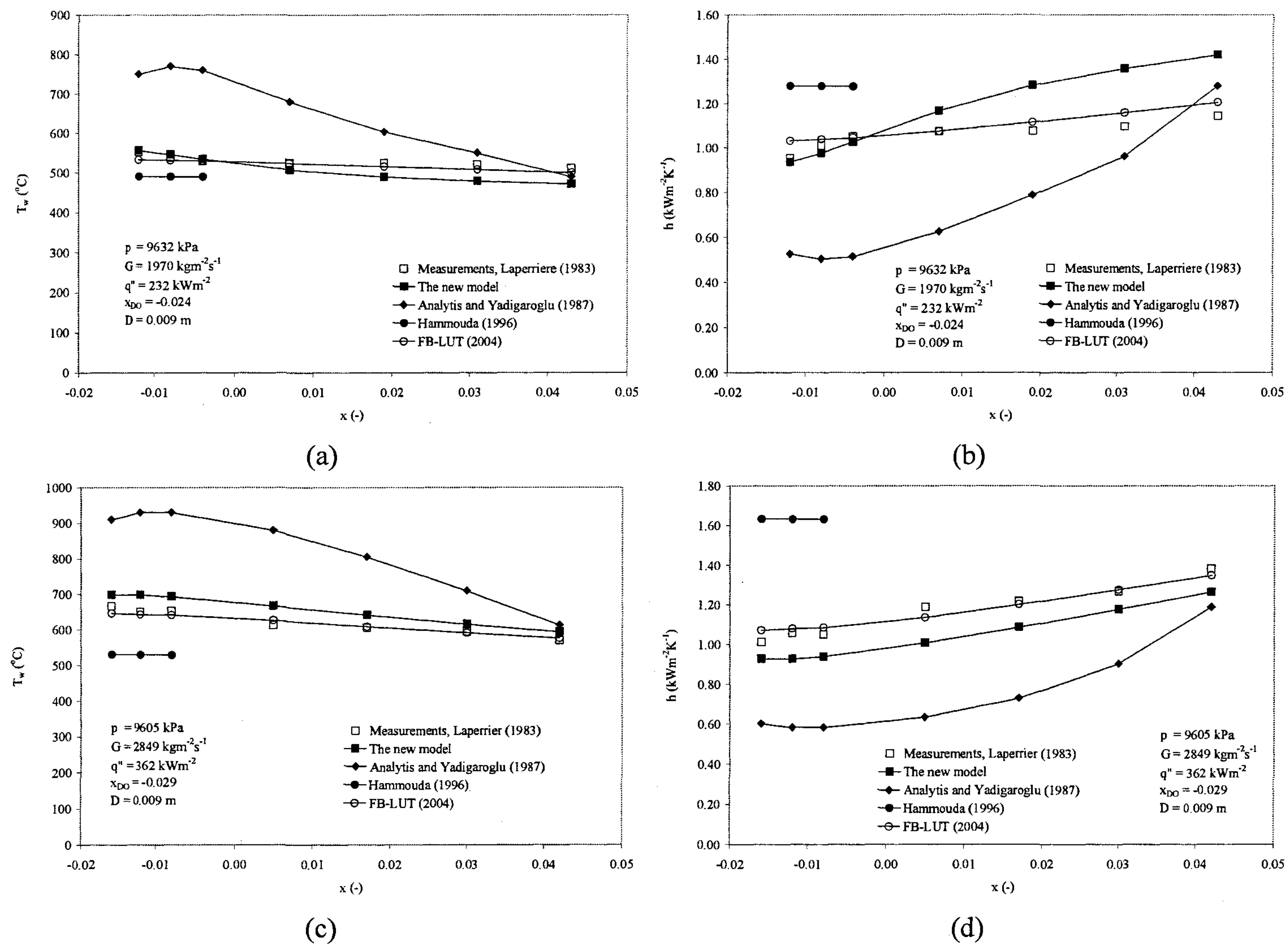

Figure 8. 27 Comparison of the new model prediction with moderate-to-high pressure data from Laperriere (1983).

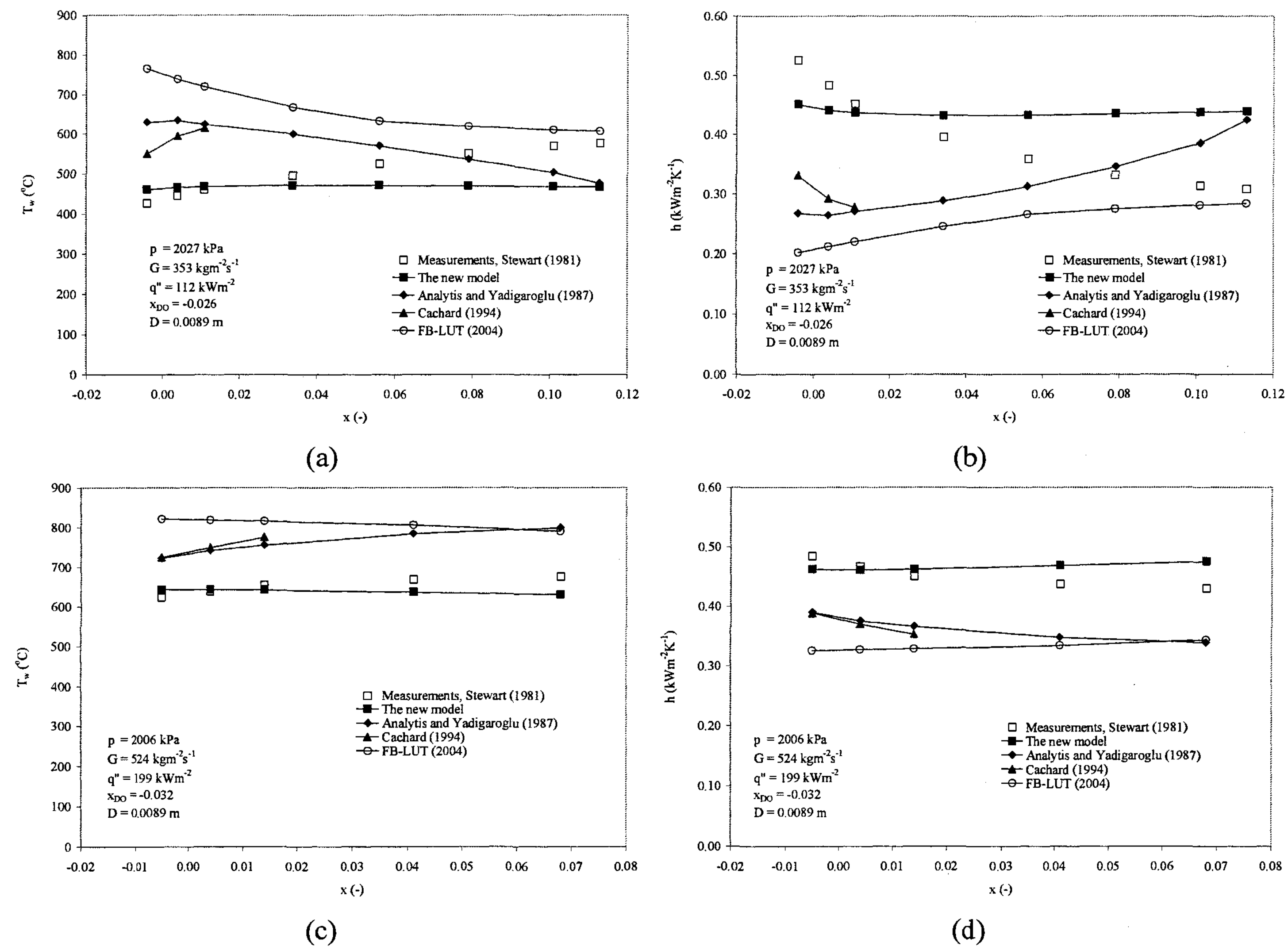

Figure 8. 28 Comparison of the new model prediction with low-to-moderate pressure data from Stewart (1981).

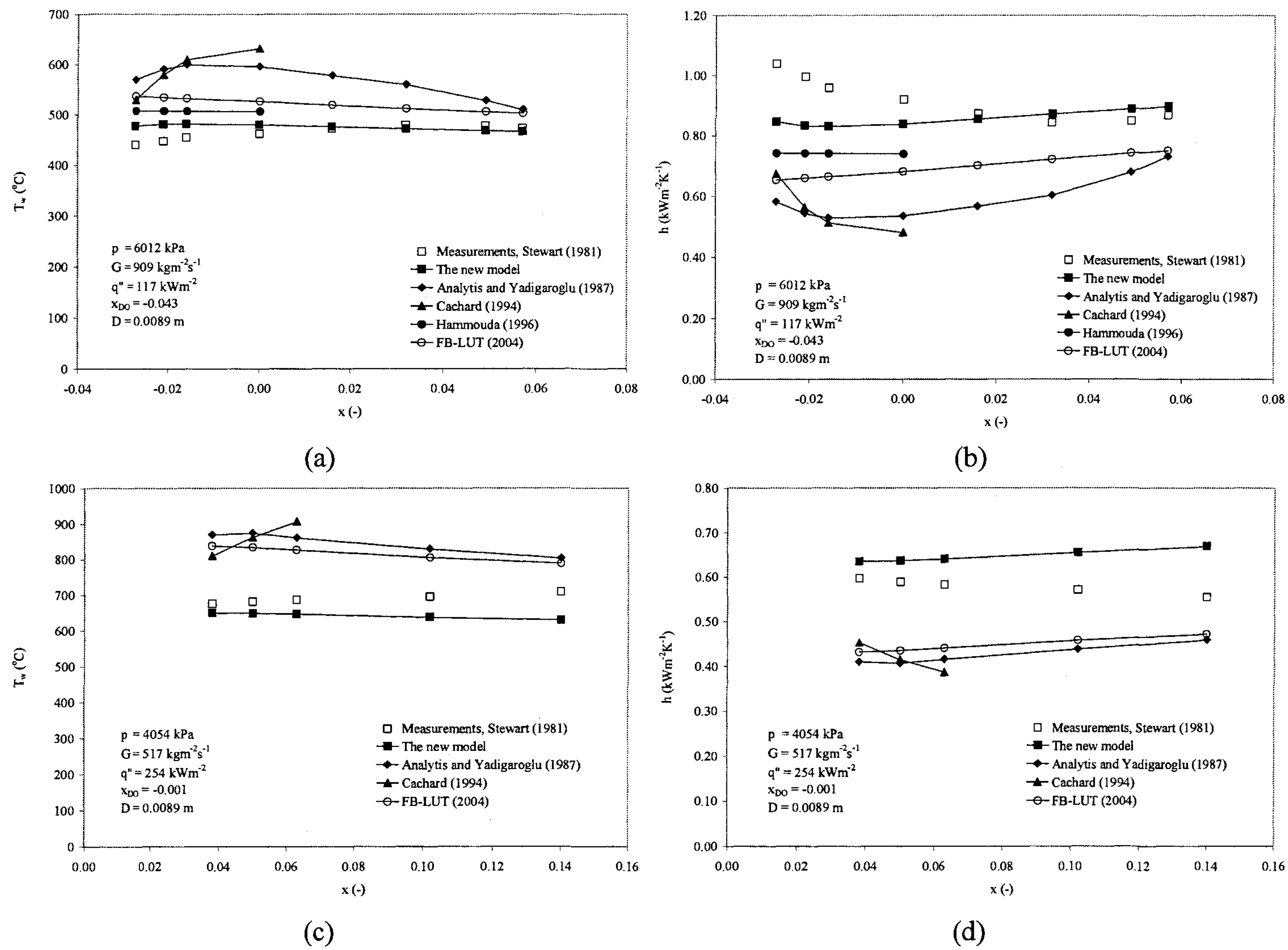

Figure 8. 29 Comparison of the new model prediction with moderate pressure data from Stewart (1981)

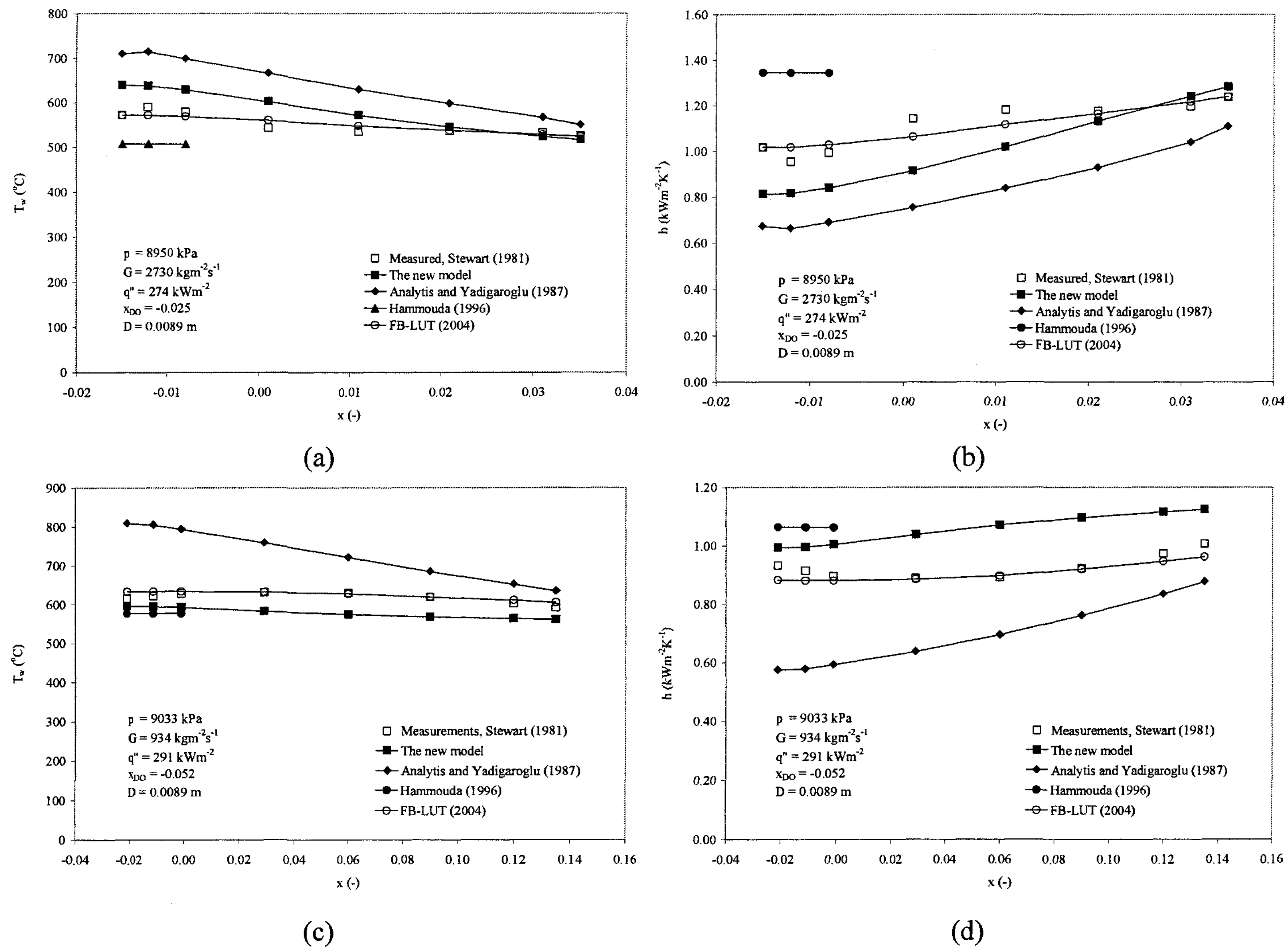

Figure 8. 30 Comparison of the new model prediction with moderate-to-high pressure data from Stewart (1981).

Subcooled and low quality data cover limited ranges of applications. This makes it difficult to give full assessment of the model prediction capabilities and parametric trends against water data. Figures 8.31 – 8.33 show the new model's prediction capability over a very wide range of flow parameters for a water-cooled 8 mm ID tube. The intent of these figures is to show that the model is capable of predicting the reasonable values over a wide range of flow conditions, and that it does not "crash" at extreme conditions. Generally the model predicts in the same manner as in R-134a. The small differences in curve shapes between water and R134a are primarily due to different properties of the two fluids.

Figure 8.30 shows that the model correctly predicts the heat flux and inlet subcooling effects on heat transfer coefficient of water for a quite wide ranges of these flow parameters. Figure 8.31 is an illustration of the range of pressure for which the model predicts correct trend at low, moderate and high mass fluxes. As can be seen from the figure, the predicted heat transfer coefficient increases with increasing pressure at all mass fluxes. Also the figure shows the change in heat transfer regions (see Section 6.2) on pressure and mass flux. Figure 8.33 shows the range of mass flux for which the model is capable of predicting the correct trend at different pressures. It seems that the model is not capable of predicting the correct trend of mass flux effect at atmospheric pressure and for a mass flux higher than 6000 $kgm^{-2}s^{-1}$. Other than that, the model appears to predict the correct parametric effect of mass flux at all pressures from atmospheric to close to critical pressure of water.

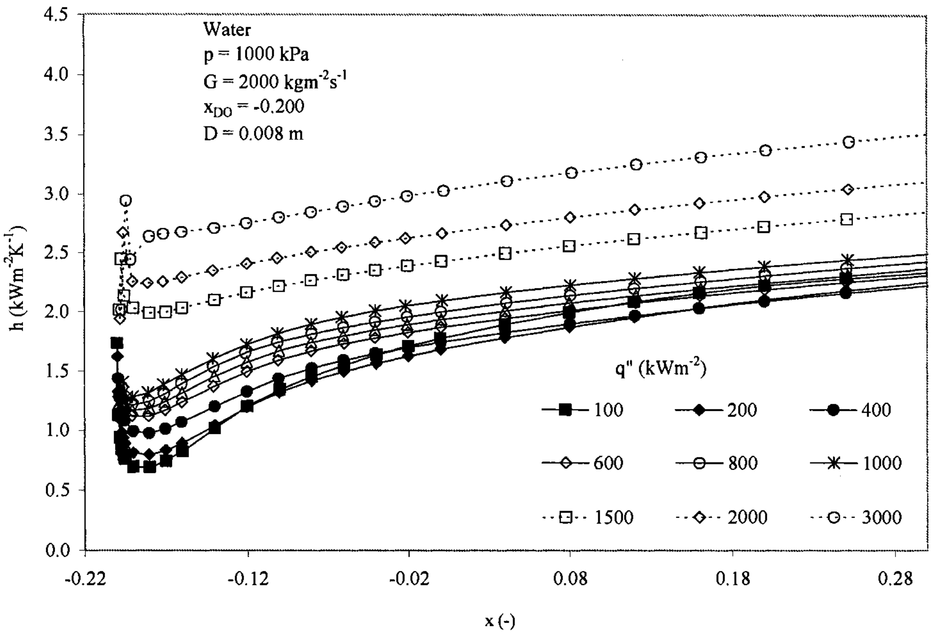

(a)

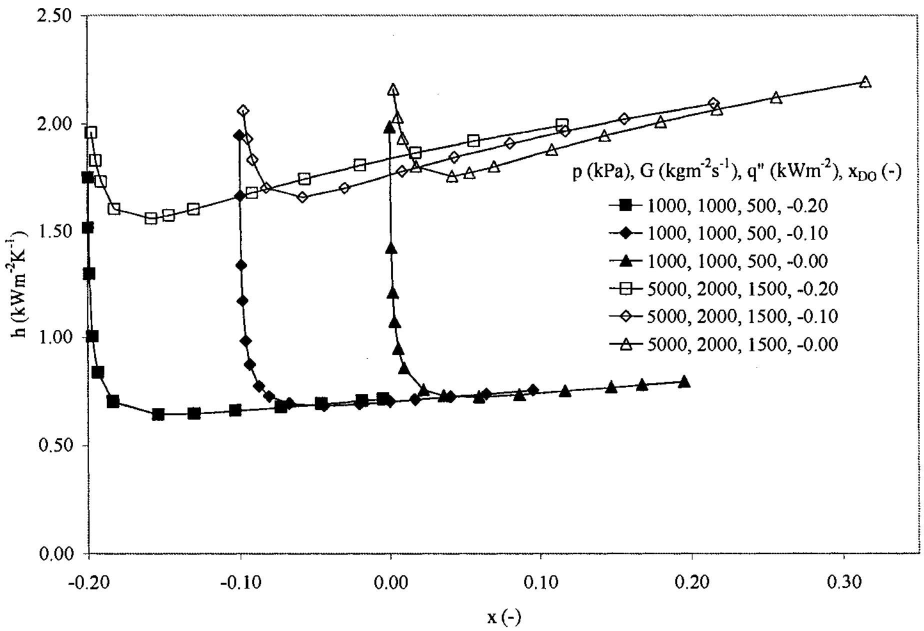

(b)

Figure 8. 31 Model's range of prediction to (a) heat flux and (b) inlet subcooling effects on heat transfer coefficient for water as a coolant.

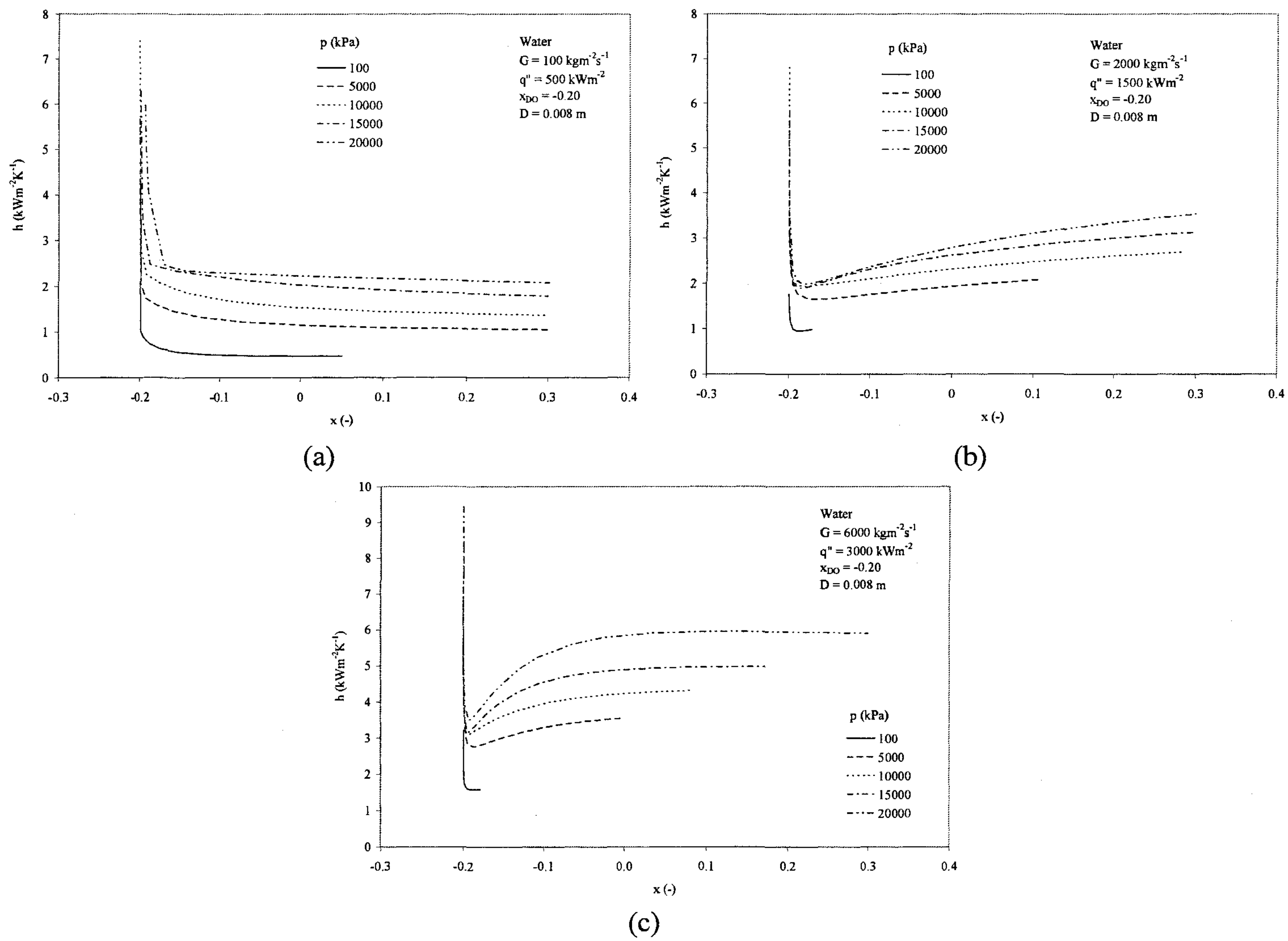

Figure 8. 32 Model's range of prediction to pressure effect on heat transfer coefficient at (a) low, (b) moderate and (c) high mass fluxes for water as a coolant.

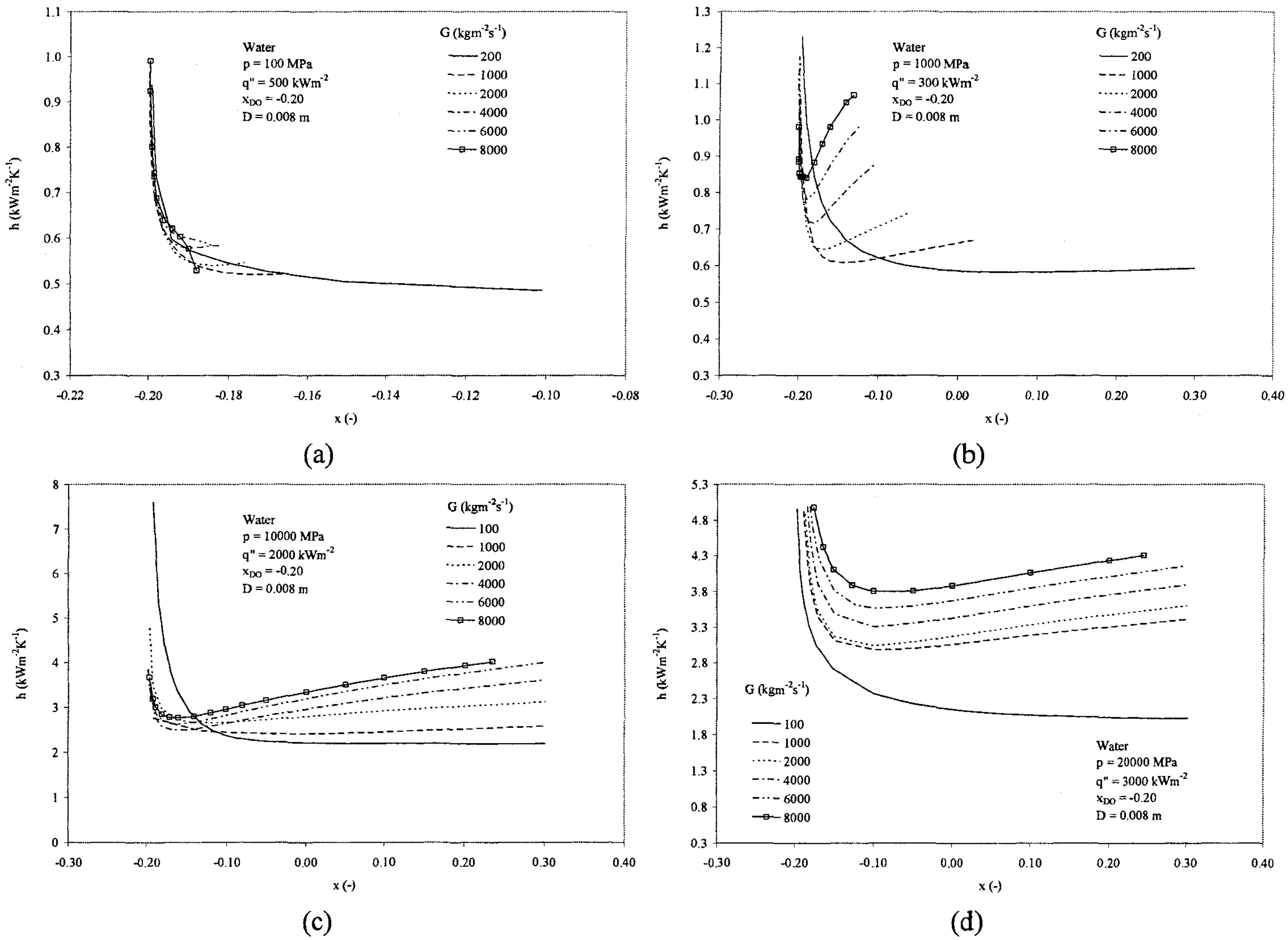

Figure 8. 33 Model's range of prediction to mass flux effect on heat transfer coefficient at (a) atmospheric, (b) low (c) moderate and (d) high pressures for water as a coolant.

CHAPTER 9 CONCLUSIONS AND FINAL REMARKS

9.1. Experimental Program

- Measurements of wall temperature and calculations of heat transfer coefficients of IAFB regime were obtained experimentally for a vertical up-flow in a circular tube using R-134a as a coolant. A total of 10,260 data points were obtained from which 6,862 data points with equilibrium quality of less than 0.1. Flow conditions covered a pressure range of 640 to 2390 kPa (water equivalent range: 4000 to 14000 kPa), a mass flux range of 500 to 4000 kg m^{-2} s^{-1} (water equivalent range: 700 to 5700 kg m^{-2} s^{-1}) and a post-CHF quality range of -0.49 to 1.0. The inlet qualities for which IAFB measurements could be obtained were dependent on mass flux and pressure and fell within the range of -0.75 to -0.03. The hot-patch technique was used to obtain the subcooled film boiling measurements.

- Four separate IAFB heat transfer regions were identified; their boundaries depend on pressure, mass flux and quality. The general observed trend of heat transfer coefficient vs. quality is that it decreases sharply just downstream of the dryout location. The trend then varies with other flow parameters.

- Effects of varying pressure, mass flux, heat flux and inlet subcooling on IAFB heat transfer coefficient were investigated and compared to reported effects by other investigators. Generally, the heat transfer coefficient increases with increased pressure and mass flux. The heat flux shows a weak effect on the heat transfer coefficient and inlet subcooling affects only the short region downstream of the CHF location.

9.2. Analytical Program

- A one-dimensional, two-fluid model of IAFB has been developed to predict the tube wall temperature of the IAFB regime.

- The new model assumes turbulent flow of the vapor, while in the liquid core, laminar flow has been assumed for Re < 2000 and turbulent flow otherwise. The heat transfer from the wall to the vapor and from the vapor to the liquid interface was modeled by modifying Kays and Crawford (1986) formulation and treating the vapor as flowing between two parallel plates.

- One of the key points of the new model is the formulation of the heat and momentum transfers of the vapor-liquid interface and the liquid core, based on the liquid velocity relative to the interface.

9.3. Assessment of the Results

- Prediction capabilities of the model to wall temperature have been assessed against R-134a data obtained in this study and water data of Laperriere (1981), Stewart (1981) and Fung (1981). The model predicts wall temperature of R-134a with an average error of -1.21 % and an RMS error of 6.37 %. The corresponding average and RMS errors in model prediction of heat transfer coefficient are 1.33% and 10.07%, respectively. Using water data, the model predicts wall temperature with an average error of -1.76% and an RMS error of 7.78%. The corresponding average and RMS errors in predicting heat transfer coefficient of water are 4.16% and 15.06%, respectively.

- The new model's prediction has been compared with other IAFB prediction methods. The new model has shown superiority in prediction capabilities covering a wide range of flow conditions.

- Overall, the model correctly predicts the dependence of wall temperature and the heat transfer coefficient on pressure, mass flux, heat flux and inlet subcooling for the range of obtained experimental data during the course of this study.

9.4. Remarks

- Friction factors appropriate for IAFB are scarce. The friction factors employed in this work are simply the ones used in previous models. More reliable friction factors are needed to improve the prediction accuracy of IAFB models.

- The effect of the lateral oscillations of the liquid core might result in significant heat transfer enhancement. This may create limitations in using Kays and Crawford (1986) formulation.

- The closure equations used in model derivation are used without including enhancement factors. This created some discrepancies in model prediction just downstream of the CHF location.

9.5. Contribution

The major contributions of this study can be summarized in two major points:

- The experimental part of this thesis has helped in filling the gaps in IAFB database between low-to-moderate and moderate-to-high pressures, and low-to-moderate to high mass fluxes. These ranges of flow conditions are considered important in performing safety analysis of nuclear power generation.

- A new model that predicts wall temperature and heat transfer coefficient for this range has been developed. The prediction accuracy of the new model is much better than that of previous models and the new model covers a wider range of conditions.

REFERENCES

Ahmad, S.Y., (1973), "Fluid-to-Fluid Modeling of Critical Heat Flux: A Compensated Distortion Model", *Int. J. Heat Mass Transfer*, Vol. 16, pp. 641–662.

Analytis, G.Th., and Yadigaroglu, G, (1987), "Analytical Modeling of Inverted Annular Film Boiling", *Nuclear Engineering and Design,* Vol. 99, pp. 201-212.

Andersen, J., (1976), "Low-Flow Film Boiling Heat Transfer on Vertical Surfaces", *AJChE Symp. Ser.*, Vol. 73, pp. 2-6.

Andreani, M., and Yadigaroglu, G., (1994), "Prediction Methods for Dispersed Flow Film Boiling", *Int. J. Multiphase Flow*, Vol. 20, pp. 1-51.

Bailey, N.A., (1972), "The Interaction of Droplet and Forced Convection in Post Dryout Heat Transfer at High Subcritical Pressures", European Two-Phase Flow Group Meeting, Rome.

Baum, A.J., Purcupile, J.C., and Dougall, R.S., (1978), "Transition and Film Boiling Heat Transfer from Vertical Surfaces", 6th Int. Heat Trans& Conf, Toronto.

Bennett, A.W., Hewitt, G.F., Kearsey, H.A., and Keeys, R.K.F., (1967), "Heat Transfer to Steam Water Mixtures Flowing in Uniformly Heated Tubes in which the Critical Heat Flux Has been Exceeded", AERE-R-5373.

Bennett, A.W., Kearsey, H.A., and Keeys, R.K.F., (1964), "Heat Transfer to Mixtures of High Pressure Steam and Water in an Annulus", Part VI, AERE-R-4352.

Berenson, P.J., (1961), "Film Boiling Heat Transfer from a Horizontal Surface", J. of Heat *Transfer*, Vol. 83, pp. 351-358.

Bertoletti, S., (1961), "Heat Transfer and Pressure Drop with Steam Water Spray", CISE R-36.

Bertoletti, S., Lombardi, G., and Silvestri, M., (1964), "Heat Transfer to Steam-Water Mixtures", CISE R-78.

Bishop, A.A., Efferding, L.E., and Tong, L.S., (1962), "A Review of Heat Transfer and Fluid Flow of Water, in the Supercritical Region and During 'Once-Thru' Operation", WCAP-2040.

Bishop, A.A., Sandberg, R.O., and Tong, L.S., (1965), "Forced Convection Heat Transfer at High Pressure After the Critical Heat Flux", *ASME-65-HT-31*.

Bishop, A.A., Sandberg, R.O., and Tong, L.S., (1964), "High Temperature Supercritical Pressure Water Loop. Part V: Forced Convection Heat Transfer to Water After the Critical Heat Flux at High Supercritical Pressures", WCAP-2056 (Pt. 5).

Brevi, R., Cumo, M., Palmieri, A., and Pitimada, D., (1969), "Heat Transfer Coefficient in Post Dryout Two-Phase Mixtures", European Two-Phase Group Meeting, Karlsruhe.

Bromley, L.A., (1952), "Effect of Heat Capacity on Condensate", *Ind. Eng. Chem.,* Vol. 44, pp. 2966-2969.

Bromley, L.A., (1950), "Heat Transfer in Stable Film Boiling", *Chem. Eng. Prog.*, Vol. 46, pp. 221-227.

Bromley, L.A., LeRoy, N.R., and Robbers, J.A., (1953), "Heat Transfer in Forced Convective Film Boiling", *Ind. Eng. Chem.*, Vol 45, pp. 2639-2646.

Cachard, de F., (1994), "Development, Implementation and Assessment of Specific Closure Laws for Inverted-Annular Film-Boiling in a Two-Fluid Model", Paul Scherrer Institute (PSI), Report 94-16.

Carey, V.P., (1992), LIQUID-VAPOR PHASE-CHANGE PHENOMENA, Hemisphere Publishing Corporation, New York, NY.

Chan, K.C., and Yadigaroglu, G., (1980), "Calculations of Film Boiling Heat Transfer Above the Quench Front During Reflooding", *Experimental and Analytical Modelling of LWR Safety Experiment,* ASME publication HTD, Vol. 7.

Chen, Y., (1987), "Experimental Study of Inverted Annular Flow Film Boiling Heat Transfer of Water", In "Heat Tramfer Science and Technology", 627-634, Eds: Wang, B. -X, Hemisphere Pub. Co.

Chen, J.C., (1986), "A Short Review of Dispersed Flow Heat Transfer in post-Dryout Boiling", *Nuclear Engineering Design*, Vol. 95, pp. 375-383.

Chen, Y.Z., and Chen, H.Y., (1998), "A Tabular Method for Prediction of the Heat Transfer During Saturated Film Boiling of Water in a Vertical Tube", *Proceedings, 11th International Heat Transfer Conference,* Korea.

Chen Y., Xu H., and Chen, H., (1996), "Experimental Results of Steady-State Film Boiling of Forced Flow Water", China Institute of Atomic Energy, Beijing, China, Presented at 2nd Research Co-ordinated Meeting of IAEA, CRP on Thermalhydraulic Relationships for AWCR, Vienna.

Chen, Y., and Li, J., (1984), "Subcooled Flow Film Boiling of Water at Atmospheric Pressure", In "Two-Phase Flow and Heat Transfer", 141-150, Eds: Chen, X -,J., and Veziroglu, T.N., N., Hemisphere Pub. Co.

Chen, Y., Fu, X., and Chen, S. P., (1988), "Experimental and Analytical Study of Inverted Annular Film Boiling of Water", in "Experimental Heat Transfer Fluid Mechanics and Thermodynamics", Elsevier Sci. Publ., pp. 1438-1443 (Shah, R. K. et al eds.).

Chen, J.C., Morgan, C.D., and Sundaram, R.K., (1984), "A Correlation of Low Flow, Low Pressure, and Low-to-Moderate Quality post-CHF Data. In *First Int. Workshop on Fundamental Aspects of Post-dryout Heat Transfer*, 2-4 April, Salt Lake City, UT, U.S.A NUREG/CP-0060.

Chen, J.C., Ozkaynak, F.T., and Sundaram, R.K., (1979), "Vapor Heat Transfer in the Post-CHF Region Including the Effect of Thermodynamic Non-Equilibrium", *Nuclear Engineering and Design,* Vol. 51, pp. 143-155.

Chen, Y., Wang, J., Yang, M., and Fu, X., (1989), "Experimental Measurement of the Minimum Film Boiling Temperature of Flowing Water", *Multiphase Flow and Heat Transfer, 2nd Int. Symposium,* Vol. 1, pp. 393-400.

Cheng, S.C., Lau, P.W.K., and Poon, K.T., (1985), "Measurements of True Quench Temperature of Subcooled Water under Forced Convective Conditions", *Int. J. Heat Mass Transfer,* Vol. 28, No. 1, pp. 235-243.

Chi, J.W.H., (1967), "Slug Flow and Film Boiling of Hydrogen", *J. of Spacecraft and Rockets,* Vol. 4, pp. 1329-1332.

Chi, J.W.H., (1966), "Forced Convection Boiling Heat Transfer to Hydrogen", *J. Spacecr. Rockets,* Vol. 3, pp. 150.

Chi, J.W.H., and Pierse, B.L., (1970), "An Experimental and Analytical Study of Film Boiling Heat Transfer to Hydrogen", *AIAA Propulsion Joint Specialist Conf., 6th*, San Diego.

Collier, J.G., (1980), CONVECTIVE BOILING AND CONDENSATION, 2nd ed., McGraw-Hill, London.

Collier, J.G., (1962), "Heat Transfer and Fluid Dynamic Research as Applied to Fog-Cooled Reactors", AECL-1631

Collier, J.G., and Thome, J.R., (1994), CONVECTIVE BOILING AND CONDENSATION, 3rd ed., Claredon Press, Oxford.

Cumo, M., and Urbani, G.C., (1974), "Post-Burnout Heat Transfer (Attainable Precision Limits of the Measured Coefficient)", CNEN/RT/ING(74)24.

Denham, M.K., (1984), "Inverted Annular Film Boiling and the Bromley Model", *IChE Symp. Series 86,* pp. 13-23.

Donevski, B., Chang, J.S., and Groeneveld, D.C., (1992), "Prediction Methods for Interfacial Parameters Used in Inverted Annular Film Boiling", *Int. J. Heal and Technology*, Vol. 10, No. 3.4, 43-70.

Dougall, R.S., and Rohsenow, W.M., (1963), "Film Boiling on the Inside of Vertical Tubes with Upward Flow of the Fluid at Low Qualities", MIT Report No. 9079-26.

El Nakla, M.A., Groeneveld, D.C., and Cheng, S.C., (2005), "Fluid-to-Fluid Modeling for Film Boiling Heat Transfer at ACR Conditions", Report No. UO-MCG-TH-2005-002, 95 pages, prepared for AECL, March.

El Nakla, M.A., Cheng, S.C., and Groeneveld, D.C., (2004), "Improvements of Prediction Accuracy, Parametric Trends and Smoothness of the Film Boiling Look-up Tables at ACR Conditions of Interest", Report No. UO-MCG-TH-2004-001, 233 pages, prepared for AECL, March.

Elias, E., and Chambre', P., (1981), "Inverted-Annular Film Boiling Heat Transfer from Vertical Surfaces", *Nucl. Engrg. Des.,* Vol. 64, pp. 249-257.

Ellion, M.E., (1954), "A Study of the Mechanism of Boiling Heat Transfer", California Institute of Technology, Report JPL-MEMO-20-88.

Era, A., Gaspari, G.P., Hassid, A., Milani, A., and Zavattarelli, R., (1967), "Heat Transfer Data in the Liquid Deficient Region for Steam-Water Mixtures at 70 kg/cm^2 Flowing in Tubular and Annular Conduits", CISE R-184.

Fung, K.K, (1981), "Subcooled and Low Quality Film Boiling of Water in Vertical Flow at Atmospheric Pressure", Ph.D. Thesis, University of Ottawa, Ottawa, On., Canada.

Fung, K.K., Gardiner, S.R.M., and Groeneveld, D.C., (1979), "Subcooled and Low Quality Flow Film Boiling of Water at Atmospheric Pressure", *Nuclear Engineering and Design*, Vol. 55, pp. 51-57.

Groeneveld, D.C., (2002), Lecture Notes, Special Course "Two-Phase Heat Transfer", University of Ottawa, Ottawa, On., Canada.

Groeneveld, D.C., (1992), "Inverted Annular and Low Quality Film Boiling: a State-of-the-Art Report", Presented in "Post-Dryout Heat Transfer" Book edited by Hewitt, G.F., Delhaye, J.M., and Zither, N.

Groeneveld, D.C., (1984), "An Inverted Annular and Low Quality Film Boiling: A State-of-Art Report", *Int. Workshop on Fundamental Aspects of PDO Heat Transfer*, Salt Lake City.

Groeneveld, D.C., (1973), "Forced Convective Heat Transfer to Superheated Steam in Rod Bundle", Atomic Energy of Canada Limited, Report AECL-4450, Chalk River, On., Canada.

Groeneveld, D.C., (1972), "The Thermal Behaviour of a Heated Surface and Beyond Dryout", Atomic Energy of Canada Limited, Report AECL-4309, Chalk River, On., Canada.

Groeneveld, D.C., (1969), "An Investigation of Heat Transfer in the Liquid Deficient Regime", AECL-3281.

Groeneveld, D.C., and Delorme, G.G.J., (1976), "Prediction of Thermal non-Equilibrium in the post-Dryout Regime", *Nuclear Engineering and Design*, Vol. 36, pp. 17-26.

Groeneveld, D.C., and Fung, K.K., (1976), "Forced Convective Transition Boiling: Review of Literature and Comparison of Predictive Methods", Atomic Energy of Canada Limited, Report AECL-5543.

Groeneveld, D.C., and Gardiner, S.R.M., (1978), "A Method of Obtaining Flow Film Boiling Data for Subcooled Water", *Int. J. Heat Mass Transfer*, Vol. (21), pp. 664-665.

Groeneveld, D.C., and Gardiner, S.R.M., (1977), "Post-CHF Heat Transfer under Forced Convective Conditions", *ASME Symposium on the Thermal and Hydraulic Aspects of Nuclear Reactor Safety*, Vol. 1, pp. 43-73, Eds: Jones, O.C. and Bankoff, S.G.

Groeneveld, D.C., and Snoek, C.W., (1986), "A Comprehensive Examination of Heat Transfer Correlations Suitable for Reactor Safety Analysis", in MULTIPHASE SCIENCE AND TECHNOLOGY, Ch. 3, pp. 181-271 (Hewitt, G. F. et al eds.).

Groeneveld, D.C., Cheng, S.C., and Doan, T., (1986), "1986 AECL-UO Critical Heat Flux Lookup Table", *Heat Transfer Engineering*, Vol. 7, Nos. 1-2, pp. 46-62.

Groeneveld, D.C., Doerffer, S., Tain, R.M., Hammouda, N., and Cheng, S.C., (1997), "Fluid-to-Fluid Modelling of the Critical Heat Flux and Post-Dryout Heat Transfer", Proceedings of Ex HFT-4, Brussels, Vol. 2, pp. 859-866, June 2-6.

Groeneveld, D.C., Leung, L.K.H., Vasic', A.Z., Guo, Y.J., and Cheng, S.C., (2003), "A Look-up Table for Fully Developed Film-Boiling Heat Transfer", Nuclear Engineering and Design, Vol. 225, pp. 83-97.

Hadaller, G., and Banerjee, S., (1969), "Heat Transfer to Superheated Steam in Round Tubes", Atomic Energy of Canada Limited, Internal Report WDI-147.

Hammouda, N., (1996), "Subcooled Film Boiling of Referigerants in Vertical up-Flow", Ph.D Thesis, University of Ottawa, Ottawa, Ontario, Canada.

Hammouda, N, Groeneveld, D.C., and Cheng, S.C., (1997), "Two-Fluid Modelling of Inverted Annular Film Boiling", *Int. J. of Heat and Mass Transfer*, Vol. 40, No. 11, pp. 2655-2670.

Hammouda, N, Groeneveld, D.C., and Cheng, S.C., (1996), "An Experimental Study of Subcooled Film Boiling of Refrigerants in Vertical up-Flow", *Int. J. of Heat and Mass Transfer*, Vol. 39, No. 18, pp. 3799-3812.

Han, S.H., and Bankoff, S.G., (1982), "Film Boiling from a Vertical Jet of Fuel Entering a Water Pool", *Nucl. Engrg. Des.*, Vol. 75, pp. 81-86.

Hein, D., and Kohler, W., (1984), "A Simple-to-Use post-Dryout Heat Transfer Model Accounting for Thermal non-Equilibrium", in *First Int. Workshop on Fundamental Aspects of Post-dryout Heat Transfer*, 2-4 April, Salt Lake City, UT, U.S.A NUREG/CP-0060.

Hench, J.E., (1964), "Forced Flow Transition Boiling Experiments in a Two Rod Test Section at High Pressures", ASME 64-WA/HT-44.

Herkenrath, H., Mork-Morkenstein, P., Jung, U., and Weckermann, F.J., (1967), "Warmeubergang an Wasser bei Erzwungener Stromung im Druckbereich von 140 bis 250 bar", EUR-3658d.

Huang, X.C., and Cheng, S.C., (1994), "Simple Method for Smoothing Multidimensional Experimental Data with Application to the CHF and Postdryout Look-up Tables", *Numerical Heat Transfer*, Part B, Vol.26, No.4, pp. 425-438, December.

Hsu, Y.Y., and Westwater, J.W., (1959), "Approximate Theory for Film Boiling on Vertical Surfaces", Chem. Engrg. Progress (Symposium), AIChE, Heat Transfer Conf., Storrs, Conn., Vol. 56, 15-24.

Hsu, C.C., Guo, Z.C., Yan, A., and Bi, H.R., (1986), "Low Pressure and Subcooled Water Flow Film Boiling Research by Visual Method", *4th Miami Int. Symp. On Multi-Phase Transport and Particulate Phenomena*, Miami Beach.

Iloeje, O.C., Plummer, D.N., Rohsenow, W.M., and Griffith, P., (1974), "A Study of Wall Rewet and Heat Transfer in Dispersed Vertical Flow", MIT Technical Report 72718-92.

Johannsen, K., (1988), "Low Quality Transition and Inverted Annular Flow Film Boiling of Water: an Updated Review", in EXPERIMENTAL HEAT TRANSFER, FLUID

MECHANICS AND THERMODYNAMICS, pp. 1416-1429, Eds: Shah, R. K., Ganic, E. N. and Young, K. T., Elsevier Science Publishing Co.

Jones, O.C., Jr., and Zuber, N., (1977), "Post-CHF Heat Transfer: A non-Eequilibrium Relaxation Model", ASME 77-HT-79.

Kalinin, E.K., Balashov, G.I., Berlin, I.I., Kostyuk, V.V., and Liventsov, V.M. (1977), "A Mathematical Model of Heat Transfer for Forced-Convective Film Boiling", *J. of Engg. Phys.*, Vol. 99, pp. 201-212.

Kalinin, E.K., Koshkin, V.K., Yarkho, S.R., Berlin, I.I., Kochelaev, Y.S., Kostyuk, V.V., Korolev, A.L., and Sdobnov, G.N., (1970), "Investigation of Film Boiling in Tubes with Subcooled Nitrogen Flow", *Fourth International Heat Transfer Conference*, B4.5, Paris.

Kaufman, J.M., (1976), "Post Critical Heat Flux Heat Transfer to Water in a Vertical Tube," M.Sc. Thesis, MIT.

Kawaji, M., and Banerjee, S., (1987), "Application of a Multifield Model to Reflooding of a Hot Vertical Tube: Part 1 - Model Structure and Interfacial Phenomena", *J. Heat Transfer, Trans.* ASME, Vol. 109, pp. 204-211.

Kays, W.M., and Crawford, M.E., (1980), CONVECTIVE HEAT AND MASS TRANSFER, 2nd Edition, McGraw-Hill Book Co.

Kays, W.M., and Leung, E.Y., (1963), "Heat Transfer in Annular Passages-Hydrodynamically Developed Turbulent Flow with Arbitrarily Prescribed Heat Flux", *Int. J. Heat Mass Transfer*, Vol. (6), pp. 537-557.

Keeys, R.K.F., Ralph, J.C., Roberts, D.N., (1971), "Post Burnout Heat Transfer in High Pressure Steam-Water Mixtures in a Tube with Cosine Heat Flux Distribution", AERE-R-6411.

Kohler, W., and Hein, D., (1986), "Influence of the Wetting State of a Heated Surface on Heat Transfer and Pressure Loss in an Evaporator Tube", Report NUREG/IA-0003.

Kumamaru, H., Koizumi, Y., and Tasaka, K., (1987), "Investigation of pre- and PDO Heat Transfer of Steam-Water Two-Phase Flow in a Rod Bundle", *Nuclear Engineering and Design,* Vol. 102, No. 1, pp. 71.

Laperriere, A., (1983), "An Analytical and Experimental Investigation of Forced Convective Film Boiling", M.A.Sc. Thesis, University of Ottawa, Ottawa, On., Canada.

Lee, D.H., (1970), "Studies of Heat Transfer and Pressure Drop Relevant to sub-Critical Once-Through Evaporators", *IAEA Symp. On Progress in Sodium-Cooled Fast Reactor Engineering,* IAEA-SM-130/56, Monaco.

Lee, Y., and Kim, K.H., (1987), "Inverted Annular Flow Boiling", *Int. J. Multiphase Flow,* Vol. 13, pp. 345-355.

Leung, L.K.H., and Groeneveld, D.C., (1988), "Development of post-Dryout Look-up Table for Loss-of-Regulation Accident Conditions", RC-34 (also CANDEV-88-68).

Mattson, R.J., Condie, K.G., Bengston, S.J., and Obenchain, C.F., (1974), "Regression Analysis of Post-CHF Flow Boiling Data", *Proc. 5th Int. Boiling Conf.*, Tokyo, Vol. 4, B.3.8, pp. 115-119.

Mayinger, F., and Langer, R., (1978), "PDO Heat Transfer", *Proc. 6th Int. Heat Transfer Conf.*, Toronto, Vol. 6, pp. 181.

Miropolskiy, Z.L., (1963), "Heat Transfer in Film Boiling of a Steam Water Mixer in Steam Generating Tubes", *Teploenergetika,* Vol. 10, pp. 49-53.

Moose, R.A., and Ganic, E.N., (1982), "On the Calculation of Wall Temperatures in the post Dryout Heat Transfer Region", *Int. J. Multiphase Flow*, Vol. 8, No. 5, pp. 525-542.

Mosaad, M., and Johannsen, K., (1989), "Experimental Study of Steady-State Film Boiling Heat Transfer of Subcooled Water Flowing Upwards in a Vertical Tube", *Experimental Thermal and Fluid Science*, Vol. 2, pp. 477-493.

Mosaad, M., and Johannsen, K., (1988), "Subcooled Film Boiling Heat Transfer to Flowing Water in a Vertical Tube at Atmospheric Pressure", *Int. Symp. on Phase Change Heat Transfer*, Chong Qiung, China, May 20-23.

Plummer, D.N., Griffith, P., and Rohsenow, W.M., (1976), "Post-Critical Heat Transfer to Flowing Liquid in a Vertical Tube", *16th National Heat Transfer Conference*, 76-CSME/ChE-13, St. Louis.

Polomik, E.E., (1967), "Transition Boiling Heat Transfer Program", Final Summary Report on Program for Feb/63-Oct/67», GEAP-5563.

Polomik, E.E., Levy, S., and Sawochka, S.G., (1961), "Heat Transfer Coefficients with Annular Flow During Once Through Boiling of Water to 100 % Quality at 800, 1000, and 1400 psi", GEAP-3703.

Saha, P., (1980), "A Non-Equilibrium Heat Transfer Model for Dispersed Droplet Post-Dryout Regime", *Int. J. Heat & Mass Transfer*, Vol. 23, pp. 483-492.

Schmidt, K.R., (1960), "Thermodynamic Investigations of Highly Loaded Boiler Heating Surfaces", AEC-TR-4033.

Sergeev, V.V., (2005), "One-Dimensional Model of Post-Dryout Heat Transfer", The 11th International Topical Meeting on Nuclear Reactor Thermal-Hydraulics (NURETH-11), paper # 196, Avignon, France, October 2-6.

Shah, M.M., (1980), "A General Predictive Technique for Heat Transfer During Saturated Film Boiling in Tubes", *Heat Transfer Engineering*, Vol. 2, pp. 51-62.

Shah, M.M., and Siddiqui, M.A., (2000), "A General Correlation for Heat Transfer During Dispersed-Flow Film Boiling in Tubes", *Heat Transfer Engineering*, Vol. 21, pp. 18-32.

Siegel, R., and Howell, J.R., (1972), THERMAL RADIATION HEAT TRANSFER, McGraw-Hill, New York.

Siviour, J.B., and Ede, A.J., (1970), "Heat Transfer in Subcooled Pool Film Boiling" *Fourth Int. Heat Transfer Conf.*, B3.12, Paris.

Slaughterbeck, D.C., Ybarrondo, L.J., and Obenchain, C.F., (1973), "Flow Film Boiling Heat Transfer Correlations: A Parametric Study with Data Comparisons", *ASME 73-HT-50.*

Stewart, J.C., (1981), "Low Quality Film Boiling at Intermediate and Elevated Pressures", M.A.Sc. Thesis, University of Ottawa.

Stewart, J.C., and Groeneveld, D.C., (1982), "Low Quality and Subcooled Film Boiling at Elevated Pressures", *Nuclear Engineering and Design,* Vol. 67, pp. 259-272.

Swenson, H.S., Carver, J.R., and Szoeke, G., (1961), "The Effects of Nucleate Boiling Versus Film Boiling on Heat Transfer in Power Boiler Tubes", *ASME* 61-WA-201.

Takenaka, N., Fujii, T., Akagawa, K., and Nishida, K., (1989), "Flow Pattern Transition and Heat Transfer of Inverted Annular Flow", *Int. J. Multiphase Flow*, Vol. 15, pp. 767-785.

Tong, L.S., (1965), BOILING HEAT TRANSFER AND TWO-PHASE FLOW, John Wiley and Sons.

Tong, L.S., and Young, J.D., (1974), "A Phenomenological Transition and Film Boiling Heat Transfer Correlation," *Fifth Int. Heat Transfer Conf.*, Vol. IV, B3.9, Tokyo.

Varone, A.F., and Rohsenow, W.M., (1984), "Post-Dryout Heat Transfer Prediction", in *First Int. Workshop on Fundamental Aspects of post-Dryout Heat Transfer*, 2-4 April, Salt Lake City, UT, U.S.A NUREG/CP-0060.

Wang, B.X., and Shi, D.H., (1984), "A Semi-Empirical Theory for Forced-Flow Turbulent Film Boiling of Subcooled Liquid Along a Horizontal Plate", *Int. J. Heat Mass Transfer,* Vol. 28, pp. 1499-1505.

Wang, B.X., Lin, Z.Z., Peng, X.E., and Yuan, H.J., (1988), "Experimental Study of Steady Turbulent Flow Film Boiling of Subcooled Liquid R 11 Flowing Upward in a Vertical Circular Tube", *Sci. Sinica*, Vol. 31.

Webb, S.W., and Chen, J.C., (1984), "A Two-Region Vapor Generation Rate Model for Convective Film Boiling", in *First Int. Workshop on Fundamental Aspects of Post-dryout Heat Transfer,* 2-4 April, Salt Lake City, UT, U.S.A NUREG/CP-0060.

Webb, S.W., Chen, J.C., and Sundaram, R.K., (1982), "Vapor Generation Rate in non-Equilibrium Convective Film Boiling", *7th Int. Heat Transfer Conf.,* Munich, Germany.

Yan, D. M., (1987), "Subcooled Forced Convection Film Boiling Heat Transfer", In Book: HEAT TRANSFER SCIENCE AND TECHNOLOGY, Hemisphere, Washington.

Yoder, G.L., and Rohsenow, W.M., (1983), "A Solution for Dispersed Flow Heat Transfer Using Equilibrium Fluid Conditions", *J. Heat Transfer*, Vol. 105, pp. 10-17.

APPENDIX-A

CALCULATING INSIDE WALL TEMPERATURE

The inside wall temperature is calculated using the measured outside wall temperature and the heat conduction equation with heat generation in the tube wall. By neglecting the axial heat conduction, the steady-state heat conduction equation with heat generation for the tube wall is

$$\frac{d^2T}{dr^2}+\frac{1}{r}\cdot\frac{dT}{dr}+\frac{q'''}{k}=0 \tag{A.1}$$

where q''' is the heat generated per unit volume (Wm^{-3}). The temperature distribution in the tube wall is obtained by double integration of equation (A.1). this will yield,

$$T=-\frac{r^2q'''}{4k}+c_1\ln r+c_2 \tag{A.2}$$

To solve for coefficients c_1 and c_2, the following boundary conditions are used:

At $r=r_o$, $T=T_o$, and $-k\left.\frac{dT}{dr}\right|_{r=r_o}=q''_{loss}$

at $r=r_i$, $T=T_i$

where

$r_i \equiv$ inside tube radius

$r_o \equiv$ outside tube radius

$T_i \equiv$ inside wall temperature

$T_o \equiv$ outside wall temperature

Substituting the boundary conditions and into Equation (A.2) and solving for the coefficients c_1 and c_2, it produces

$$c_1 = \frac{q''' r_o^2 - 2q''_{loss} r_o}{2k}$$

$$c_2 = T_o + \frac{q''' r_o^2}{4k} + \frac{2q''_{loss} r_o - q''' r_o^2}{2k} \ln r_o$$

In this analysis, the heat loss from the wall to atmosphere, q''_{loss}, is neglected as was described in Section 5.6.1. It follows that the inside wall temperature is

$$T_i = T_o - \frac{q''' r_o^2}{2k} \ln \frac{r_o}{r_i} + \left(r_o^2 - r_i^2\right) \frac{q'''}{4k} \quad \text{(A.3)}$$

In Equation (A.3), the heat generation is calculated as

$$q''' = \frac{2q'' r_i}{\left(r_o^2 - r_i^2\right)} \quad \text{(A.4)}$$

The tube wall thermal conductivity, k_w, of Inconel 600 is evaluated from the curve fit of manufacturer's data:

$$k_w = 11.4601 + 0.0165946 T_w \quad \text{(A.5)}$$

APPENDIX-B

QUALITY ASSURANCE AND ERROR ANALYSIS

B.1. Quality Assurance

B.1.1. Leakage detection

Leakage detection is performed by filling the whole test loop with nitrogen at 400 psi. All of the potential leaking sites are checked using soap-water solution. The system is considered as leak-proof if the pressure change is less than 4 psi after 24 hours of nitrogen inside the testing facility.

B.1.2. Transient temperature test

This procedure is employed to check the response of thermocouples by quickly turning on and off the power supply to the test section. The response speed of all of the thermocouples installed on the test section is found acceptable.

B.1.3. Calibration of pressure

Pressure calibration is performed while the loop is filled with nitrogen. The reading of pressure gauge mounted on the bottom of the test section, p_{gauge}, is treated as a standard. The values of the inlet and outlet pressures indicated by the data acquisition system (DAS) are recorded and compared with the values of the pressure gauge. The results are showed in Figure B.1. The discrepancies between the reading from the pressure gauge and the inlet and outlet pressures are less than 0.5%.

B.1.4. Calibration of voltage and current

Values of voltage and current indicated in DAS are compared with the readings of voltmeter and ammeter mounted on the power supply. The results are shown in Figures B.2 and B.3. Very good agreement is found in the results of voltage and current

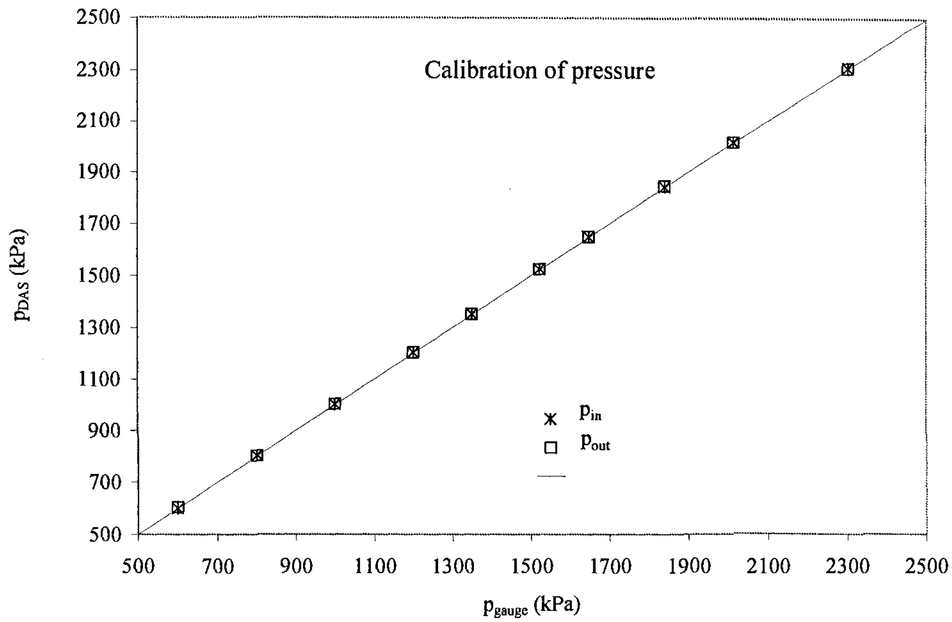

(a)

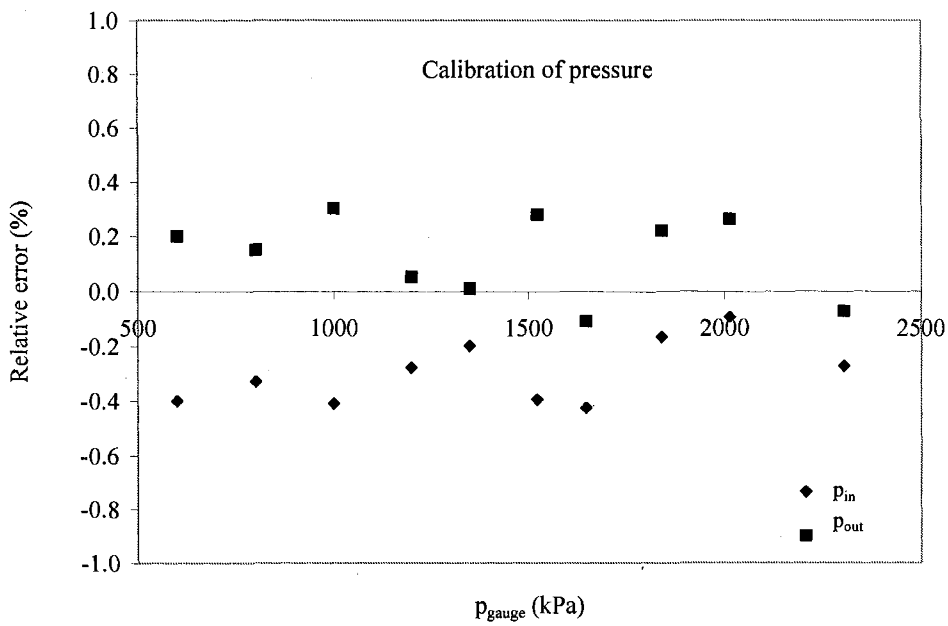

(b)

Figure B.1 Result of calibration of Pressure.

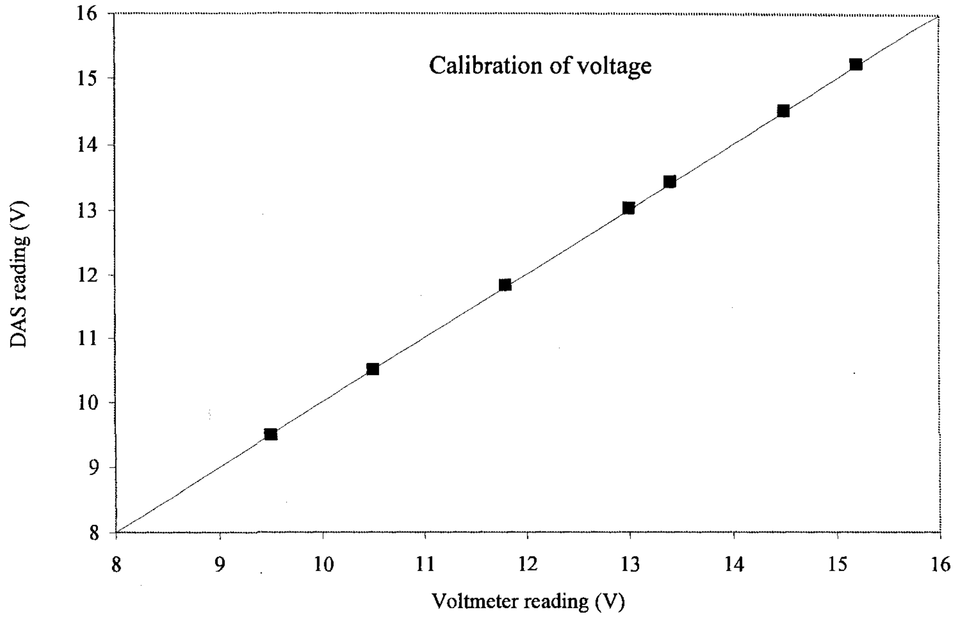

(a)

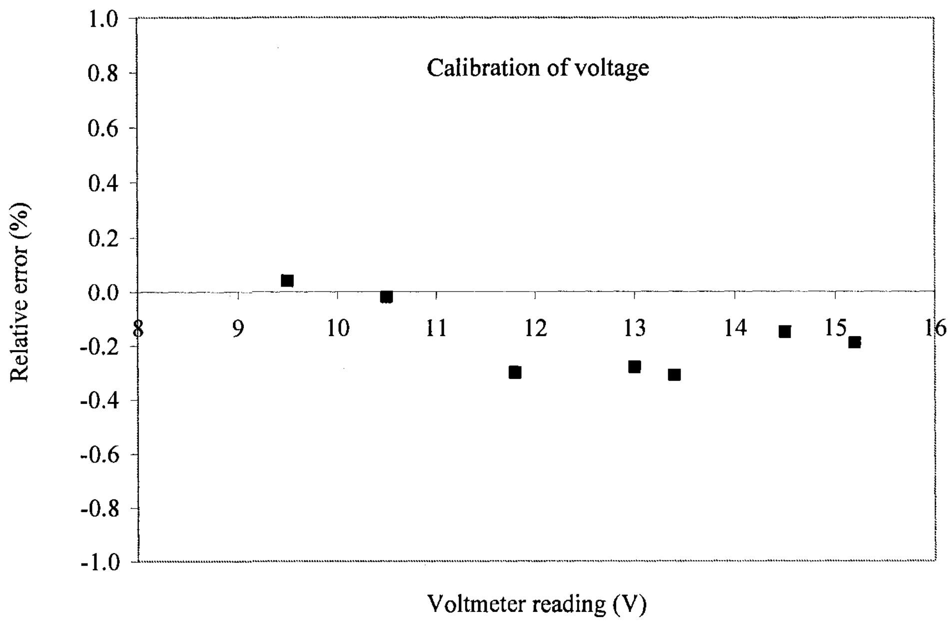

(b)

Figure B.2 Result of calibration of voltage.

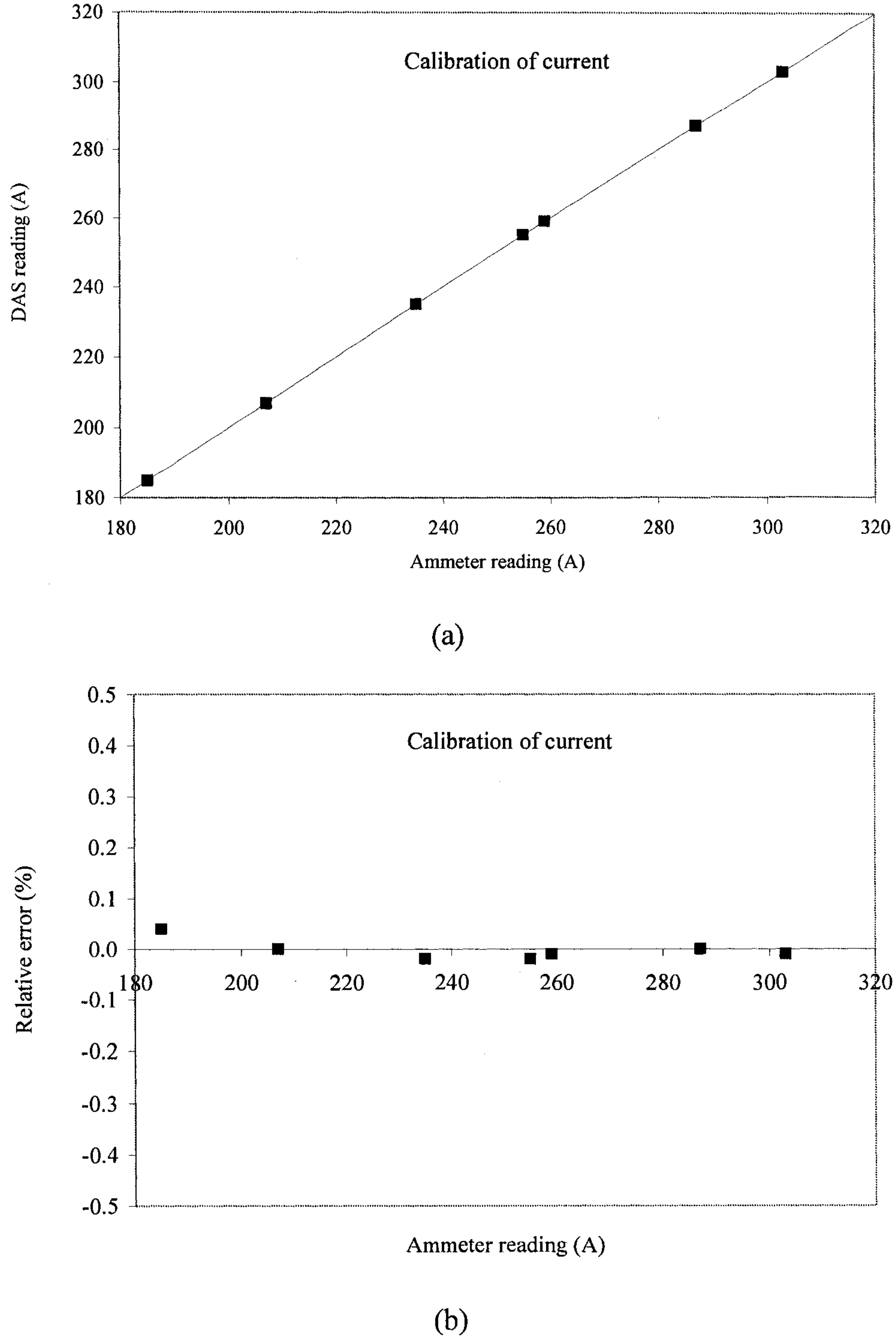

Figure B.3 Result of calibration of current.

calibration. The differences between the voltages and the currents are within 0.35% and 0.1%, respectively.

B.1.5. Calibration of RTDs and thermocouples

RTDs and thermocouples for measuring inlet fluid temperature are calibrated by means of comparison with a standard mercury thermometer. The calibration results are shown in Figures B.4. The discrepancies between the mercury thermometer and the RTDs and thermocouples were within 0.7% and 2%, respectively.

B.2. Analysis of Measurement Uncertainties

B.2.1. General

When uncertainties, U_v, are introduced by K different components or steps, v, of the measuring process (for example by calibration, data acquisition or data processing), the total uncertainty is determined as

$$\frac{U_v^2}{v^2} = \sum_{k=1}^{K} \left(\frac{U_v}{v} \right)_k^2 \qquad \text{(B.1)}$$

The uncertainty in a calculated result is a function of the uncertainty in each of the individual measurements used in calculating that result. Assuming a result, R, is a function of a number of independent variable, $v_1, v_2, \ldots, v_n$, then

$$R = f(v_1, v_2, \ldots, v_n)$$

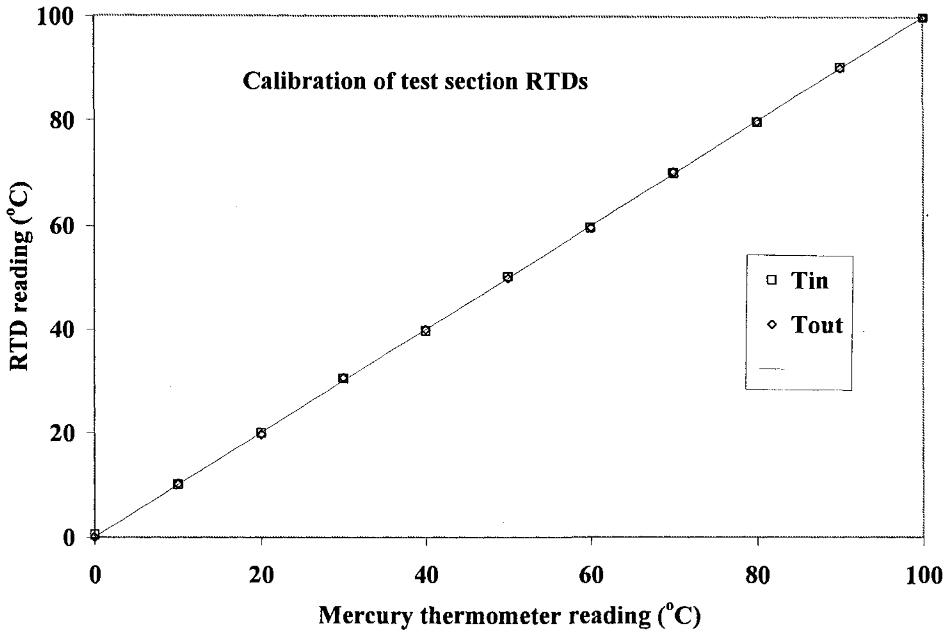

(a)

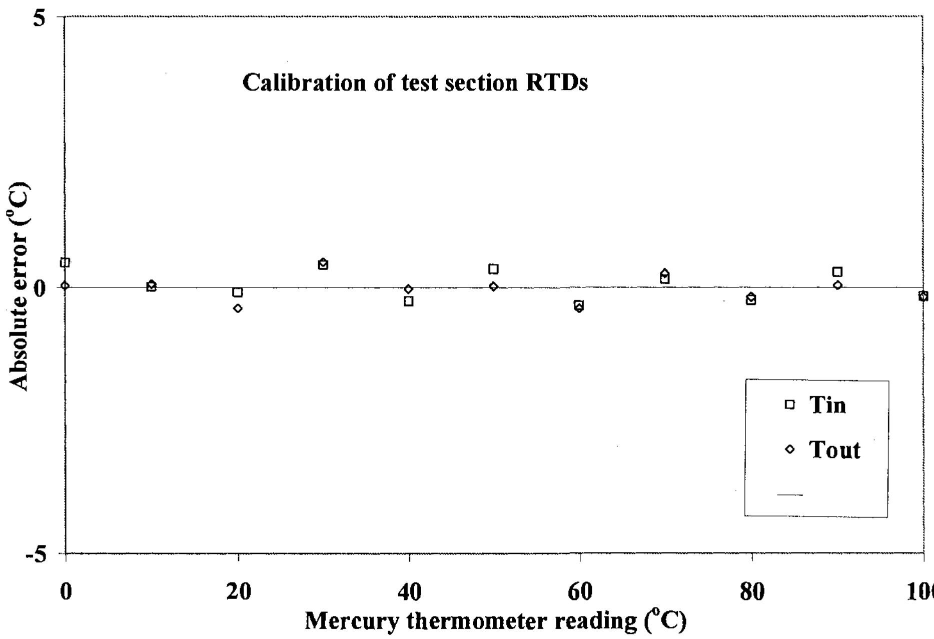

(b)

Figure B.4 Calibration results of RTDs used for measuring fluid temperature.

The uncertainty on the result, U_R, becomes

$$U_R = \sqrt{\left(\frac{\partial R}{\partial v_1}\right)^2 U_1^{\;2} + \left(\frac{\partial R}{\partial v_2}\right)^2 U_2^{\;2} + \cdots + \left(\frac{\partial R}{\partial v_n}\right)^2 U_n^{\;2}} \tag{B.2}$$

where $U_1, U_2, \ldots, U_n$ are the corresponding uncertainties of the $v_1, v_2, \ldots, v_n$. The $(\partial R/\partial v_i)$ is the sensitivity coefficient. This type of uncertainty is called "combined standard uncertainty". Each variable's contribution is just the square of the associated uncertainty expressed as a standard deviation multiplied by the square of the relevant sensitivity coefficient. Equation (B.2) can be re-written in non-dimensional form as

$$\frac{U_R^2}{R^2} = \sum_{i=1}^{n} \left(\frac{v_i}{R}\frac{\partial R}{\partial v_i}\right)^2 \left(\frac{U_i}{v_i}\right)^2 \tag{B.3}$$

The uncertainties in directly measured variables assessed by Equation (B.1) are shown in Table B.1. The evaluation for the uncertainties in calculated results are described below in details.

B.2.2. Uncertainty in mass flux

The mass flux is calculated as follows:

$$G = \frac{4\dot{m}}{D^2 \pi}$$

The uncertainty is given by

Table B1 Evaluation of Uncertainties for the Directly Measured Variable

Measured Variable	Symbol	Units	Error Source	Device Range	Used Range	Uncertainties
Test section inside diameter	D	mm	Measuring device accuracy ± 0.001" => ± 0.0254 mm.	5.461	5.461	$U_D = 0.0254$ mm
Test section heated length	Lh	m	Measuring device accuracy ± 1mm.	1.1	0.9 - 1.2	$U_{Lh} = 0.001$ m
Pressure	P	kPa	Viatran pressure transducer Model 245 0 - 500 psi, 0 - 3447 kPa, output 0 - 5 V accuracy ± 0.1% FSO (Full Scale Output), (3447 kPa => ± 3.447 kPa) connected to National Instrument DAS AT-MIO-16E-1 with SCXI-1121 and terminal block SCXI-1320 accuracy ±0.15% of full scale reading, (3447 kPa => ± 5.171 kPa).	0 - 3447	635 - 2390	$(U_P)_{max}$=4.31 kPa $\frac{U_P}{P} = 0.0018$
Mass flow rate	ṁ	kg s^{-1}	Miro Motion mass flow sensor DS040S119SC with RFT9739 Transmitter, 0 - 20 kg min^{-1} (0.333 kg s^{-1}), output 4 - 20 mA accuracy ±0.2% FSO (Full Scale Output), (0.333 kg s^{-1} => ± 0.000666 kg s^{-1}) connected to National Instrument DAS AT-MIO-16E-1 with SCXI-1120 accuracy ± 0.6% of reading and terminal block SCXI-1327 accuracy ± 0.06% of reading (the range of mass flux during experiments are from 2826 kg m^{-2} s^{-1} => 0.0662 kg s^{-1} to 4648 kg m^{-2} s^{-1} => 0.1089 kg s^{-1}).	0 - 0.333	0.0237 - 0.1523	$(U_{\dot{m}})_{max} = 0.001134 kgs^{-1}$ $\frac{U_{\dot{m}}}{\dot{m}} = \sqrt{(0.006)^2 + (0.0006)^2 + \left(\frac{0.000666}{\dot{m}}\right)^2}$

Table B1 (concluded)

Measured Variable	Symbol	Units	Error Source	Device Range	Used Range	Uncertainties
Test section electrical voltage	U	V	Sorensen power supply DCR 40 - 300, 0 - 40 V, output 0 - 5 V connected to National Instrument DAS AT-MIO-16E-1 with SCXI-1120 accuracy ± 0.6% of reading and terminal block SCXI-1327 accuracy ± 0.06% of reading.	0 - 40	0 - 40	$(U_U)_{max}$=0.241 V $\frac{U_U}{U} = 0.006$
Test section electrical current	I	A	Sorensen power supply DCR 40 - 300, 0 - 320 A, remote current monitor (pins no. 11 and no. 17) output 0 - 2.24 V scaled with Labview to current 0 - 320 A, connected to National Instrument DAS AT-MIO-16E-1 with SCXI-1120 accuracy ± 0.6% of reading and terminal block SCXI-1327 accuracy ± 0.06% of reading.	0 - 320	0 - 320	$(U_I)_{max}$=1.93 A $\frac{U_I}{I} = 0.006$
Inlet temperature	Tin	°C	OMEGA 3-wire platinum RTD 1/8" probe accuracy ± 0.8 °C connected to National Instrument DAS AT-MIO-16E-1 with SCXI-1121 and terminal block SCXI-1320 accuracy ± 0.15% of full sacle reading (100 °C => ± 0.15 °C).	0 - 100	0 - 76	$(U_{Tin})_{max}$=0.813 °C $\frac{U_{Tin}}{Tin} = \sqrt{\left(\frac{0.8}{Tin}\right)^2 + \left(\frac{0.15}{Tin}\right)^2}$
HFC-134a property	–	–	UO property code for HFC-134a based on Tillner-Roth and Baehr (1994) formulation accuracy ± 0.5%.	–	–	$\frac{U_{Prop}}{Prop} = 0.005$

$$\frac{U_G}{G} = \sqrt{\left(2\frac{U_D}{D}\right)^2 + \left(\frac{U_{\dot{m}}}{\dot{m}}\right)^2}$$

which ranged from 0.015 – 0.0127 in this experiment (G = 2826 – 4648 kg m-2 s-1) .

B.2.3. Uncertainty in power

The power is calculated as follows:

$$Power = U \times I$$

The uncertainty is given by

$$\frac{U_{Power}}{Power} = \sqrt{\left(\frac{U_U}{U}\right)^2 + \left(\frac{U_I}{I}\right)^2}$$

APPENDIX-C

FLUID-TO-FLUID MODELING TECHNIQUES USED TO CALCULATE EQUIVALENT FLOW CONDITIONS

Fluid-to-Fluid Modeling Techniques Used to Calculate Equivalent Flow Conditions

C.1. Introduction

Fluid-to-fluid modeling is a technique to model a thermalhydraulic phenomenon in a working fluid (usually water) by using a modeling fluid (usually a member of the Freon family). Fluid-to-fluid modeling uses dimensional analysis (or what is known as Buckingham Pi theory). In this approach, non-dimensional groups are formed from the independent and dependent variables of the process. Two different processes are assumed to be scaled if the values of the dimensionless groups are equal for both processes. This method has proven to be very useful for discovering the important non-dimensional groups that should be used as the basis for correlating empirical information, e.g. friction factors and heat transfer coefficients. The method of dimensional analysis is applied successfully to model the critical heat flux phenomenon [e.g. Ahmad (1973)].

Fluid-to-fluid modeling techniques for film boiling are not well established. This introduces considerable difficulties in designing simulation experiments for instance for the case where film boiling heat transfer occurs. Unlike for the case of CHF, scaling laws which consider thermodynamic equilibrium, film boiling is more difficult to model and less predictable. This can be attributed to many reasons such as the involvement of radiation heat transfer, existence of non-equilibrium thermodynamics, etc.

In a first attempt to model film boiling phenomenon, Groeneveld et al. (1997) suggested using dimensionless groups similar to those used to model CHF. A more thorough study on fluid-to-fluid modeling of film boiling heat transfer was performed by El Nakla et al.

(2005). They showed that dimensional analysis can successfully be applied to model film boiling heat transfer.

C.2. General Description

The derivation of fluid to fluid modeling scheme is explained in detail by El Nakla et al. (2005). It starts with selecting the parameters that are important in representing the film boiling heat transfer phenomena. The wall superheat can be expressed as a function of the following parameters

$$\Delta T = f\left(q, \rho_f, \rho_g, G, \Delta H, H_{fg}, \mu_g, D, k_g\right) \tag{C.1}$$

where

$$\Delta T = T_W - T_{sat}$$

and

$$\Delta H = H - H_g$$

Performing dimensional analysis to Equation (C.1) yields

$$\frac{\Delta T . k_g . \rho_g^2 D^2}{\mu_g^3} = f\left(\frac{q . \rho_g^2 . D^3}{\mu_g^3}, \frac{\rho_f}{\rho_g}, \mathrm{Re}, x\right) \tag{C.2}$$

Equation (C.2) can further be simplified to

$$\frac{\Delta T.k_g.\rho_g^2}{\mu_g G^2} = f\left(\frac{\rho_f}{\rho_g}, \mathrm{Re}, \frac{q.\rho_g^2}{G^3}, x\right) \quad \text{(C.3)}$$

Table C.1 summarizes the equations used to model each flow parameter.

C.3. Assessment of Proposed Fluid-to-Fluid Modeling Relationship against the Film Boiling Look-up Table

The film boiling look-up table [El Nakla et al. (2004)] was used to assess the proposed fluid-to-fluid relationships [Equation (C.3)] using 4968 fully developed film boiling data points of R-134a. The film boiling look-up table is for an 8 mm tube diameter. To account for the differences in diameters of R-134a experimental data and the look-up table diameter, a correction factor was used as follows:

$$h_{D_{LUT}} = \left(\frac{D_{LUT}}{D_{equiv}}\right)^{-0.2} h_{D_{equiv}} \quad \text{(C.4)}$$

After applying Equation (C.3), the equivalent heat transfer coefficients of all data used in the assessment were predicted with an average and RMS errors of 1.55% and 17.22%, respectively, compared to the film boiling look-up table. These errors include the uncertainty of the fluid-to-fluid modeling technique, the film boiling look-up table, the Freon data and the thermophysical properties. The equivalent heat transfer coefficient is compared to the look-up table in Figure C.1. The figure shows converted R-134a data from different data sets and for different flow conditions. Reasonable agreement between equivalent heat transfer coefficient and look-up table values is observed in the figure.

Table C.1 Summary of parameters used in fluid-to-fluid modeling

Parameter	Dimensionless ratio	Modeling Equation
Modeling Pressure	$\left(\frac{\rho_f}{\rho_g}\right)_{equiv} = \left(\frac{\rho_f}{\rho_g}\right)_R$	Pressure is modeled by iteration
Modeling Mass Flux	$\left(\frac{GD}{\mu_g}\right)_{equiv} = \left(\frac{GD}{\mu_g}\right)_R = \mathrm{Re}$	$G_{equiv} = \mathrm{Re}_R \frac{(\mu_g)_{p=p_{equiv}}}{D_{equiv}}$
Modeling Heat Flux	$\left(\frac{q.\rho_g^2}{G^3}\right)_{equiv} = \left(\frac{q.\rho_g^2}{G^3}\right)_R$	$q_{equiv} = \left(\frac{q.\rho_g^2}{G^3}\right)_R \left(\frac{G^3}{\rho_g^2}\right)_{equiv}$
Modeling Quality	$(x)_{equiv} = (x)_R$	$(x)_{equiv} = (x)_R$
Modeling Wall Temperature	$\left(\frac{\Delta T.k_g.\rho_g^2}{\mu_g G^2}\right)_{equiv} = \left(\frac{\Delta T.k_g.\rho_g^2}{\mu_g G^2}\right)$	$T_{W,equiv} = \left(\frac{\Delta T.k_g.\rho_g^2}{\mu_g G^2}\right)_R \left(\frac{\mu_g G^2}{k_g \rho_g^2}\right)_{equiv} + T_{sat,equiv}$
Modeling Tube Diameter	$D_{equiv} = D_R$	$D_{equiv} = D_R$
Heat Transfer Coefficient		$h_{equiv} = \frac{q_{equiv}}{\Delta T_{W,equiv}}$

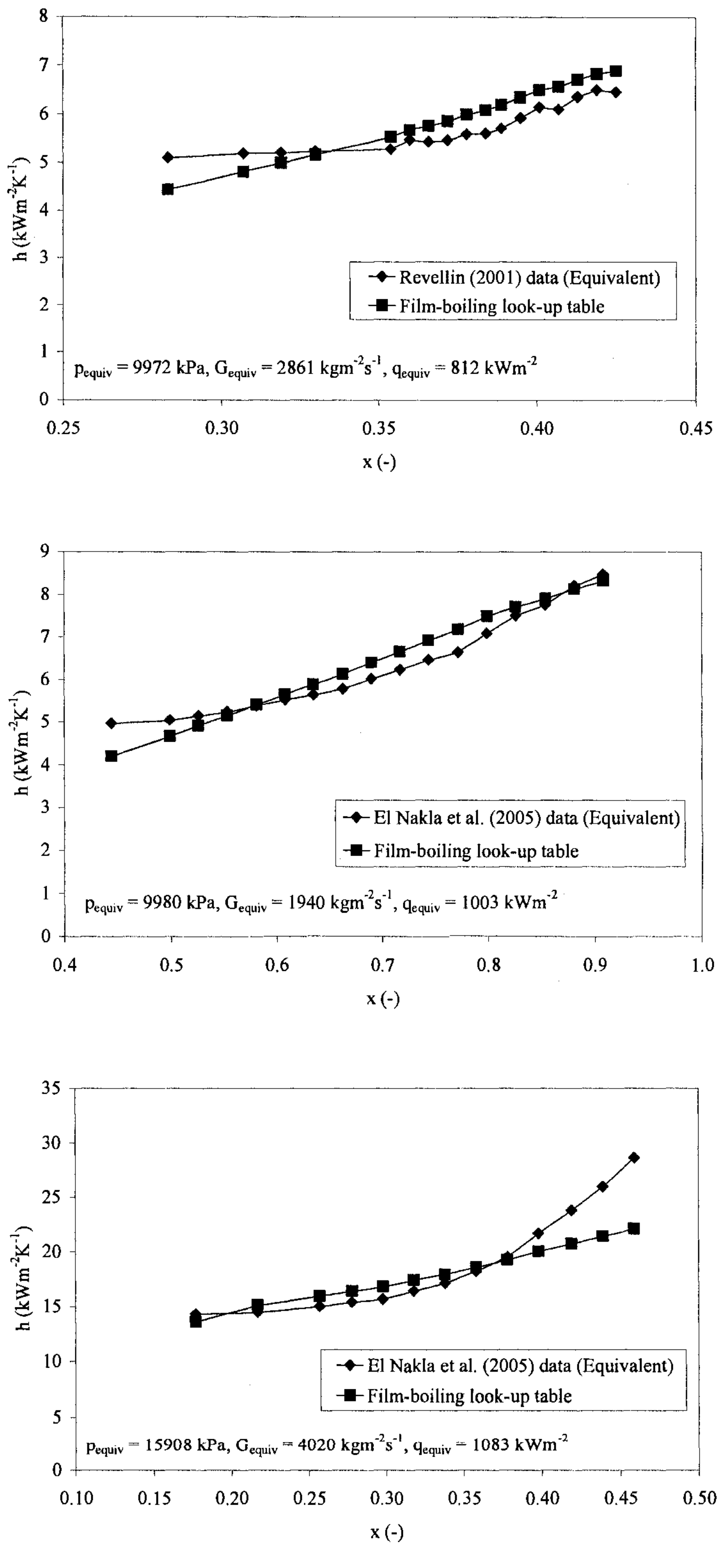

Figure C.1 Equivalent heat transfer coefficients compared to the film-boiling look-up values at different flow conditions and from different data sets.

APPENDIX-D

EXPERIMENTAL DATA

The experimental data are listed, respectively, by column as in the following table:

Symbol	Meaning	Unit
Run	Serial number of run	-
p	Pressure at test section outlet	kPa
Δp	Pressure drop	kPa
m	Mass flowrate	kgs^{-1}
G	Mass flux	$kgm^{-2}s^{-1}$
power	Power supplied to test section	kW
q"	Wall heat flux	kWm^{-2}
hp-power	Hot-patch power	kW
T_{in}	Inlet temperature to the test section	^oC
x_{in}	Inlet quality to the test section	-
x_{DO}	Quality at CHF location	-
T_{hp}	Hot-patch block temperature	^oC

For the effect of hot-patch data, the same symbols are used except for the column labelled "Run". This is replaced with "Time" measured in seconds from the time the hot-patch power is switched off.

Experimental Data

Run	p	Δp	m	G	power	q	hp-power	T_{in}	x_{in}	x_{DO}	T_{hp}	Distance from CHF location (m)											
-	kPa	kPa	Kgs^{-1}	$Kgm^{-2}s^{-1}$	kW	kWm^{-2}	kW	°C	-	-	°C	0.01	0.05	0.10	0.20	0.30	0.40	0.50	0.60	0.70	0.80	0.90	1.00
												Inside wall temperature (°C)											
1	634.3	8.08	0.0495	528.3	0.595	30.3	0.240	14.32	-0.071	0.050	99.0	98.0	109.1	114.8	118.0	119.9	122.4	125.2	126.9	129.5	131.5	134.0	136.2
2	640.3	7.41	0.0493	526.1	0.595	30.3	0.240	10.81	-0.101	0.021	116.8	91.7	94.6	99.9	110.3	115.3	118.5	122.8	125.2	128.3	130.0	132.0	133.6
3	639.0	11.45	0.0476	508.5	0.602	30.6	0.240	20.12	-0.028	0.098	84.9	102.7	118.1	122.8	126.4	128.5	130.6	132.5	134.2	136.3	137.2	137.9	139.3
4	645.1	7.07	0.0530	565.7	0.787	40.1	0.240	8.33	-0.122	-0.005	125.5	112.8	119.0	129.0	138.4	145.1	149.7	152.8	154.6	156.5	157.9	159.9	161.2
5	636.3	6.40	0.0468	499.7	0.791	40.3	0.240	14.32	-0.072	0.060	94.6	121.9	140.8	146.5	151.4	153.1	154.4	156.9	158.1	160.5	162.7	164.9	166.6
6	638.3	9.76	0.0450	480.0	0.795	40.5	0.240	11.02	-0.099	0.040	130.0	127.3	136.9	144.5	149.8	152.5	156.1	158.8	160.4	162.6	164.2	165.8	167.8
7	633.6	14.48	0.0479	510.7	0.803	40.9	0.240	19.91	-0.028	0.102	86.4	127.0	149.3	155.7	160.3	161.4	162.0	163.0	163.9	165.5	166.7	167.8	168.8
8	636.3	12.79	0.0474	506.3	0.988	50.3	0.240	10.81	-0.099	0.036	140.5	154.9	172.5	178.6	183.8	185.3	186.0	187.1	187.8	188.4	188.9	189.6	190.3
9	638.3	6.73	0.0474	506.3	0.991	50.4	0.240	14.53	-0.071	0.064	93.1	143.8	171.3	178.3	183.4	184.4	184.0	185.0	185.8	186.4	187.4	188.9	191.0
10	637.7	14.81	0.0485	517.3	0.997	50.7	0.240	19.50	-0.032	0.101	88.4	146.3	174.3	182.8	187.1	187.8	187.9	187.4	187.4	187.4	187.7	187.3	187.8
11	642.4	7.74	0.0507	541.5	0.998	50.8	0.240	8.33	-0.121	0.006	133.9	143.6	161.6	172.4	178.3	180.7	183.2	184.7	185.5	185.7	185.3	185.8	186.2
12	641.0	6.73	0.0501	534.9	1.180	60.1	0.240	8.33	-0.120	0.012	139.9	168.0	193.0	201.8	207.3	209.1	209.1	207.9	206.4	205.2	204.2	202.1	199.0
13	637.0	11.78	0.0476	508.5	1.183	60.2	0.240	14.74	-0.069	0.070	92.6	164.6	198.8	207.5	212.1	211.3	210.9	209.0	208.6	209.2	207.8	206.3	204.3
14	635.0	14.14	0.0487	519.5	1.185	60.3	0.240	18.67	-0.038	0.099	91.1	166.2	198.5	208.5	211.8	212.1	210.1	208.6	207.8	207.2	206.0	202.4	200.3
15	640.3	12.79	0.0495	528.3	1.186	60.4	0.240	10.60	-0.103	0.032	149.0	178.1	202.4	209.9	213.4	213.5	213.0	211.4	210.2	209.2	209.0	207.6	205.5
16	640.3	6.40	0.0509	543.7	1.379	70.2	0.240	8.33	-0.120	0.015	146.0	193.3	226.0	233.2	237.1	235.2	233.1	230.5	228.5	226.1	224.4	221.2	216.0
17	637.7	0.67	0.0963	1027.5	0.405	20.6	0.336	19.08	-0.036	0.047	185.8	116.1	92.5	84.9	83.4	82.5	83.9	85.3	86.5	87.2	87.9	88.6	89.6
18	637.7	1.35	0.0989	1056.1	0.595	30.3	0.336	19.29	-0.034	0.048	191.3	138.2	122.2	117.0	116.5	115.2	115.0	115.9	115.4	114.5	114.3	114.5	113.8
19	639.0	0.00	0.0967	1031.9	0.596	30.3	0.336	14.32	-0.073	0.011	171.8	121.4	107.9	104.1	106.1	108.3	111.1	114.4	116.3	117.7	117.9	118.9	120.2
20	642.4	0.67	0.0967	1031.9	0.598	30.4	0.336	9.78	-0.110	-0.025	160.2	95.8	79.0	74.2	83.3	90.2	96.5	102.2	106.2	110.6	114.1	119.2	123.0
21	634.3	0.67	0.0940	1003.3	0.697	35.5	0.336	7.51	-0.124	-0.036	158.7	104.0	84.9	84.6	94.7	102.7	109.3	115.7	121.4	126.5	130.1	132.7	136.5
22	637.0	3.03	0.0963	1027.5	0.786	40.0	0.336	14.32	-0.073	0.014	174.5	146.0	140.2	138.7	141.3	142.8	144.0	144.9	144.3	143.4	142.3	141.4	139.6
23	630.9	1.01	0.0967	1031.9	0.788	40.1	0.336	7.51	-0.122	-0.036	162.6	119.2	117.1	134.0	142.0	141.9	143.5	144.3	144.7	144.7	145.6	145.0	142.7
24	636.3	1.68	0.0975	1040.7	0.795	40.5	0.336	9.78	-0.107	-0.021	164.5	128.2	121.9	120.0	127.2	133.0	138.5	143.2	146.0	147.2	146.9	148.5	150.0
25	637.0	5.72	0.0971	1036.3	0.799	40.7	0.336	19.08	-0.036	0.051	195.6	160.6	152.2	148.6	147.6	145.4	143.1	142.5	139.6	137.8	136.7	134.5	132.6
26	632.9	3.37	0.0950	1014.3	0.988	50.3	0.336	7.51	-0.123	-0.033	166.2	146.2	145.9	170.0	171.0	172.7	174.7	175.3	174.2	172.6	171.2	167.6	160.1
27	641.0	4.04	0.0992	1058.3	0.989	50.3	0.336	9.78	-0.109	-0.023	166.6	151.4	153.9	158.7	162.7	166.7	169.6	172.4	173.2	172.6	169.4	167.2	163.4
28	636.3	5.72	0.0940	1003.3	0.991	50.4	0.336	14.32	-0.072	0.019	177.0	168.6	169.8	170.9	173.7	174.3	173.7	171.7	168.8	165.6	162.0	159.7	154.8
29	637.7	8.08	0.1022	1091.3	0.998	50.8	0.336	19.29	-0.034	0.050	198.0	181.4	177.3	174.5	173.0	169.9	167.0	163.5	158.6	155.2	152.5	149.1	145.1
30	635.6	6.73	0.0969	1034.1	1.181	60.1	0.336	9.98	-0.105	-0.015	168.7	173.5	185.3	190.5	194.1	195.6	196.6	196.5	194.8	191.1	185.8	181.2	173.7

Run	p	Δp	m	G	power	q	hp-power	T_{in}	x_{in}	x_{DO}	T_{hp}	Distance from CHF location (m)											
-	kPa	kPa	Kgs^{-1}	$Kgm^{-2}s^{-1}$	kW	kWm^{-2}	kW	°C	-	-	°C	0.01	0.05	0.10	0.20	0.30	0.40	0.50	0.60	0.70	0.80	0.90	1.00
												Inside wall temperature (°C)											
31	635.6	9.43	0.0930	992.3	1.182	60.2	0.336	19.50	-0.032	0.063	199.8	200.3	199.3	197.7	195.0	189.9	184.9	179.0	173.9	168.1	164.7	160.6	156.3
32	632.9	6.40	0.0979	1045.1	1.183	60.2	0.336	7.51	-0.123	-0.033	168.2	169.2	185.0	192.0	193.9	195.9	195.9	197.5	195.1	191.9	190.1	183.9	172.7
33	637.0	9.09	0.0967	1031.9	1.189	60.5	0.336	14.32	-0.073	0.018	179.4	188.4	196.0	197.8	198.6	196.3	194.5	191.6	186.5	180.5	176.3	171.8	165.6
34	637.0	10.44	0.0967	1031.9	1.379	70.2	0.336	10.40	-0.103	-0.010	170.6	173.7	214.7	218.9	222.2	220.5	218.7	216.5	208.2	202.9	197.7	188.3	175.9
35	641.7	10.77	0.0971	1036.3	1.380	70.2	0.336	19.70	-0.033	0.060	202.2	221.4	222.2	219.7	216.4	210.7	201.6	193.6	186.6	179.6	175.0	170.9	165.9
36	633.6	8.75	0.0973	1038.5	1.381	70.3	0.336	7.51	-0.123	-0.031	169.4	191.3	208.9	216.0	219.9	221.3	221.3	220.2	216.2	211.2	203.9	195.9	185.9
37	639.0	10.77	0.0954	1018.7	1.384	70.4	0.336	14.32	-0.073	0.021	178.8	208.2	220.2	223.1	223.4	219.8	215.0	208.3	201.2	194.6	186.9	180.0	172.0
38	645.1	10.44	0.0965	1029.7	1.478	75.3	0.336	19.70	-0.034	0.061	203.1	227.9	231.5	229.6	225.6	216.7	206.6	199.9	192.1	186.2	179.7	174.4	168.2
39	635.0	10.77	0.0959	1023.1	1.482	75.5	0.336	7.51	-0.124	-0.029	170.7	203.1	223.9	231.0	234.3	235.1	233.5	230.1	223.1	216.1	209.0	200.0	191.3
40	637.0	18.52	0.1890	2017.1	0.590	30.0	0.408	19.50	-0.032	0.019	210.6	132.3	118.4	110.4	107.4	106.6	108.0	109.4	109.9	108.7	107.7	109.2	111.7
41	637.7	12.46	0.1886	2012.7	0.598	30.4	0.408	14.74	-0.070	-0.018	213.0	127.1	105.3	96.7	94.6	95.5	99.2	102.8	105.3	107.4	108.9	111.9	116.3
42	628.2	12.79	0.1896	2023.7	0.602	30.7	0.408	10.19	-0.100	-0.049	208.3	113.8	87.0	74.7	78.5	82.9	86.2	89.6	91.0	91.4	91.8	95.5	102.6
43	637.0	16.16	0.1875	2001.7	0.794	40.4	0.408	14.74	-0.069	-0.016	215.4	147.9	135.1	130.8	130.5	132.2	136.1	138.2	139.1	139.4	138.0	139.3	140.4
44	635.0	24.91	0.1888	2014.9	0.796	40.5	0.408	19.50	-0.031	0.021	210.9	152.6	145.4	139.3	136.3	136.2	136.5	135.4	133.5	131.0	127.6	123.8	121.3
45	633.6	12.46	0.1923	2052.2	0.797	40.6	0.360	6.48	-0.131	-0.085	174.5	100.5	88.4	101.3	120.0	118.5	114.1	108.6	105.7	105.4	105.1	107.7	113.7
46	630.2	11.78	0.1892	2019.3	0.803	40.9	0.408	10.19	-0.101	-0.049	211.1	137.7	119.6	114.2	117.5	121.3	125.0	128.2	130.7	132.8	135.3	138.8	147.5
47	636.3	13.80	0.1915	2043.5	0.987	50.3	0.408	10.19	-0.104	-0.051	212.5	156.3	146.7	146.3	149.0	152.5	155.6	158.9	161.9	163.8	165.3	169.2	173.0
48	639.0	29.63	0.1855	1979.7	0.989	50.3	0.408	19.50	-0.033	0.022	210.3	169.6	168.3	163.4	160.9	159.4	157.6	155.1	150.9	146.5	141.9	138.1	131.5
49	632.9	11.45	0.1900	2028.1	0.990	50.4	0.360	6.48	-0.131	-0.083	182.7	133.8	149.1	152.7	152.9	153.0	153.2	153.6	153.4	154.0	155.5	156.2	154.6
50	631.6	21.21	0.1869	1995.1	0.999	50.9	0.408	14.94	-0.065	-0.011	212.0	165.8	161.1	158.9	158.9	160.5	161.9	162.2	161.1	159.3	157.4	156.0	154.9
51	643.0	34.68	0.1882	2008.3	1.181	60.1	0.408	19.50	-0.035	0.021	208.7	184.5	188.4	187.3	183.4	179.9	177.2	172.7	166.9	159.5	154.1	147.7	138.6
52	634.3	13.13	0.1898	2025.9	1.184	60.3	0.360	6.68	-0.130	-0.081	190.9	158.4	162.9	166.4	170.7	174.4	178.6	182.3	185.2	187.1	188.4	190.0	192.8
53	636.3	18.18	0.1908	2036.9	1.189	60.5	0.408	10.19	-0.104	-0.050	213.5	174.2	174.2	178.4	180.2	183.5	185.9	187.5	188.3	187.2	186.6	185.7	185.7
54	634.3	26.60	0.1875	2001.7	1.193	60.7	0.408	14.74	-0.068	-0.013	212.9	182.5	185.3	184.8	184.8	185.1	185.1	184.5	181.3	177.9	173.2	168.2	163.8
55	637.0	32.66	0.1849	1973.1	1.383	70.4	0.408	14.94	-0.068	-0.010	214.5	199.4	207.2	208.3	207.1	206.8	205.1	202.2	198.9	192.3	184.8	176.5	168.9
56	641.0	23.23	0.1900	2028.1	1.385	70.5	0.408	10.19	-0.106	-0.050	213.5	191.3	199.4	204.3	206.7	208.5	209.9	211.2	209.9	207.8	203.3	199.5	193.5
57	647.8	40.40	0.1910	2039.1	1.388	70.7	0.408	19.08	-0.040	0.016	206.6	199.1	209.4	207.1	202.9	199.5	194.6	189.4	182.2	174.6	165.6	155.3	145.8
58	633.6	17.17	0.1933	2063.2	1.392	70.9	0.360	6.68	-0.130	-0.080	196.6	182.4	189.9	194.1	200.8	204.8	208.3	210.3	212.3	213.2	211.5	210.4	208.2
59	636.3	35.01	0.1882	2008.3	1.478	75.3	0.408	14.94	-0.067	-0.011	216.3	206.8	218.5	220.5	218.7	216.8	214.0	211.2	205.8	197.4	189.2	181.4	173.7
60	651.8	41.07	0.1908	2036.9	1.481	75.4	0.408	19.29	-0.040	0.016	204.5	206.5	218.8	217.2	213.6	208.6	202.5	196.3	188.0	178.5	170.1	160.7	151.2
61	646.4	27.61	0.1910	2039.1	1.575	80.2	0.408	9.98	-0.110	-0.053	213.7	208.6	220.3	225.7	228.4	230.2	230.2	229.6	226.6	222.9	217.1	212.5	205.2
62	634.3	21.88	0.1923	2052.2	1.586	80.7	0.360	7.10	-0.127	-0.076	202.7	201.2	214.2	221.4	227.1	229.6	232.0	233.4	232.2	230.9	227.7	224.5	218.5
63	636.3	30.97	0.2850	3041.8	0.501	25.5	0.408	18.46	-0.040	-0.006	194.3	110.8	105.7	97.7	89.9	87.8	88.8	90.5	91.9	92.8	93.6	96.2	102.2

Run	p	Δp	m	G	power	q	hp-power	T_{in}	x_{in}	x_{DO}	T_{hp}	Distance from CHF location (m)											
-	kPa	kPa	Kgs^{-1}	$Kgm^{-2}s^{-1}$	kW	kWm^{-2}	kW	°C	-	-	°C	0.01	0.05	0.10	0.20	0.30	0.40	0.50	0.60	0.70	0.80	0.90	1.00
												Inside wall temperature (°C)											
64	635.0	25.59	0.2846	3037.4	0.599	30.5	0.408	14.94	-0.067	-0.033	187.0	105.6	104.3	105.7	103.6	101.9	101.5	101.8	102.4	103.4	104.3	108.1	115.7
65	635.0	34.00	0.2807	2995.6	0.600	30.6	0.408	18.46	-0.040	-0.005	195.5	124.3	118.9	110.2	103.7	102.8	104.4	105.7	106.8	107.4	106.9	109.7	115.2
66	639.0	28.62	0.2862	3055.0	0.790	40.2	0.408	15.15	-0.067	-0.032	188.5	128.4	131.7	132.8	128.6	127.4	128.6	129.8	131.1	132.1	132.5	133.9	139.3
67	639.0	40.06	0.2815	3004.4	0.797	40.6	0.408	18.25	-0.043	-0.007	197.3	142.9	143.7	136.7	131.0	130.5	131.9	133.0	133.1	132.2	130.6	130.1	130.6
68	637.7	46.12	0.2835	3026.4	0.987	50.3	0.408	18.46	-0.041	-0.005	198.5	158.7	164.5	158.0	155.7	154.2	153.8	153.4	151.7	149.4	146.0	143.3	141.7
69	637.7	34.00	0.2802	2991.2	0.990	50.4	0.408	14.94	-0.068	-0.032	190.0	147.6	157.7	155.8	153.1	153.8	155.0	155.8	156.5	156.5	155.2	154.9	155.4
70	632.9	42.42	0.2858	3050.6	1.181	60.1	0.408	15.15	-0.064	-0.028	190.9	164.1	180.5	178.0	176.8	176.8	177.7	178.0	176.7	174.7	172.5	169.8	163.8
71	631.6	56.22	0.2819	3008.8	1.187	60.4	0.408	18.46	-0.038	-0.001	199.4	175.7	185.1	180.5	177.2	175.6	174.2	172.2	168.2	163.9	158.5	154.0	148.9
72	633.6	25.59	0.2811	3000.0	1.187	60.4	0.360	9.57	-0.108	-0.074	147.7	108.0	125.6	175.2	167.6	162.9	164.7	165.8	165.9	167.1	168.5	168.9	163.5
73	637.0	27.27	0.2821	3011.0	1.293	65.8	0.360	9.57	-0.109	-0.076	152.3	124.3	157.6	201.8	188.1	185.1	186.5	188.7	189.3	189.0	191.4	193.7	196.9
74	635.6	29.29	0.2846	3037.4	1.378	70.2	0.360	9.57	-0.108	-0.075	156.5	135.5	164.9	200.5	186.2	185.4	185.0	188.6	191.6	191.6	191.3	189.6	180.6
75	635.0	62.62	0.2829	3019.8	1.384	70.5	0.408	18.46	-0.040	-0.002	200.6	181.0	192.5	188.9	180.4	177.4	173.7	172.5	170.0	164.6	156.2	148.3	133.2
76	634.3	49.15	0.2815	3004.4	1.386	70.6	0.408	15.15	-0.065	-0.027	191.4	180.5	201.6	198.4	198.4	199.1	198.3	197.8	195.1	191.5	187.1	182.5	174.4
77	635.0	31.98	0.2850	3041.8	1.475	75.1	0.360	9.57	-0.108	-0.074	162.3	151.0	194.8	217.2	206.0	204.9	205.7	209.4	211.3	211.4	210.5	209.7	207.0
78	641.0	68.34	0.2823	3013.2	1.579	80.4	0.408	18.46	-0.042	-0.004	201.2	205.2	221.2	218.6	216.2	212.9	209.7	204.4	197.0	189.5	180.3	172.4	162.6
79	638.3	35.35	0.2829	3019.8	1.581	80.5	0.360	9.57	-0.110	-0.075	172.9	166.8	202.8	214.2	208.7	211.4	210.8	212.4	211.4	210.0	210.5	205.5	192.9
80	639.7	55.89	0.2825	3015.4	1.587	80.8	0.408	15.15	-0.067	-0.029	192.0	195.4	221.1	219.2	218.3	217.4	217.0	215.0	211.2	206.1	198.9	193.2	183.9
81	633.6	39.39	0.2858	3050.6	1.674	85.2	0.360	9.78	-0.106	-0.072	180.2	179.8	224.7	230.1	228.9	229.6	230.7	231.0	230.7	229.6	226.7	223.2	218.3
82	633.6	55.89	0.3781	4035.8	0.600	30.5	0.480	18.67	-0.037	-0.007	225.3	113.2	108.7	113.4	110.7	103.2	101.4	100.9	100.5	100.4	101.3	104.2	108.1
83	637.7	63.63	0.3857	4117.1	0.803	40.9	0.480	18.67	-0.039	-0.009	225.0	131.3	131.3	139.0	134.5	126.5	124.6	124.9	125.2	125.2	124.6	125.7	129.5
84	634.3	42.76	0.3725	3976.4	0.805	41.0	0.480	14.53	-0.070	-0.039	221.9	115.1	111.2	124.3	146.5	137.8	134.2	130.5	128.9	127.8	127.9	130.1	134.4
85	637.7	47.13	0.3761	4013.8	0.991	50.5	0.480	14.53	-0.071	-0.040	222.6	131.4	134.3	154.1	164.4	153.8	151.5	150.6	149.6	149.6	149.7	150.9	156.0
86	632.9	73.39	0.3775	4029.2	0.993	50.6	0.480	18.87	-0.035	-0.004	224.3	147.8	155.7	162.1	153.8	150.1	148.1	146.1	144.8	143.7	142.2	141.1	141.7
87	640.3	49.49	0.3777	4031.4	1.079	54.9	0.480	14.53	-0.072	-0.041	223.1	138.3	145.5	168.1	172.4	164.2	161.8	160.8	159.9	159.9	159.8	160.2	163.5
88	638.3	78.78	0.3783	4038.0	1.178	60.0	0.480	18.87	-0.038	-0.006	223.3	160.0	173.7	181.8	171.8	166.3	164.5	163.8	161.9	159.7	156.1	154.6	154.0
89	626.2	41.07	0.3763	4016.0	1.182	60.2	0.480	10.60	-0.096	-0.065	210.5	111.4	109.5	136.4	200.5	182.5	178.2	173.9	170.5	168.9	169.3	172.6	177.5
90	642.4	53.53	0.3767	4020.4	1.187	60.4	0.480	14.32	-0.075	-0.043	223.0	145.2	157.8	181.5	181.8	173.8	171.2	171.4	171.6	170.9	169.9	170.4	171.5
91	631.6	41.41	0.3721	3972.0	1.283	65.3	0.480	10.40	-0.100	-0.068	213.2	124.5	129.2	165.4	207.5	187.4	185.5	183.7	182.1	180.8	182.1	183.8	186.6
92	643.7	56.56	0.3783	4038.0	1.285	65.4	0.480	14.53	-0.074	-0.042	222.9	151.3	167.9	193.2	190.4	183.5	181.3	180.9	179.7	179.7	178.8	178.9	178.4
93	642.4	87.20	0.3781	4035.8	1.380	70.2	0.480	19.08	-0.038	-0.005	221.6	160.0	171.3	175.5	172.5	164.6	161.0	159.2	160.4	158.0	153.1	141.6	121.7
94	646.4	60.26	0.3754	4007.2	1.383	70.4	0.480	14.53	-0.075	-0.042	222.7	158.8	179.2	204.8	198.6	192.1	190.3	190.4	189.5	188.9	187.0	184.2	179.8
95	631.6	44.78	0.3767	4020.4	1.383	70.4	0.480	10.81	-0.097	-0.065	217.9	141.0	153.9	194.7	208.1	196.1	192.9	193.4	193.1	194.4	194.4	194.0	197.5
96	647.8	63.63	0.3793	4049.0	1.483	75.5	0.480	14.53	-0.075	-0.043	222.6	164.2	188.7	215.6	207.4	201.4	199.8	199.5	199.8	198.7	195.4	190.6	184.6

Run	p	Δp	m	G	power	q	hp-power	T_{in}	x_{in}	x_{DO}	T_{hp}	Distance from CHF location (m)											
-	kPa	kPa	Kgs^{-1}	$Kgm^{-2}s^{-1}$	kW	kWm^{-2}	kW	°C	-	-	°C	0.01	0.05	0.10	0.20	0.30	0.40	0.50	0.60	0.70	0.80	0.90	1.00
												Inside wall temperature (°C)											
97	634.3	47.13	0.3773	4027.0	1.488	75.7	0.480	10.81	-0.098	-0.066	219.6	148.5	167.6	211.1	215.6	211.7	207.0	203.8	202.8	201.9	203.2	202.6	201.5
98	649.8	67.00	0.3756	4009.4	1.578	80.3	0.480	14.53	-0.076	-0.043	222.4	171.9	200.5	224.7	215.2	209.2	206.2	208.0	207.0	205.2	200.7	197.5	191.5
99	635.0	50.16	0.3742	3994.0	1.578	80.3	0.480	10.81	-0.099	-0.066	221.0	156.7	182.3	224.4	221.7	217.4	213.4	213.2	212.3	211.5	211.1	210.6	210.6
100	648.4	94.27	0.3756	4009.4	1.584	80.7	0.480	18.87	-0.042	-0.009	219.1	184.1	212.9	220.4	209.0	203.1	200.0	197.7	193.2	188.1	181.5	176.2	166.4
101	651.1	96.96	0.3781	4035.8	1.675	85.3	0.480	18.67	-0.045	-0.011	217.0	187.9	219.1	227.8	216.9	212.6	208.5	204.8	200.7	194.5	187.4	181.0	172.8
102	653.1	70.36	0.3837	4095.1	1.680	85.5	0.480	14.32	-0.079	-0.047	223.1	175.2	207.1	234.5	224.0	216.6	214.5	216.1	215.3	212.1	208.0	203.9	199.0
103	788.5	11.78	0.0427	455.8	0.396	20.2	0.312	26.13	-0.039	0.141	240.0	133.9	101.0	92.7	87.9	88.8	91.7	93.9	95.8	97.8	99.6	103.3	107.5
104	796.6	11.45	0.0489	521.7	0.400	20.4	0.312	28.41	-0.023	0.135	202.4	121.8	101.8	95.6	93.0	93.0	93.7	95.2	96.8	98.4	99.7	102.0	104.0
105	802.6	9.43	0.0468	499.7	0.405	20.6	0.312	20.12	-0.093	0.072	201.6	112.4	82.5	77.8	79.8	83.6	88.3	89.2	91.1	93.4	95.7	98.5	102.1
106	788.5	10.10	0.0454	484.4	0.597	30.4	0.312	20.12	-0.088	0.086	212.3	137.6	115.6	113.1	114.3	116.8	120.9	122.9	124.0	127.2	130.5	133.5	135.9
107	791.8	13.47	0.0419	447.0	0.598	30.5	0.312	26.34	-0.038	0.151	241.5	155.6	132.2	126.7	121.9	123.9	126.7	128.9	130.7	133.9	137.0	140.0	142.4
108	799.3	12.46	0.0481	512.9	0.602	30.6	0.312	28.20	-0.025	0.140	218.2	148.0	132.2	128.2	127.0	126.9	126.9	129.4	131.3	133.6	135.5	136.9	138.2
109	795.2	9.43	0.0501	534.9	0.603	30.7	0.360	14.94	-0.132	0.048	196.0	122.3	101.9	104.6	111.2	115.6	120.1	124.6	125.6	128.2	130.9	134.3	138.9
110	797.2	8.75	0.0452	482.2	0.789	40.2	0.360	8.75	-0.183	0.022	206.0	121.4	98.1	108.7	123.0	133.6	143.4	146.2	150.0	154.3	158.5	163.3	169.8
111	792.5	15.49	0.0466	497.6	0.793	40.4	0.312	28.00	-0.025	0.150	222.1	169.9	158.3	155.7	155.8	155.5	155.5	158.1	159.7	160.6	162.1	162.6	163.8
112	791.8	10.44	0.0439	469.0	0.793	40.4	0.360	14.94	-0.131	0.079	198.1	145.5	136.1	138.2	145.7	147.3	151.0	154.9	155.7	157.8	161.8	165.3	168.7
113	792.5	12.46	0.0464	495.4	0.797	40.6	0.312	20.12	-0.089	0.086	218.7	160.6	147.6	147.0	147.3	149.0	152.8	153.4	155.2	158.7	162.9	164.9	167.3
114	793.2	15.49	0.0443	473.4	0.798	40.6	0.312	26.34	-0.039	0.145	241.5	173.9	160.1	157.3	153.4	153.5	156.3	158.2	160.4	163.2	165.8	167.3	169.1
115	795.9	16.16	0.0441	471.2	0.987	50.2	0.312	27.17	-0.033	0.157	238.7	193.1	184.7	183.1	178.7	177.7	181.6	183.2	184.0	186.9	188.5	189.7	190.9
116	793.2	11.11	0.0458	488.8	0.987	50.2	0.360	8.95	-0.179	0.027	208.4	152.0	143.2	152.7	163.2	169.8	176.1	178.1	180.8	183.6	187.7	191.6	197.6
117	794.5	15.15	0.0448	477.8	0.992	50.5	0.312	20.53	-0.087	0.100	223.5	183.2	177.6	178.1	178.1	178.2	180.8	180.7	181.4	184.1	187.6	188.2	187.2
118	798.6	12.46	0.0458	488.8	0.995	50.7	0.360	14.74	-0.135	0.072	200.1	167.5	168.1	172.3	177.8	178.5	180.1	183.3	183.8	184.3	185.4	185.7	185.9
119	799.3	16.16	0.0472	504.1	1.000	50.9	0.312	28.00	-0.027	0.150	224.8	189.4	183.9	183.5	182.8	182.5	182.7	183.4	183.6	183.8	185.0	185.2	185.5
120	793.9	14.14	0.0483	515.1	1.180	60.1	0.360	14.53	-0.135	0.066	201.4	186.6	195.4	199.9	204.1	203.8	204.8	206.3	205.7	204.9	205.3	204.8	204.2
121	799.3	15.15	0.0458	488.8	1.182	60.1	0.312	26.13	-0.043	0.145	233.5	208.2	206.6	206.8	200.7	200.9	203.2	204.3	205.1	205.9	207.1	209.0	208.4
122	798.6	14.81	0.0470	501.9	1.186	60.4	0.312	27.79	-0.028	0.155	227.6	207.4	206.4	206.0	206.6	205.8	204.2	204.2	203.7	203.4	203.2	202.9	202.6
123	795.9	15.15	0.0460	491.0	1.189	60.5	0.312	20.74	-0.086	0.101	227.1	202.4	204.4	205.9	204.1	204.4	205.2	204.5	205.0	206.2	208.9	207.9	206.6
124	789.8	14.14	0.0458	488.8	1.191	60.6	0.360	9.37	-0.175	0.037	208.7	177.4	180.1	189.2	194.6	198.9	205.0	206.3	207.9	209.2	211.4	212.8	214.6
125	793.2	14.14	0.0460	491.0	1.376	70.0	0.312	25.09	-0.049	0.142	229.0	223.9	229.2	230.1	222.7	223.2	224.3	224.5	225.0	224.0	224.2	223.2	220.8
126	795.9	13.47	0.0507	541.5	1.386	70.5	0.360	14.32	-0.138	0.058	201.8	206.6	222.7	228.1	231.1	229.9	229.4	228.4	225.1	223.8	222.6	220.0	217.8
127	793.2	13.80	0.0499	532.7	1.391	70.8	0.312	27.58	-0.029	0.148	230.0	228.2	229.0	229.8	229.2	227.3	225.7	223.7	221.6	220.7	219.5	217.3	215.8
128	790.5	14.14	0.0460	491.0	1.391	70.8	0.312	21.36	-0.079	0.113	230.8	222.8	230.3	232.3	227.3	226.9	227.8	226.5	226.6	226.5	227.8	226.8	225.0
129	791.2	13.80	0.0456	486.6	1.393	70.9	0.360	9.78	-0.172	0.046	208.7	200.0	212.1	220.7	222.8	225.8	229.5	230.6	231.0	230.7	231.5	232.8	233.4

Run	p	Δp	m	G	power	q	hp-power	T_{in}	x_{in}	x_{DO}	T_{hp}	Distance from CHF location (m)											
-	kPa	kPa	Kgs^{-1}	$Kgm^{-2}s^{-1}$	kW	kWm^{-2}	kW	°C	-	-	°C	0.01	0.05	0.10	0.20	0.30	0.40	0.50	0.60	0.70	0.80	0.90	1.00
												Inside wall temperature (°C)											
130	793.2	2.36	0.0948	1012.1	0.405	20.6	0.360	24.47	-0.054	0.039	182.5	111.3	90.8	84.0	84.0	84.3	86.3	88.4	88.8	89.7	90.7	93.5	96.9
131	792.5	1.68	0.1002	1069.3	0.409	20.8	0.360	26.54	-0.037	0.052	197.6	122.5	97.2	89.7	88.0	88.2	88.2	89.4	89.8	89.8	90.7	92.0	93.9
132	791.8	0.67	0.0963	1027.5	0.589	30.0	0.360	24.68	-0.052	0.042	184.5	132.7	118.5	114.6	115.8	115.9	116.8	117.3	116.7	116.4	116.7	117.8	120.6
133	798.6	1.01	0.0981	1047.3	0.593	30.2	0.360	26.54	-0.039	0.053	200.3	140.7	122.6	117.1	116.6	116.1	115.2	116.3	116.1	114.8	115.1	114.9	113.9
134	793.9	0.67	0.0979	1045.1	0.597	30.4	0.360	20.74	-0.085	0.007	189.8	128.5	107.9	101.6	102.8	104.6	108.6	112.6	113.6	115.5	117.4	120.1	122.8
135	791.2	1.01	0.0940	1003.3	0.790	40.2	0.360	24.68	-0.052	0.047	186.2	152.5	145.7	144.4	145.3	145.2	145.2	144.1	143.0	140.5	139.9	139.1	139.7
136	797.2	0.00	0.0948	1012.1	0.793	40.3	0.360	13.91	-0.142	-0.044	174.5	121.0	106.6	105.1	113.7	119.1	126.4	133.7	137.1	140.7	144.3	148.5	154.3
137	788.5	2.36	0.0967	1031.9	0.795	40.5	0.360	26.75	-0.033	0.062	203.5	161.8	149.2	145.8	145.8	144.5	143.0	140.7	139.5	137.5	135.8	134.5	132.7
138	795.2	0.34	0.0956	1020.9	0.795	40.5	0.360	21.15	-0.082	0.015	193.9	152.6	142.2	140.2	142.4	142.7	143.9	145.1	144.7	144.2	143.9	143.8	143.1
139	795.2	0.67	0.0965	1029.7	0.798	40.6	0.360	9.78	-0.174	-0.078	166.3	99.6	93.4	97.2	102.2	104.9	109.6	114.3	118.3	120.5	125.1	134.1	147.5
140	789.8	4.04	0.0961	1025.3	0.985	50.1	0.360	27.17	-0.030	0.068	206.4	179.7	172.3	169.5	170.1	167.9	163.9	159.7	157.0	152.8	151.1	148.5	145.4
141	795.2	3.37	0.0954	1018.7	0.988	50.3	0.360	24.47	-0.055	0.045	187.9	172.2	169.7	169.6	170.8	169.9	167.7	165.0	162.5	158.8	157.1	154.5	152.2
142	796.6	0.34	0.0954	1018.7	0.988	50.3	0.360	9.78	-0.174	-0.075	168.9	126.8	122.6	125.5	133.0	138.5	146.0	153.7	157.2	161.9	166.5	171.7	178.2
143	793.2	2.02	0.0944	1007.7	0.989	50.3	0.360	21.36	-0.080	0.021	195.6	171.7	168.9	168.5	170.3	170.0	169.5	168.8	166.8	164.2	162.7	159.6	156.9
144	797.9	1.01	0.0940	1003.3	0.989	50.3	0.360	14.12	-0.140	-0.039	177.4	144.8	142.7	143.2	150.8	155.2	161.4	167.6	168.7	169.7	170.7	172.9	175.1
145	806.0	1.68	0.0992	1058.3	0.991	50.4	0.360	7.10	-0.199	-0.104	170.0	118.0	109.6	111.6	109.3	104.5	101.8	99.1	99.5	104.6	111.9	128.7	152.1
146	798.6	2.36	0.0926	987.9	1.183	60.2	0.360	21.36	-0.082	0.023	196.8	191.8	194.1	195.3	196.2	194.7	192.3	189.2	184.9	181.9	177.2	172.7	169.3
147	795.9	0.67	0.0983	1049.5	1.184	60.3	0.360	7.51	-0.192	-0.093	176.0	147.9	148.2	150.2	156.5	160.5	168.5	176.6	181.3	186.8	192.4	197.9	207.5
148	796.6	3.03	0.0967	1031.9	1.185	60.3	0.360	14.53	-0.136	-0.036	179.7	168.5	174.6	179.7	184.9	188.9	192.2	194.6	193.9	192.4	190.0	188.7	185.4
149	793.9	3.70	0.0944	1007.7	1.187	60.4	0.360	27.37	-0.030	0.073	207.8	198.5	194.7	192.0	192.2	189.2	183.3	176.7	171.2	166.5	164.1	160.8	158.6
150	797.2	2.02	0.0948	1012.1	1.187	60.4	0.360	9.98	-0.173	-0.071	171.3	151.1	157.6	161.2	169.4	175.3	182.6	189.9	191.9	194.4	194.4	194.9	196.6
151	792.5	4.38	0.0946	1009.9	1.191	60.6	0.360	24.88	-0.050	0.052	189.7	190.4	193.4	194.3	195.2	191.9	187.8	184.5	179.9	173.5	170.1	165.9	161.4
152	791.8	2.69	0.0938	1001.1	1.377	70.1	0.360	7.71	-0.189	-0.083	180.7	174.1	202.5	207.0	210.4	212.0	213.8	214.8	215.7	215.9	213.8	208.3	197.4
153	794.5	2.02	0.0938	1001.1	1.378	70.2	0.360	21.57	-0.078	0.027	197.6	208.7	217.1	218.2	218.8	214.7	210.8	206.1	200.1	192.1	187.8	181.8	175.7
154	791.2	3.37	0.0944	1007.7	1.385	70.5	0.360	24.47	-0.053	0.052	190.1	207.9	215.0	216.4	216.4	211.3	206.5	200.1	192.6	185.2	180.2	176.1	172.2
155	791.8	4.04	0.0934	996.7	1.386	70.6	0.360	27.79	-0.026	0.080	208.9	215.9	214.9	211.7	210.4	204.8	195.9	190.0	183.5	177.3	174.0	169.9	166.0
156	796.6	4.04	0.0932	994.5	1.387	70.6	0.360	9.98	-0.173	-0.066	172.1	175.2	189.8	206.6	210.8	213.4	214.9	218.6	217.4	215.7	213.4	206.3	194.6
157	795.9	4.38	0.0942	1005.5	1.391	70.8	0.360	14.53	-0.136	-0.031	181.4	188.8	204.1	210.0	215.4	216.9	218.5	217.8	214.0	209.3	206.3	198.5	186.2
158	802.6	0.00	0.0936	998.9	1.575	80.2	0.360	21.77	-0.080	0.029	197.8	226.7	238.7	240.5	238.9	232.5	225.9	220.5	211.9	202.4	196.5	187.8	181.4
159	791.2	4.38	0.0913	974.7	1.580	80.5	0.360	8.33	-0.183	-0.073	183.7	198.2	215.0	221.6	231.9	235.4	240.0	241.3	239.2	236.8	230.3	224.4	221.7
160	793.2	3.03	0.0913	974.7	1.583	80.6	0.360	27.17	-0.032	0.079	209.1	233.4	234.2	230.8	227.7	216.4	208.0	201.7	194.2	186.6	182.4	178.6	175.2
161	797.9	13.80	0.1896	2023.7	0.590	30.0	0.360	25.30	-0.049	-0.001	158.7	119.1	111.8	106.5	105.3	106.1	108.6	110.0	110.6	110.8	111.5	112.3	114.4
162	796.6	20.20	0.1896	2023.7	0.601	30.6	0.360	29.24	-0.016	0.032	153.3	122.4	120.9	116.3	113.3	112.6	112.3	111.8	109.9	107.1	105.3	104.2	103.6

Run	p	Δp	m	G	power	q	hp-power	T_{in}	x_{in}	x_{DO}	T_{hp}	Distance from CHF location (m)											
-	kPa	kPa	Kgs^{-1}	$Kgm^{-2}s^{-1}$	kW	kWm^{-2}	kW	°C	-	-	°C	0.01	0.05	0.10	0.20	0.30	0.40	0.50	0.60	0.70	0.80	0.90	1.00
												Inside wall temperature (°C)											
163	796.6	17.84	0.1892	2019.3	0.790	40.2	0.360	25.51	-0.047	0.002	161.7	138.5	138.1	135.0	134.4	134.8	136.5	137.1	136.1	134.3	133.5	132.1	131.3
164	798.6	11.45	0.1892	2019.3	0.791	40.3	0.360	19.91	-0.093	-0.045	157.5	124.4	125.5	125.5	125.8	126.0	126.4	127.2	127.8	128.6	130.3	134.1	137.5
165	795.2	24.24	0.1869	1995.1	0.797	40.6	0.360	29.24	-0.015	0.035	156.6	140.3	145.4	141.4	136.5	133.9	131.7	131.4	126.4	123.5	120.6	118.1	116.4
166	795.9	12.12	0.1886	2012.7	0.989	50.3	0.408	14.12	-0.139	-0.083	211.7	152.3	146.8	145.9	146.5	147.0	147.6	147.9	147.6	148.2	148.8	149.3	149.8
167	798.6	22.22	0.1888	2014.9	0.990	50.4	0.360	25.51	-0.047	0.003	164.1	156.0	161.2	160.4	160.5	159.5	159.1	158.9	156.2	152.3	149.4	145.8	143.7
168	795.9	28.28	0.1890	2017.1	0.992	50.5	0.360	29.24	-0.015	0.035	159.8	157.2	166.9	163.2	156.2	151.5	148.0	146.3	140.1	136.2	131.5	128.3	125.9
169	801.3	13.47	0.1879	2006.1	0.993	50.6	0.360	19.91	-0.095	-0.044	159.6	145.3	151.7	153.1	154.5	155.1	156.0	158.1	158.6	159.1	160.5	162.3	164.5
170	799.9	25.92	0.1869	1995.1	1.182	60.2	0.360	25.51	-0.048	0.004	166.1	173.0	182.7	183.6	182.0	180.7	179.4	177.1	172.2	166.3	161.8	157.3	153.3
171	793.9	12.79	0.1861	1986.3	1.187	60.4	0.408	14.32	-0.137	-0.079	215.8	168.4	166.8	167.9	169.2	169.2	169.2	169.2	169.5	170.1	173.1	176.9	181.3
172	794.5	31.98	0.1867	1992.9	1.192	60.7	0.360	29.24	-0.015	0.037	163.6	175.4	188.2	184.7	175.5	168.8	164.4	160.3	151.4	144.7	140.3	136.1	133.4
173	798.6	17.84	0.1912	2041.3	1.192	60.7	0.360	19.91	-0.093	-0.043	160.4	163.9	175.2	177.5	180.5	181.5	182.8	183.3	182.2	180.9	180.9	179.8	177.0
174	793.9	30.97	0.1890	2017.1	1.380	70.2	0.360	25.30	-0.047	0.005	167.9	188.8	203.3	205.1	201.5	198.5	195.5	191.7	184.8	176.6	170.3	163.3	157.6
175	795.9	35.01	0.1869	1995.1	1.386	70.6	0.360	29.24	-0.015	0.038	166.6	191.7	207.8	203.8	191.9	183.7	176.5	171.4	160.8	152.5	147.4	142.5	140.8
176	798.6	21.21	0.1898	2025.9	1.387	70.6	0.360	19.70	-0.095	-0.043	160.4	180.7	196.8	201.0	204.6	204.8	205.3	205.2	202.3	198.6	196.4	191.1	182.8
177	796.6	15.49	0.1904	2032.5	1.389	70.7	0.408	14.74	-0.135	-0.077	222.9	189.9	194.7	197.0	198.9	199.5	199.1	198.9	198.7	199.9	201.9	202.2	203.3
178	796.6	17.84	0.1871	1997.3	1.577	80.3	0.408	14.53	-0.136	-0.076	228.0	207.1	216.6	220.2	222.3	222.9	222.8	222.4	222.1	221.7	220.5	217.8	212.7
179	795.9	25.59	0.1892	2019.3	1.578	80.3	0.360	20.12	-0.091	-0.037	160.1	195.9	216.7	223.6	226.3	226.4	224.6	223.3	218.6	211.1	206.3	199.8	188.0
180	793.9	38.04	0.1865	1990.7	1.583	80.6	0.360	29.45	-0.013	0.042	170.7	207.7	226.9	222.3	206.0	196.0	187.2	179.4	166.7	159.2	152.0	146.6	142.6
181	798.6	34.34	0.1904	2032.5	1.583	80.6	0.360	25.71	-0.046	0.008	169.0	206.4	225.0	226.5	220.1	212.2	207.4	202.8	191.0	182.6	174.1	165.2	159.6
182	790.5	15.82	0.2013	2149.0	1.780	90.6	0.410	10.19	-0.168	-0.111	213.4	203.1	221.5	218.7	195.6	183.4	180.9	178.4	179.3	184.6	192.6	204.9	225.3
183	793.9	22.89	0.1894	2021.5	1.872	95.3	0.410	10.19	-0.170	-0.109	218.5	220.5	236.8	231.2	208.5	199.2	196.6	195.2	196.1	202.1	210.9	223.1	239.2
184	793.9	23.23	0.2809	2997.8	0.794	40.4	0.408	20.12	-0.090	-0.053	181.8	115.0	120.0	132.9	135.9	129.3	129.5	129.8	130.4	131.0	132.5	138.0	147.5
185	803.3	35.35	0.2802	2991.2	0.799	40.7	0.360	26.54	-0.041	-0.008	161.1	128.6	137.5	137.8	129.7	128.1	128.1	128.6	128.8	128.9	129.0	129.1	133.1
186	796.6	42.08	0.2852	3044.0	0.987	50.3	0.360	26.54	-0.038	-0.005	162.7	143.6	159.5	158.9	152.7	148.1	147.1	145.3	144.8	144.2	143.5	142.1	143.4
187	793.9	25.59	0.2809	2997.8	0.996	50.7	0.408	20.12	-0.090	-0.052	186.3	142.5	154.1	162.2	158.1	154.9	155.1	157.0	157.1	158.1	158.2	161.1	166.7
188	791.8	23.90	0.2866	3059.4	1.186	60.4	0.480	15.36	-0.128	-0.084	237.2	151.4	149.2	175.5	190.8	180.5	169.4	163.6	158.3	157.4	157.8	161.4	170.3
189	793.9	30.64	0.2856	3048.4	1.186	60.4	0.408	19.91	-0.092	-0.054	190.5	159.8	179.0	185.3	180.7	178.8	179.9	180.1	179.1	178.5	178.0	177.6	178.7
190	793.2	49.15	0.2774	2960.4	1.187	60.4	0.360	26.96	-0.033	0.002	165.5	164.2	181.5	178.7	173.0	168.8	164.6	161.6	159.2	156.0	152.7	149.7	147.7
191	789.8	24.24	0.2864	3057.2	1.293	65.8	0.480	15.15	-0.129	-0.085	237.5	163.5	170.2	197.0	199.1	184.2	180.9	177.7	174.6	174.9	176.5	180.2	186.9
192	798.6	35.69	0.2835	3026.4	1.379	70.2	0.408	19.91	-0.093	-0.055	194.4	156.2	180.9	184.7	178.6	174.8	174.3	175.4	176.4	174.9	172.8	167.1	156.8
193	797.9	55.55	0.2835	3026.4	1.384	70.5	0.360	26.54	-0.039	-0.004	168.9	168.1	191.6	189.0	180.3	173.7	167.8	163.9	160.7	156.3	153.1	146.7	134.1
194	793.9	23.57	0.2838	3028.6	1.386	70.6	0.480	15.15	-0.130	-0.085	237.2	157.2	171.5	190.0	186.3	175.4	175.4	173.9	172.2	172.0	175.0	176.0	171.0
195	793.9	24.91	0.2815	3004.4	1.480	75.4	0.480	15.15	-0.130	-0.085	236.3	177.8	196.7	220.8	216.9	204.7	201.2	200.6	200.3	199.5	202.7	205.0	209.5

Run	p	Δp	m	G	power	q	hp-power	T_{in}	x_{in}	x_{DO}	T_{hp}	Distance from CHF location (m)											
-	kPa	kPa	Kgs^{-1}	$Kgm^{-2}s^{-1}$	kW	kWm^{-2}	kW	°C	-	-	°C	0.01	0.05	0.10	0.20	0.30	0.40	0.50	0.60	0.70	0.80	0.90	1.00
												Inside wall temperature (°C)											
196	797.9	61.27	0.2838	3028.6	1.583	80.6	0.360	26.54	-0.039	-0.003	169.9	192.5	220.1	217.0	206.9	199.2	196.3	189.9	185.8	178.8	171.9	164.6	157.2
197	793.2	42.08	0.2802	2991.2	1.587	80.8	0.408	19.91	-0.091	-0.051	198.3	191.4	221.6	223.6	221.0	219.2	217.1	215.7	212.3	208.5	205.5	200.9	198.1
198	799.3	26.93	0.2850	3041.8	1.589	80.9	0.480	15.36	-0.131	-0.085	235.1	171.0	196.8	202.7	196.8	191.9	190.9	190.3	190.0	193.6	192.8	190.0	181.0
199	796.6	67.00	0.2807	2995.6	1.780	90.6	0.360	26.54	-0.038	-0.001	170.3	205.4	236.2	233.6	220.2	212.8	208.5	200.9	194.0	185.3	176.5	168.9	160.9
200	793.2	98.98	0.3829	4086.3	1.796	91.4	0.408	27.17	-0.032	-0.002	183.6	177.2	218.5	234.5	219.6	206.8	199.3	192.3	186.6	181.3	176.1	169.2	165.3
201	789.8	93.26	0.3808	4064.3	1.621	82.5	0.408	27.17	-0.030	-0.001	183.7	169.3	204.4	219.7	201.4	191.5	188.3	183.1	177.8	173.3	168.8	162.8	159.5
202	793.9	86.52	0.3777	4031.4	1.439	73.3	0.408	27.37	-0.030	-0.001	183.4	158.7	186.4	201.9	187.1	177.2	175.6	171.0	167.4	164.0	160.6	157.1	156.0
203	787.1	81.47	0.3839	4097.3	1.257	64.0	0.408	27.37	-0.028	0.001	182.8	144.6	166.9	182.7	171.6	163.2	161.0	157.0	154.7	152.8	150.8	148.8	149.4
204	788.5	74.07	0.3806	4062.1	1.089	55.4	0.408	27.37	-0.028	0.000	181.3	133.8	150.0	164.4	156.1	148.8	146.9	144.8	142.8	141.8	140.8	140.2	140.2
205	788.5	67.00	0.3767	4020.4	0.903	46.0	0.408	27.58	-0.026	0.001	180.5	122.1	131.4	144.0	139.4	132.6	131.3	129.2	128.4	128.5	128.6	128.9	131.1
206	789.8	58.92	0.3775	4029.2	0.721	36.7	0.408	27.58	-0.027	0.000	179.3	106.1	110.8	120.9	120.2	114.8	111.9	111.0	110.9	111.1	112.0	115.8	121.4
207	799.9	77.77	0.3779	4033.6	1.810	92.1	0.408	23.85	-0.062	-0.031	171.8	163.8	209.5	242.4	223.3	213.1	211.0	205.2	202.3	199.6	196.9	193.7	195.0
208	805.3	69.35	0.3728	3978.6	1.618	82.3	0.408	24.05	-0.062	-0.032	171.2	151.2	187.3	224.9	212.7	200.8	198.6	194.8	191.6	190.5	189.4	187.9	190.0
209	793.9	65.31	0.3758	4011.6	1.439	73.3	0.408	23.85	-0.059	-0.030	171.3	139.4	168.1	204.4	198.5	186.7	184.6	182.1	180.0	179.2	178.4	180.3	183.0
210	791.2	58.24	0.3785	4040.2	1.258	64.0	0.408	23.64	-0.060	-0.031	171.0	126.2	147.3	181.5	184.5	172.4	168.9	166.2	164.8	165.4	165.9	169.2	174.6
211	790.5	51.51	0.3763	4016.0	1.082	55.1	0.408	23.64	-0.060	-0.031	169.7	112.5	125.7	153.2	172.3	160.2	154.1	151.2	150.1	150.6	151.8	158.1	167.5
212	794.5	46.80	0.3719	3969.8	1.706	86.8	0.480	18.46	-0.104	-0.069	228.8	164.3	185.7	229.6	229.5	215.4	213.6	210.9	211.0	212.4	213.5	217.2	222.1
213	790.5	44.44	0.3730	3980.8	1.614	82.2	0.480	18.25	-0.104	-0.069	229.8	158.4	175.1	218.6	224.2	209.6	207.1	204.4	204.2	205.8	207.4	209.7	213.8
214	801.3	41.75	0.3793	4049.0	1.536	78.2	0.480	18.05	-0.110	-0.076	230.1	147.7	156.4	197.2	222.6	206.1	200.2	197.8	196.6	199.0	201.4	204.9	207.3
215	795.9	39.73	0.3761	4013.8	1.436	73.1	0.480	18.25	-0.106	-0.072	229.8	141.0	140.5	169.0	218.5	203.0	195.0	190.0	187.7	190.2	192.8	196.2	200.6
216	797.2	39.05	0.3717	3967.6	1.350	68.7	0.480	18.46	-0.105	-0.071	230.1	136.6	132.9	155.8	208.7	198.2	188.4	182.9	180.0	182.2	184.4	187.6	193.5
217	800.6	39.73	0.3719	3969.8	1.267	64.5	0.480	18.46	-0.106	-0.072	229.5	128.4	116.5	127.9	188.5	194.8	185.9	179.8	176.6	175.8	176.6	180.8	188.1
218	956.8	18.18	0.0429	458.0	1.383	70.4	0.360	36.31	-0.013	0.227	229.6	231.6	237.3	234.8	231.4	231.4	230.9	228.9	227.7	228.5	230.8	230.6	231.9
219	968.3	16.16	0.0460	491.0	1.180	60.1	0.360	33.61	-0.038	0.181	236.5	208.2	203.8	202.6	201.6	199.5	201.3	200.9	200.9	202.2	204.9	206.0	208.6
220	973.6	16.83	0.0516	550.3	0.991	50.4	0.360	32.78	-0.048	0.143	238.0	188.7	180.1	178.8	176.0	175.4	177.2	177.4	178.1	179.9	183.0	185.4	188.8
221	967.6	15.15	0.0413	440.4	0.784	39.9	0.360	32.36	-0.050	0.184	238.6	170.7	154.8	151.3	147.8	147.8	150.3	150.5	151.7	155.4	159.0	162.4	165.0
222	958.2	12.79	0.0495	528.3	0.605	30.8	0.360	32.57	-0.045	0.145	238.9	154.9	130.5	125.7	122.6	122.8	124.4	125.4	126.8	129.3	132.6	136.4	141.8
223	951.4	11.78	0.0419	447.0	0.396	20.2	0.360	32.36	-0.044	0.174	238.1	133.7	101.8	94.0	90.4	90.7	93.1	93.8	94.4	96.6	99.3	102.6	108.6
224	965.6	14.48	0.0470	501.9	1.386	70.5	0.360	25.09	-0.113	0.107	208.2	211.6	222.4	224.7	223.2	223.8	224.4	223.4	223.8	224.2	226.2	226.2	227.0
225	954.1	15.49	0.0462	493.2	1.183	60.2	0.360	24.68	-0.112	0.106	209.7	193.4	198.2	200.0	199.6	200.8	201.8	201.5	202.5	203.2	206.0	206.5	207.6
226	961.5	15.49	0.0460	491.0	0.998	50.8	0.360	24.68	-0.115	0.100	210.3	176.9	173.8	175.0	175.0	175.3	177.4	177.8	179.0	182.5	185.9	186.4	187.8
227	966.9	12.79	0.0450	480.0	0.791	40.3	0.360	24.68	-0.117	0.098	209.7	156.5	145.7	146.0	146.0	147.4	151.1	152.3	153.2	157.1	161.0	162.6	165.3
228	962.9	10.77	0.0446	475.6	0.594	30.2	0.360	24.68	-0.115	0.096	208.2	135.3	114.9	112.8	115.3	117.4	121.1	122.3	123.6	126.7	129.8	132.6	135.5

Run	p	Δp	m	G	power	q	hp-power	T_{in}	x_{in}	x_{DO}	T_{hp}	Distance from CHF location (m)											
-	kPa	kPa	Kgs^{-1}	$Kgm^{-2}s^{-1}$	kW	kWm^{-2}	kW	°C	-	-	°C	0.01	0.05	0.10	0.20	0.30	0.40	0.50	0.60	0.70	0.80	0.90	1.00
												Inside wall temperature (°C)											
229	960.2	9.76	0.0431	460.2	0.408	20.8	0.360	24.88	-0.112	0.101	206.7	114.1	82.7	78.2	81.7	85.9	90.8	91.7	94.0	96.0	98.0	101.1	104.5
230	958.8	15.15	0.0446	475.6	1.394	71.0	0.360	19.70	-0.156	0.076	202.3	205.5	219.9	223.4	224.7	225.5	226.8	227.7	228.8	229.4	229.7	230.5	230.5
231	957.5	15.49	0.0435	464.6	1.193	60.7	0.360	20.12	-0.152	0.080	204.2	187.2	193.6	196.8	198.7	200.9	202.9	204.2	204.9	207.4	209.6	210.5	212.6
232	960.2	14.48	0.0429	458.0	0.988	50.3	0.360	19.91	-0.155	0.075	204.2	166.2	163.1	166.7	169.1	171.6	175.8	177.5	179.2	181.6	186.2	187.8	190.5
233	960.2	11.45	0.0423	451.4	0.789	40.2	0.360	20.32	-0.151	0.076	203.2	145.5	131.5	134.7	139.2	142.3	146.5	148.4	151.2	155.5	159.7	163.3	167.8
234	960.2	9.76	0.0427	455.8	0.600	30.6	0.360	20.32	-0.151	0.069	201.7	121.8	97.0	97.5	105.5	111.5	118.3	121.2	123.6	125.6	128.8	132.0	136.7
235	966.2	14.14	0.0441	471.2	1.381	70.3	0.360	14.12	-0.206	0.028	194.1	191.4	204.2	212.8	215.2	218.7	219.5	221.3	223.7	227.1	228.9	230.2	230.7
236	958.8	14.14	0.0435	464.6	1.186	60.4	0.360	14.53	-0.199	0.032	195.3	171.6	177.4	185.6	189.4	195.3	200.4	202.2	204.3	205.7	209.9	211.1	212.2
237	963.5	12.12	0.0433	462.4	0.998	50.8	0.360	14.94	-0.198	0.030	196.2	150.8	146.4	155.0	162.9	167.3	175.1	177.5	180.4	182.4	186.8	189.7	193.5
238	965.6	9.43	0.0437	466.8	0.791	40.3	0.360	15.15	-0.197	0.024	196.2	124.9	107.6	115.0	127.4	136.0	144.7	149.3	151.1	153.5	157.5	160.9	164.1
239	970.3	13.13	0.0460	491.0	1.526	77.7	0.360	10.19	-0.240	-0.012	183.8	191.0	207.4	219.4	225.0	230.6	236.9	237.5	238.5	238.9	239.0	241.9	245.3
240	963.5	13.13	0.0458	488.8	1.444	73.5	0.360	10.19	-0.237	-0.011	184.4	182.2	195.9	206.2	214.2	219.9	227.7	229.0	229.6	231.0	231.6	232.5	236.4
241	962.9	11.45	0.0466	497.6	1.262	64.3	0.360	9.98	-0.239	-0.021	183.5	160.9	166.6	177.6	188.2	195.0	204.7	209.1	210.1	212.7	214.0	215.5	217.2
242	974.3	9.76	0.0446	475.6	1.084	55.2	0.360	10.19	-0.242	-0.017	181.6	136.8	134.9	145.4	158.0	169.4	180.3	183.7	185.9	190.4	193.1	195.6	198.1
243	972.3	8.08	0.0446	475.6	0.898	45.7	0.360	9.98	-0.243	-0.023	179.5	112.0	101.2	114.2	125.5	139.2	152.1	157.1	160.9	165.1	169.3	172.4	177.4
244	965.6	13.47	0.0450	480.0	1.477	75.2	0.360	9.78	-0.242	-0.010	193.4	186.4	201.0	214.4	221.6	226.7	233.5	235.1	237.5	239.8	241.0	242.0	244.0
245	963.5	13.80	0.0437	466.8	1.382	70.4	0.360	9.37	-0.244	-0.008	193.7	174.0	185.2	198.6	209.5	215.3	222.5	224.3	227.7	230.0	231.2	232.6	235.4
246	959.5	13.13	0.0439	469.0	1.279	65.1	0.360	8.95	-0.246	-0.014	193.2	161.1	165.9	179.5	193.2	200.6	208.8	211.9	214.5	218.0	220.2	222.8	225.0
247	964.2	12.12	0.0437	466.8	1.182	60.1	0.360	8.75	-0.250	-0.019	192.6	147.4	147.7	160.2	176.6	185.3	195.0	197.9	202.6	206.8	209.0	211.1	214.0
248	965.6	10.44	0.0431	460.2	1.082	55.1	0.360	8.54	-0.252	-0.020	191.6	133.7	129.1	141.4	157.9	169.5	180.8	186.1	189.0	193.2	195.7	199.0	202.3
249	966.9	9.43	0.0431	460.2	0.989	50.3	0.360	8.54	-0.252	-0.023	190.4	120.0	112.5	125.0	139.1	153.6	166.6	171.8	175.7	180.4	183.1	186.8	190.2
250	962.2	13.13	0.0458	488.8	1.526	77.7	0.360	7.30	-0.261	-0.032	189.4	186.2	200.8	212.5	221.8	228.6	236.4	238.5	239.1	239.1	239.7	239.9	238.6
251	977.7	12.79	0.0479	510.7	1.444	73.5	0.360	7.30	-0.267	-0.049	188.2	174.7	184.8	196.6	207.8	216.3	225.7	229.1	230.9	232.1	232.3	232.0	232.0
252	976.3	12.12	0.0468	499.7	1.353	68.9	0.360	7.30	-0.266	-0.046	187.0	161.8	170.9	182.4	195.5	204.4	215.2	219.1	221.5	224.5	224.0	225.5	224.1
253	975.0	11.11	0.0460	491.0	1.261	64.2	0.360	7.30	-0.266	-0.044	185.7	151.4	155.2	166.1	179.8	190.9	202.4	206.9	208.9	211.8	214.1	215.5	215.5
254	973.0	9.76	0.0456	486.6	1.173	59.7	0.360	7.30	-0.265	-0.043	183.9	139.8	140.6	151.2	164.7	176.7	189.8	195.9	199.1	202.3	203.8	204.8	206.8
255	972.3	9.09	0.0446	475.6	1.087	55.3	0.360	7.30	-0.265	-0.040	182.1	127.9	126.3	137.4	148.9	162.5	176.5	184.1	187.3	190.4	193.0	195.0	196.3
256	971.0	8.08	0.0441	471.2	0.990	50.4	0.360	7.51	-0.262	-0.039	178.4	113.4	109.5	121.7	130.3	143.1	157.7	167.3	173.0	177.5	180.6	183.0	184.4
257	971.0	7.74	0.0460	491.0	0.902	45.9	0.360	7.51	-0.262	-0.050	175.7	96.8	92.3	110.6	117.4	126.4	140.2	149.9	157.1	162.4	167.7	171.2	174.5
258	975.7	6.73	0.0959	1023.1	1.629	82.9	0.336	29.87	-0.075	0.030	210.0	231.2	240.2	238.6	231.3	227.3	222.8	216.1	207.8	201.1	190.9	184.2	174.8
259	978.4	7.07	0.0967	1031.9	1.531	77.9	0.336	30.28	-0.072	0.031	212.5	225.3	230.4	228.5	223.5	220.4	215.4	208.3	201.3	194.3	187.4	181.7	171.7
260	977.0	1.68	0.0940	1003.3	1.435	73.0	0.336	30.49	-0.070	0.035	213.7	217.0	220.6	219.6	213.7	210.1	206.9	201.7	195.4	189.5	183.7	177.5	171.8
261	976.3	0.34	0.0934	996.7	1.348	68.6	0.336	30.28	-0.071	0.033	214.4	210.0	210.5	208.9	205.3	201.8	200.1	195.2	190.1	183.6	179.3	173.5	168.0

Run	p	Δp	m	G	power	q	hp-power	T_{in}	x_{in}	x_{DO}	T_{hp}	Distance from CHF location (m)											
-	kPa	kPa	Kgs^{-1}	$Kgm^{-2}s^{-1}$	kW	kWm^{-2}	kW	°C	-	-	°C	0.01	0.05	0.10	0.20	0.30	0.40	0.50	0.60	0.70	0.80	0.90	1.00
												Inside wall temperature (°C)											
262	976.3	1.01	0.0952	1016.5	1.264	64.3	0.336	30.28	-0.071	0.030	214.7	202.0	200.4	199.4	197.1	195.8	192.3	189.3	184.4	178.8	175.2	169.7	166.0
263	977.0	1.01	0.0921	983.5	1.170	59.6	0.336	30.28	-0.072	0.032	215.0	193.6	189.5	187.9	187.0	184.6	183.0	180.6	177.0	173.9	169.5	164.9	160.5
264	977.0	0.34	0.0946	1009.9	1.075	54.7	0.336	30.28	-0.072	0.028	214.7	185.2	178.4	176.5	174.1	172.5	172.8	171.6	168.9	166.1	163.6	161.1	159.4
265	977.7	0.34	0.0928	990.1	0.992	50.5	0.336	30.07	-0.074	0.027	213.8	177.4	167.5	165.7	162.9	163.0	164.4	162.9	161.2	159.1	157.1	154.8	153.7
266	975.0	0.67	0.0936	998.9	0.902	45.9	0.336	30.07	-0.073	0.026	212.3	168.4	156.8	154.3	153.3	152.8	154.8	153.9	153.4	152.4	149.9	148.2	147.1
267	976.3	1.01	0.0942	1005.5	0.813	41.4	0.336	29.87	-0.075	0.022	211.7	159.8	144.7	141.3	139.1	141.4	144.3	144.9	145.3	144.1	141.5	140.1	139.1
268	976.3	1.68	0.0924	985.7	0.723	36.8	0.336	29.87	-0.075	0.023	210.2	149.2	131.3	127.9	126.6	128.0	131.8	133.9	133.9	133.3	132.0	131.4	130.7
269	977.7	1.68	0.0940	1003.3	0.634	32.3	0.336	30.07	-0.074	0.021	208.1	140.6	118.6	114.1	111.6	115.3	118.8	120.9	122.5	123.1	121.8	122.1	121.4
270	978.4	2.02	0.0952	1016.5	0.541	27.5	0.336	30.07	-0.074	0.019	206.3	130.0	105.1	98.8	97.0	100.9	104.7	106.8	108.5	110.3	111.6	112.5	113.1
271	979.0	2.02	0.0944	1007.7	0.447	22.8	0.336	30.07	-0.074	0.018	205.1	119.9	91.3	84.5	83.0	86.3	90.0	92.5	94.7	96.1	97.5	99.5	101.7
272	979.7	1.35	0.0930	992.3	0.361	18.4	0.336	29.87	-0.076	0.016	203.3	110.0	78.0	68.3	68.2	70.9	74.1	77.0	79.2	81.9	83.5	86.4	89.1
273	979.0	3.03	0.0938	1001.1	1.632	83.1	0.336	24.26	-0.125	-0.017	216.5	226.1	237.2	238.9	236.3	235.8	232.6	226.5	220.8	213.3	208.0	202.2	195.5
274	978.4	2.36	0.0942	1005.5	1.535	78.1	0.336	24.26	-0.124	-0.019	216.2	216.9	225.9	226.7	225.5	224.0	223.4	219.4	213.4	207.3	203.1	196.0	192.1
275	978.4	1.68	0.0946	1009.9	1.435	73.0	0.336	24.05	-0.126	-0.022	215.9	208.3	213.9	215.7	216.9	216.9	214.4	211.2	206.4	203.5	198.4	194.0	188.5
276	978.4	1.68	0.0948	1012.1	1.346	68.5	0.336	23.85	-0.128	-0.025	215.3	200.0	201.4	202.9	205.1	206.5	204.7	202.2	199.6	196.2	193.0	189.8	185.9
277	979.0	1.35	0.0940	1003.3	1.254	63.8	0.336	23.85	-0.128	-0.026	214.4	189.5	189.1	190.5	192.0	191.2	195.4	193.6	191.2	189.6	187.4	184.0	182.3
278	977.7	1.01	0.0944	1007.7	1.171	59.6	0.336	24.05	-0.126	-0.025	213.2	182.9	178.8	179.7	180.6	184.8	185.8	184.9	184.4	183.0	180.6	178.3	174.4
279	976.3	0.00	0.0942	1005.5	1.081	55.0	0.336	24.26	-0.124	-0.024	212.0	174.5	167.4	167.9	168.8	171.8	175.5	175.6	175.0	174.3	172.8	170.6	168.1
280	975.0	0.67	0.0946	1009.9	0.990	50.4	0.336	24.26	-0.123	-0.025	210.8	164.6	153.9	153.5	154.8	159.8	163.5	164.7	164.3	164.6	164.2	162.9	161.1
281	973.6	0.67	0.0946	1009.9	0.899	45.8	0.336	24.26	-0.123	-0.025	209.3	155.3	141.5	140.2	140.5	145.7	151.4	153.3	154.4	154.8	155.2	154.8	154.3
282	974.3	1.35	0.0942	1005.5	0.808	41.1	0.336	24.05	-0.125	-0.028	207.8	145.1	126.9	124.2	125.0	131.1	137.6	139.8	142.0	144.1	144.6	144.7	145.3
283	974.3	1.35	0.0956	1020.9	0.724	36.8	0.336	24.26	-0.123	-0.029	205.6	135.0	113.3	109.4	110.2	116.3	123.1	126.4	129.8	132.6	133.3	135.1	136.9
284	979.7	1.01	0.0952	1016.5	0.631	32.1	0.336	24.05	-0.127	-0.033	203.2	124.0	97.5	92.4	93.3	99.8	105.4	109.9	113.3	116.7	118.8	122.8	126.0
285	979.0	0.67	0.0952	1016.5	0.545	27.7	0.336	24.26	-0.125	-0.032	201.4	112.8	83.1	76.9	79.6	84.6	90.1	94.6	98.0	101.1	104.4	108.6	112.6
286	977.7	2.69	0.0944	1007.7	1.618	82.4	0.336	19.91	-0.161	-0.055	207.2	212.9	226.2	230.7	232.2	234.0	233.1	230.3	225.9	221.3	217.6	212.1	201.3
287	975.7	2.69	0.0952	1016.5	1.529	77.9	0.336	19.91	-0.161	-0.056	207.2	206.5	216.6	220.8	224.0	223.2	224.1	222.0	218.2	214.7	211.2	205.4	197.6
288	979.0	1.68	0.0932	994.5	1.438	73.2	0.336	20.12	-0.160	-0.054	206.9	196.3	204.7	207.7	207.0	209.6	214.6	214.0	210.5	208.2	205.5	200.6	195.0
289	975.7	1.68	0.0940	1003.3	1.350	68.7	0.336	20.12	-0.159	-0.055	206.3	188.5	200.0	204.2	204.8	202.3	204.5	203.9	202.8	201.8	199.9	194.3	181.4
290	974.3	1.01	0.0948	1012.1	1.259	64.1	0.336	20.12	-0.158	-0.057	205.7	180.4	179.7	182.4	183.2	187.6	193.7	194.9	194.4	193.8	192.7	190.9	185.9
291	979.7	0.34	0.0948	1012.1	1.171	59.6	0.336	19.91	-0.162	-0.062	205.1	171.1	166.7	168.5	169.6	174.9	181.0	182.8	183.5	184.3	184.3	183.7	180.4
292	977.0	0.34	0.0950	1014.3	1.081	55.0	0.336	19.91	-0.161	-0.062	203.0	160.2	151.3	151.8	153.1	159.5	167.1	170.2	171.5	173.8	174.7	176.7	177.8
293	977.0	0.67	0.0942	1005.5	0.984	50.1	0.336	19.91	-0.161	-0.062	201.5	150.0	137.5	137.5	139.5	146.9	153.9	157.2	160.1	163.5	165.2	166.8	169.1
294	984.4	0.67	0.0950	1014.3	0.902	45.9	0.336	19.91	-0.164	-0.067	200.3	139.5	124.1	122.9	125.5	133.4	140.9	145.4	149.2	153.3	155.0	156.9	158.4

Run	p	Δp	m	G	power	q	hp-power	T_{in}	x_{in}	x_{DO}	T_{hp}	Distance from CHF location (m)											
-	kPa	kPa	Kgs^{-1}	$Kgm^{-2}s^{-1}$	kW	kWm^{-2}	kW	°C	-	-	°C	0.01	0.05	0.10	0.20	0.30	0.40	0.50	0.60	0.70	0.80	0.90	1.00
												Inside wall temperature (°C)											
295	975.7	0.34	0.0946	1009.9	0.811	41.3	0.336	19.70	-0.162	-0.066	198.4	129.5	109.7	107.9	110.5	117.7	125.1	129.9	132.7	136.9	140.5	144.1	147.5
296	979.0	0.00	0.0959	1023.1	0.721	36.7	0.336	19.70	-0.164	-0.070	196.9	119.2	95.3	93.5	96.4	102.7	109.8	114.8	118.2	123.6	126.2	131.4	135.9
297	977.7	3.37	0.0932	994.5	1.805	91.9	0.336	15.15	-0.202	-0.091	200.3	222.1	238.1	242.8	245.0	248.0	247.3	246.4	243.1	240.0	235.5	228.7	214.0
298	973.6	2.36	0.0932	994.5	1.716	87.4	0.336	15.36	-0.198	-0.089	199.3	215.5	228.5	232.4	235.7	234.8	237.5	237.2	236.1	233.9	230.8	225.5	212.8
299	977.7	2.02	0.0942	1005.5	1.618	82.4	0.336	15.15	-0.202	-0.095	200.0	203.0	216.8	234.5	234.0	232.5	231.6	231.3	229.6	228.3	226.5	218.9	202.1
300	978.4	1.68	0.0932	994.5	1.529	77.9	0.336	14.94	-0.204	-0.097	200.0	196.2	204.1	208.2	211.0	218.4	220.0	221.5	222.8	222.7	220.5	217.1	207.3
301	977.7	1.01	0.0950	1014.3	1.442	73.4	0.336	14.94	-0.203	-0.100	199.4	186.5	190.5	193.8	194.9	201.1	208.4	210.5	212.3	213.2	213.7	213.2	207.4
302	978.4	1.01	0.0948	1012.1	1.346	68.5	0.336	14.74	-0.205	-0.103	198.8	176.0	176.3	178.6	179.8	185.1	193.3	196.4	198.9	202.0	204.2	205.2	203.8
303	978.4	0.67	0.0948	1012.1	1.263	64.3	0.336	14.74	-0.205	-0.104	197.9	166.7	163.0	165.3	167.4	175.1	183.4	187.0	190.8	191.8	196.5	198.7	195.3
304	977.7	0.67	0.0942	1005.5	1.165	59.3	0.336	14.74	-0.205	-0.104	195.4	156.2	147.8	148.7	149.8	156.1	164.0	168.0	171.1	174.6	180.7	186.1	188.7
305	975.0	0.67	0.0963	1027.5	1.082	55.1	0.336	14.74	-0.204	-0.106	193.6	145.9	135.0	135.8	138.1	144.0	150.6	154.4	158.5	162.1	167.8	174.2	177.6
306	977.0	0.34	0.0936	998.9	0.986	50.2	0.336	14.74	-0.205	-0.105	192.1	134.6	119.8	120.6	122.4	127.6	132.6	135.0	137.0	140.4	146.2	154.3	162.4
307	977.0	0.34	0.0946	1009.9	0.900	45.8	0.336	14.74	-0.205	-0.107	190.2	125.1	107.5	108.6	110.6	116.4	122.6	126.2	128.4	132.3	135.2	141.6	149.6
308	978.4	0.34	0.0936	998.9	0.812	41.3	0.336	14.74	-0.205	-0.108	188.1	113.1	93.5	98.1	100.6	103.5	109.0	113.2	115.7	118.5	121.3	127.1	136.4
309	977.7	3.37	0.0924	985.7	1.803	91.7	0.336	10.19	-0.243	-0.132	189.6	214.0	228.8	230.8	231.9	233.0	237.7	240.7	242.6	243.7	244.3	241.0	229.7
310	977.7	2.02	0.0932	994.5	1.712	87.1	0.336	10.19	-0.243	-0.134	189.6	206.0	220.1	222.4	221.1	223.7	231.5	234.3	236.4	238.0	239.0	236.8	234.1
311	978.4	1.68	0.0926	987.9	1.622	82.5	0.336	9.98	-0.245	-0.136	189.7	195.7	207.3	209.7	208.1	210.3	218.4	220.8	224.8	228.4	231.3	230.3	228.3
312	979.7	1.68	0.0928	990.1	1.535	78.0	0.336	9.98	-0.245	-0.138	189.4	189.2	194.9	195.2	193.0	195.2	201.3	204.0	208.0	213.9	220.6	222.0	225.4
313	978.4	1.01	0.0940	1003.3	1.440	73.2	0.336	9.98	-0.245	-0.140	188.4	178.9	180.7	180.7	178.5	182.6	184.6	186.5	189.9	197.7	206.2	210.4	212.4
314	975.0	0.67	0.0932	994.5	1.342	68.2	0.336	9.78	-0.245	-0.141	187.5	166.0	159.3	157.1	149.5	144.8	138.6	134.7	136.3	145.4	157.6	173.6	183.8
315	973.0	1.35	0.0948	1012.1	1.253	63.7	0.336	9.98	-0.243	-0.141	186.9	157.0	148.3	144.9	138.5	134.3	130.4	125.3	124.5	129.6	139.7	156.1	169.0
316	977.0	0.67	0.0928	990.1	1.166	59.3	0.336	9.98	-0.244	-0.142	186.3	148.5	137.9	134.2	127.5	125.2	122.4	117.7	114.8	116.9	123.6	139.6	150.3
317	977.0	0.67	0.0934	996.7	1.083	55.1	0.336	9.78	-0.246	-0.145	185.4	141.4	129.6	126.5	122.5	119.1	117.8	113.9	110.5	109.9	113.4	124.0	135.4
318	978.4	2.69	0.0942	1005.5	0.989	50.3	0.336	9.78	-0.247	-0.148	183.9	131.0	119.5	117.4	113.6	111.2	109.0	107.0	102.7	101.6	102.9	108.1	114.1
319	977.0	3.70	0.0926	987.9	1.799	91.5	0.336	5.86	-0.278	-0.168	183.9	207.7	218.5	217.5	210.5	211.2	215.3	217.8	222.7	229.7	240.4	243.4	246.3
320	977.0	0.34	0.0940	1003.3	1.703	86.6	0.336	5.65	-0.280	-0.172	183.6	199.3	198.3	194.3	183.2	175.1	170.4	167.7	172.4	181.0	198.5	216.0	228.8
321	977.0	2.69	0.0932	994.5	1.613	82.0	0.336	5.45	-0.282	-0.174	182.3	190.0	189.6	184.4	172.0	166.4	161.7	157.8	157.9	166.1	181.0	200.8	217.3
322	977.7	2.02	0.0938	1001.1	1.539	78.2	0.336	5.24	-0.284	-0.178	181.4	183.7	181.2	175.3	163.3	159.2	154.8	150.1	149.3	157.3	168.6	188.1	206.0
323	977.7	1.68	0.0942	1005.5	1.449	73.7	0.336	5.24	-0.284	-0.179	180.2	173.2	171.6	163.6	151.1	146.7	143.6	139.0	137.0	143.2	150.3	169.7	184.5
324	978.4	0.67	0.0934	996.7	1.358	69.1	0.336	5.03	-0.286	-0.181	179.3	165.1	163.2	155.2	146.6	139.3	136.5	132.0	128.5	130.5	136.8	153.6	166.4
325	979.0	1.35	0.0954	1018.7	1.269	64.5	0.336	5.03	-0.286	-0.185	177.5	153.4	153.3	145.4	136.9	129.8	126.4	122.2	119.1	121.6	122.8	134.2	145.6
326	973.6	1.68	0.0934	996.7	1.159	59.0	0.336	5.03	-0.284	-0.182	175.6	139.8	140.6	136.0	126.9	119.5	116.8	113.5	110.6	109.8	111.4	117.8	125.8
327	965.6	25.59	0.1853	1977.5	1.580	80.4	0.408	29.45	-0.075	-0.012	189.9	208.9	224.1	225.6	221.9	215.3	211.2	210.2	199.9	192.2	186.1	176.4	168.4

Run	p	Δp	m	G	power	q	hp-power	T_{in}	x_{in}	x_{DO}	T_{hp}	Distance from CHF location (m)											
-	kPa	kPa	Kgs^{-1}	$Kgm^{-2}s^{-1}$	kW	kWm^{-2}	kW	°C	-	-	°C	0.01	0.05	0.10	0.20	0.30	0.40	0.50	0.60	0.70	0.80	0.90	1.00
												Inside wall temperature (°C)											
328	957.5	23.23	0.1912	2041.3	1.382	70.3	0.408	29.45	-0.072	-0.012	190.5	195.9	205.8	206.1	203.9	203.0	198.6	196.5	188.8	182.6	178.2	169.8	161.5
329	962.2	19.19	0.1884	2010.5	1.189	60.5	0.408	29.66	-0.072	-0.012	190.9	180.7	186.1	184.2	182.9	182.5	180.2	180.2	174.5	171.9	167.6	161.9	155.6
330	963.5	16.50	0.1884	2010.5	0.988	50.3	0.408	29.66	-0.072	-0.014	191.0	165.2	164.5	161.1	159.9	159.9	159.7	160.8	157.8	155.9	154.7	150.7	146.2
331	962.9	13.47	0.1884	2010.5	0.795	40.5	0.408	29.66	-0.072	-0.015	190.1	149.1	143.8	138.0	136.8	136.9	138.7	141.0	140.5	139.0	138.9	137.0	134.8
332	964.2	10.77	0.1865	1990.7	0.597	30.4	0.408	29.66	-0.073	-0.016	188.7	130.8	119.0	110.0	107.4	107.7	110.2	113.0	113.7	114.2	115.4	118.3	120.0
333	961.5	19.86	0.1886	2012.7	1.582	80.5	0.408	25.09	-0.111	-0.049	188.3	207.0	222.9	223.7	224.6	223.1	222.4	221.6	215.4	211.2	206.8	199.3	192.0
334	963.5	16.83	0.1912	2041.3	1.387	70.6	0.408	24.68	-0.115	-0.055	187.4	177.1	188.4	187.4	188.9	187.9	187.6	188.9	187.3	182.9	181.3	174.9	164.7
335	963.5	13.80	0.1871	1997.3	1.191	60.6	0.408	24.68	-0.115	-0.055	186.2	162.6	169.6	167.4	168.9	167.4	169.2	171.0	168.7	168.7	168.8	165.3	156.5
336	963.5	11.45	0.1892	2019.3	0.998	50.8	0.408	24.68	-0.115	-0.057	184.8	147.8	150.2	145.9	146.7	147.0	147.5	150.7	150.7	151.0	152.5	152.0	146.3
337	963.5	9.76	0.1865	1990.7	0.794	40.4	0.408	24.68	-0.115	-0.058	182.4	136.9	131.7	126.3	126.3	125.9	127.2	129.8	130.3	131.6	133.7	137.6	142.6
338	962.9	14.81	0.1879	2006.1	1.514	77.1	0.420	21.77	-0.140	-0.077	245.0	219.9	205.6	203.1	202.6	205.0	207.0	208.2	206.0	203.1	198.1	193.7	188.9
339	961.5	13.47	0.1908	2036.9	1.416	72.1	0.420	21.77	-0.139	-0.078	245.8	215.6	196.2	192.8	191.9	194.4	195.9	197.9	196.7	195.1	191.1	188.6	185.0
340	966.2	12.12	0.1867	1992.9	1.321	67.2	0.420	21.77	-0.141	-0.079	246.0	210.7	185.9	181.8	180.2	182.5	183.4	185.7	185.5	184.6	182.0	181.3	179.5
341	973.0	13.13	0.1847	1970.9	1.604	81.7	0.420	16.60	-0.188	-0.122	240.4	215.1	216.9	216.2	200.9	191.3	184.2	182.7	178.2	177.2	175.5	179.7	185.9
342	957.5	10.10	0.1875	2001.7	1.504	76.5	0.420	16.39	-0.183	-0.120	238.8	205.3	198.7	204.2	192.1	180.8	174.3	169.3	164.3	163.2	161.0	164.5	171.0
343	965.6	12.46	0.1908	2036.9	1.418	72.2	0.420	16.39	-0.186	-0.125	237.1	195.8	177.0	188.6	185.6	176.1	169.5	165.6	159.0	159.5	157.3	159.0	164.3
344	967.6	15.49	0.1832	1955.5	1.892	96.3	0.420	11.84	-0.225	-0.158	228.6	205.2	222.3	231.9	218.2	205.3	196.6	191.9	184.6	182.1	179.5	184.3	193.9
345	971.0	14.14	0.1875	2001.7	1.786	90.9	0.420	11.43	-0.230	-0.165	225.4	191.5	191.4	210.2	207.0	196.0	187.8	183.0	175.8	173.0	169.5	171.5	180.2
346	964.9	15.49	0.1882	2008.3	1.955	99.5	0.420	9.57	-0.243	-0.177	213.3	172.3	166.1	190.5	194.6	182.3	173.5	166.9	158.8	156.6	155.5	157.6	159.2
347	960.2	13.13	0.1933	2063.2	1.848	94.1	0.420	9.37	-0.243	-0.179	212.4	163.7	128.4	164.1	192.0	184.6	175.7	168.6	159.9	158.3	154.7	152.6	155.1
348	966.9	61.61	0.2817	3006.6	1.799	91.6	0.384	34.44	-0.031	0.009	202.7	213.9	238.0	234.9	213.9	202.0	198.2	189.4	180.0	172.6	165.2	155.6	148.0
349	956.8	59.59	0.2838	3028.6	1.631	83.0	0.384	34.44	-0.028	0.012	196.6	201.2	223.8	220.4	201.2	191.9	188.2	179.9	172.1	165.8	159.5	151.1	144.2
350	960.2	54.20	0.2850	3041.8	1.442	73.4	0.384	34.44	-0.029	0.009	194.8	187.2	206.0	204.1	187.2	179.7	177.2	170.5	164.5	159.9	155.3	147.5	142.5
351	965.6	48.48	0.2827	3017.6	1.266	64.5	0.384	34.23	-0.033	0.005	193.3	173.7	189.9	187.6	173.2	167.5	165.9	160.8	156.9	153.7	150.2	144.0	134.0
352	966.9	43.77	0.2833	3024.2	1.081	55.0	0.384	34.23	-0.033	0.004	191.1	159.4	171.2	169.6	156.2	151.9	151.5	147.9	145.5	143.5	141.5	136.8	131.7
353	960.9	39.73	0.2856	3048.4	0.900	45.8	0.384	34.02	-0.033	0.003	188.7	145.1	152.4	150.7	142.1	138.1	136.1	134.0	132.9	132.0	131.0	127.5	126.0
354	958.8	36.02	0.2842	3033.0	0.726	37.0	0.384	34.23	-0.030	0.005	186.6	131.5	132.7	130.5	123.2	119.6	118.2	117.2	117.4	117.5	117.6	117.5	118.2
355	961.5	31.31	0.2842	3033.0	0.545	27.7	0.384	34.23	-0.031	0.004	184.2	114.8	109.7	107.6	100.7	97.9	97.1	97.2	97.5	98.4	99.3	101.0	103.7
356	965.6	44.44	0.2751	2936.3	1.621	82.5	0.420	30.49	-0.066	-0.022	197.0	198.0	227.0	226.0	213.2	207.1	203.0	197.8	193.6	189.6	185.5	179.5	173.9
357	958.2	41.41	0.2786	2973.6	1.448	73.7	0.420	30.07	-0.067	-0.024	199.8	186.0	209.8	209.4	200.4	194.8	190.2	186.2	182.4	180.1	177.9	173.6	169.1
358	962.9	35.69	0.2813	3002.2	1.259	64.1	0.420	29.87	-0.070	-0.029	201.7	170.8	190.0	191.4	180.5	175.8	174.6	172.2	170.5	169.5	168.5	167.3	165.6
359	975.0	29.96	0.2838	3028.6	1.082	55.1	0.420	29.45	-0.078	-0.038	202.3	153.1	166.2	173.8	165.2	159.8	157.3	156.7	156.5	157.5	158.5	159.1	159.7
360	969.6	26.60	0.2846	3037.4	0.903	46.0	0.420	29.24	-0.078	-0.039	202.3	138.8	144.5	153.3	144.7	138.4	138.6	138.7	139.4	141.1	142.9	144.7	148.6

Run	p	Δp	m	G	power	q	hp-power	T_{in}	x_{in}	x_{DO}	T_{hp}	Distance from CHF location (m)											
-	kPa	kPa	Kgs^{-1}	$Kgm^{-2}s^{-1}$	kW	kWm^{-2}	kW	°C	-	-	°C	0.01	0.05	0.10	0.20	0.30	0.40	0.50	0.60	0.70	0.80	0.90	1.00
												Inside wall temperature (°C)											
361	960.9	24.24	0.2829	3019.8	0.723	36.8	0.420	29.45	-0.073	-0.034	201.7	126.6	123.8	129.4	124.9	119.3	117.4	117.1	117.6	119.7	121.9	124.7	131.5
362	961.5	40.74	0.2811	3000.0	1.711	87.1	0.420	27.17	-0.093	-0.050	244.6	219.1	234.7	233.5	220.9	215.6	214.2	211.7	206.0	200.7	192.4	185.8	178.3
363	961.5	38.04	0.2838	3028.6	1.610	82.0	0.420	26.96	-0.095	-0.053	243.1	213.2	224.3	225.1	211.4	206.5	205.1	204.2	199.1	195.4	187.6	182.4	175.4
364	960.9	35.35	0.2848	3039.6	1.514	77.1	0.420	27.37	-0.091	-0.049	241.5	207.4	214.1	216.8	207.3	201.0	197.3	196.8	192.3	189.8	182.3	178.2	172.5
365	960.9	34.00	0.2856	3048.4	1.416	72.1	0.420	27.17	-0.093	-0.052	239.4	172.8	178.2	182.9	176.2	169.4	165.3	166.0	165.5	162.6	156.4	153.2	148.5
366	960.9	31.31	0.2846	3037.4	1.320	67.2	0.420	26.96	-0.095	-0.054	237.3	194.3	189.9	197.5	185.7	178.9	178.4	178.5	177.0	175.2	170.1	167.9	164.7
367	960.2	29.29	0.2838	3028.6	1.234	62.8	0.420	26.96	-0.095	-0.054	234.9	189.0	180.0	187.9	176.7	170.2	169.8	170.1	168.6	167.7	163.0	162.3	159.0
368	959.5	27.27	0.2873	3066.0	1.133	57.7	0.420	26.96	-0.094	-0.054	232.2	181.2	165.2	176.2	167.4	159.5	158.7	159.0	158.5	158.1	155.4	154.5	152.5
369	960.9	25.25	0.2850	3041.8	1.042	53.1	0.420	26.96	-0.095	-0.055	228.9	174.7	151.6	164.1	159.3	150.0	147.8	148.7	148.7	148.7	146.8	146.7	145.9
370	964.9	22.89	0.2807	2995.6	0.865	44.0	0.420	27.37	-0.093	-0.053	225.9	165.5	130.4	139.1	138.9	129.8	127.2	127.3	125.6	127.6	126.3	127.7	127.8
371	966.9	22.56	0.2805	2993.4	0.676	34.4	0.420	27.17	-0.095	-0.056	218.0	147.5	94.2	91.1	97.2	124.8	119.3	109.7	100.0	99.1	99.2	97.7	98.4
372	962.2	32.66	0.2825	3015.4	1.871	68.0	0.420	22.81	-0.131	-0.089	188.8	173.4	228.6	261.3	240.5	233.8	230.9	234.6	228.9	225.8	219.0	212.8	206.0
373	965.6	28.95	0.2846	3037.4	1.732	63.0	0.420	22.81	-0.132	-0.091	194.1	172.2	213.8	249.1	229.7	222.0	220.1	223.7	222.1	217.4	211.3	206.9	202.1
374	967.6	26.26	0.2811	3000.0	1.587	80.8	0.420	22.81	-0.133	-0.090	196.7	166.7	190.7	196.4	193.5	184.4	182.8	183.8	184.8	185.0	182.7	181.7	177.0
375	963.5	24.91	0.2827	3017.6	1.500	76.4	0.420	22.60	-0.133	-0.091	198.3	163.3	176.6	219.4	211.8	199.8	198.3	200.4	199.3	197.6	194.1	192.2	189.8
376	966.9	23.57	0.2844	3035.2	1.422	72.4	0.420	22.60	-0.134	-0.093	199.6	159.3	160.0	203.1	209.6	193.3	190.5	191.7	188.5	189.6	186.7	185.7	184.2
377	963.5	23.23	0.2805	2993.4	1.327	67.6	0.420	22.81	-0.131	-0.090	200.3	155.8	144.3	183.4	205.2	185.6	183.6	181.9	181.6	180.6	177.8	177.7	177.1
378	963.5	23.57	0.2850	3041.8	1.915	97.5	0.420	16.60	-0.184	-0.141	238.5	189.2	184.0	241.6	262.4	246.1	242.8	242.1	239.8	236.7	231.4	230.4	228.7
379	963.5	23.23	0.2862	3055.0	1.803	91.8	0.420	16.60	-0.184	-0.141	238.5	182.1	145.8	184.1	262.6	249.9	240.0	237.2	234.0	229.9	224.7	224.3	223.2
380	962.2	60.60	0.3796	4051.1	1.920	97.7	0.420	26.96	-0.095	-0.063	244.2	195.9	206.8	238.5	236.5	220.4	214.8	211.0	204.6	200.3	196.6	192.2	188.7
381	961.5	57.23	0.3787	4042.4	1.792	91.2	0.420	26.96	-0.095	-0.063	245.4	193.1	196.4	226.6	227.7	211.6	205.8	203.0	197.8	194.4	187.6	182.9	181.4
382	960.9	53.87	0.3835	4092.9	1.702	86.7	0.420	26.75	-0.097	-0.065	240.0	184.4	180.6	212.2	222.1	204.8	197.0	196.2	191.0	189.1	183.2	180.4	178.7
383	961.5	50.16	0.3851	4110.5	1.601	81.5	0.420	26.75	-0.097	-0.066	234.9	176.3	167.1	197.0	215.0	198.3	190.2	188.1	185.2	182.9	177.9	175.3	173.6
384	961.5	48.14	0.3767	4020.4	1.511	76.9	0.420	26.96	-0.095	-0.063	233.7	173.2	159.3	185.8	207.3	191.1	185.3	180.9	177.3	176.3	171.3	170.0	169.0
385	958.2	43.77	0.3833	4090.7	1.318	67.1	0.420	26.96	-0.094	-0.063	232.2	164.1	137.1	157.5	191.8	178.6	168.7	165.1	162.7	161.2	158.3	157.8	157.7
386	960.2	40.40	0.3701	3950.0	1.878	95.6	0.420	22.60	-0.132	-0.099	223.4	166.8	152.0	192.6	264.3	238.4	225.9	221.1	215.9	214.1	208.0	206.1	205.6
387	960.9	40.74	0.3818	4075.3	1.797	91.5	0.420	22.40	-0.134	-0.102	219.8	157.9	125.4	148.9	250.1	244.9	226.0	216.4	212.0	208.6	203.6	204.3	205.0
388	1305.6	15.49	0.0466	497.6	1.388	70.6	0.360	39.64	-0.100	0.140	179.9	198.3	214.3	219.0	219.9	219.7	217.9	217.5	213.8	215.2	213.2	211.5	209.3
389	1300.2	16.16	0.0499	532.7	1.194	60.8	0.360	40.06	-0.094	0.125	180.2	181.9	194.6	198.5	200.1	198.9	199.5	199.4	197.8	198.3	197.0	196.5	195.4
390	1305.6	16.50	0.0479	510.7	0.984	50.1	0.360	40.48	-0.090	0.133	180.3	166.8	171.9	173.3	175.1	176.3	176.9	175.8	175.9	176.3	176.4	175.8	175.2
391	1307.6	14.48	0.0458	488.8	0.797	40.6	0.360	40.89	-0.085	0.143	180.4	151.2	150.2	150.8	151.7	152.2	152.6	153.9	153.9	155.1	155.7	156.7	157.8
392	1305.6	14.81	0.0487	519.5	1.393	70.9	0.360	34.85	-0.143	0.087	177.9	195.7	213.9	218.3	219.5	217.9	219.3	219.2	217.9	216.6	214.9	212.9	209.8
393	1306.3	15.49	0.0476	508.5	1.182	60.1	0.360	35.27	-0.139	0.091	178.0	178.8	191.5	195.7	197.6	198.3	198.9	199.1	199.9	197.2	196.6	194.8	192.5

Run	p	Δp	m	G	power	q	hp-power	T_{in}	x_{in}	x_{DO}	T_{hp}	Distance from CHF location (m)											
-	kPa	kPa	Kgs^{-1}	$Kgm^{-2}s^{-1}$	kW	kWm^{-2}	kW	°C	-	-	°C	0.01	0.05	0.10	0.20	0.30	0.40	0.50	0.60	0.70	0.80	0.90	1.00
												Inside wall temperature (°C)											
394	1306.3	14.48	0.0408	436.0	0.998	50.8	0.360	35.06	-0.141	0.121	178.1	162.1	168.4	171.7	174.4	176.8	177.3	177.5	178.7	178.2	178.1	178.6	178.6
395	1300.9	12.46	0.0528	563.5	0.799	40.7	0.360	35.06	-0.139	0.059	177.6	144.2	142.9	145.0	148.6	149.9	151.1	152.6	154.4	155.2	155.3	156.7	156.7
396	1303.6	14.14	0.0464	495.4	1.490	75.8	0.360	29.66	-0.191	0.052	174.8	198.8	221.8	228.7	231.4	230.9	231.5	231.1	230.9	228.5	225.3	222.0	219.4
397	1304.9	14.48	0.0507	541.5	1.389	70.7	0.360	29.87	-0.190	0.031	175.2	190.5	210.3	216.8	219.8	220.4	220.4	220.4	220.4	218.6	216.7	214.3	211.7
398	1307.0	14.48	0.0413	440.4	1.175	59.8	0.360	30.28	-0.187	0.078	175.3	173.3	184.8	191.1	195.4	196.7	197.2	198.5	198.5	197.2	198.1	196.9	196.2
399	1304.9	12.12	0.0509	543.7	0.992	50.5	0.360	30.49	-0.184	0.026	175.4	154.8	157.8	163.2	169.9	172.9	173.6	175.1	175.0	176.0	177.2	177.3	178.2
400	1307.6	11.45	0.0505	539.3	0.899	45.8	0.360	30.49	-0.185	0.024	174.8	146.7	145.5	150.3	158.0	161.1	163.2	164.3	166.4	166.8	167.4	168.3	168.7
401	1303.6	14.14	0.0522	556.9	1.388	70.6	0.360	24.68	-0.238	-0.024	172.0	180.1	198.0	208.0	216.1	218.6	218.6	220.0	220.4	219.8	218.5	217.7	214.6
402	1304.3	13.13	0.0483	515.1	1.189	60.5	0.360	25.09	-0.234	-0.008	172.2	163.5	171.9	181.0	192.0	194.5	195.6	198.4	199.3	198.9	200.2	200.0	202.8
403	1305.6	10.10	0.0474	506.3	0.991	50.4	0.360	25.51	-0.231	-0.006	171.7	141.6	141.0	148.1	162.0	166.9	170.5	173.9	175.9	176.6	178.1	179.5	181.3
404	1308.3	13.47	0.0481	512.9	1.575	80.2	0.360	20.32	-0.280	-0.042	172.7	190.8	211.2	224.3	235.2	236.5	236.2	238.8	238.8	236.2	235.8	234.4	233.7
405	1310.3	13.47	0.0468	499.7	1.381	70.3	0.360	20.74	-0.277	-0.038	172.6	172.7	186.1	197.6	211.6	214.9	218.4	218.7	219.0	220.7	219.6	219.7	221.4
406	1304.3	10.10	0.0499	532.7	1.188	60.5	0.360	20.53	-0.276	-0.057	171.9	149.3	154.2	165.2	182.3	187.8	193.2	196.3	197.9	197.1	199.6	200.5	202.8
407	1311.0	12.79	0.0487	519.5	1.482	75.5	0.360	15.77	-0.322	-0.090	180.9	170.8	182.0	195.7	215.0	220.9	223.9	228.4	229.5	229.7	229.6	227.5	227.0
408	1307.0	11.45	0.0487	519.5	1.384	70.5	0.360	15.77	-0.321	-0.091	179.3	159.8	167.1	179.8	200.3	208.6	214.4	218.1	219.0	220.1	221.4	219.8	216.9
409	1307.0	10.77	0.0483	515.1	1.279	65.1	0.360	15.77	-0.321	-0.092	176.4	146.4	150.5	162.5	182.0	193.4	199.5	205.6	207.8	209.0	210.4	209.5	207.7
410	1309.0	11.11	0.0472	504.1	1.483	75.5	0.360	10.81	-0.366	-0.127	163.4	158.1	167.8	174.5	187.9	192.9	200.9	209.9	218.7	222.8	227.0	228.1	227.0
411	1311.7	10.10	0.0470	501.9	1.378	70.2	0.360	10.19	-0.373	-0.135	162.8	144.5	151.7	157.3	170.4	179.4	186.6	198.1	203.8	211.2	218.7	221.5	219.8
412	1312.3	9.09	0.0497	530.5	1.281	65.2	0.360	9.98	-0.375	-0.152	161.6	134.7	139.5	143.7	153.2	156.7	164.8	174.8	185.0	195.6	206.3	211.3	210.1
413	1312.3	8.42	0.0491	523.9	1.182	60.2	0.360	9.78	-0.377	-0.154	159.8	122.3	128.2	131.5	139.9	144.4	148.3	156.7	168.4	181.1	193.7	200.1	201.2
414	1312.3	13.47	0.0408	436.0	1.577	80.3	0.360	9.78	-0.377	-0.097	210.2	175.8	180.0	192.1	207.6	219.5	230.9	235.3	238.9	242.5	243.6	243.4	240.0
415	1300.2	12.79	0.0396	422.8	1.375	70.0	0.360	9.37	-0.376	-0.094	204.4	155.1	155.9	166.2	181.4	193.8	207.1	212.0	218.8	222.9	224.9	226.1	224.4
416	1308.3	11.45	0.0361	385.4	1.181	60.1	0.360	9.16	-0.381	-0.078	200.4	145.5	149.8	150.9	146.3	148.8	162.0	173.9	185.3	192.8	200.4	204.6	205.8
417	1307.0	9.43	0.0363	387.6	0.989	50.3	0.360	9.37	-0.378	-0.084	197.1	117.0	124.7	128.3	128.2	133.1	140.6	146.4	157.5	166.2	174.8	179.5	185.0
418	1306.3	10.44	0.0487	519.5	1.627	82.8	0.360	9.78	-0.374	-0.138	205.5	180.7	185.3	194.6	206.5	219.0	232.6	238.1	240.7	242.7	242.2	239.9	235.8
419	1317.1	10.10	0.0493	526.1	1.438	73.2	0.360	9.78	-0.378	-0.150	200.3	158.8	157.8	166.9	177.2	189.9	204.8	213.1	217.8	222.0	224.1	224.8	221.4
420	1311.0	8.08	0.0491	523.9	1.254	63.8	0.360	9.78	-0.376	-0.151	196.4	135.0	131.9	142.1	148.4	160.9	174.5	180.6	189.9	196.6	203.2	205.1	203.4
421	1313.7	9.43	0.0921	983.5	1.382	70.3	0.360	44.86	-0.047	0.074	195.1	204.4	213.3	209.4	206.4	199.7	195.6	191.4	186.2	179.4	175.5	169.8	162.6
422	1309.6	10.44	0.0926	987.9	1.179	60.0	0.360	45.06	-0.044	0.074	193.0	189.8	193.1	190.3	187.5	182.1	179.3	176.5	172.0	166.6	163.7	159.5	152.6
423	1307.0	6.40	0.0891	950.5	0.986	50.2	0.360	45.27	-0.041	0.079	190.6	172.7	173.3	169.5	167.4	163.5	161.9	160.4	155.3	153.3	151.1	147.6	141.9
424	1307.6	5.39	0.0928	990.1	0.799	40.7	0.360	45.48	-0.039	0.073	188.1	159.0	153.2	149.7	147.5	144.8	144.2	143.6	141.5	138.5	137.2	134.9	131.8
425	1309.6	5.05	0.0934	996.7	0.603	30.7	0.360	45.69	-0.038	0.072	183.8	140.8	129.9	125.4	123.2	121.4	121.7	122.0	119.7	119.2	118.7	118.1	117.4
426	1310.3	5.05	0.0915	976.9	0.407	20.7	0.360	45.90	-0.036	0.073	178.1	121.0	105.8	99.0	96.9	96.3	97.2	98.0	97.3	97.4	97.5	97.4	96.8

Run	p	Δp	m	G	power	q	hp-power	T_{in}	x_{in}	x_{DO}	T_{hp}	Distance from CHF location (m)											
-	kPa	kPa	Kgs^{-1}	$Kgm^{-2}s^{-1}$	kW	kWm^{-2}	kW	°C	-	-	°C	0.01	0.05	0.10	0.20	0.30	0.40	0.50	0.60	0.70	0.80	0.90	1.00
												Inside wall temperature (°C)											
427	1301.6	9.09	0.0971	1036.3	1.485	75.6	0.360	40.27	-0.089	0.028	177.0	204.7	220.7	222.4	220.8	214.6	209.2	207.3	201.5	193.9	188.3	180.8	171.2
428	1307.6	4.38	0.0921	983.5	1.380	70.3	0.360	35.06	-0.141	-0.020	192.5	196.9	206.9	210.1	211.6	210.3	209.0	207.4	203.5	198.1	194.5	187.3	177.7
429	1309.6	3.70	0.0938	1001.1	1.184	60.3	0.360	35.06	-0.142	-0.025	189.1	179.5	184.9	187.6	190.0	190.6	189.9	190.0	187.8	183.7	181.8	177.6	172.2
430	1309.0	3.37	0.0932	994.5	0.992	50.5	0.360	35.06	-0.142	-0.027	183.4	161.2	160.2	159.9	163.6	164.5	166.6	168.7	168.0	167.6	166.3	164.1	161.8
431	1310.3	3.37	0.0919	981.3	0.794	40.4	0.360	35.06	-0.142	-0.029	177.2	140.2	134.1	131.7	134.6	137.1	141.0	144.9	146.0	146.7	147.1	146.9	146.0
432	1309.0	2.69	0.0911	972.5	0.603	30.7	0.360	35.06	-0.142	-0.030	172.4	121.4	108.2	101.6	104.3	107.6	112.2	116.7	118.6	121.1	123.6	125.8	124.9
433	1309.6	4.38	0.0938	1001.1	1.803	91.8	0.312	29.45	-0.195	-0.084	183.6	217.2	237.4	245.0	244.2	244.6	245.3	242.3	234.7	230.2	225.7	217.7	209.3
434	1307.0	3.37	0.0952	1016.5	1.710	87.1	0.312	29.24	-0.196	-0.088	183.7	209.4	227.5	234.5	235.2	237.2	236.5	231.7	228.7	224.9	221.1	218.7	212.8
435	1303.6	3.37	0.0942	1005.5	1.618	82.4	0.312	29.24	-0.195	-0.087	183.6	204.5	219.0	226.0	226.0	225.3	223.7	222.5	221.7	219.0	214.9	204.3	190.2
436	1304.9	2.69	0.0936	998.9	1.529	77.9	0.312	29.24	-0.196	-0.088	183.5	195.1	207.3	214.5	216.6	219.5	220.5	217.2	215.4	213.7	211.9	207.0	201.3
437	1307.6	2.36	0.0942	1005.5	1.440	73.3	0.312	29.66	-0.193	-0.087	183.0	186.6	195.8	202.2	204.4	207.7	211.9	210.4	210.1	208.0	206.1	202.6	198.7
438	1309.6	1.68	0.0934	996.7	1.355	69.0	0.312	29.66	-0.193	-0.087	182.1	177.8	184.7	190.4	192.0	195.7	201.7	202.6	201.7	201.9	200.5	197.3	192.8
439	1305.6	2.36	0.0928	990.1	1.256	63.9	0.312	29.66	-0.192	-0.087	180.4	169.1	172.7	177.2	178.7	182.8	189.7	192.0	193.1	192.7	192.2	190.7	189.7
440	1306.3	3.03	0.0932	994.5	1.175	59.8	0.312	29.66	-0.192	-0.089	179.7	161.9	162.1	165.1	167.1	172.8	179.4	182.3	183.0	185.5	184.6	183.7	184.2
441	1308.3	1.68	0.0940	1003.3	1.080	55.0	0.312	29.66	-0.193	-0.091	179.0	153.4	150.1	152.4	153.8	160.0	167.2	171.1	173.2	173.4	175.5	175.1	176.9
442	1309.6	2.02	0.0934	996.7	0.992	50.5	0.312	29.66	-0.193	-0.092	177.7	147.3	140.5	140.5	140.7	146.3	153.0	156.8	158.8	160.7	164.0	165.6	167.6
443	1309.6	2.36	0.0934	996.7	0.904	46.0	0.312	29.66	-0.193	-0.094	176.6	138.8	130.0	128.8	128.7	133.9	140.8	144.1	146.1	149.6	153.3	155.8	159.6
444	1309.0	0.67	0.0921	983.5	0.810	41.3	0.312	29.45	-0.195	-0.095	175.6	127.1	116.9	115.9	115.3	120.7	127.5	131.5	134.9	138.8	142.6	146.1	146.8
445	1307.0	0.67	0.0936	998.9	0.719	36.6	0.312	29.66	-0.192	-0.095	174.8	116.6	104.1	103.5	101.9	105.9	112.3	117.1	121.1	125.4	129.7	133.8	136.7
446	1303.6	0.67	0.0944	1007.7	0.634	32.3	0.312	29.66	-0.191	-0.096	172.0	105.2	91.4	92.7	90.4	92.4	97.0	101.5	105.1	109.3	113.4	116.7	120.6
447	1304.3	1.01	0.0950	1014.3	1.901	96.8	0.360	24.05	-0.244	-0.119	236.9	244.2	255.2	254.2	248.1	247.3	244.6	241.3	241.1	238.3	235.5	228.8	223.1
448	1309.0	0.34	0.0946	1009.9	1.797	91.5	0.360	24.05	-0.245	-0.122	236.9	235.6	244.9	244.5	235.1	234.3	235.2	233.3	233.7	232.6	231.5	227.7	216.0
449	1311.0	1.35	0.0940	1003.3	1.708	87.0	0.360	24.26	-0.244	-0.121	237.3	228.2	234.5	233.8	226.2	226.9	228.4	225.9	226.0	226.3	226.5	221.4	213.0
450	1305.6	2.02	0.0948	1012.1	1.617	82.3	0.360	24.26	-0.242	-0.121	236.6	219.6	223.8	222.8	217.5	217.4	218.5	218.3	218.6	219.6	220.6	216.9	210.2
451	1308.3	0.34	0.0942	1005.5	1.526	77.7	0.360	24.26	-0.243	-0.123	236.1	211.7	213.6	211.5	206.1	205.8	208.2	208.6	208.9	211.1	213.5	211.0	206.7
452	1307.0	0.34	0.0948	1012.1	1.447	73.6	0.360	24.47	-0.241	-0.122	235.5	204.5	202.6	200.1	196.4	196.1	198.9	200.4	201.9	203.0	206.5	206.0	202.4
453	1307.6	2.36	0.0932	994.5	1.351	68.8	0.360	24.47	-0.241	-0.122	234.0	195.9	189.1	185.7	181.8	182.5	184.7	185.9	188.1	190.7	194.8	196.8	195.2
454	1311.7	1.68	0.0950	1014.3	1.261	64.2	0.360	24.26	-0.245	-0.128	232.8	185.7	175.8	172.4	168.3	169.1	172.6	174.8	176.9	178.4	182.5	185.3	186.7
455	1311.7	4.04	0.0940	1003.3	1.171	59.6	0.360	24.47	-0.243	-0.126	231.0	172.1	157.1	154.0	151.6	153.7	156.7	159.0	160.1	161.4	164.3	169.0	173.8
456	1308.3	1.68	0.0944	1007.7	1.076	54.8	0.360	24.47	-0.241	-0.127	229.6	160.7	141.4	139.5	137.6	141.1	144.9	145.6	145.5	146.2	148.5	153.7	160.0
457	1311.7	0.34	0.0950	1014.3	0.987	50.2	0.360	24.47	-0.243	-0.130	228.4	151.6	128.9	126.4	126.2	128.9	130.3	130.1	129.1	128.3	130.0	134.6	139.6
458	1310.3	2.69	0.0954	1018.7	0.897	45.7	0.360	24.47	-0.242	-0.131	226.6	141.5	116.5	115.8	116.0	117.1	120.0	120.6	119.8	119.8	120.6	123.7	129.2
459	1311.0	1.35	0.0948	1012.1	0.814	41.4	0.360	24.26	-0.244	-0.134	224.5	131.5	105.1	106.8	106.2	108.6	115.1	118.1	120.0	122.5	125.0	127.2	131.7

Run	p	Δp	m	G	power	q	hp-power	T_{in}	x_{in}	x_{DO}	T_{hp}	Distance from CHF location (m)											
-	kPa	kPa	Kgs^{-1}	$Kgm^{-2}s^{-1}$	kW	kWm^{-2}	kW	°C	-	-	°C	0.01	0.05	0.10	0.20	0.30	0.40	0.50	0.60	0.70	0.80	0.90	1.00
												Inside wall temperature (°C)											
460	1313.7	2.02	0.0950	1014.3	0.721	36.7	0.360	24.47	-0.243	-0.134	221.1	121.1	91.6	96.4	99.8	101.7	103.3	105.8	108.3	110.6	113.0	114.6	117.6
461	1304.9	0.34	0.0926	987.9	1.884	95.9	0.360	19.91	-0.282	-0.155	221.8	229.8	245.1	246.5	236.2	235.7	236.9	236.6	237.0	239.5	242.0	240.6	229.3
462	1307.0	2.02	0.0936	998.9	1.795	91.4	0.360	19.70	-0.285	-0.160	221.9	220.0	233.8	235.2	225.8	223.0	225.0	226.1	227.1	230.3	234.3	231.9	224.3
463	1313.7	0.67	0.0936	998.9	1.708	87.0	0.360	19.70	-0.287	-0.163	221.6	213.2	223.4	223.6	215.4	214.1	215.4	216.8	219.4	222.6	226.9	227.5	220.2
464	1313.7	2.69	0.0934	996.7	1.618	82.4	0.360	19.50	-0.289	-0.166	221.3	203.1	208.5	206.9	200.1	199.1	199.9	200.1	202.1	206.7	212.8	215.7	217.8
465	1300.9	2.36	0.0942	1005.5	1.524	77.6	0.360	19.50	-0.284	-0.164	219.8	188.9	183.7	181.1	172.2	168.6	167.6	165.3	165.9	169.4	175.9	185.2	193.1
466	1302.2	1.35	0.0942	1005.5	1.433	73.0	0.360	19.50	-0.285	-0.166	218.0	177.2	169.2	167.0	157.7	153.3	149.4	146.4	145.2	147.8	153.8	164.3	177.0
467	1302.2	0.00	0.0938	1001.1	1.351	68.8	0.360	19.50	-0.285	-0.166	215.6	163.9	155.0	153.4	144.9	139.9	135.0	130.5	130.5	132.8	137.4	147.5	160.0
468	1303.6	0.00	0.0946	1009.9	1.259	64.1	0.360	19.29	-0.287	-0.171	212.0	154.6	142.0	142.5	138.3	131.4	126.8	123.5	123.5	123.9	125.0	132.9	140.7
469	1302.2	0.00	0.0950	1014.3	1.166	59.3	0.360	19.50	-0.285	-0.170	208.9	140.4	128.0	130.3	126.9	121.4	115.9	113.8	112.7	113.2	115.0	119.9	127.2
470	1300.2	0.34	0.0924	985.7	1.080	55.0	0.360	19.50	-0.284	-0.167	203.5	131.8	121.0	123.9	121.7	116.1	111.3	108.3	107.3	108.4	109.5	112.9	117.1
471	1306.3	1.01	0.0934	996.7	0.996	50.7	0.360	19.50	-0.286	-0.172	199.5	129.9	118.1	124.3	118.0	114.4	112.6	110.9	109.8	110.0	110.3	110.8	111.4
472	1312.3	0.67	0.0959	1023.1	1.984	101.0	0.360	14.94	-0.330	-0.205	202.6	223.5	240.3	240.2	230.1	228.1	228.8	230.4	232.7	235.7	242.0	243.5	239.6
473	1313.7	1.35	0.0921	983.5	1.887	96.1	0.360	14.74	-0.333	-0.204	203.2	210.6	211.5	206.5	190.9	183.3	180.0	176.0	176.0	185.3	194.6	206.3	211.2
474	1316.4	1.01	0.0944	1007.7	1.793	91.3	0.360	14.74	-0.334	-0.209	202.6	193.7	194.5	190.2	172.7	164.3	159.3	157.1	156.8	162.6	171.2	185.1	197.9
475	1311.0	1.01	0.0934	996.7	1.703	86.7	0.360	14.53	-0.333	-0.209	201.9	187.2	186.8	182.8	165.6	158.4	155.0	149.5	150.0	154.2	160.4	174.6	187.9
476	1310.3	2.36	0.0940	1003.3	1.612	82.1	0.360	14.32	-0.335	-0.213	201.7	181.5	180.8	176.2	160.2	154.3	150.6	147.3	146.7	149.6	154.4	165.6	178.0
477	1314.4	1.01	0.0940	1003.3	1.524	77.6	0.360	14.32	-0.337	-0.216	201.4	174.1	171.2	167.5	152.5	146.6	143.8	139.6	137.0	139.2	141.4	151.2	162.8
478	1313.7	1.01	0.0956	1020.9	1.443	73.5	0.360	14.32	-0.336	-0.218	200.5	164.7	162.8	159.1	144.8	140.1	137.6	133.4	131.1	132.4	133.7	139.8	149.2
479	1313.0	0.67	0.0936	998.9	1.350	68.7	0.360	14.32	-0.336	-0.217	198.9	153.6	151.5	150.6	140.0	132.8	130.3	128.2	125.8	124.9	125.8	128.6	136.1
480	1307.0	0.34	0.0948	1012.1	1.264	64.4	0.360	14.32	-0.334	-0.217	197.7	144.2	141.4	142.2	133.3	128.9	125.0	122.1	119.6	119.1	120.0	121.2	124.9
481	1309.0	1.35	0.0948	1012.1	1.170	59.6	0.360	14.32	-0.334	-0.219	196.2	131.7	128.6	136.4	128.4	124.1	121.6	118.0	116.8	116.5	115.7	115.8	116.7
482	1309.6	16.16	0.1925	2054.4	1.390	70.8	0.420	45.48	-0.040	0.027	218.7	207.6	213.8	208.7	194.6	182.6	176.7	171.7	163.9	158.3	154.3	150.8	146.3
483	1308.3	16.16	0.1871	1997.3	1.189	60.5	0.420	45.48	-0.039	0.028	218.6	192.5	195.8	190.2	178.9	170.9	165.0	161.2	157.3	149.7	146.4	144.1	142.2
484	1310.3	14.81	0.1935	2065.4	0.990	50.4	0.420	45.48	-0.040	0.023	218.1	177.1	176.1	169.6	160.2	155.6	151.6	147.9	143.1	141.5	137.6	134.1	131.6
485	1308.3	13.13	0.1910	2039.1	0.790	40.2	0.420	45.48	-0.039	0.024	217.0	162.3	156.2	148.7	140.2	136.8	134.5	133.6	131.8	128.0	126.4	124.6	122.5
486	1310.3	11.45	0.1894	2021.5	0.597	30.4	0.420	45.69	-0.038	0.024	215.4	147.3	134.8	125.4	117.7	115.6	114.2	114.9	114.4	112.5	111.7	110.9	110.6
487	1310.3	16.16	0.1908	2036.9	1.710	87.0	0.420	40.89	-0.086	-0.017	258.2	240.7	239.1	233.9	224.7	217.6	213.2	207.9	198.0	190.2	180.6	171.6	165.6
488	1306.3	15.82	0.1910	2039.1	1.513	77.0	0.420	40.89	-0.084	-0.017	261.5	233.5	220.4	214.5	206.9	201.6	198.3	194.5	188.3	181.1	172.1	165.9	160.2
489	1307.6	14.81	0.1879	2006.1	1.389	70.7	0.420	40.68	-0.087	-0.019	213.9	201.9	211.9	208.4	202.6	198.4	194.5	191.9	185.3	180.2	176.6	172.1	167.5
490	1313.0	14.81	0.1902	2030.3	1.325	67.4	0.420	41.10	-0.084	-0.018	263.6	226.0	202.9	195.5	189.2	186.1	183.4	181.4	176.7	171.7	164.5	159.5	154.7
491	1307.0	13.47	0.1915	2043.5	1.133	57.7	0.420	41.10	-0.082	-0.017	263.9	217.8	184.3	175.7	168.8	167.2	167.0	165.6	163.0	159.2	153.6	150.6	146.8
492	1309.0	11.45	0.1886	2012.7	0.954	48.5	0.420	40.89	-0.085	-0.020	264.6	208.9	165.8	156.2	148.9	148.0	147.2	148.4	147.2	146.1	142.0	140.6	138.3

Run	p	Δp	m	G	power	q	hp-power	T_{in}	x_{in}	x_{DO}	T_{hp}	Distance from CHF location (m)											
-	kPa	kPa	Kgs^{-1}	$Kgm^{-2}s^{-1}$	kW	kWm^{-2}	kW	°C	-	-	°C	0.01	0.05	0.10	0.20	0.30	0.40	0.50	0.60	0.70	0.80	0.90	1.00
												Inside wall temperature (°C)											
493	1309.0	10.10	0.1902	2030.3	0.772	39.3	0.420	40.89	-0.085	-0.022	264.6	199.8	145.0	134.6	126.6	125.4	126.5	127.4	128.5	127.1	124.9	125.1	124.3
494	1310.3	9.09	0.1964	2096.2	0.582	29.6	0.420	40.27	-0.092	-0.032	263.4	187.6	121.0	110.8	102.3	98.8	98.4	99.2	100.3	101.3	101.6	102.3	103.3
495	1311.0	13.80	0.1900	2028.1	1.573	80.1	0.420	35.48	-0.138	-0.070	211.4	211.2	227.1	224.3	221.9	219.3	218.4	217.6	215.0	209.5	204.6	199.9	194.8
496	1309.6	12.12	0.1904	2032.5	1.382	70.4	0.420	35.06	-0.142	-0.075	209.8	179.4	192.8	189.0	186.3	185.8	186.4	187.2	184.7	183.1	180.1	174.4	164.5
497	1307.6	10.44	0.1879	2006.1	1.189	60.5	0.420	35.06	-0.141	-0.075	207.6	178.1	186.6	182.9	178.9	178.1	180.3	183.5	183.4	181.2	180.7	177.4	175.9
498	1311.0	9.09	0.1875	2001.7	0.984	50.1	0.420	35.06	-0.142	-0.077	202.0	158.6	161.0	157.6	151.9	152.7	153.9	158.4	160.4	159.8	161.2	160.3	160.0
499	1318.4	9.09	0.1875	2001.7	0.795	40.5	0.420	35.06	-0.145	-0.081	199.5	141.1	137.1	134.4	129.3	127.2	128.5	131.6	134.8	136.3	138.0	139.0	139.8
500	1308.3	9.09	0.1857	1981.9	0.698	35.5	0.420	35.06	-0.141	-0.077	197.3	131.8	124.3	120.6	117.0	113.8	114.1	117.9	118.6	120.4	123.6	125.2	127.0
501	1307.6	10.77	0.1877	2003.9	1.577	80.3	0.420	30.28	-0.187	-0.118	195.0	193.6	223.6	223.8	217.4	220.1	221.1	223.1	220.5	221.1	220.4	216.3	215.3
502	1306.3	9.43	0.1882	2008.3	1.377	70.1	0.420	30.28	-0.186	-0.119	194.2	159.5	185.4	189.6	181.4	182.9	184.1	189.0	189.6	189.1	189.6	186.9	178.5
503	1310.3	9.09	0.1902	2030.3	1.180	60.1	0.420	30.07	-0.190	-0.124	192.0	152.5	168.0	185.0	173.6	169.5	170.4	177.9	181.1	181.9	184.3	184.4	185.1
504	1311.0	9.43	0.1879	2006.1	0.991	50.4	0.420	29.87	-0.192	-0.127	188.6	129.1	127.5	148.3	163.4	146.9	145.4	149.2	150.9	153.8	158.5	163.5	169.9
505	1311.7	9.09	0.1894	2021.5	1.480	75.4	0.456	24.88	-0.239	-0.166	225.8	173.0	190.9	223.3	208.2	204.2	202.8	208.8	210.8	211.4	215.4	216.9	216.3
506	1309.6	9.76	0.1886	2012.7	1.379	70.2	0.456	24.88	-0.238	-0.165	223.8	146.4	152.1	196.0	185.0	172.8	175.8	181.6	185.0	187.2	188.6	189.7	184.6
507	1312.3	9.76	0.1879	2006.1	1.284	65.4	0.456	25.09	-0.237	-0.165	220.6	149.1	133.9	157.4	215.8	182.1	178.3	183.6	186.4	189.7	193.4	195.9	199.7
508	1309.6	43.77	0.2821	3011.0	1.584	80.7	0.420	45.06	-0.044	0.002	212.3	192.2	209.8	213.9	203.6	188.4	179.5	175.2	167.4	164.0	158.2	151.9	146.6
509	1309.0	41.41	0.2829	3019.8	1.386	70.6	0.420	45.27	-0.042	0.003	208.1	176.4	191.1	194.9	187.3	175.1	169.1	164.7	158.1	154.1	151.4	146.3	142.5
510	1304.9	38.72	0.2838	3028.6	1.187	60.4	0.420	45.27	-0.040	0.004	200.9	161.6	171.0	174.9	168.8	159.2	155.5	153.0	149.6	145.5	142.5	138.4	135.3
511	1309.0	35.35	0.2831	3022.0	0.999	50.8	0.420	45.27	-0.042	0.002	195.2	147.3	152.9	155.9	151.2	143.3	140.9	140.3	136.4	134.6	133.9	131.6	131.1
512	1313.7	31.98	0.2817	3006.6	0.793	40.3	0.420	45.27	-0.043	-0.001	189.2	131.0	131.8	134.4	131.4	125.2	123.6	123.6	121.9	121.9	121.5	120.5	118.8
513	1308.3	32.32	0.2819	3008.8	1.522	77.5	0.420	40.06	-0.093	-0.047	237.4	196.1	198.4	208.2	197.6	187.8	184.0	182.5	177.3	173.0	166.5	162.1	158.3
514	1310.3	30.97	0.2825	3015.4	1.426	72.6	0.420	40.27	-0.092	-0.046	237.1	191.8	188.6	199.5	189.9	180.8	177.6	176.0	171.6	169.0	163.7	159.6	156.7
515	1309.0	29.63	0.2833	3024.2	1.331	67.7	0.420	40.06	-0.093	-0.049	236.9	187.4	178.7	189.7	181.8	173.6	170.7	168.6	165.7	163.3	159.0	155.2	152.6
516	1308.3	28.28	0.2854	3046.2	1.229	62.6	0.420	40.27	-0.091	-0.047	236.0	182.7	166.7	178.3	172.6	163.8	159.7	159.6	157.8	156.3	154.2	149.8	147.5
517	1307.0	26.60	0.2815	3004.4	1.135	57.8	0.420	40.27	-0.091	-0.046	235.4	178.9	158.1	169.3	164.5	156.5	154.0	152.2	150.4	149.6	147.5	144.5	142.8
518	1310.3	23.57	0.2862	3055.0	0.946	48.2	0.420	40.27	-0.092	-0.049	233.9	169.2	135.6	145.2	146.2	137.4	134.7	134.0	133.0	132.8	131.2	130.5	130.3
519	1308.3	22.56	0.2833	3024.2	0.776	39.5	0.420	40.27	-0.091	-0.049	231.6	159.8	115.0	120.6	129.4	121.6	116.5	116.4	114.5	115.0	113.9	113.8	114.5
520	1309.6	22.22	0.2809	2997.8	0.580	29.5	0.420	40.06	-0.094	-0.052	229.5	149.8	93.5	91.9	93.5	103.5	105.2	107.9	102.1	100.4	97.8	95.1	95.4
521	1306.3	30.30	0.2846	3037.4	1.529	77.9	0.420	38.60	-0.107	-0.061	215.8	179.0	187.8	206.6	199.4	187.1	184.4	182.1	178.2	174.8	170.4	165.7	162.5
522	1309.6	28.62	0.2846	3037.4	1.413	71.9	0.420	38.81	-0.106	-0.061	219.4	176.7	176.9	194.5	189.8	177.8	175.5	173.7	170.5	168.8	164.8	161.6	158.9
523	1309.0	26.93	0.2862	3055.0	1.318	67.1	0.420	38.39	-0.110	-0.065	221.4	173.1	165.3	182.9	181.3	169.3	166.5	165.5	163.5	162.5	158.7	157.1	155.1
524	1309.0	25.59	0.2833	3024.2	1.219	62.1	0.420	38.60	-0.108	-0.063	223.6	171.2	156.8	171.9	171.4	160.1	157.7	157.3	155.5	154.5	151.5	150.8	149.1
525	1304.3	24.24	0.2833	3024.2	1.133	57.7	0.420	38.81	-0.104	-0.060	224.4	168.8	148.7	161.9	162.3	151.8	149.6	148.7	147.8	147.1	144.6	144.2	143.1

Run	p	Δp	m	G	power	q	hp-power	T_{in}	x_{in}	x_{DO}	T_{hp}	Distance from CHF location (m)											
-	kPa	kPa	Kgs^{-1}	$Kgm^{-2}s^{-1}$	kW	kWm^{-2}	kW	°C	-	-	°C	0.01	0.05	0.10	0.20	0.30	0.40	0.50	0.60	0.70	0.80	0.90	1.00
												Inside wall temperature (°C)											
526	1304.9	23.23	0.2840	3030.8	1.043	53.1	0.420	38.39	-0.108	-0.065	224.2	163.1	135.3	147.4	155.2	142.9	138.7	139.1	138.0	137.7	136.7	136.5	136.3
527	1317.7	22.56	0.2856	3048.4	0.947	48.2	0.420	38.18	-0.114	-0.072	220.3	153.9	117.9	125.6	147.7	143.4	134.7	131.2	128.0	128.3	127.7	127.7	128.5
528	1307.6	26.93	0.2821	3011.0	1.572	80.0	0.480	35.90	-0.133	-0.082	196.2	162.1	183.9	189.2	178.5	175.3	175.3	177.8	176.9	174.8	172.9	169.8	165.7
529	1307.0	24.91	0.2838	3028.6	1.478	75.3	0.480	35.69	-0.135	-0.084	196.6	156.0	175.4	208.6	214.6	199.0	192.3	194.0	192.1	190.7	190.3	188.4	185.2
530	1306.3	23.90	0.2840	3030.8	1.382	70.3	0.480	35.69	-0.135	-0.084	197.0	150.3	165.3	195.4	205.2	188.8	183.3	185.0	183.7	183.6	183.2	181.6	180.9
531	1309.6	23.23	0.2831	3022.0	1.280	65.2	0.480	35.48	-0.138	-0.088	197.1	141.7	150.7	178.3	197.8	180.5	173.9	175.2	174.1	174.3	175.2	173.5	172.1
532	1311.7	21.88	0.2829	3019.8	1.181	60.1	0.480	35.48	-0.139	-0.089	196.8	134.1	137.9	160.8	190.1	172.7	163.4	164.7	165.5	165.6	166.0	164.8	162.6
533	1307.6	30.64	0.2819	3008.8	2.106	107.2	0.420	34.02	-0.151	-0.103	209.9	185.5	234.0	276.9	265.3	249.0	243.5	239.6	230.5	226.6	217.7	210.1	203.8
534	1306.3	27.61	0.2864	3057.2	1.899	96.7	0.420	33.81	-0.153	-0.106	219.7	183.5	211.1	254.5	249.5	231.7	225.9	224.0	218.9	214.6	207.3	202.0	197.2
535	1302.9	24.91	0.2875	3068.2	1.715	87.3	0.420	33.81	-0.152	-0.106	225.9	179.9	187.7	229.5	235.8	216.9	210.0	208.7	205.0	202.9	197.6	194.2	190.3
536	1309.6	22.22	0.2827	3017.6	1.517	77.2	0.420	34.02	-0.152	-0.106	232.3	176.6	163.7	195.4	221.9	200.7	191.3	190.8	188.3	187.7	184.3	182.3	180.3
537	1307.6	21.88	0.2831	3022.0	1.341	68.3	0.420	34.23	-0.149	-0.104	237.8	172.8	140.2	157.3	209.1	190.7	174.6	172.5	171.6	170.7	168.5	168.4	167.9
538	1308.3	22.89	0.2821	3011.0	1.703	86.7	0.420	32.78	-0.163	-0.117	240.7	187.9	182.3	216.9	234.0	213.3	205.0	205.4	203.0	200.8	196.1	194.2	191.2
539	1311.7	22.22	0.2827	3017.6	1.608	81.9	0.420	32.57	-0.166	-0.120	234.5	177.2	160.3	187.1	234.3	211.9	198.2	195.9	192.2	191.9	188.5	188.1	186.3
540	1310.3	22.22	0.2868	3061.6	1.507	76.7	0.420	32.78	-0.164	-0.119	230.8	169.9	141.0	159.4	227.7	211.1	192.3	187.1	182.3	182.9	179.7	180.5	180.0
541	1305.6	22.22	0.2844	3035.2	1.428	72.7	0.420	32.78	-0.162	-0.117	246.2	180.1	148.1	166.5	215.4	196.5	185.5	178.9	175.5	176.3	173.7	174.5	175.1
542	1312.3	22.22	0.2844	3035.2	1.331	67.8	0.420	32.78	-0.165	-0.120	248.5	175.7	129.8	131.5	166.1	219.0	191.3	177.3	168.6	165.7	163.1	165.2	167.6
543	1307.0	21.88	0.2852	3044.0	1.587	80.8	0.480	30.70	-0.183	-0.131	238.4	160.9	162.3	199.2	244.8	218.1	204.3	207.4	207.1	205.7	207.7	207.2	204.9
544	1308.3	21.88	0.2809	2997.8	1.491	75.9	0.480	30.70	-0.183	-0.132	229.8	149.1	140.8	161.3	245.4	223.1	205.4	199.4	200.3	199.6	199.1	197.4	195.1
545	1307.6	80.80	0.3754	4007.2	1.971	100.3	0.480	44.44	-0.050	-0.009	199.0	170.9	195.5	217.1	221.0	206.2	196.7	187.2	177.8	173.5	169.2	162.3	152.3
546	1313.7	75.75	0.3728	3978.6	1.784	90.8	0.480	44.44	-0.052	-0.012	194.4	158.4	179.4	199.5	207.4	195.6	188.1	180.5	171.8	168.5	165.3	159.6	150.3
547	1314.4	69.69	0.3789	4044.6	1.579	80.4	0.480	44.23	-0.054	-0.015	190.5	145.8	162.7	181.5	192.5	182.8	176.8	170.8	163.6	161.1	158.7	153.9	145.9
548	1311.7	64.64	0.3746	3998.4	1.389	70.7	0.480	44.23	-0.053	-0.015	188.0	134.1	147.9	164.5	178.2	169.7	165.1	160.5	154.6	152.5	150.3	146.8	139.9
549	1306.3	75.08	0.3787	4042.4	2.271	115.6	0.420	41.73	-0.076	-0.039	226.3	193.1	217.0	240.8	241.0	224.0	211.0	204.8	197.0	190.4	181.8	175.2	169.6
550	1310.3	69.35	0.3769	4022.6	2.079	105.8	0.420	41.73	-0.077	-0.041	230.0	187.7	200.1	222.8	226.9	212.5	202.3	196.3	187.3	183.5	176.0	171.1	166.3
551	1309.0	65.31	0.3781	4035.8	1.898	96.6	0.420	41.73	-0.077	-0.041	232.1	182.3	184.6	205.0	212.7	200.2	191.6	186.3	180.6	176.3	169.7	165.7	161.8
552	1306.3	61.61	0.3771	4024.8	1.690	86.0	0.420	41.73	-0.076	-0.041	233.8	176.3	169.5	186.8	196.7	185.6	178.0	174.8	170.0	166.6	161.3	158.5	155.5
553	1304.3	57.23	0.3802	4057.7	1.513	77.0	0.420	41.73	-0.075	-0.041	234.1	169.1	152.7	167.3	182.4	173.8	167.5	164.6	161.3	157.8	153.7	151.9	149.6
554	1308.3	52.18	0.3748	4000.6	1.330	67.7	0.420	41.94	-0.075	-0.041	233.9	162.8	138.8	150.2	166.1	161.2	155.6	152.8	149.2	147.2	143.1	142.4	141.4
555	1307.6	47.47	0.3746	3998.4	1.137	57.9	0.420	41.73	-0.076	-0.043	234.0	155.8	122.4	130.7	146.5	148.3	142.6	140.0	137.8	135.2	132.1	131.6	131.2
556	1307.6	43.09	0.3779	4033.6	0.950	48.4	0.420	41.73	-0.076	-0.044	233.7	149.1	108.2	112.8	124.9	133.3	132.2	128.7	124.0	123.0	120.2	119.4	119.6
557	1307.6	40.40	0.3775	4029.2	0.762	38.8	0.420	41.52	-0.079	-0.047	232.6	140.7	91.0	91.5	95.6	101.5	104.9	113.5	114.5	115.0	111.3	108.5	108.1
558	1310.3	41.75	0.3802	4057.7	2.099	106.8	0.420	33.81	-0.154	-0.118	226.4	162.3	140.0	168.5	249.7	247.5	230.5	220.9	212.5	208.2	202.6	201.0	198.7

Run	p	Δp	m	G	power	q	hp-power	T_{in}	x_{in}	x_{DO}	T_{hp}	Distance from CHF location (m)											
-	kPa	kPa	Kgs^{-1}	$Kgm^{-2}s^{-1}$	kW	kWm^{-2}	kW	°C	-	-	°C	0.01	0.05	0.10	0.20	0.30	0.40	0.50	0.60	0.70	0.80	0.90	1.00
												Inside wall temperature (°C)											
559	1309.0	43.43	0.3787	4042.4	2.180	111.0	0.420	33.81	-0.154	-0.117	229.1	166.5	153.0	188.6	263.4	249.9	235.4	225.4	218.4	213.8	207.4	204.8	201.6
560	1665.8	17.17	0.0470	501.9	1.382	70.3	0.360	54.89	-0.055	0.205	192.3	204.6	217.6	216.3	213.2	208.7	206.2	205.4	203.7	202.9	202.0	201.2	200.3
561	1670.6	16.83	0.0481	512.9	0.793	40.3	0.360	54.68	-0.057	0.180	189.9	157.5	155.3	153.4	151.7	149.3	149.6	149.9	150.1	150.3	149.9	149.5	149.4
562	1667.9	13.47	0.0487	519.5	0.398	20.3	0.360	54.89	-0.051	0.172	186.8	124.2	109.9	105.7	104.5	103.4	103.8	104.1	103.7	104.4	105.1	106.3	108.4
563	1665.8	15.82	0.0489	521.7	1.384	70.5	0.360	44.65	-0.164	0.085	210.6	202.2	211.6	213.8	213.8	213.0	211.7	210.9	209.5	205.9	204.4	201.7	199.4
564	1669.9	15.82	0.0481	512.9	1.188	60.5	0.360	45.27	-0.158	0.090	207.6	188.5	192.7	193.8	194.1	193.3	193.2	192.9	191.2	190.4	188.9	186.9	184.9
565	1669.9	15.15	0.0481	512.9	0.997	50.7	0.360	45.90	-0.152	0.091	204.2	173.2	171.3	172.2	172.8	172.8	172.7	173.1	172.4	172.1	171.0	169.4	167.9
566	1669.2	13.13	0.0470	501.9	0.790	40.2	0.360	46.53	-0.145	0.097	199.6	155.3	147.9	147.2	149.0	149.2	149.6	150.5	150.5	150.7	150.8	150.9	151.1
567	1667.9	9.76	0.0472	504.1	0.404	20.6	0.360	46.73	-0.142	0.088	195.4	120.1	101.0	95.3	97.7	99.8	102.1	104.5	104.5	105.5	106.5	107.0	107.9
568	1667.2	15.15	0.0472	504.1	1.387	70.6	0.420	35.69	-0.259	0.035	214.6	195.5	202.7	208.1	212.9	213.3	213.8	213.5	213.0	211.7	210.5	209.9	208.3
569	1665.2	13.80	0.0474	506.3	1.178	60.0	0.420	35.69	-0.259	0.028	214.3	179.7	177.4	182.3	189.6	190.5	191.4	193.5	193.7	193.2	192.3	190.7	189.1
570	1667.2	12.12	0.0466	497.6	0.998	50.8	0.420	35.90	-0.257	0.029	213.6	162.0	152.0	155.7	164.9	167.7	170.4	173.1	173.8	174.1	174.0	173.4	172.9
571	1665.8	9.76	0.0472	504.1	0.790	40.2	0.420	35.90	-0.257	0.020	212.7	143.4	122.2	121.6	131.5	138.4	143.3	148.1	148.5	149.8	151.1	152.0	152.5
572	1665.2	12.46	0.0472	504.1	1.380	70.3	0.420	26.34	-0.355	-0.061	212.9	173.1	171.5	181.5	198.3	205.0	208.8	212.8	213.8	214.0	213.0	213.3	214.6
573	1666.5	11.11	0.0470	501.9	1.187	60.4	0.420	25.71	-0.361	-0.072	211.5	153.0	141.8	152.3	167.7	178.8	185.2	191.5	193.3	194.1	193.7	194.8	196.0
574	1669.9	8.75	0.0462	493.2	0.992	50.5	0.420	25.51	-0.365	-0.076	209.9	139.0	131.3	141.9	148.8	156.0	159.2	162.3	163.3	164.5	166.0	167.4	169.2
575	1668.5	10.44	0.0950	1014.3	1.388	70.7	0.360	53.84	-0.063	0.065	196.8	206.1	215.6	212.4	204.9	198.0	193.2	188.5	181.9	178.4	173.5	170.6	165.6
576	1669.9	11.11	0.0956	1020.9	1.189	60.5	0.360	54.68	-0.054	0.071	192.8	189.3	196.9	192.8	187.0	180.6	177.1	173.5	166.9	164.1	161.3	158.5	158.5
577	1666.5	9.43	0.0940	1003.3	0.983	50.0	0.360	54.89	-0.051	0.073	188.3	173.8	175.8	171.8	167.2	162.4	160.3	158.1	153.0	150.9	148.8	147.6	147.6
578	1666.5	8.08	0.0936	998.9	0.796	40.5	0.360	55.51	-0.043	0.078	184.9	158.6	157.6	153.3	149.5	145.9	144.5	143.1	140.8	137.8	136.2	135.5	135.0
579	1662.5	6.73	0.0936	998.9	0.603	30.7	0.360	55.72	-0.040	0.079	179.7	142.2	135.7	130.6	127.6	125.1	124.7	124.2	121.7	120.7	119.8	119.8	121.8
580	1675.3	6.06	0.0950	1014.3	1.390	70.8	0.360	44.44	-0.169	-0.041	151.8	183.0	205.5	210.9	212.3	210.3	208.0	205.4	200.5	194.5	190.4	185.0	179.4
581	1677.3	5.72	0.0938	1001.1	1.183	60.2	0.360	45.06	-0.163	-0.036	148.2	168.8	184.2	188.7	190.9	189.9	189.1	188.1	185.1	180.8	178.0	174.2	171.7
582	1671.2	5.39	0.0944	1007.7	0.994	50.6	0.360	45.69	-0.154	-0.031	143.4	153.9	165.4	167.4	169.9	170.6	170.6	169.9	167.0	164.9	163.1	160.7	157.6
583	1669.2	4.04	0.0938	1001.1	1.387	70.6	0.360	39.43	-0.221	-0.091	181.8	186.2	197.7	203.4	207.4	207.9	209.1	209.2	206.7	202.5	200.0	195.0	187.5
584	1669.2	4.04	0.0934	996.7	1.194	60.8	0.360	39.64	-0.219	-0.091	175.7	169.1	175.8	179.4	183.9	187.1	189.7	191.3	191.2	189.4	186.6	183.5	180.4
585	1667.2	3.37	0.0940	1003.3	0.987	50.2	0.360	40.06	-0.213	-0.090	168.7	149.9	150.7	150.9	155.7	158.5	163.0	167.5	169.8	170.0	169.0	168.3	167.1
586	1669.2	2.69	0.0946	1009.9	0.798	40.6	0.360	40.06	-0.214	-0.094	162.3	134.3	129.0	126.9	130.2	133.5	138.6	143.7	147.3	148.9	150.5	152.3	155.5
587	1670.6	3.03	0.0928	990.1	1.382	70.4	0.420	35.48	-0.263	-0.113	190.0	180.1	187.9	193.0	199.5	203.4	207.1	209.5	209.2	207.7	204.9	201.5	197.4
588	1664.5	3.03	0.0942	1005.5	1.183	60.2	0.420	35.48	-0.261	-0.116	191.0	166.4	166.0	168.1	173.9	177.6	183.1	188.5	190.6	191.2	189.8	187.8	186.8
589	1668.5	2.69	0.0944	1007.7	0.987	50.2	0.420	35.90	-0.258	-0.116	191.0	153.7	148.3	146.8	151.0	153.3	159.1	164.8	167.7	169.9	170.6	170.9	171.1
590	1665.2	0.34	0.0963	1027.5	0.789	40.2	0.420	35.48	-0.261	-0.125	190.2	137.3	127.3	122.8	128.5	130.3	134.8	139.3	140.6	143.4	146.2	147.8	149.5
591	1661.8	1.68	0.0967	1031.9	1.577	80.3	0.420	30.49	-0.311	-0.165	189.3	186.9	199.7	205.7	213.5	218.1	221.1	226.2	226.2	225.0	223.2	221.4	222.6

Run	p	Δp	m	G	power	q	hp-power	T_{in}	x_{in}	x_{DO}	T_{hp}	Distance from CHF location (m)											
-	kPa	kPa	Kgs^{-1}	$Kgm^{-2}s^{-1}$	kW	kWm^{-2}	kW	°C	-	-	°C	0.01	0.05	0.10	0.20	0.30	0.40	0.50	0.60	0.70	0.80	0.90	1.00
												Inside wall temperature (°C)											
592	1666.5	2.02	0.0961	1025.3	1.382	70.3	0.420	30.70	-0.311	-0.166	189.7	172.1	177.5	181.4	188.4	192.8	198.7	204.6	206.2	208.1	207.3	208.1	209.8
593	1669.2	0.67	0.0954	1018.7	1.189	60.5	0.420	30.70	-0.312	-0.169	189.4	161.8	162.6	164.1	168.4	170.9	176.6	182.4	185.7	186.5	188.2	188.4	189.3
594	1666.5	1.01	0.0919	981.3	0.983	50.0	0.420	30.70	-0.311	-0.166	186.2	131.8	132.9	135.9	146.5	144.4	145.3	146.2	146.0	148.3	150.7	153.6	155.5
595	1669.9	1.68	0.0948	1012.1	1.776	90.4	0.432	26.96	-0.350	-0.194	235.5	217.5	222.9	224.4	224.3	221.4	222.1	220.7	220.0	220.5	221.6	222.0	221.7
596	1663.1	2.69	0.0948	1012.1	1.576	80.2	0.432	26.96	-0.348	-0.195	234.0	198.2	197.8	198.3	195.3	192.8	191.0	190.1	189.5	190.1	191.9	193.1	193.6
597	1665.8	1.35	0.0952	1016.5	1.766	89.9	0.420	24.47	-0.374	-0.223	195.8	200.2	216.8	220.7	227.0	229.2	232.8	236.4	237.0	234.6	233.9	232.4	234.0
598	1665.8	1.01	0.0956	1020.9	1.580	80.4	0.420	24.47	-0.374	-0.226	194.7	182.9	196.6	200.1	202.3	202.9	206.9	210.8	211.5	211.8	211.1	211.8	213.0
599	1666.5	1.01	0.0971	1036.3	1.376	70.0	0.420	24.47	-0.374	-0.231	190.3	148.7	158.9	161.6	157.9	158.1	159.1	163.1	166.6	168.9	173.7	178.0	182.7
600	1669.9	7.74	0.1892	2019.3	1.584	80.7	0.360	55.31	-0.047	0.019	206.1	211.6	227.9	225.9	211.5	198.6	187.3	180.1	173.8	168.0	164.1	160.3	159.2
601	1662.5	7.07	0.1875	2001.7	1.374	69.9	0.360	55.31	-0.044	0.020	200.8	196.0	208.8	206.9	195.2	181.6	176.2	170.8	164.7	160.2	156.8	153.9	152.8
602	1667.2	7.41	0.1855	1979.7	1.186	60.4	0.360	55.51	-0.044	0.021	195.4	180.0	189.7	187.5	178.0	169.9	163.4	159.7	155.4	151.4	148.9	146.7	146.1
603	1669.9	7.41	0.1863	1988.5	0.990	50.4	0.360	55.51	-0.044	0.018	192.1	164.9	170.3	168.4	160.5	152.9	150.0	147.3	143.9	141.2	139.4	137.2	137.2
604	1667.2	8.42	0.1871	1997.3	0.793	40.3	0.360	55.51	-0.044	0.017	187.7	148.8	149.1	146.5	139.9	134.5	133.6	132.6	129.7	128.9	128.1	127.4	126.7
605	1669.2	8.08	0.1877	2003.9	0.603	30.7	0.360	54.68	-0.054	0.006	177.3	129.0	125.3	123.1	118.0	115.2	115.0	115.1	115.0	114.2	114.5	114.3	114.8
606	1667.2	3.37	0.1933	2063.2	1.895	96.4	0.420	51.54	-0.089	-0.013	197.8	208.8	249.7	247.3	233.3	223.8	215.3	204.3	196.4	186.9	177.0	169.9	165.1
607	1667.9	3.70	0.1915	2043.5	1.697	86.4	0.420	51.54	-0.089	-0.014	199.0	202.2	234.4	232.2	219.4	209.5	203.0	194.9	187.0	180.3	173.6	165.7	161.2
608	1666.5	5.39	0.1904	2032.5	1.518	77.3	0.420	51.75	-0.086	-0.012	199.6	194.8	217.4	214.9	203.0	194.1	187.3	183.6	177.3	172.3	164.6	159.6	156.1
609	1668.5	8.42	0.1912	2041.3	1.329	67.6	0.420	51.96	-0.084	-0.012	199.3	185.4	198.1	195.9	185.3	178.3	174.6	171.4	167.6	162.9	156.7	152.6	149.2
610	1667.2	9.09	0.1902	2030.3	1.149	58.5	0.420	51.96	-0.084	-0.013	198.7	176.2	178.6	176.7	166.7	161.5	159.9	158.0	156.2	152.3	149.2	144.3	142.0
611	1666.5	8.75	0.1896	2023.7	0.955	48.6	0.420	51.96	-0.084	-0.014	197.8	166.6	158.2	156.9	147.5	142.9	142.2	142.1	141.4	139.5	137.1	134.1	132.7
612	1669.2	8.08	0.1923	2052.2	0.767	39.1	0.420	51.75	-0.087	-0.019	196.6	155.3	134.2	133.2	126.1	121.6	120.7	121.5	121.6	121.5	119.5	119.2	119.0
613	1661.8	7.41	0.1917	2045.7	0.565	28.8	0.420	51.75	-0.084	-0.018	195.0	144.9	111.9	110.9	105.6	101.8	101.6	101.3	101.6	101.7	101.0	101.4	101.9
614	1670.6	7.41	0.1904	2032.5	0.394	20.0	0.420	51.75	-0.087	-0.021	192.9	135.3	93.2	91.6	88.5	85.5	84.8	84.2	84.8	84.9	84.1	84.6	85.6
615	1669.9	8.08	0.1884	2010.5	1.578	80.3	0.360	44.86	-0.163	-0.097	205.0	199.3	230.4	234.0	225.4	219.2	214.3	213.7	210.1	206.3	202.2	197.5	191.9
616	1668.5	8.08	0.1873	1999.5	1.375	70.0	0.360	44.86	-0.163	-0.098	193.3	179.0	205.6	213.8	204.9	197.0	197.3	196.3	194.0	192.0	189.8	186.7	182.7
617	1666.5	7.41	0.1871	1997.3	1.181	60.1	0.360	44.86	-0.162	-0.098	185.5	160.0	179.7	193.1	181.2	176.3	175.2	177.5	177.1	176.6	175.7	173.4	171.7
618	1667.9	7.41	0.1861	1986.3	0.998	50.8	0.360	44.86	-0.162	-0.100	176.1	132.2	141.8	158.8	155.2	148.6	147.6	149.1	149.4	151.0	153.1	152.2	146.9
619	1670.6	7.74	0.1873	1999.5	0.799	40.7	0.360	44.86	-0.163	-0.102	165.3	110.2	109.0	114.3	164.5	155.4	144.1	132.8	130.5	132.9	135.2	137.1	139.9
620	1672.6	8.08	0.1910	2039.1	1.695	86.3	0.420	41.31	-0.202	-0.127	187.1	174.4	224.5	252.4	229.4	218.5	216.2	217.7	213.2	210.8	203.7	200.2	196.1
621	1668.5	8.08	0.1925	2054.4	1.517	77.2	0.420	41.10	-0.203	-0.130	183.5	159.2	183.5	229.3	220.1	200.0	197.3	199.2	198.3	196.8	193.1	192.0	190.9
622	1671.9	7.74	0.1906	2034.7	1.429	72.8	0.420	40.89	-0.206	-0.133	200.0	167.9	180.3	215.4	206.9	189.2	188.5	189.0	188.5	188.7	186.6	185.4	184.9
623	1670.6	8.08	0.1919	2047.9	1.323	67.4	0.420	40.89	-0.206	-0.134	199.0	161.3	156.4	191.7	204.1	180.1	175.7	176.1	176.7	178.0	176.8	175.3	174.8
624	1673.9	8.08	0.1917	2045.7	1.231	62.6	0.420	40.89	-0.207	-0.135	197.3	153.6	127.7	141.2	214.1	187.1	173.8	165.3	164.8	166.2	164.6	166.3	167.1

Run	p	Δp	m	G	power	q	hp-power	T_{in}	x_{in}	x_{DO}	T_{hp}	Distance from CHF location (m)											
-	kPa	kPa	Kgs^{-1}	$Kgm^{-2}s^{-1}$	kW	kWm^{-2}	kW	°C	-	-	°C	0.01	0.05	0.10	0.20	0.30	0.40	0.50	0.60	0.70	0.80	0.90	1.00
												Inside wall temperature (°C)											
625	1667.2	7.74	0.1898	2025.9	1.575	80.2	0.360	36.31	-0.253	-0.187	224.1	170.4	180.1	230.5	240.1	216.0	216.4	216.8	215.1	217.0	218.9	219.5	217.4
626	1659.1	7.74	0.1894	2021.5	1.482	75.4	0.360	36.31	-0.250	-0.185	225.9	166.1	170.3	217.4	231.3	206.6	206.9	207.2	206.4	208.6	210.8	210.7	207.9
627	1671.9	8.08	0.1917	2045.7	1.706	86.9	0.420	35.69	-0.261	-0.186	250.9	207.4	211.2	244.7	231.2	215.7	215.9	217.7	218.8	218.0	214.4	213.4	212.6
628	1669.9	8.08	0.1910	2039.1	1.521	77.4	0.420	35.48	-0.263	-0.189	249.8	196.8	173.8	207.9	224.6	198.5	195.3	195.9	197.3	199.0	196.4	197.2	197.4
629	1669.2	8.75	0.1927	2056.6	1.426	72.6	0.420	35.48	-0.262	-0.190	251.2	192.0	149.1	157.7	235.1	206.3	191.5	184.8	187.5	187.6	186.6	188.0	189.0
630	1669.9	37.03	0.2774	2960.4	1.776	90.4	0.360	55.72	-0.042	0.004	196.9	183.2	203.6	213.4	209.0	194.1	183.4	176.9	169.6	164.9	160.4	154.7	148.1
631	1669.2	36.02	0.2761	2947.2	1.581	80.5	0.360	55.31	-0.047	-0.001	191.1	169.8	187.4	198.4	195.6	183.2	175.3	169.3	162.1	158.8	155.9	150.6	147.0
632	1663.8	34.34	0.2796	2984.6	1.381	70.3	0.360	55.10	-0.047	-0.004	186.2	154.3	170.4	181.0	180.4	170.6	162.1	160.2	154.3	151.3	149.7	145.6	143.8
633	1666.5	31.31	0.2807	2995.6	1.190	60.6	0.360	54.89	-0.051	-0.008	181.4	142.0	152.8	163.1	164.9	157.0	153.5	149.8	145.3	143.1	142.5	140.5	139.7
634	1670.6	28.62	0.2807	2995.6	0.984	50.1	0.360	54.68	-0.054	-0.013	175.6	127.7	134.2	142.9	147.8	141.8	139.7	137.2	134.0	134.1	132.3	131.2	130.2
635	1667.9	30.30	0.2761	2947.2	2.079	105.8	0.420	50.91	-0.096	-0.042	243.8	212.9	228.3	238.8	231.1	216.4	208.3	200.3	191.3	186.8	179.4	173.1	168.1
636	1672.6	28.62	0.2759	2945.0	1.879	95.6	0.420	50.91	-0.097	-0.044	245.7	206.0	211.9	222.5	216.9	203.8	195.7	190.9	184.7	180.2	173.6	168.3	164.5
637	1671.9	27.94	0.2755	2940.6	1.700	86.5	0.420	50.91	-0.097	-0.045	246.6	199.9	196.2	206.2	202.3	191.6	187.0	181.4	176.0	173.2	167.2	163.5	160.6
638	1669.2	26.26	0.2772	2958.2	1.526	77.7	0.420	50.91	-0.096	-0.045	246.9	193.3	180.9	190.0	188.0	178.8	173.3	170.7	167.3	164.7	159.6	156.8	154.4
639	1671.9	24.91	0.2765	2951.6	1.336	68.0	0.420	50.91	-0.097	-0.047	246.9	185.4	163.9	172.0	172.2	163.9	160.4	158.3	155.7	154.0	150.1	148.2	146.8
640	1673.9	23.23	0.2770	2956.0	1.138	57.9	0.420	50.91	-0.098	-0.049	246.9	177.2	145.5	152.3	155.4	148.6	145.8	143.9	141.8	140.9	138.3	137.3	136.5
641	1671.2	22.22	0.2770	2956.0	0.952	48.5	0.420	50.91	-0.097	-0.049	246.1	168.9	129.6	133.8	139.9	135.3	132.2	130.4	128.8	128.3	126.1	125.7	125.8
642	1678.6	20.20	0.2747	2931.9	0.762	38.8	0.420	50.70	-0.102	-0.054	244.6	160.5	112.3	113.2	119.2	121.0	119.1	116.4	114.5	113.5	111.8	111.4	112.1
643	1677.3	19.53	0.2761	2947.2	1.907	97.1	0.420	40.48	-0.212	-0.159	272.1	202.8	180.7	205.9	245.7	226.0	215.8	210.8	206.6	205.3	201.2	199.0	197.3
644	1668.5	19.86	0.2761	2947.2	1.709	87.0	0.420	40.27	-0.212	-0.160	261.2	187.3	146.1	152.3	207.1	238.7	219.2	203.9	197.0	192.6	189.1	188.1	187.9
645	1666.5	23.23	0.2823	3013.2	1.574	80.1	0.360	45.48	-0.155	-0.111	202.3	148.1	160.8	188.1	219.1	201.4	195.4	189.4	186.5	185.8	185.4	184.1	181.9
646	1666.5	84.17	0.3791	4046.8	2.169	110.4	0.480	55.31	-0.046	-0.002	209.5	168.6	184.1	201.4	212.6	204.8	195.3	185.8	177.2	169.4	158.9	152.0	145.9
647	1665.8	79.12	0.3793	4049.0	1.974	100.5	0.480	55.31	-0.046	-0.002	206.6	158.3	171.4	187.2	200.6	195.5	188.0	180.5	171.6	163.7	155.7	148.6	139.9
648	1663.1	74.07	0.3754	4007.2	1.778	90.5	0.480	55.51	-0.042	0.001	205.5	151.3	160.3	174.5	188.0	185.0	179.1	173.3	163.1	156.6	149.9	143.6	135.6
649	1667.9	70.70	0.3804	4059.9	1.577	80.3	0.480	55.51	-0.044	-0.002	204.4	140.0	146.9	159.5	174.1	174.5	170.8	167.1	159.0	153.1	147.1	140.8	133.4
650	1667.9	66.66	0.3808	4064.3	1.382	70.4	0.480	55.31	-0.046	-0.005	202.2	130.6	134.1	144.6	158.8	162.2	160.3	158.5	152.2	147.6	143.1	137.5	130.3
651	1667.9	62.62	0.3779	4033.6	1.190	60.6	0.480	55.51	-0.044	-0.003	200.2	120.9	122.3	131.0	143.3	148.5	148.5	148.5	144.0	140.8	137.5	132.5	126.0
652	1671.9	72.05	0.3783	4038.0	2.171	110.5	0.480	52.59	-0.078	-0.034	192.4	157.0	178.9	200.8	219.6	212.1	203.8	195.9	187.8	181.4	173.6	166.9	158.2
653	1668.5	67.00	0.3791	4046.8	2.173	110.6	0.480	50.70	-0.098	-0.054	188.5	153.7	176.5	201.7	224.2	216.4	208.3	200.5	192.3	187.6	181.9	176.1	168.3
654	1669.2	63.29	0.3775	4029.2	1.973	100.4	0.480	50.70	-0.099	-0.055	185.4	141.5	160.0	182.8	208.4	205.7	199.6	193.5	187.7	181.9	176.6	171.5	164.0
655	1669.9	58.92	0.3789	4044.6	1.776	90.4	0.480	50.70	-0.099	-0.056	181.9	128.8	143.9	164.4	190.6	194.1	189.3	184.6	178.6	174.5	170.1	165.4	158.8
656	1670.6	59.59	0.3785	4040.2	2.164	110.2	0.540	48.20	-0.127	-0.078	203.5	146.4	164.9	193.6	226.7	221.9	214.9	207.6	200.7	195.7	191.7	187.2	179.4
657	1671.9	55.55	0.3777	4031.4	1.969	100.2	0.540	48.20	-0.127	-0.079	214.3	140.6	152.3	176.4	208.7	210.6	204.8	198.9	194.1	189.7	184.2	180.4	173.5

Run	p	Δp	m	G	power	q	hp-power	T_{in}	x_{in}	x_{DO}	T_{hp}	Distance from CHF location (m)											
-	kPa	kPa	Kgs^{-1}	$Kgm^{-2}s^{-1}$	kW	kWm^{-2}	kW	°C	-	-	°C	0.01	0.05	0.10	0.20	0.30	0.40	0.50	0.60	0.70	0.80	0.90	1.00
												Inside wall temperature (°C)											
658	1665.8	51.51	0.3777	4031.4	1.782	90.7	0.540	48.20	-0.125	-0.078	216.3	132.9	139.2	159.1	189.9	198.5	194.1	189.6	184.9	181.1	176.8	172.9	166.6
659	1666.5	17.84	0.0487	519.5	1.182	60.1	0.360	54.89	-0.051	0.194	191.7	189.8	197.3	196.0	194.2	191.6	191.1	189.3	189.7	188.8	187.4	186.3	185.4
660	2026.8	17.84	0.0466	497.6	1.387	70.6	0.360	60.96	-0.095	0.192	210.3	206.2	214.8	213.2	211.5	205.5	203.8	202.1	199.5	196.6	195.3	193.7	192.4
661	2036.2	18.18	0.0466	497.6	1.186	60.4	0.360	60.75	-0.098	0.183	208.5	192.2	193.7	192.7	192.1	189.7	187.5	185.3	183.9	181.6	180.4	178.8	177.6
662	2028.8	17.84	0.0470	501.9	0.991	50.4	0.360	60.75	-0.094	0.177	206.4	175.2	174.2	172.9	172.0	169.1	167.9	167.4	165.9	164.5	164.0	162.9	161.8
663	2031.5	16.16	0.0476	508.5	0.791	40.3	0.360	60.75	-0.095	0.167	204.3	161.8	154.4	152.1	151.8	149.7	149.1	149.1	147.9	147.4	146.9	146.1	145.6
664	2030.8	14.81	0.0460	491.0	0.598	30.4	0.360	60.75	-0.095	0.170	200.7	146.3	133.5	130.2	129.3	128.5	128.4	128.9	128.0	127.4	127.5	127.3	127.0
665	2028.1	13.13	0.0456	486.6	0.401	20.4	0.360	60.75	-0.094	0.167	197.3	128.6	112.4	108.2	107.3	106.7	107.6	108.4	107.7	107.8	107.9	108.1	107.8
666	2028.8	16.83	0.0470	501.9	1.389	70.7	0.360	50.29	-0.225	0.059	192.9	194.5	206.6	211.4	211.1	210.0	208.2	208.4	205.5	202.1	200.7	198.0	196.3
667	2028.8	16.50	0.0483	515.1	1.186	60.4	0.360	50.91	-0.217	0.053	191.0	179.6	186.5	189.8	191.0	190.3	190.3	189.8	188.3	186.5	184.8	183.1	181.2
668	2030.1	14.81	0.0468	499.7	0.988	50.3	0.360	50.49	-0.223	0.050	188.9	162.5	163.4	166.1	170.0	170.6	171.4	171.2	170.2	169.3	168.2	166.4	165.3
669	2026.8	12.79	0.0450	480.0	0.791	40.3	0.360	50.08	-0.226	0.050	185.9	146.7	139.6	140.2	145.0	147.2	149.1	151.1	150.6	150.7	150.5	149.7	149.5
670	2028.8	10.10	0.0462	493.2	0.592	30.1	0.360	49.66	-0.232	0.031	182.5	126.9	112.2	109.1	113.6	119.9	122.5	127.3	127.8	129.0	130.3	130.7	131.4
671	2041.6	14.81	0.0472	504.1	1.392	70.9	0.360	39.85	-0.353	-0.069	173.7	176.6	187.2	198.6	206.6	207.9	209.5	211.2	210.5	208.8	206.0	203.6	199.9
672	2033.5	12.46	0.0479	510.7	1.192	60.7	0.360	39.23	-0.357	-0.084	164.0	154.4	160.7	167.3	180.2	186.3	189.0	191.7	192.3	192.5	190.2	190.1	188.4
673	2036.2	12.46	0.0468	499.7	0.984	50.1	0.360	39.23	-0.358	-0.085	149.7	140.4	143.6	150.8	160.7	165.6	168.3	171.0	171.7	171.9	170.4	170.6	172.9
674	2045.6	12.46	0.0470	501.9	1.379	70.2	0.420	29.87	-0.469	-0.144	229.4	171.7	163.4	172.4	189.2	199.7	204.7	209.7	211.0	211.0	209.0	209.1	206.2
675	2032.8	11.11	0.0464	495.4	1.187	60.4	0.420	29.87	-0.463	-0.141	225.8	157.4	145.3	156.6	167.9	176.5	182.9	189.3	190.7	189.4	188.4	188.9	189.5
676	2034.2	9.09	0.0456	486.6	0.985	50.1	0.420	29.66	-0.466	-0.145	222.2	140.0	124.6	140.2	144.8	152.8	159.1	164.9	166.3	167.1	166.4	166.9	167.3
677	2039.5	10.77	0.0956	1020.9	1.612	82.1	0.360	64.11	-0.054	0.090	194.8	225.5	239.0	234.7	213.4	204.5	199.9	192.4	184.8	179.7	176.6	174.0	170.6
678	2028.8	12.12	0.0952	1016.5	1.447	73.6	0.360	64.74	-0.042	0.099	206.4	215.1	223.6	218.7	199.8	192.0	188.2	182.3	175.4	170.8	168.4	166.1	162.7
679	2030.1	12.46	0.0954	1018.7	1.257	64.0	0.360	64.11	-0.051	0.087	207.1	201.6	206.1	200.9	184.6	179.2	177.0	172.8	167.0	163.6	160.5	158.3	154.9
680	2028.8	13.13	0.0956	1020.9	1.077	54.8	0.360	63.90	-0.053	0.082	207.0	189.4	188.1	183.4	174.5	167.6	164.5	158.4	154.6	153.0	151.2	149.6	147.9
681	2028.1	12.46	0.0952	1016.5	0.899	45.8	0.360	64.32	-0.047	0.085	207.0	176.9	171.3	166.4	157.6	153.3	151.0	147.6	143.5	142.2	141.0	139.8	138.3
682	2027.4	10.10	0.0915	976.9	0.727	37.0	0.360	64.53	-0.044	0.091	206.5	163.2	153.0	147.1	139.6	137.5	136.4	133.6	131.6	129.9	129.3	127.2	126.5
683	2026.1	9.09	0.0950	1014.3	0.552	28.1	0.360	64.74	-0.041	0.086	205.5	148.8	134.2	127.5	121.2	120.5	120.3	119.4	118.1	116.6	116.4	117.3	117.3
684	2030.8	7.74	0.0950	1014.3	0.364	18.5	0.360	64.53	-0.045	0.079	204.3	132.8	113.6	106.4	99.9	99.9	101.6	100.5	100.6	101.1	101.7	103.4	104.1
685	2025.4	11.78	0.0942	1005.5	1.620	82.5	0.360	60.75	-0.093	0.052	206.5	224.9	236.0	233.8	221.3	215.1	209.0	199.6	192.1	188.2	184.3	181.5	178.7
686	2026.1	11.78	0.0946	1009.9	1.436	73.1	0.360	60.12	-0.101	0.041	207.1	211.1	219.4	217.8	206.5	201.3	197.8	189.5	182.9	179.9	177.0	173.0	170.3
687	2021.4	12.46	0.0952	1016.5	1.257	64.0	0.360	59.91	-0.102	0.036	207.4	199.2	201.9	200.3	192.6	187.9	185.3	181.2	176.1	171.0	168.5	165.1	163.1
688	2024.7	11.78	0.0938	1001.1	1.081	55.0	0.360	59.91	-0.104	0.034	206.8	185.4	184.8	182.8	177.8	174.5	171.2	168.0	163.7	160.9	159.0	156.6	153.9
689	2035.5	10.10	0.0934	996.7	0.902	45.9	0.360	60.54	-0.099	0.037	205.5	171.7	166.7	164.2	159.1	157.5	156.6	153.8	150.7	148.9	147.7	146.6	144.6
690	2030.1	8.08	0.0938	1001.1	0.721	36.7	0.360	60.54	-0.097	0.035	204.6	156.5	147.2	143.5	138.9	138.7	139.5	138.8	137.5	135.8	135.3	135.3	134.0

Run	p	Δp	m	G	power	q	hp-power	T_{in}	x_{in}	x_{DO}	T_{hp}	Distance from CHF location (m)											
-	kPa	kPa	Kgs^{-1}	$Kgm^{-2}s^{-1}$	kW	kWm^{-2}	kW	°C	-	-	°C	0.01	0.05	0.10	0.20	0.30	0.40	0.50	0.60	0.70	0.80	0.90	1.00
												Inside wall temperature (°C)											
691	2028.8	7.07	0.0930	992.3	0.539	27.5	0.360	60.54	-0.097	0.033	203.7	142.8	127.3	122.5	118.9	119.9	120.6	121.1	120.4	120.1	120.7	121.4	122.8
692	2032.1	6.06	0.0942	1005.5	0.366	18.6	0.360	60.33	-0.101	0.025	202.5	128.6	108.0	101.7	96.9	97.6	100.2	100.2	100.6	102.2	103.7	106.8	109.3
693	2027.4	11.78	0.0967	1031.9	1.618	82.4	0.360	54.68	-0.170	-0.029	204.6	218.2	230.6	232.6	227.3	223.1	218.7	211.2	204.6	200.0	195.3	189.8	184.2
694	2028.1	11.11	0.0936	998.9	1.437	73.1	0.360	54.26	-0.176	-0.032	204.6	205.3	213.3	215.4	209.9	207.8	205.8	199.9	195.5	191.7	188.0	184.0	180.0
695	2026.1	10.10	0.0919	981.3	1.269	64.6	0.360	54.05	-0.178	-0.035	204.7	192.8	196.0	197.5	193.9	194.4	192.9	188.3	184.8	182.3	179.7	176.5	173.4
696	2022.7	8.75	0.0928	990.1	1.082	55.1	0.360	54.47	-0.171	-0.033	204.1	178.4	176.5	176.7	175.2	175.8	175.8	175.1	172.8	169.9	168.5	165.7	164.1
697	2028.1	6.73	0.0905	965.9	0.902	45.9	0.360	54.68	-0.171	-0.031	203.5	164.4	157.9	157.3	154.5	157.8	159.1	159.6	159.0	157.4	156.9	155.8	155.4
698	2023.4	5.72	0.0965	1029.7	0.721	36.7	0.360	54.26	-0.174	-0.046	202.2	148.8	136.0	133.0	130.5	133.0	138.1	139.5	140.5	141.5	141.7	141.8	142.0
699	2026.8	4.04	0.0969	1034.1	0.543	27.7	0.360	54.05	-0.178	-0.053	200.7	134.0	115.4	110.3	106.7	109.4	113.2	115.0	117.2	119.7	122.2	124.5	126.7
700	2033.5	10.10	0.0952	1016.5	1.622	82.6	0.360	48.61	-0.247	-0.102	202.0	215.2	224.3	226.6	224.2	223.1	223.3	218.1	215.2	211.7	208.4	204.1	199.6
701	2030.1	8.42	0.0921	983.5	1.445	73.6	0.360	48.61	-0.245	-0.099	202.0	199.2	205.5	207.9	206.7	207.8	209.4	208.1	205.8	201.8	200.2	196.9	188.8
702	2034.2	7.41	0.0901	961.5	1.264	64.3	0.360	48.82	-0.244	-0.098	201.7	186.4	186.0	187.8	188.2	189.3	192.7	193.3	192.2	190.8	188.7	185.3	179.6
703	2033.5	6.73	0.0882	941.8	1.077	54.8	0.360	49.03	-0.241	-0.095	201.1	170.9	166.8	166.5	167.0	169.9	174.4	176.4	177.0	177.0	176.2	174.1	171.6
704	2032.8	4.71	0.0948	1012.1	0.901	45.9	0.360	48.82	-0.244	-0.111	199.8	156.8	145.7	143.9	142.9	145.7	152.4	155.5	159.1	161.1	162.5	162.6	162.6
705	2034.8	1.68	0.1010	1078.1	0.717	36.5	0.360	48.20	-0.252	-0.130	198.3	140.3	124.4	121.9	117.7	119.9	124.6	127.8	131.9	136.1	140.2	143.4	146.3
706	2038.9	6.40	0.0938	1001.1	1.626	82.8	0.360	41.94	-0.328	-0.181	198.6	213.8	221.0	217.6	215.5	217.7	220.0	219.6	219.0	217.7	217.8	214.9	207.7
707	2028.1	5.05	0.0926	987.9	1.449	73.7	0.360	41.73	-0.326	-0.181	198.3	198.3	201.9	197.9	198.7	200.5	202.4	202.1	202.3	202.7	204.2	203.8	202.5
708	2030.1	4.38	0.0919	981.3	1.258	64.0	0.360	41.94	-0.324	-0.181	197.4	181.6	180.6	176.5	175.0	178.7	184.1	187.1	189.3	191.9	193.3	194.0	193.8
709	2033.5	2.36	0.0975	1040.7	1.082	55.1	0.360	41.52	-0.330	-0.198	195.3	164.1	162.2	159.1	153.9	156.3	163.4	169.2	172.5	176.9	180.5	182.6	183.3
710	2034.2	1.01	0.0983	1049.5	0.896	45.6	0.360	41.31	-0.333	-0.205	193.1	145.5	137.6	141.4	130.8	130.3	136.9	140.5	145.5	151.3	157.3	162.4	167.0
711	2031.5	5.05	0.0907	968.1	1.801	91.7	0.360	36.52	-0.387	-0.233	192.5	222.6	235.0	228.5	224.2	225.8	229.7	229.6	229.3	228.8	229.4	227.3	220.7
712	2039.5	5.05	0.0919	981.3	1.622	82.6	0.360	36.31	-0.393	-0.243	191.9	209.0	221.3	210.4	209.3	211.5	212.4	212.2	213.6	213.3	216.0	216.5	216.2
713	2038.2	3.70	0.0948	1012.1	1.438	73.2	0.360	36.10	-0.395	-0.253	191.0	191.0	203.2	191.5	185.5	188.7	192.7	194.5	196.5	198.9	203.7	204.9	206.6
714	2032.1	1.68	0.0959	1023.1	1.261	64.2	0.360	35.69	-0.397	-0.260	189.8	168.1	184.6	181.4	170.6	172.3	178.7	182.3	187.4	193.5	196.1	198.3	199.6
715	2042.9	0.00	0.0994	1060.5	1.083	55.1	0.360	35.48	-0.404	-0.274	186.1	134.9	128.5	171.4	149.5	143.6	149.3	153.7	159.6	167.0	174.4	180.9	189.1
716	2036.9	5.05	0.1871	1997.3	1.584	80.7	0.432	66.00	-0.027	0.058	204.3	197.0	210.4	211.8	203.0	187.5	178.9	171.9	165.6	159.4	156.2	155.0	153.9
717	2032.1	3.70	0.1892	2019.3	1.384	70.5	0.432	65.79	-0.029	0.054	216.8	188.9	193.7	194.3	186.9	174.7	168.0	162.2	157.5	152.6	150.1	149.0	148.4
718	2033.5	3.70	0.1902	2030.3	1.193	60.7	0.432	65.58	-0.032	0.049	216.5	176.1	178.5	178.1	171.7	162.7	156.9	152.5	148.2	144.9	143.2	141.7	140.2
719	2036.9	3.37	0.1886	2012.7	0.999	50.9	0.432	65.58	-0.033	0.047	216.3	164.3	161.5	160.5	155.0	147.0	144.1	141.2	137.1	136.0	134.9	134.1	133.3
720	2042.2	3.70	0.1908	2036.9	0.796	40.5	0.432	65.58	-0.035	0.043	215.4	151.2	144.2	142.3	137.7	131.5	129.7	128.0	125.5	125.0	124.5	123.9	123.1
721	2028.8	5.05	0.1902	2030.3	1.578	80.3	0.432	59.49	-0.110	-0.027	215.2	183.7	203.0	206.2	193.4	184.6	180.8	179.2	178.1	173.7	167.8	159.6	144.6
722	2040.2	5.72	0.1900	2028.1	1.380	70.2	0.432	59.29	-0.117	-0.034	214.3	175.8	190.1	193.7	183.0	176.9	173.3	169.8	170.6	169.4	163.2	156.9	145.9
723	2038.2	5.72	0.1892	2019.3	1.184	60.3	0.432	59.08	-0.119	-0.038	212.8	162.6	170.7	175.9	169.1	162.2	159.1	158.2	156.3	155.7	155.7	152.0	142.7

Run	p	Δp	m	G	power	q	hp-power	T_{in}	x_{in}	x_{DO}	T_{hp}	Distance from CHF location (m)											
-	kPa	kPa	Kgs^{-1}	$Kgm^{-2}s^{-1}$	kW	kWm^{-2}	kW	°C	-	-	°C	0.01	0.05	0.10	0.20	0.30	0.40	0.50	0.60	0.70	0.80	0.90	1.00
												Inside wall temperature (°C)											
724	2042.2	5.72	0.1879	2006.1	0.989	50.3	0.432	59.29	-0.117	-0.037	210.1	151.9	154.3	158.5	153.0	146.2	144.1	143.4	142.7	142.3	141.3	139.0	133.4
725	2044.9	6.40	0.1910	2039.1	0.802	40.8	0.432	58.87	-0.124	-0.046	209.0	142.6	139.5	144.0	139.8	133.5	133.2	132.8	132.7	132.3	132.5	132.2	132.6
726	2039.5	5.72	0.1890	2017.1	1.572	80.0	0.432	55.51	-0.164	-0.080	207.5	175.6	203.2	206.4	194.4	189.0	186.7	184.6	184.1	181.4	177.0	169.4	158.0
727	2042.2	5.72	0.1890	2017.1	1.382	70.3	0.432	54.89	-0.173	-0.090	206.6	176.8	196.3	210.3	200.5	191.9	187.8	185.2	183.7	181.6	178.8	176.3	174.6
728	2047.6	5.72	0.1906	2034.7	1.193	60.7	0.432	54.26	-0.183	-0.102	204.8	158.6	169.4	187.1	181.9	173.9	170.0	168.7	168.2	168.0	166.9	165.6	164.7
729	2040.2	6.06	0.1908	2036.9	0.989	50.3	0.432	54.47	-0.177	-0.099	202.4	143.9	152.6	163.2	161.2	150.6	148.1	147.7	147.6	147.1	147.3	145.6	142.7
730	2041.6	6.40	0.1902	2030.3	0.790	40.2	0.432	54.47	-0.178	-0.100	200.0	127.8	120.5	125.3	147.2	143.6	137.7	134.1	132.5	133.0	131.8	132.8	135.0
731	2039.5	6.06	0.1873	1999.5	1.591	81.0	0.432	50.29	-0.229	-0.143	199.5	154.4	183.4	210.8	199.3	190.6	186.8	187.9	187.9	188.5	184.8	179.4	169.7
732	2038.9	6.06	0.1908	2036.9	1.390	70.8	0.432	49.87	-0.233	-0.151	196.4	151.2	163.1	198.2	221.5	201.7	195.2	190.5	189.1	188.7	187.8	187.5	189.2
733	2044.9	6.40	0.1904	2032.5	1.283	65.3	0.432	49.87	-0.236	-0.154	191.9	138.4	137.7	157.9	225.4	203.7	191.4	182.4	177.7	177.1	178.9	180.4	183.8
734	2037.5	35.69	0.2794	2982.4	2.164	110.2	0.480	60.96	-0.094	-0.029	211.4	183.6	206.7	224.8	229.9	217.6	210.5	199.0	192.7	186.0	180.0	174.9	171.0
735	2036.9	33.67	0.2821	3011.0	1.965	100.0	0.480	61.17	-0.091	-0.027	213.8	173.2	190.9	207.6	216.1	207.5	200.1	190.8	183.6	179.4	174.6	171.3	169.0
736	2036.9	31.65	0.2823	3013.2	1.780	90.6	0.480	60.96	-0.094	-0.031	215.1	164.1	176.6	191.7	202.7	194.8	187.8	183.2	176.8	172.5	168.8	165.9	163.7
737	2033.5	29.96	0.2827	3017.6	1.579	80.4	0.480	60.96	-0.093	-0.031	215.9	155.6	162.8	176.2	189.1	183.6	179.9	175.0	170.4	167.3	162.4	159.5	157.8
738	2033.5	28.28	0.2840	3030.8	1.382	70.4	0.480	60.96	-0.093	-0.033	216.0	145.5	148.1	158.9	172.6	170.5	167.2	164.6	160.9	156.8	154.6	152.5	151.6
739	2036.2	25.59	0.2833	3024.2	1.190	60.6	0.480	60.75	-0.097	-0.037	215.6	135.0	134.0	142.1	155.3	157.5	156.1	154.0	151.7	149.3	145.7	143.7	143.6
740	2028.1	23.57	0.2819	3008.8	0.997	50.8	0.480	60.96	-0.091	-0.033	215.4	125.7	122.3	127.9	138.2	142.5	142.9	142.4	140.4	138.3	136.0	134.2	133.8
741	2032.1	28.62	0.2815	3004.4	1.996	101.6	0.480	55.72	-0.159	-0.095	210.3	163.5	181.8	205.5	226.4	216.2	209.5	205.6	200.6	196.4	191.8	189.4	187.7
742	2032.8	26.26	0.2821	3011.0	1.784	90.8	0.480	55.72	-0.159	-0.096	207.5	150.2	162.9	183.3	208.6	203.8	198.4	193.1	189.9	186.8	183.0	181.6	179.9
743	2032.1	24.58	0.2823	3013.2	1.573	80.1	0.480	55.72	-0.159	-0.097	205.7	140.0	145.6	161.7	187.9	192.3	187.5	182.7	179.6	176.2	173.5	171.8	170.7
744	2028.8	22.56	0.2815	3004.4	1.380	70.2	0.480	55.72	-0.158	-0.097	203.3	128.4	129.4	140.3	162.6	175.2	175.6	173.0	169.9	166.4	163.2	161.6	161.3
745	2030.8	23.90	0.2811	3000.0	1.977	100.7	0.540	51.75	-0.208	-0.137	229.4	153.8	161.9	185.1	226.7	228.0	219.8	212.9	207.6	205.1	200.3	198.9	198.3
746	2025.4	21.88	0.2802	2991.2	1.774	90.3	0.540	51.75	-0.206	-0.136	229.7	146.0	145.2	161.0	198.5	214.7	208.7	200.7	196.2	193.6	189.4	187.9	187.4
747	2024.1	66.32	0.3771	4024.8	2.367	120.5	0.540	58.87	-0.117	-0.063	219.4	148.5	160.2	180.1	208.5	219.4	218.8	213.9	204.8	193.8	181.9	173.8	169.3
748	2038.2	60.60	0.3732	3983.0	2.170	110.5	0.540	59.08	-0.119	-0.065	217.0	139.8	146.3	164.3	190.9	204.6	208.4	207.6	201.4	192.1	181.0	171.9	162.9
749	2026.1	59.25	0.3783	4038.0	1.968	100.2	0.540	58.87	-0.117	-0.065	213.9	128.4	133.1	147.3	171.3	186.6	194.5	197.6	195.5	191.4	179.5	171.1	161.5
750	2042.9	59.59	0.3787	4042.4	2.456	125.0	0.540	56.35	-0.155	-0.100	206.0	133.5	144.2	169.5	206.8	225.1	228.7	224.7	213.6	204.5	195.8	187.8	181.0
751	2385.0	17.51	0.0485	517.3	1.382	70.4	0.360	65.58	-0.153	0.153	202.8	204.8	211.4	211.0	209.5	203.4	200.2	197.0	194.8	191.2	187.2	185.2	183.5
752	2388.3	17.51	0.0479	510.7	1.187	60.4	0.360	65.16	-0.159	0.144	203.3	192.8	194.5	193.8	191.7	187.5	185.3	183.1	179.5	177.2	174.6	173.3	172.1
753	2387.7	17.84	0.0474	506.3	0.987	50.2	0.360	65.79	-0.148	0.150	204.7	177.2	175.2	173.9	172.4	169.1	167.8	166.6	164.6	160.8	159.6	159.7	158.3
754	2385.6	16.83	0.0495	528.3	0.791	40.3	0.360	65.58	-0.151	0.128	203.3	162.4	156.2	154.3	153.1	150.9	150.8	150.8	149.2	146.2	145.4	144.8	145.9
755	2393.1	15.15	0.0466	497.6	0.599	30.5	0.360	66.21	-0.144	0.146	201.9	147.8	135.7	133.3	133.0	131.1	132.2	133.2	133.4	131.5	129.6	131.8	134.7
756	2387.0	13.13	0.0479	510.7	0.404	20.5	0.360	66.42	-0.139	0.136	199.7	133.0	115.0	111.1	109.9	109.3	110.6	111.9	111.5	111.8	112.2	115.2	120.4

Run	p	Δp	m	G	power	q	hp-power	T_{in}	x_{in}	x_{DO}	T_{hp}	Distance from CHF location (m)											
-	kPa	kPa	Kgs^{-1}	$Kgm^{-2}s^{-1}$	kW	kWm^{-2}	kW	°C	-	-	°C	0.01	0.05	0.10	0.20	0.30	0.40	0.50	0.60	0.70	0.80	0.90	1.00
												Inside wall temperature (°C)											
757	2387.0	17.51	0.0474	506.3	1.382	70.4	0.360	60.96	-0.218	0.094	201.1	200.1	210.0	211.5	210.0	206.1	204.0	202.0	198.5	194.7	190.7	188.7	186.4
758	2388.3	17.17	0.0491	523.9	1.180	60.1	0.360	60.54	-0.224	0.070	200.7	185.9	191.0	192.5	191.8	190.2	187.9	186.9	184.4	182.6	179.7	176.2	173.9
759	2386.3	16.50	0.0481	512.9	0.984	50.1	0.360	60.33	-0.226	0.068	199.8	171.3	170.7	171.2	171.5	171.1	169.8	170.3	168.6	165.9	162.9	162.6	162.1
760	2384.3	14.81	0.0476	508.5	0.790	40.2	0.360	60.54	-0.223	0.067	198.7	157.2	150.6	150.3	151.5	151.8	152.7	153.0	151.7	150.4	148.4	148.8	150.0
761	2389.0	13.13	0.0472	504.1	0.598	30.5	0.360	60.75	-0.221	0.064	197.3	141.4	129.3	128.1	129.6	130.2	131.8	133.4	134.0	134.2	132.9	133.5	137.0
762	2383.0	10.77	0.0466	497.6	0.405	20.6	0.360	61.17	-0.213	0.069	195.6	126.9	108.9	104.4	105.0	106.2	108.8	111.5	111.9	113.0	114.2	116.9	121.0
763	2391.0	16.50	0.0476	508.5	1.385	70.5	0.360	55.93	-0.289	0.021	194.8	194.3	204.9	210.0	210.6	209.5	208.1	206.0	203.5	198.7	194.4	190.4	188.1
764	2385.0	15.82	0.0481	512.9	1.182	60.1	0.360	54.68	-0.304	-0.004	193.2	176.3	181.7	185.6	189.9	190.2	190.6	189.0	186.5	183.6	181.0	177.4	175.1
765	2389.0	14.48	0.0481	512.9	0.985	50.1	0.360	55.51	-0.294	0.000	191.5	161.5	162.4	164.4	169.0	170.1	169.8	171.1	171.0	169.0	166.2	164.4	163.8
766	2394.4	12.46	0.0476	508.5	0.798	40.6	0.360	54.89	-0.305	-0.015	188.2	145.6	138.0	138.0	143.3	146.2	149.5	152.9	153.6	154.2	152.8	152.3	153.0
767	2383.0	11.11	0.0476	508.5	0.596	30.3	0.360	55.72	-0.289	-0.007	186.7	131.0	117.4	114.7	119.2	122.5	127.0	131.4	134.3	135.1	134.2	135.8	139.3
768	2386.3	15.82	0.0472	504.1	1.379	70.2	0.360	50.91	-0.355	-0.043	187.4	185.0	197.5	203.8	209.6	210.0	209.8	208.1	205.2	201.6	198.3	194.6	192.2
769	2383.6	15.15	0.0466	497.6	1.183	60.2	0.360	50.08	-0.365	-0.056	186.5	169.6	174.1	179.2	188.1	191.1	190.9	191.1	190.0	187.5	184.7	182.6	180.9
770	2383.0	13.13	0.0470	501.9	0.991	50.4	0.360	50.29	-0.362	-0.062	185.7	153.9	152.5	156.1	164.9	169.0	171.2	173.5	173.0	171.0	170.4	168.9	169.5
771	2393.7	11.11	0.0474	506.3	0.789	40.2	0.360	50.49	-0.364	-0.073	181.3	134.3	125.2	126.1	133.9	138.8	144.8	150.8	153.6	154.3	153.3	153.6	155.4
772	2393.1	13.80	0.0481	512.9	1.387	70.6	0.360	40.27	-0.498	-0.189	174.7	164.7	172.9	181.1	194.5	202.5	206.1	209.8	209.9	208.6	206.1	203.8	201.7
773	2392.4	12.12	0.0489	521.7	1.186	60.4	0.360	40.27	-0.497	-0.201	167.8	157.8	156.8	161.4	173.5	182.8	187.2	191.6	192.4	192.0	190.0	188.8	188.8
774	2385.6	10.10	0.0474	506.3	0.988	50.3	0.360	39.85	-0.499	-0.202	162.7	132.1	130.5	134.7	142.2	150.1	159.8	169.4	172.3	173.5	173.7	174.4	177.2
775	2387.0	12.46	0.0458	488.8	1.774	90.3	0.300	28.62	-0.641	-0.349	231.8	200.2	201.6	210.4	227.6	232.9	236.1	238.8	238.4	237.8	234.3	230.0	226.5
776	2403.2	12.12	0.0448	477.8	1.584	80.6	0.300	28.00	-0.657	-0.364	232.4	186.2	182.8	191.0	205.0	212.2	217.4	222.2	224.3	225.4	221.6	219.8	217.0
777	2377.6	9.76	0.0462	493.2	1.389	70.7	0.300	27.79	-0.646	-0.372	232.1	168.5	162.4	171.1	179.7	187.1	197.5	203.2	205.4	207.5	206.2	204.5	205.9
778	2386.3	8.08	0.0446	475.6	1.189	60.5	0.300	27.58	-0.653	-0.375	231.8	147.5	136.5	152.3	154.4	159.9	171.2	179.4	184.2	187.5	187.7	190.2	193.0
779	2377.6	8.75	0.0462	493.2	1.576	80.2	0.300	23.43	-0.699	-0.418	232.8	188.4	188.0	191.3	196.1	199.9	207.2	213.8	218.2	217.4	215.2	213.5	211.2
780	2385.6	10.44	0.0464	495.4	1.684	85.7	0.300	21.57	-0.726	-0.442	232.5	197.1	198.2	201.2	206.9	210.1	214.3	220.9	224.4	224.1	223.0	223.3	221.5
781	2378.9	9.43	0.0474	506.3	1.576	80.2	0.300	20.95	-0.730	-0.456	232.2	186.9	188.3	191.0	196.2	199.0	203.6	212.2	215.0	216.2	215.9	216.4	216.4
782	2352.0	8.42	0.0441	471.2	1.475	75.1	0.300	20.74	-0.718	-0.430	231.9	177.3	178.4	181.1	185.4	188.8	194.6	203.4	206.7	207.9	207.4	208.8	210.0
783	2391.7	7.74	0.0476	508.5	1.390	70.8	0.300	20.32	-0.744	-0.477	230.3	166.1	165.8	171.2	173.7	175.9	182.9	192.2	198.4	201.2	200.8	200.8	202.5
784	2397.8	6.40	0.0472	504.1	1.281	65.2	0.300	20.12	-0.750	-0.484	229.4	154.8	152.9	163.8	164.0	165.4	174.7	183.3	186.7	189.7	190.5	192.8	194.5
785	2408.5	5.39	0.0460	491.0	1.181	60.1	0.300	19.91	-0.758	-0.488	227.9	143.9	134.4	159.4	156.6	156.4	164.6	171.8	177.9	180.8	182.5	184.2	187.9
786	2393.7	11.11	0.0967	1031.9	1.619	82.4	0.360	71.88	-0.058	0.100	200.7	223.8	237.0	232.1	210.9	201.0	195.7	185.3	178.1	175.0	171.9	169.5	165.3
787	2391.0	12.46	0.0965	1029.7	1.441	73.4	0.360	72.10	-0.053	0.101	205.7	211.2	221.0	216.4	196.6	189.1	184.5	176.9	171.3	167.1	164.6	162.1	158.6
788	2380.9	12.79	0.0979	1045.1	1.259	64.1	0.360	72.10	-0.050	0.099	207.5	199.1	204.2	200.1	182.9	177.0	173.5	166.2	160.5	158.5	156.4	154.9	153.8
789	2382.3	13.47	0.0967	1031.9	1.085	55.3	0.360	72.10	-0.050	0.097	208.2	187.8	188.0	183.9	168.6	164.1	161.9	156.1	151.5	149.8	148.1	146.5	145.9

Run	p	Δp	m	G	power	q	hp-power	T_{in}	x_{in}	x_{DO}	T_{hp}	Distance from CHF location (m)											
-	kPa	kPa	Kgs^{-1}	$Kgm^{-2}s^{-1}$	kW	kWm^{-2}	kW	°C	-	-	°C	0.01	0.05	0.10	0.20	0.30	0.40	0.50	0.60	0.70	0.80	0.90	1.00
												Inside wall temperature (°C)											
790	2388.3	13.80	0.0946	1009.9	0.904	46.0	0.360	72.10	-0.052	0.096	208.8	176.5	170.9	166.6	156.4	152.7	149.7	145.1	141.6	140.4	139.1	138.3	138.0
791	2392.4	12.79	0.0938	1001.1	0.716	36.4	0.360	72.31	-0.050	0.096	208.2	162.5	152.3	146.8	138.4	136.6	135.5	134.0	131.5	129.6	127.7	127.7	126.6
792	2397.8	11.11	0.0921	983.5	0.548	27.9	0.360	72.73	-0.046	0.100	207.9	148.7	135.4	129.6	122.8	121.9	121.7	120.8	119.2	117.5	117.3	117.9	118.6
793	2395.7	10.10	0.0913	974.7	0.360	18.3	0.360	73.15	-0.038	0.106	207.3	134.6	116.0	110.0	104.2	104.2	104.6	104.0	103.4	103.2	103.4	104.3	106.2
794	2397.1	10.77	0.0971	1036.3	1.620	82.5	0.360	65.58	-0.155	0.002	204.8	222.1	234.4	234.3	220.2	215.3	210.4	200.4	191.9	187.9	183.9	180.5	177.1
795	2393.1	11.78	0.0989	1056.1	1.443	73.5	0.360	66.21	-0.144	0.007	207.0	210.4	218.9	218.0	206.8	202.2	198.6	192.8	187.2	181.4	176.0	172.0	168.0
796	2396.4	11.78	0.0992	1058.3	1.257	64.0	0.360	65.79	-0.151	-0.004	207.9	198.5	201.8	199.6	191.6	187.3	185.5	181.8	176.1	171.0	168.1	165.4	162.5
797	2395.7	11.78	0.0961	1025.3	1.082	55.1	0.360	66.00	-0.148	0.001	207.9	184.4	184.4	182.2	172.6	171.8	172.1	169.4	166.1	161.7	159.5	157.4	153.7
798	2390.4	10.44	0.0973	1038.5	0.898	45.7	0.360	66.21	-0.143	0.001	207.9	171.0	166.4	164.2	158.7	158.1	157.8	156.4	153.1	150.4	149.2	147.8	146.0
799	2392.4	8.75	0.0919	981.3	0.719	36.6	0.360	66.63	-0.137	0.012	207.3	157.0	148.1	145.0	140.8	139.6	141.3	139.5	137.8	137.6	137.4	137.0	135.7
800	2394.4	7.07	0.0954	1018.7	0.538	27.4	0.360	66.84	-0.135	0.006	206.7	144.2	129.1	124.5	120.3	121.5	122.7	121.8	122.5	122.0	122.7	123.0	124.2
801	2388.3	5.72	0.0926	987.9	0.365	18.6	0.360	66.63	-0.136	0.006	205.3	130.4	110.6	105.2	101.4	101.8	102.8	103.1	103.5	104.8	106.1	107.9	110.8
802	2388.3	11.45	0.0959	1023.1	1.614	82.2	0.360	60.12	-0.230	-0.072	210.5	206.5	219.5	222.7	214.3	212.0	211.7	208.9	205.9	201.1	196.3	188.8	175.7
803	2387.0	11.11	0.0952	1016.5	1.435	73.0	0.360	59.91	-0.232	-0.076	209.9	207.5	214.9	214.8	210.5	208.4	207.3	202.1	196.5	192.6	188.7	184.4	179.2
804	2389.0	10.44	0.0948	1012.1	1.262	64.3	0.360	59.91	-0.233	-0.079	209.6	195.3	198.0	197.3	195.5	194.9	193.9	189.6	185.8	183.3	180.8	176.5	172.4
805	2389.7	8.42	0.0919	981.3	1.077	54.8	0.360	60.12	-0.231	-0.075	209.0	181.3	178.8	178.1	176.7	178.1	178.1	175.6	173.0	171.8	170.7	169.0	167.5
806	2391.7	7.41	0.0917	979.1	0.902	45.9	0.360	60.12	-0.231	-0.079	207.8	167.3	159.5	157.7	156.7	157.9	160.4	160.1	158.6	158.9	159.1	160.0	161.9
807	2385.0	5.05	0.0981	1047.3	0.718	36.6	0.360	60.12	-0.229	-0.089	205.7	153.6	140.7	136.1	132.5	134.7	137.9	138.8	139.5	141.3	143.0	144.3	147.5
808	2383.6	3.70	0.0979	1045.1	0.548	27.9	0.360	59.91	-0.231	-0.094	202.7	136.9	120.6	116.3	110.7	111.5	113.9	116.0	117.3	119.7	122.0	125.4	131.3
809	2395.7	2.02	0.0965	1029.7	0.361	18.4	0.360	60.12	-0.233	-0.097	200.8	121.3	100.4	93.9	80.2	72.4	73.5	96.8	104.6	103.7	102.7	105.6	109.5
810	2389.7	6.73	0.0973	1038.5	1.619	82.4	0.360	48.40	-0.390	-0.234	201.8	216.6	229.9	228.4	226.4	225.6	228.9	227.4	224.4	223.9	223.4	223.7	222.8
811	2386.3	5.72	0.0934	996.7	1.440	73.3	0.360	48.20	-0.392	-0.232	200.9	202.1	210.0	205.9	203.9	206.6	210.8	211.7	211.3	211.6	212.0	210.1	209.0
812	2384.3	4.38	0.0965	1029.7	1.262	64.3	0.360	47.99	-0.393	-0.242	198.8	183.2	193.6	189.0	180.8	184.4	189.8	192.2	194.1	196.5	198.9	200.1	200.4
813	2384.3	3.03	0.0975	1040.7	1.077	54.8	0.360	47.99	-0.393	-0.247	195.4	162.8	171.3	173.0	159.7	161.0	165.7	169.3	173.1	177.0	180.9	182.4	183.0
814	2393.1	2.02	0.0967	1031.9	0.905	46.1	0.360	47.78	-0.400	-0.255	193.6	145.3	141.0	157.8	139.7	135.6	140.3	145.2	149.5	155.4	161.1	164.3	168.7
815	2388.3	4.71	0.1877	2003.9	1.967	100.1	0.432	69.99	-0.085	0.012	220.1	209.8	228.2	234.1	225.9	209.4	198.5	191.0	182.5	176.5	174.2	172.9	171.1
816	2389.0	3.70	0.1886	2012.7	1.784	90.8	0.432	69.99	-0.085	0.010	221.3	199.2	212.7	219.3	213.5	199.4	189.8	184.0	176.2	170.8	169.3	165.6	165.0
817	2393.7	3.37	0.1890	2017.1	1.584	80.7	0.432	70.20	-0.084	0.010	222.0	187.0	197.0	203.3	199.0	187.5	180.2	175.2	168.6	163.2	163.6	163.7	166.6
818	2393.7	4.04	0.1892	2019.3	1.380	70.2	0.432	70.20	-0.084	0.008	221.7	176.3	180.2	186.3	183.5	174.1	168.8	164.9	159.5	158.5	155.7	154.6	153.6
819	2391.0	3.37	0.1900	2028.1	1.181	60.1	0.432	69.99	-0.086	0.003	221.1	164.2	162.8	168.0	167.4	159.8	155.3	153.3	149.1	146.7	147.1	146.2	145.3
820	2389.7	3.70	0.1886	2012.7	0.989	50.3	0.432	70.20	-0.082	0.006	220.1	152.3	147.0	151.2	151.8	145.7	143.6	141.7	139.0	137.7	137.5	136.7	136.9
821	2393.1	3.70	0.1892	2019.3	0.794	40.4	0.432	69.99	-0.087	-0.001	219.2	142.3	131.9	134.6	136.1	131.6	129.7	128.8	126.3	125.9	126.2	126.1	126.9
822	2392.4	4.38	0.1879	2006.1	1.782	90.7	0.432	65.58	-0.153	-0.057	219.8	197.6	215.5	227.8	222.0	208.2	199.8	195.9	188.7	184.8	183.4	180.2	178.0

Run	p	Δp	m	G	power	q	hp-power	T_{in}	x_{in}	x_{DO}	T_{hp}	Distance from CHF location (m)											
-	kPa	kPa	Kgs^{-1}	$Kgm^{-2}s^{-1}$	kW	kWm^{-2}	kW	°C	-	-	°C	0.01	0.05	0.10	0.20	0.30	0.40	0.50	0.60	0.70	0.80	0.90	1.00
												Inside wall temperature (°C)											
823	2391.0	4.71	0.1890	2017.1	1.587	80.8	0.432	65.58	-0.153	-0.059	219.2	184.5	197.9	210.4	206.7	194.8	188.2	185.3	179.3	176.2	176.1	174.5	173.4
824	2396.4	4.71	0.1871	1997.3	1.382	70.3	0.432	65.58	-0.155	-0.062	218.4	171.5	178.8	190.3	189.1	179.0	174.6	172.3	167.8	166.6	166.4	166.1	165.5
825	2392.4	4.71	0.1892	2019.3	1.180	60.1	0.432	65.37	-0.156	-0.066	217.8	159.4	160.8	171.1	172.3	163.8	160.6	158.6	155.4	155.1	155.2	154.6	154.2
826	2391.0	4.71	0.1898	2025.9	0.988	50.3	0.432	65.37	-0.156	-0.068	215.6	145.3	141.6	149.7	154.9	147.6	145.2	144.2	141.6	141.7	142.7	142.8	142.6
827	2397.1	4.71	0.1919	2047.9	0.791	40.3	0.432	65.16	-0.161	-0.076	214.1	133.0	125.6	130.4	138.0	134.1	131.7	130.7	128.6	128.9	129.2	129.1	129.3
828	2393.7	5.05	0.1871	1997.3	1.772	90.2	0.432	60.54	-0.226	-0.130	213.5	186.4	210.1	235.1	231.5	216.1	206.9	204.9	198.9	195.9	195.7	192.4	188.5
829	2394.4	4.71	0.1906	2034.7	1.578	80.3	0.432	60.12	-0.232	-0.140	212.9	172.7	189.4	214.8	216.3	201.6	195.2	192.4	187.3	187.2	186.3	184.4	181.1
830	2395.7	5.05	0.1929	2058.8	1.382	70.3	0.432	60.12	-0.233	-0.143	211.7	157.2	165.9	186.6	200.1	185.8	177.6	177.5	173.6	173.6	174.7	173.8	172.2
831	2393.1	5.05	0.1888	2014.9	1.187	60.4	0.432	60.12	-0.232	-0.142	209.9	143.7	143.5	158.6	183.6	172.4	164.4	162.8	159.3	159.8	161.0	161.8	163.8
832	2394.4	5.05	0.1894	2021.5	1.584	80.6	0.432	55.51	-0.297	-0.203	204.7	148.1	150.7	183.2	245.1	219.1	204.2	199.4	192.8	192.2	193.9	193.5	195.4
833	2394.4	35.35	0.2792	2980.2	2.162	110.1	0.480	69.99	-0.087	-0.015	222.1	172.1	180.2	195.4	212.1	210.1	205.5	196.6	184.0	174.2	165.5	159.2	153.1
834	2391.0	34.00	0.2811	3000.0	1.981	100.8	0.480	69.99	-0.086	-0.015	218.2	163.0	168.7	182.1	198.9	200.1	196.5	191.2	179.4	170.5	162.5	155.6	148.7
835	2391.0	31.65	0.2817	3006.6	1.778	90.5	0.480	69.78	-0.089	-0.020	216.4	153.6	156.3	167.8	183.9	188.0	186.9	183.9	174.9	165.9	159.8	152.2	145.8
836	2391.0	30.64	0.2825	3015.4	1.584	80.7	0.480	69.78	-0.089	-0.021	214.0	144.3	144.8	155.0	169.3	175.2	177.2	176.0	169.7	162.8	157.7	151.2	143.7
837	2390.4	28.28	0.2798	2986.8	1.386	70.6	0.480	69.78	-0.089	-0.021	212.1	136.8	134.9	143.1	155.1	161.5	164.9	165.7	161.6	159.1	153.3	147.7	141.4
838	2387.7	26.26	0.2813	3002.2	1.193	60.7	0.480	69.99	-0.085	-0.019	210.9	128.2	124.1	129.6	138.9	145.0	149.7	153.6	152.2	149.2	148.0	144.4	141.2
839	2385.6	30.64	0.2805	2993.4	2.175	110.7	0.480	65.37	-0.154	-0.081	209.2	163.6	175.5	195.6	218.3	218.7	214.4	207.1	197.5	188.1	183.3	178.2	170.5
840	2385.6	29.29	0.2813	3002.2	1.973	100.4	0.480	65.37	-0.154	-0.083	207.1	153.1	161.5	178.9	201.1	206.3	204.6	199.6	190.8	181.5	178.2	172.2	164.8
841	2394.4	27.27	0.2823	3013.2	1.776	90.4	0.480	65.16	-0.160	-0.090	206.2	142.3	147.0	161.2	181.7	191.5	193.9	191.7	183.9	176.9	173.3	166.8	160.3
842	2389.7	25.25	0.2809	2997.8	1.590	80.9	0.480	64.95	-0.161	-0.093	205.3	135.7	136.7	147.9	166.4	177.1	181.2	183.2	177.5	172.1	168.5	162.8	156.1
843	2387.0	23.23	0.2835	3026.4	1.382	70.4	0.480	64.95	-0.160	-0.093	203.8	125.6	122.4	129.0	142.3	152.2	164.3	168.6	168.1	168.4	164.6	159.3	153.2
844	2393.1	25.92	0.2819	3008.8	2.167	110.3	0.480	60.12	-0.232	-0.160	221.6	153.2	159.7	181.1	214.6	224.1	223.0	216.5	208.1	203.7	197.6	193.8	188.8
845	2385.6	24.24	0.2819	3008.8	1.977	100.7	0.480	60.33	-0.226	-0.155	216.7	140.2	138.6	153.7	185.7	205.0	211.5	210.4	202.9	197.4	191.2	186.9	181.4
846	2385.0	22.56	0.2819	3008.8	1.778	90.5	0.480	60.33	-0.226	-0.156	211.3	130.1	119.1	118.0	146.9	171.8	187.9	200.5	199.4	193.9	188.6	183.4	176.9
847	2385.0	73.39	0.3769	4022.6	2.363	120.3	0.480	70.20	-0.081	-0.026	190.0	133.0	139.5	153.1	169.6	182.5	190.7	198.9	195.0	185.1	175.1	162.7	149.4
848	2409.2	67.00	0.3717	3967.6	2.169	110.4	0.480	70.62	-0.083	-0.028	188.8	127.4	132.6	144.2	158.7	170.4	179.3	188.3	188.1	182.4	176.7	164.3	152.6
849	2389.7	65.65	0.3752	4005.0	1.968	100.2	0.480	70.62	-0.076	-0.023	188.1	121.8	124.7	134.4	146.5	156.5	165.5	174.5	177.0	175.7	174.4	166.5	153.5
850	2390.4	61.95	0.3785	4040.2	1.775	90.4	0.480	70.62	-0.076	-0.024	186.7	114.4	116.3	124.4	134.3	141.9	149.8	157.9	162.6	165.0	167.3	165.0	157.6
851	2392.4	64.30	0.3721	3972.0	2.760	140.5	0.552	64.95	-0.162	-0.098	226.9	142.8	149.4	168.0	195.2	215.1	222.8	230.5	221.8	208.8	197.7	181.7	166.9
852	2390.4	62.28	0.3777	4031.4	2.562	130.4	0.552	64.95	-0.162	-0.099	226.1	137.3	138.7	154.5	178.9	198.2	209.1	220.4	216.2	207.3	198.7	183.9	169.8
853	2397.8	59.25	0.3721	3972.0	2.366	120.4	0.552	65.37	-0.158	-0.096	221.2	130.1	128.7	142.0	163.0	179.2	192.3	205.4	206.8	203.2	199.6	186.3	171.9
854	2392.4	56.56	0.3779	4033.6	2.176	110.8	0.552	65.16	-0.159	-0.099	220.4	120.9	115.1	126.2	146.1	161.0	174.1	187.2	194.1	195.2	196.4	189.4	179.0
855	2370.8	53.87	0.3802	4057.7	1.969	100.2	0.552	64.95	-0.154	-0.096	219.3	114.8	104.6	109.3	129.4	143.3	154.9	166.3	175.3	180.9	186.4	186.5	187.4

Effect of hot-patch experimental data

Time	p	Δp	m	G	power	q	hp-power	T_{in}	x_{in}	x_{DO}	T_{hp}	Distance from CHF location (m)											
s	kPa	kPa	Kgs^{-1}	$Kgm^{-2}s^{-1}$	kW	kWm^{-2}	kW	°C	-	-	°C	0.01	0.05	0.10	0.20	0.30	0.40	0.50	0.60	0.70	0.80	0.90	1.00
												Inside wall temperature (°C)											
0	2389.7	4.71	0.0950	1014.3	1.619	82.3	0.360	41.73	-0.481	-0.321	161.8	166.4	226.9	232.9	213.4	216.5	225.5	227.4	228.1	229.3	232.2	227.1	213.0
237	2385.6	4.38	0.0932	994.5	1.616	82.3	0.000	41.94	-0.476	-0.447	76.5	75.3	75.8	75.7	221.3	216.6	224.4	226.5	227.5	230.3	231.6	227.1	212.9
0	968.3	21.21	0.1888	2014.9	1.676	85.3	0.360	24.88	-0.117	-0.061	188.3	213.8	232.8	233.6	232.4	224.0	218.8	222.7	216.4	213.2	211.2	201.9	185.8
469	951.4	22.56	0.1840	1964.3	1.671	85.1	0.000	24.88	-0.111	-0.101	45.8	42.6	42.6	42.9	235.4	230.3	221.8	223.9	217.0	213.2	211.5	201.5	185.5
0	635.0	23.23	0.1886	2012.7	1.578	80.3	0.360	7.92	-0.120	-0.069	197.2	206.4	216.9	222.8	227.1	227.9	229.7	231.3	229.4	226.6	224.0	216.3	201.0
393	641.0	25.59	0.1809	1931.3	1.580	80.4	0.000	6.89	-0.131	-0.121	35.3	29.8	190.5	217.2	229.0	229.4	227.4	232.2	226.9	224.4	220.8	211.3	194.6
418	637.7	24.91	0.1884	2010.5	1.579	80.4	0.000	6.68	-0.132	-0.123	32.1	28.6	33.9	213.8	227.8	227.4	227.4	231.7	227.6	225.4	222.3	213.9	197.6
475	637.7	23.23	0.1890	2017.1	1.578	80.3	0.000	6.89	-0.130	-0.121	30.5	27.4	27.3	28.2	218.7	224.5	225.4	231.1	227.9	225.4	225.6	219.0	203.8
578	637.0	23.57	0.1867	1992.9	1.573	80.1	0.000	6.89	-0.129	-0.120	30.0	26.5	26.7	27.0	32.4	219.0	227.4	231.7	228.8	227.4	228.0	221.2	206.2
0	961.5	13.47	0.0452	482.2	1.440	80.3	0.360	9.98	-0.240	-0.007	179.9	179.9	195.8	207.2	214.1	219.7	227.5	226.0	226.6	228.9	231.1	227.3	216.4
335	972.3	13.47	0.0472	504.1	1.442	80.4	0.000	9.98	-0.243	-0.204	48.3	43.5	207.4	221.8	218.9	220.9	227.5	225.4	224.0	226.0	228.1	224.5	213.7
398	957.5	12.79	0.0481	512.9	1.438	80.2	0.000	9.98	-0.237	-0.199	44.8	41.8	42.9	216.9	218.4	220.6	227.8	226.3	226.1	228.3	230.5	226.7	214.9
450	950.1	12.79	0.0458	488.8	1.438	80.2	0.000	9.98	-0.234	-0.194	42.7	40.6	40.9	202.4	216.5	221.2	228.8	227.2	227.3	229.5	231.7	227.9	216.4